CONSTRAINTS ON THE SCALE OF TOROIDAL FUSION EXPERIMENTS WITH APPLICATION TO THE DESIGN OF A HELICAL AXIS STELLARATOR

by
Jean-Marie Noterdaeme

Burgerlijk Werktuigkundig Electrotechnisch Ingenieur
Rijksuniversiteit Gent, Belgium (1977)

Master of Science in Nuclear Engineering
Massachusetts Institute of Technology, Cambridge (1978)

Submitted to the Department of
Nuclear Engineering
in Partial Fulfillment of the Requirements
for the Degree of

DOCTOR OF PHILOSOPHY

in Nuclear Engineering

at the
MASSACHUSETTS INSTITUTE OF TECHNOLOGY
May 1983

Signature of Author _____
Department of Nuclear Engineering
May 10,1983

Certified by _____
Dr. D.B. Montgomery, Thesis Supervisor

Accepted by _____
Prof. A.F. Henry, Chairman, Nuclear Engineering Departmental Committee

Constraints on the Scale of Toroidal Fusion Experiments with Application to the Design of a Helical Axis Stellarator

by
Jean-Marie Noterdaeme

submitted to the Department of Nuclear Engineering on May 10, 1983
in partial fulfillment of the requirements for the Degree of
Doctor of Philosophy in Nuclear Engineering

Abstract

A key issue if we want to resolve some of the unanswered questions related to the plasma physics properties of magnetic fusion concepts is: what is the minimum scale of an experiment to test those properties. A general step by step method has been developed to answer this question. It can be applied to any particular toroidal concept and is based on the fact that we can consider small scale experiments as models of larger experiments by applying the method of similarities. A minimum scale for the experiment arise then from a combination of three factors: constraints on the parameter space in which one or more of the dimensionless parameters can be dropped so as to be able to obtain a scaled experiment; constraints resulting from factors that are not included in the similarity scaling; and constraints on the possibility of actually obtaining the parameters (geometrical, plasma physics and technological) mandated by similarity considerations. Those three sets of constraints have been investigated.

Applying the constraints to the design of a helical axis stellarator we find a limit on the combination of toroidal field, current density and major radius $\frac{(\frac{B_T}{\nabla \Psi})}{(\frac{1}{2\times 10^7 A/m^2})(\frac{B_T}{m})} < 0.45$.

Another major constraint for this concept is the ability to obtain the plasma physics parameters dictated by similarity considerations. This depends on the heating method used. A minimum scale experiment with 2 periods and no linkage of the toroidal and poloidal coils, would have a major radius of $1.2m$, a toroidal field of $3.5T$ and $2MW$ of ECRH power (for $\beta = 1\%$, $\nu_* = 10$).

Thesis Supervisor: Dr. D.B. Montgomery
Title: Associate Director for Engineering Systems, Plasma Fusion Center
Thesis Reader: Prof. L.M. Lidsky
Title: Professor of Nuclear Engineering

... and they shall beat their swords into plowshares,
and their spears into pruning hooks;
nation shall not lift up sword against nation,
neither shall they learn war any more.
Isaiah 2, 4

To Michèle

Acknowledgments

It was a pleasure to work with Dr. D.B. Montgomery as thesis supervisor. He had from the start a very clear idea of what the main trust of the thesis was. In the shifting interests along the way he kept the goal firmly in sight and helped me focus on the most important aspects.

Professor L.M. Lidsky, my thesis reader has taught me much more than plasma physics and engineering. I want to express towards him, the words he used in his thesis to thank his advisor, Professor David J. Rose : " An expression of my true gratitude would seem obsequious to those who do not know him, insufficient to those who do ".

I am indebted to Dr. P.A.Politzer for his critical comments on the manuscript. His comments have definitely improved the readability of this thesis. I would also like to thank him for making available to me the results of his numerical calculations, related to the influence on the magnetic geometry, of the ring current and the vertical field for a helical axis stellarator. It is based on those results that I was able to develop the model presented in Appendix D. He also made availale the computer program he used for his calculations.

In addition, I would like to offer my thanks to numerous people of the Plasma Fusion Center and the Francis Bitter National Magnet Laboratory for helpful discussions and insight: Don Blackfield, Boyd Blackwell, Emmanuel Bobrov, Catherine Fiore, Bob Granetz, Martin Greenwald, Ken Kreischer, Brian Labombard, Bill Marable, Earl Marmar, Joel Schultz, Bob Weggel, and Steve Wolfe.

Special thanks to John Aspinal and Peter Roemer. John provided the computer code SOLVE and, as a real wizard, always knew what to do when the computer did not understand me anymore. The perspective views included in this thesis were made using a program Peter developed for his thesis.

My officemates, Ko Kato, John Machuzak and Tom Morizio made working here enjoyable and provided some valuable help and insight.

A word of praise to Layla McKnight, Beth Nadworny and Laurie Pfeifer for the many little things that need to be done and usually go unnoticed, especially when they are well done. Appendix A and B were issued as separate reports and were typed by Anna Kotsopoulos, who suffered through many revisions without complaints. Beverly Colby, the PFC librarian, was very helpful in locating references, and in obtaining some that were difficult to get.

I would like to thank my parents for having provided me with a sound education and basis upon which to build further.

My dear wife Michèle has done a titanic job in those last two years. Not only did she obtained her medical degree, but she managed to give us a marvelous little son, and to take care of him. She ran the household singlehandedly to free me of all practical concerns. At the same time she typed most of this thesis and labeled all the figures. And still, she was there when I needed her.

I very much appreciate the support of the Belgian National Foundation for Scientific Research who supported me for those two years. My thanks also to Professor F. Van Massenhove of the University of Ghent for being my supervisor there.

Table of Contents

List of Figures

List of Tables

1. Introduction.

1.1. Goal of the thesis

The starting point of this thesis was a question asked during a discussion about the the design of magnetic fusion experiments. "Why can't we build a 1 Gauss machine ?" And as some apparently simple questions usually do, it posed an important problem. What in fact are the constraints that set a minimum scale for an experiment ? The answer to this question depends strongly on the experimental objective (what we want to achieve). It is thus important at first to more clearly delineate the task. Since the answer also depends on the experimental format (how we want to achieve it) we have concentrated on identifying general constraints and developing a step by step method to find the minimum scale so that the method can be applied to any particular toroidal experiment. This is the primary goal of this thesis. The secondary goal is then to apply the method to the design of a specific type of helical axis stellarator, thus identifying the constraints and minimum size for this particular variation.

1.2. Definition of the problem

The constraints on the scale of an experiment depend in part on the goal for the experiment. A machine built to investigate single particle containment, and to

trace out magnetic surfaces, as was the case for CLASP [1] resulted in a small ($R = 30\,cm$, $a = 11.5\,cm$, $B = 1T$) high shear stellarator. This simple machine was subjected to quite different design constraints than a machine like ZEPHYR [2] designed to investigate α particle heating and ignition physics. A machine built to test radio-frequency heating may be quite different from a machine used to test refueling by pellet injection.

The question that was the starting point of this thesis, as alluded to in the previous section, namely the question of the constraints on the scale of a fusion experiment, was asked specifically in the context of the ability to test the plasma physics properties of a particular concept. We will thus restrict ourselves to addressing the issues of constraints for experiments with a specific goal : the experimental investigation of plasma physics properties of a particular concept. This restriction not only more clearly delineates the task, but is also justified on the following grounds.

The goal of investigating the plasma physics properties of a concept in itself is a very important and timely problem. Present experiments are mainly in the tokamak/mirror line. Their success is squeezing out the investigation of alternative concepts that may result in a better end product. While both the tokamak and the mirror have obtained results, that in terms of temperature and $n\tau$ are closer to the Lawson criterion than any other concepts, they have significant drawbacks (low power density, large recirculating power fraction) that could make them unattractive as power producing reactors. The successes of the tokamak and mirror lines in terms of plasma physics parameters have been rewarded with funds for increasingly larger machines, at the expense of other, possibly more reactor-friendly concepts still in the earlier stages of their development. This policy could prove to be disastrous in the long term, when fusion research will be faced with the realities of commercialization.

At that point fusion research and development could encounter a fate similar to many projects that fail not so much because of scientific or technical problems, but because the end product was neither wanted or needed. Fusion research

should keep in mind that in the end it should provide humanity with a source of energy that is more attractive than the energy sources it intends to replace.

While a number of alternative concepts have potential advantages that could make them better commercial reactors, their weak point is often that little is known about their plasma physics properties. It is thus important to fill this gap in our knowledge, and to do it now, before we are definitively engaged in the path that will only give us the choice between the tokamak and the mirror.

The investigation of the plasma physics properties of a concept is not only important and timely, but the question of constraints on the minimum scale is particularly relevant for those experiments. Indeed, building the machine and performing the experiments is in this case the only way to go.

Less ambitious experiments, which were justifiable in the past, have either already been done or could now be performed by other means. Since fast computers have become available, and because the equations governing the phenomena are well known and tractable, an experiment as CLASP to investigate single particle containment and to map out magnetic surfaces, could now more easily and with confidence be done on a computer. Thus there is no need to build a machine.

More ambitious experiments related to α-particle heating and ignition physics, as well as experiments testing heating methods or refueling for example can be considered as more or less concept independent. Those extremely important aspects could thus be tested on whatever concept or scheme that makes it easiest. Testing refueling by pellet injection in Alcator C is an extremely valuable experiment and the results are independent of the fact that Alcator C is a tokamak. Some of those experiments could thus be performed in existing machines, while others require a very specific and rather well-known (Lawson criterion) set of constraints. The question of identifying the constraints that set a minimum scale is thus less pertinent for those experiments.

We have thus restricted ourselves to looking at the constraints for experiments with the goal : experimental investigation of the plasma physics properties of a concept. We have then to ask ourselves whether the plasma physics properties of a concept can be investigated in an experiment smaller than the full scale reactor size. Only if this question can be answered positively and if we find a method to obtain on a small experiment results that have relevance to the full scale reactor, is it even remotely significant to address the issue of the constraints that set a minimum scale.

1.3. The use of similarity and the resulting constraints

Two approaches to investigate the plasma physics properties of a concept are possible:

The first one is to rely on experiments only. We can the try to model the plasma physics processes that occur in a reactor size experiment in a scale version. The issue of relevance of the results of scaled experiments is then answered in the same way that is used in other fields like hydraulics and aerodynamics : by the use of similarity. This method is widely applied in those fields to obtain from scaled versions (small models) results that can then be translated into results of significance for the full scale object. The relevance of the scaled experiment is justified based on the fact that, under some conditions, it models the same processes as in the large version, and thus allows us to obtain information on them. Sometimes the requirements are so stringent that no small experiments could be build.

A second approach is then to rely partly on theory. Small experiments may be used to check certain aspects of a theory. If this results in less stringent constraints for the experiment than the first approach, it may be a first, confidence building, step towards a second, larger experiment that then would model the plasma physics processes of a reactor. For this second approach too, when we look at the minimum size, we have to compare machines that fulfill the goal to the same extend. This again can be done by using the method of

similarity.

The difference in applying the method of similarity for the first and second approach is only in the following: the family of machines, among which we choose the one which, within constraints, is the minimum scale member contains also the reactor, if we use the first approach. Using the second approach, we choose the minimum scale member among a family which does not contain the reactor. Each member of the family however, is similar in that it will test theory to the same extend. Let us briefly discuss the method and how it automatically results in the constraints that set a minimum scale for a model.

The use of similarity [3] requires that a constant scale factor exists between the geometry of the different members of the family. and the model. It further requires that a certain number of dimensionless parameters be kept constant between them. Three additional steps have to be taken and those steps give the constraints that result in a minimum scale.

First applying similarity considerations must be possible i.e. the degrees of freedom and the number of dimensionless parameters that have to be kept constant must be indeed such that there is some freedom left in making a scaled experiment. This sometimes entails not keeping one or more dimensionless parameters constant, in cases where it would give us additional freedom without interfering with the results of an experiment. An example in hydraulics is neglecting to keep the Mach number constant in cases where the fluid can be assumed incompressible. It increases our degrees of freedom in making a scaled experiment, but restricts us to look at incompressible fluids only.

The second step is to consider effects that have not, or could not, be included in similarity considerations. Again a typical example in hydraulics is that, when one makes a scaled version of a simple pipe, the relative roughness of the inside of the pipe should stay constant. This would mean that if we scale down a large pipe with normal finish on the inside, the scaled version needs a highly polished surface. If we can not achieve this highly polished surface, we have to discuss under what conditions it is justifiable to neglect the influence of this, or

alternatively we have to find some clever ways of obtaining something similar to it.

The third step is to investigate whether the model, as obtained from similarity considerations can actually be built, and whether the new values of the variables derived from similarity conditions can be achieved.

In the case of plasma physics experiments, the geometry that has to be to scale as required by the similarity considerations, is the magnetic geometry. There must thus be a constant scale factor on all linear dimensions between the full scale system and the model (to keep the relative direction of the magnetic field), and a constant scale factor on all the currents (scale factor on the magnitude of the magnetic field). We can then identify what the dimensionless parameters are that should be kept constant. The total number of dimensionless parameters to be kept constant, however, equals the degrees of freedom and thus, strictly speaking, no scaled model could be built.

We therefore investigate in a first step, how we can gain more freedom by dropping one or more of the dimensionless parameters. Relying on theoretical models and experiments we set conditions under which we can actually justify dropping some of those parameters. It is also shown that the choice of the parameters we drop, depends on what we want to investigate.

The second step is to investigate effects that were not included in the similarity considerations for plasma physics, in particular the neutrals and the impurities. For both we address specifically the mechanisms for their presence in the plasma, and we evaluate their level and obtain the conditions under which we can neglect their influence. We also qualitatively discuss what factors affect their level and importance, and how some appropriate methods can be used to control them.

The third step, investigating whether the new values of the variable, obtained by similarity conditions, can in practice be achieved, has to be addressed on two fronts.

One front is whether the plasma physics parameters thus derived can indeed be obtained. It is discussed in terms of plasma production and heating. The other front is the engineering parameters. This discussion is rather extensive because there is such a wide variety of choices, but at the same time some of the limits are rather stringent. Two major constraints are current density limits and stress limits. Both are critically reviewed. They will, together with the specifics of a particular geometry, set constraints on a combination of magnetic field and size. Another constraint, less stringent in absolute terms, is however, extremely important : the cost of the experiment. It is a function of the size, mass, engineering choices, pulse length of the experiment, stored energy etc.. but also in part, on what is already available at a particular site. To approach the problem in sufficient generality we concentrate on developing some relations between stored energy, pulse length and mass of the system in order to be able to translate the current density and stress limits, as well as the availability of energy and funds, into limits on the size and field of the machine. The discussion of the method of similarity and the resulting constraints are addressed in chapter 2, except for the constraints resulting from engineering considerations, which are discussed in chapter 3.

The constraints that can arise because of the specific geometry of a particular concept are not addressed in general, but they are discussed later for a particular choice of concept : the stellarator with helical magnetic axis.

The use of similarity, and the additional steps that automatically result in the constraints and limits that set a minimum scale for the experiment, clearly suggest a method to find this minimum scale. For a particular choice of concept and geometry we can identify values of dimensionless parameters that would yield relevant experiments. For a choice of values for β and ν for example, we can then plot in a diagram of size versus magnetic field, the corresponding plasma density and temperature. In this diagram the constraints and limits can be drawn, yielding a design window. Within the limits a choice can then be made according to minimum size, minimum cost, minimum heating power, or

other considerations.

1.4. Application to the design of a stellarator with helical magnetic axis

To illustrate the method and address more specifically some of the concept dependent constraints, we apply the method to the design of a stellarator with helical magnetic axis. This is done in chapter 4.

The stellarator with helical magnetic axis being a somewhat unfamiliar concept, is briefly introduced -its main properties, possible variations and the reasons for this choice. The method of similarity does not say anything in particular about geometry and as this varies markedly from one concept to another, it was not discussed in the general case. It is, however, a very important aspect because it can have an impact both on the dimensionless parameters that can be achieved and on the constraints and limits.

The geometry is thus discussed in detail for this particular concept. We identify the parameters that define the geometry and separate them into hard parameters (number of periods, aspect ratio) and soft parameters (current in the ring, vertical field). The influence of the soft parameters is discussed. The choice for the hard parameters is made and justified, based on some geometrical constraints and on the interaction of the geometry with the dimensionless parameters.

Based on theoretically achievable values and on values one would like to achieve in terms of relevance of the experiment, a choice is made for the dimensionless variables. Using the "three steps" constraints developed earlier, we identify the parameter space in a size versus magnetic field diagram where relevant experiments can be performed. Within this design window further constraints and/or choices, result in an unique configuration of size and magnetic field that can be the reference case for a more detailed design.

1.5. Organization of the thesis and major contributions

This report is organized as follows. Chapter 2 groups the constraints and limits resulting from plasma physics considerations. There we discuss the method of similarity and address the first two steps and the first part of the third: whether we can drop one or more of the dimensionless parameters; the factors that are not included in the similarity scaling; and the issue pertaining to the possibility of achieving the plasma physics parameters mandated by similarity considerations. Chapter 3 addresses in more detail the engineering and technological considerations (second part of the third step). Chapter 4 applies the method developed in the previous chapters to the design of a helical axis stellarator. Chapter 5 summarizes the results.

The major original contribution of this thesis is the global approach to the problem that provides a structured, justifiable method for the design of a small experiment. Within this framework the goal can be chosen, and limits and constraints identified that set a minimum scale for the experiment.

The most important original contributions in each of the three chapters (plasma physics, engineering, and the helical axis stellarator) are :

- development of a qualitative model for plasma-wall interaction that explains a large number of different experimental results related to recycling at the wall and impurity production; while quantitative models exist that are applicable to particular machines, this model gives a qualitative explanation of the different, and seemingly unrelated behaviors observed on different machines.
- development of a method to analyze circular toroidal coils; it takes into account both in-plane reactions as provided, for example by a central supporting column and the reactions resulting from the out-of-plane structure; the method confirmed that circular toroidal coils need not necessarily be dominated by moments and highlighted the importance of proper distribution of the net reaction force between external and internal reaction forces to obtain this result.
- development of a simple model that explains the variation of position and

winding law of the magnetic axis of a helical axis stellarator in terms of vertical field and poloidal ring current; the model results in some simple analytical expressions and provides a method to obtain efficiently and accurately the variation of the major parameters associated with the helical magnetic axis.

2. Plasma Physics and Dimensionless Parameters

2.1. Introduction

Nothing but a full scale operating reactor can prove the scientific and engineering feasibility of a fusion reactor in a definitive fashion. However, as building such a reactor requires a large investment, it is imperative to gather as much information as possible on smaller and less costly experiments. Can useful information indeed be gathered on small experiments about the behavior of large experiment? Under certain conditions this is indeed the case. From the method of similarity [3] we know that if certain dimensionless constants are the same in a small experiment as in a full scale system, then the phenomena described will be similar and results obtained on the experiment can be related to the behavior of the full scale system.

In plasma physics and fusion research, although the method is known, there seem to be a tendency to build experiments more to obtain absolute values close to a reactor rather than combinations of parameters such that the dimensionless parameters have the same value as for a reactor.

From arguments based on ignition temperature, power density, and constraints related to the need for tritium breeding we can say that the plasma physics parameters at which a D-T reactor will operate are rather well known. However,

crucial information on energy confinement time, and β limits is still unavailable. While it is laudable to try to obtain parameters as close as possible to reactor values in terms of n, T, $n\tau$ it is of vital importance to obtain scaling laws and relationships for the energy confinement time and the β limits. Relationships obtained in machines that do not achieve record temperature, density or $n\tau$ product may be more relevant to a reactor if the dimensionless parameters have the proper value than relationships obtained on machines that shoot for reactor relevant temperature and densities. To put it even more bluntly, the scientific progress and understanding of plasma physics achieved on machines whose parameters do not show up on the famous $n\tau$, T diagram may bear more relevance to reactor regimes than the experiments performed to achieve records and to approach the ignition curve.

The use of dimensionless parameters is also called for when we want to find the minimum scale machine to test certain aspects of a theory. Indeed, when looking for the minimum scale, we should compare machines that test the theory to the same extend. In this chapter we intend to discuss the method of similarity and derive the dimensionless parameters applicable to plasma physics experiments. We will then investigate the plasma physics constraints that result from the three additional steps we have to take as mentioned in the introduction. We will investigate the applicability of the method and the implication of not keeping constant one or more of the dimensionless parameters. This will restrict the parameter space in which meaningful experiments can be performed. The presence of neutrals and impurities can spoil the similarity between a model and the original. Therefore we investigate separately under what conditions their influence as to the application of similarity scaling laws can be neglected. From this we will obtain a parameter space where useful experiments can be performed. Whether experiments can actually be performed in this parameter space will depend on a number of constraints making areas of the parameter space inaccessible. Some of those constraints, related to plasma physics parameters, will be discussed here, while others, more technically related, are the focus of

the next chapter.

2.2. Similarity Scaling Laws

The application of similarity, and similarity scaling laws is routinely used in fields as hydraulics and aerodynamics to obtain from scaled models information that is more generally applicable.

The central point of the method is that if certain dimensionless combinations of parameters have the same value for the different members of a family of devices, the phenomena will be governed by identical relations. The results of an experiment on one member of the family, can then be related to results for any other member.

Two methods can be applied to derive the dimensionless combinations that govern a certain phenomenon.

The first method is to count the number of independent parameters and the number of dimensions. The theorem of Buckingham [3] then argues that the number of dimensionless parameters equals the number of independent parameters, minus the number of dimensions. Once the number of dimensionless parameters is known it is easy to construct them. This first method to derive the dimensionless parameters is applicable even if no explicit knowledge is available on the equations governing the phenomena, but requires some care and proper judgment in the selection of the parameters. An excellent work on dimensional analysis, and its application to model experiments was written by P.W. Bridgman [4].

A second method to obtain the dimensionless parameters is available if we know the underlying equations. By writing down the equations and investigating under which transformations those equations are invariant one can identify the dimensionless combinations that have to be constant in order for the equations to model the same phenomena. This second method allows one to

derive dimensionless parameters without having to know explicitly which are dependent and which are independent variables.

We will now present a simple example from hydraulics to clarify both methods, their advantages and limitations.

2.2.1. A Simple Example

Suppose a centrifugal pump needs to pump a certain volume of water. We want to know what the power rating should be for the motor driving the pump. The problem can be solved by building a model and measuring the power needed to drive the model. How should we choose the parameters so that from the power measured on the model, the power needed on the full scale pump can be calculated.

To apply the first method we identify the independent parameters. They are the type of fluid used (μ and ρ), some linear dimension (D), the flow to be pumped (Q) and the rotational speed of the pump (ω). For a given fluid, pump, and rotational speed, we can still vary the flow rate by using a throttle valve. Rather than using the flow to be pumped (Q) as an independent parameter, we could use the pressure drop (Δp) over the pump. But the pressure drop is not an *additional* independent variable. Or *instead* of the rotational speed (ω) one could use (Δp). A thought experiment however (what can we vary independently) can convince us that for an incompressible fluid, there are only five independent parameters. The five we have chosen have the following dimensions

$$[\mu] = \frac{kg}{ms}$$
$$[\rho] = \frac{kg}{m^3}$$
$$[D] = m$$
$$[Q] = \frac{m^3}{s}$$
$$[\omega] = \frac{1}{s}$$

There are thus three dimensions (kg, m, s). The number of dimensionless constants is $5 - 3 = 2$. The construction of the dimensionless parameters is

then simple. We take the general form

$$\Pi = \mu^{\alpha} \rho^{\beta} D^{\gamma} Q^{\delta} \omega^{\epsilon}$$

and request that Π be dimensionless, i.e. the total exponent for each dimension must be zero. This results in three equations (one per dimension)

$$\alpha + \beta = 0$$

$$-\alpha - 3\beta + \gamma + 3\delta = 0$$

$$-\alpha - \delta - \epsilon = 0$$

We can solve this set of equations for β, γ and ϵ as a function of α and δ. Two independent solutions of this set of equations are then found by choosing $\alpha = -1$, $\delta = 1$ and $\alpha = 0$, $\delta = 1$. This results in the two independent parameters

$$\Pi_1 = \frac{\rho}{\mu} \frac{Q}{D} = Re$$

and

$$\Pi_2 = \frac{Q}{\omega D^3}$$

Other choices for α and δ would have been possible, but they would not affect what follows. From similarity we know that if we build a model, and keep the same value for those two dimensionless parameters as in the full scale model we can calculate the power on the full scale machine from the power needed to drive the model. Building a model to 1/5 scale, while using the same fluid (water, same μ and ρ) we need to set the flow in the model (to keep Π_1 constant) to 1/5 the value we need in the large pump and the speed at 5^2 the rotational speed of the large pump (to keep Π_2 constant).

If we had chosen the pressure drop (Δp) rather than the rotational speed (ω) as an independent parameter, then the dimensionless parameter

$$\Pi_3 = \frac{\Delta p D^3}{\mu Q}$$

would be used instead of Π_2.

The way to calculate the power P needed for the full scale machine from the experiment is based on the fact that, if normalized (made dimensionless) the value of the dependent parameters too is identical in both machines. Thus $\frac{P}{\omega^2 \rho Q D^2}$ is identical in both machines, so that the full scale machine will need 1/5 the power the model needed. Note that parameter scans (how for example the power varies when varying the flow) can be made on the scaled model, the functional dependence

$$\frac{P}{\omega^2 \rho Q D^2} = F\left(Re, \frac{Q}{\omega D^3}\right)$$

being independent of the scale of the machine.

Let us now solve the same problem by using the second method. The equations governing the phenomena are the Navier-Stokes equation, and the continuity equation. For steady state ($\frac{\partial}{\partial t} = 0$), and incompressible fluids ($\rho = constant$) those equations are

$$\rho \bar{v} \cdot \bar{\nabla} \bar{v} = \bar{F} - \bar{\nabla} p - \mu \bar{\nabla}^2 \bar{v}$$

$$\bar{\nabla} \cdot \bar{v} = 0$$

We can now find the independent linear transformation $\rho \rightarrow k_\rho \rho$, $D \rightarrow k_D D$, $\bar{v} \rightarrow k_v \bar{v}$, $\bar{F} \rightarrow k_F \bar{F}$, $p \rightarrow k_p p$, $\mu \rightarrow k_\mu \mu$, that keep the equations invariant. By substituting those transformations into the equations and requesting that the equations do not change we obtain

$$\frac{k_\rho k_v^2}{k_D} = k_F = \frac{k_p}{k_D} = \frac{k_\mu k_v}{k_D^2}.$$

This can also be written as

$$\frac{k_\rho k_v^2}{k_D} = \frac{k_\mu k_v}{k_D^2}$$

$$\frac{k_\rho k_v^2}{k_D} = k_F$$

$$\frac{k_p}{k_D} = \frac{k_\mu k_v}{k_D^2}$$

and thus three dimensionless parameters can be constructed.

$$\Pi_{1'} = \frac{\rho v D}{\mu}$$

$$\Pi_{2'} = \frac{\rho v^2}{F D}$$

$$\Pi_{3'} = \frac{p D}{\mu v}$$

The Navier-Stokes equation, using those dimensionless parameters, can be written in dimensionless form, and result in a relationship between the dimensionless parameters. Two of them can thus be taken as independent (for example $\Pi_{1'}$ and $\Pi_{2'}$), the third one is then a dependent dimensionless parameter $\Pi_{3'}$. There are three independent transformations

$$k_D = \alpha$$

$$k_v = \alpha^{-1}$$

$$k_F = \alpha^{-3}$$

$$k_p = \alpha^{-2}$$

and

$$k_v = \beta$$

$$k_\rho = \beta^{-2}$$

$$k_\mu = \beta^{-1}$$

and

$$k_p = \gamma$$

$$k_\rho = \gamma$$

$$k_\mu = \gamma$$

$$k_F = \gamma$$

The power then transforms as (since $P \sim D^3 F v$)

$$P \rightarrow \alpha^{-1}\beta\gamma P.$$

Taking a linear scale $\alpha = \frac{1}{5}$ and the other scales $\beta = \gamma = 1$, we immediately see that the power increases by a factor 5 in the model. It is easy to show that the three dimensionless parameters are independent of the transformation.

$$\Pi_{1'} = \frac{\rho(\beta^{-2}\gamma)v(\beta\alpha^{-1})D(\alpha)}{\mu(\beta\gamma)} = \frac{\rho v D}{\mu}$$

$$\Pi_{2'} = \frac{v^2(\alpha^{-2}\beta^2)\rho(\beta^{-2}\gamma)}{F(\alpha^{-3}\gamma)D(\alpha)} = \frac{v^2\rho}{FD}$$

$$\Pi_{3'} = \frac{p(\alpha^{-2}\gamma)D(\alpha)}{\mu(\beta^{-1}\gamma)v(\alpha^{-1}\beta)} = \frac{pD}{\mu v}$$

The first two dimensionless parameters are related to the two independent parameters we derived using the first method. Indeed, using $Q \sim D^2 v$, and $F \sim \rho\omega^2 D$ we have

$$\Pi_{1'} = \frac{\rho}{\mu}\frac{Q}{D} = \Pi_1$$

$$\Pi_{2'} = \left(\frac{Q}{\omega D^3}\right)^2 = (\Pi_2)^2$$

The third dimensionless parameter also can be related to Π_3, using $Q \sim D^2 v$, we obtain

$$\Pi_{3'} = \frac{pD}{\mu v} = \frac{pD^3}{\mu D^2 v} = \frac{pD^3}{\mu Q} = \Pi_3.$$

Note that if we had not assumed $\rho = constant$, and taken the more complete equation, we would have one more equation between the k's and one less independent transformation. We could have constructed an additional dimensionless parameter: the Mach number (ratio of fluid velocity to sound velocity). This additional dimensionless parameter could also have been obtained from the first method had we included the gas constant R and the temperature of the fluid T as independent parameters. The total number of independent parameters would then have been 7 with 4 dimensions $(kg, m, s, °C)$, giving

indeed one additional dimensionless parameter. Neglecting the Mach number as a dimensionless parameter that one has to keep constant, corresponds thus to assuming the fluid to be incompressible.

With this simple example we have illustrated the two methods to obtain dimensionless parameters. We will use both when we address the issue for plasma physics. The first method is easiest to derive the dimensionless parameters, while the second allows us to trace back what the underlying assumptions are if we drop a given parameter.

2.2.2. Dimensionless Parameters for Plasma Physics

In this section we intend to derive the dimensionless parameters applicable to plasma physics experiments.

B. Kadomtsev was the first to point to the possibility of applying dimensional analysis to tokamaks [5]. He proposed to use dimensional analysis to guide the design of larger experiments by basing them on information developed on smaller ones. While we would rather use it to identify the value needed for small plasma physics experiments, from target values for a reactor (which we argue are pretty well known) the methodology is basically the same. Kadomtsev applied it specifically to tokamaks it is, however, applicable to other confinement schemes.

First, as for any scaling experiment, the geometry must be to scale. For plasma physics experiments this means essentially the magnetic geometry.

For a tokamak type machine it requires the aspect ratio $\frac{R}{a}$ and the profile of the rotational transform $q(r) = \frac{rB_t}{RB_t}$ to be the same. Note that for a family of geometrically similar devices we have still two degrees of freedom left namely a geometrical length (say R or a) and a value for the magnetic field (B).

Strict similarity of geometry for stellarators requires, in addition to aspect ratio and q profile, the same number of periods (l and m number of the windings), and the same winding law of the helical windings. That for example the winding law can have an influence on the transport of the particles because of its impact

on the location of the ripple and the superbanana losses was clearly pointed out in a numerical study done by Mynick [6]. But even in the case of stellarators a family of geometrically similar machines has two and only two free parameters, a geometrical length and the magnitude of the magnetic field.

It is not possible to go here in detail on the influence the geometry can have on plasma physics quantities, for all possible concepts and geometries. The differences due to the geometry, thus from one family of devices to another, is a separate issue. While it is very important (the β limit in a tokamak for example may be linked to the aspect ratio) it is not addressed here. It is rather our aim here to show that experiments on one (small) member of the family may yield information on many similar devices, and thus test certain theories (for example precisely this link between aspect ratio and β limit). We will address the influence of the geometry on the plasma physics parameters specifically for one device, the helical axis stellarator in chapter 4. There the number of parameters defining this particular geometry will be identified, their influence on the magnetic geometry pinpointed and theories relating this magnetic geometry to limits on plasma physics parameters reviewed.

We take here the general approach that, for a given geometry there are two free parameters, a dimension a and a magnetic field B, characterizing a member of the family of similar devices. In addition to those two parameters (a and B) there are a number of parameters related to the plasma.

Let us assume a pure, fully ionized single ion species plasma at rest and in steady state, with walls infinitely far away. Assumption of a pure single ion species plasma implies the presence only of electrons and single ion species ions with the exclusion of any other component. Assumption of a fully ionized plasma rules out the presence of neutrals, and any quantum effects related to ionization and radiation. Assuming the plasma to be at rest rules out macroscopic motions. Assumption of steady state rules out the dependence on initial parameters. We have then only electrons and ions, whose motion is governed by classical laws of motions and by the Maxwell's equations for the electromagnetic field. We

will of course not try to model the behavior of each electron and ion separately, but are interested in the overall behavior. This can be thought of as taking the average as usual in plasma kinetic theory. It is further assumed that each particle distribution function can be, for the given geometry, completely defined by a single independent parameter, the temperature. Possible loss cones are identical for devices with similar geometry. The independent parameters are then n_e and n_i the electron and ion density, T_e and T_i the electron and ion temperature (in units of energy), e and Ze the electron and ion charge, m and M the mass of the electron and ion, ϵ_o and μ_o the permitivity and permeability of free space.

The inclusion of ϵ_o, μ_o may seem strange at first. A simple reason is that, if we do not include them, we could not make some combination of the parameters dimensionless. A more complete justification, with numerous examples, is given in the work by P.W. Bridgman [4], mentioned earlier. He shows there in general that, when listing the parameters, one has to include what he calls the dimensional constants of proportionality corresponding to the variables used. Note that we did not include k, the Boltzman constant, since we measure the temperature in energy. That we obtain the correct number of dimensionless parameters this way can be confirmed by taking the equations governing the phenomena (the Boltzman equation and Maxwell's equations) and applying the second method. This is shown in Appendix G, where we also address the special case of externally imposed currents, as in tokamaks.

From those twelve quantities with four basic dimensions (kg, m, A, s) we can construct eight dimensionless parameters. They are :

1. ν the collisionality, defined as the ratio between a connection length and the electron mean free path. Its specific definition can take on different forms, and even be normalized so as to obtain a specific value. It is standard for example to define the collisionality ν_* in tokamaks such that $\nu_* = 1$ at the transition between plateau and banana regime for neoclassical diffusion. The definition in

this case becomes

$$\nu_* = \left(\frac{qR}{v_{Te}\tau_e}\right)\frac{1}{\epsilon^{3/2}}$$
$$= \frac{4}{3}\sqrt{\pi}n\frac{e^4}{(4\pi\epsilon_o)^2}\ln\Lambda\frac{qR}{\epsilon^{3/2}T_e^2}$$

with

$$v_{T_e} = \sqrt{\frac{T_e}{m}}$$

2. $\frac{\rho_\theta}{a}$ the ratio larmor radius to the size of the machine. Except for an electron temperature much higher than the ion temperature the ion larmor radius is much larger than the electron larmor radius. It is also more relevant to take the larmor radius in the poloidal field rather than in the toroidal field because of toroidal effects [7]. Thus

$$K = \frac{\rho_\theta}{a} = \frac{\sqrt{MT_i}}{eB_\theta}$$

3. β the ratio of plasma pressure (taking into account electrons and ions) to magnetic pressure. It is given by

$$\beta = \frac{n(T_e + T_i)}{B^2/2\mu_o}$$

4. N_λ the number of particles per Debye sphere. This fourth parameter takes the form

$$N_\lambda = \frac{4\pi}{3}n(\lambda_D)^3 = \frac{4\pi}{3}\left(\frac{\epsilon_o}{e^2}\right)^{3/2}\frac{T_e^{3/2}}{n^{1/2}}$$

5,6. Two parameters related to the choice of the ion species, namely $\frac{Z_i}{e}$ and $\frac{m}{M}$. Choosing hydrogen (or deuterium) fixes those parameters.

7,8. The last two parameters are $\frac{n_e}{n_i}$ and $\frac{T_e}{T_i}$. The ratio $\frac{n_e}{n_i}$ is always very close to 1, even for plasmas where charge neutrality is slightly violated. The ratio $\frac{T_e}{T_i}$ will be close to 1 for reactors as presently envisaged, it should thus also be close to 1 for any experiment.

This in fact leaves us with four dimensionless parameters. Since we have only four degrees of freedom (size, magnetic field, plasma density and temperature),

we have no freedom left in making a scaled experiment. The machine is then completely defined by choosing β, ν, K, and N_λ. Indeed as

$$\beta \sim \frac{nT}{B^2}$$
$$\nu \sim \frac{na}{T^2}$$
$$K \sim \frac{\sqrt{T}}{aB}$$
$$N_\lambda \sim \sqrt{\frac{T^3}{n}}$$

This can be written as

$$n \sim \nu^{-6} K^{-6} \beta^3 N^{-8}$$
$$T \sim \nu^{-2} K^{-2} \beta N^{-2}$$
$$a \sim \nu^3 K^2 \beta^{-1} N^4$$
$$B \sim \nu^{-4} K^{-4} \beta^{3/2} N^{-5}$$

Which is another way of saying that by choosing ν, K, β, N, for a given geometry the parameters of the machine are completely defined.

It is interesting to note that the product

$$aB \sim \nu^{-1} K^{-2} \beta^{1/2} N^{-1}$$

is a more sluggish function of the dimensionless parameters than n, T, a or B separately and is thus useful to classify a large range of different machines. The stored energy, proportional to a^3B^2, falls too into this category.

$$a^3 B^2 \sim \nu K^2 N^2$$

Any parameter is a function of those four dimensionless parameters only. For example, the energy confinement time τ, written in dimensionless form is, for a given geometry, function only of β, ν, K, N

$$\frac{\tau}{\frac{mB}{e}} = F_1(\beta, \nu, K, N)$$

Similarly the power needed for maintaining a plasma at a certain temperature, if expressed in dimensionless form, is a function only of β, ν, K, N.

$$\frac{P}{\frac{nT_e^3}{\tau}} = F_2(\beta, \nu, K, N)$$

The functions F are unknown, and, if we have to keep all four parameters in the same range as for a reactor we have no degree of freedom left and are thus unable to identify the function on a scaled version. By making appropriate assumptions, and disregarding one or more of the dimensionless parameters, it is possible to obtain information on the function by making experiments on a scaled model. In the next section we will describe the assumptions that go into this and show how a scaled experiment can yield relevant information on reactor relevant plasmas.

2.3. Increasing the degrees of freedom by not keeping constant one or more of the dimensionless parameters

By not keeping constant one or more of the dimensionless parameters it is possible to gain more freedom in designing a scaled experiment. Connor and Taylor, [8-10] have derived the dimensionless parameters using the second method described earlier. They have used for the plasma several different sets of equations (ranging from the Boltzman equations with Maxwells equations to a resistive MHD model) and derived for each set the dimensionless parameters. The different set of equations result in different numbers of dimensionless parameters. It is thus possible, when we neglect to keep constant one or more of the four dimensionless parameters derived earlier, to trace back what the underlying model is and thus what additional assumptions have to be made.

Keeping all four dimensionless parameters corresponds to a plasma governed by the Boltzman equation and the four Maxwell equations (and assuming $T_e = T_i$). In this model electric fields and magnetic fields are self-consistent solutions of the equations. Collisions, as well as effects due to the finite larmor radius of the

particles, are taken into account. As mentioned earlier, this leaves us no degree of freedom to make a scaled experiment.

Let us now look at the possibility of not keeping constant some parameters. We will investigate how it increases our freedom in making scaled models, but also investigate what additional assumptions are necessary and what the resulting constraints are.

2.3.1. Dropping N_λ

If we choose not to keep N_λ the number of particles per Debye sphere constant, we have one degree of freedom for which we can take B. This gives us a scaling as

$$a \sim B^{-4/5}$$
$$n \sim B^{8/5}$$
$$T \sim B^{2/5}$$

This means that if we want to decrease the size with respect to a reactor, we have to increase the magnetic field, increase the density and temperature.

Let us show how a scaled model could give information on how the power needed to heat a reactorscale plasma varies with n or T. Take as typical value for a reactor $a = 1.5m$, $B = 5T$ and assume we want to identify the variation of the power needed as a function of density and temperature in the range $10^{19}m^{-3} < n < 10^{20}m^{-3}$ and $1\text{keV} < T < 10\text{keV}$. If we build a model of the reactor with $B = 14T$ we would need $a = 1.5m \times (\frac{14}{5})^{-4/5} = 0.65m$ The range variation for n would change from $10^{19}m^{-3} < n < 10^{20}m^{-3}$ to $5.2 \times 10^{19}m^{-3} < n_s < 5.2 \times 10^{20}m^{-3}$. The temperature would have to be scaled from $1keV < T < 10keV$ to $1.5keV < T_s < 15keV$. In the model the power needed for the reactor could be scaled from the power needed on the model by

$$\frac{P}{P_s} \sim \frac{nTa^3B}{n_sT_sa_s^3B_s} \sim \left(\frac{B}{B_s}\right)^{3/5} = 0.52$$

Note that the model would need almost twice the power the full scale system needs. This simple example shows first that if we only drop one parameter thus

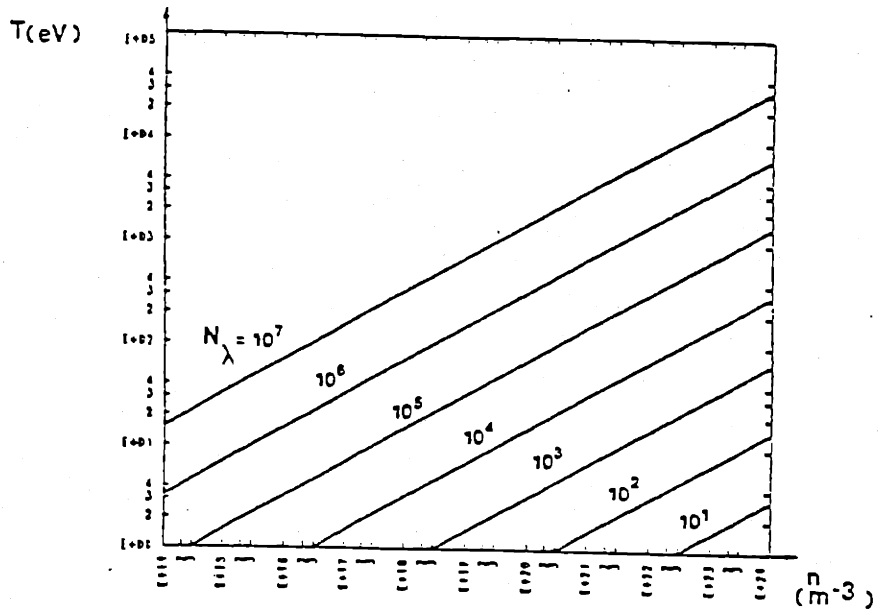

Figure 2.1 N_λ, Number of particles per Debye sphere as a function of temperature and density.

---

little freedom is gained. We will later investigate how we can gain more freedom by dropping a second dimensionless parameter.

What are the underlying assumptions if we drop N_λ as parameter, and what are the resulting constraints ? By using the second method it can be shown [8–10] that we only obtain three parameters β, ν, $\frac{\rho_e}{a}$ (thus we can neglect keeping N_λ constant), if we start from a set of equations including the Boltzman equations and the Maxwell equations, but where the additional assumption of charge neutrality is made. Dropping N_λ thus corresponds to neglecting effects associated with electrical fields set up by the plasma. We have now to look at the conditions under which we can indeed make this assumption and thus neglect keeping N_λ constant.

We have

$$N_\lambda = \frac{4\pi}{3} n_e \lambda_D^3 = 1.73 \times 10^2 \left(\frac{T_e}{e}\right)^{3/2} \left(\frac{n_e}{10^{20}}\right)^{-1/2}$$

This number is large for a reactor, and thus should be large for any relevant experiment, even if we do not keep it constant.

Within what range can we change N_λ without too much affecting the processes related to charge neutrality. For Debye shielding to be a valid concept there must be sufficient particles in the Debye sphere. A quantitative value can be found by noting that the factor $\ln \Lambda$, in the formula for collision frequencies gives the dominance of small angle collisions over large angle collisions. The value of Λ is 9 times the number of particles per Debye sphere [11]. Setting a minimum of $\ln \Lambda = 10$, so that small angle collisions are at least 10 times more frequent than large angle deflections, we obtain $N_\lambda > 2500$. This result in a limit in the n, T diagram shown in Figure 2.1.

In some cases it is not N_λ itself on which there is a limit but rather some combination of N_λ with another dimensionless parameter. An example [12] was given by Ioffe. In an unstabilised mirror, losses were reduced by a large factor when the Debye sphere of the ions was comparable to the size of the machine. This is a completely different, and for a reactor, irrelevant regime. If the Debye sphere is larger than the size of the machine, the particles behave as independent single particles and collective effects are suppressed. In general we need thus $\frac{\lambda_D}{a} \ll 1$ with

$$\lambda_D = 7.45 \times 10^{-7} \left(\frac{T_e}{e}\right)^{1/2} \left(\frac{n_e}{10^{20}}\right)^{-1/2} \sim \sqrt{\frac{T}{n}} \sim \frac{T^2}{n} \sqrt{\frac{n}{T^3}}$$

we have

$$\frac{\lambda_D}{a} \sim \frac{1}{\nu N_\lambda}$$

Thus we will have some limit on the product of ν and N_λ. For a particular choice of ν it would translate into a minimum value for N_λ. Alternatively we can put the requirement $\frac{\lambda_D}{a} \ll 1$ with a as parameter in the n, T diagram.

$$7.45 \times 10^{-7} \left(\frac{T_e}{e}\right)^{1/2} \left(\frac{n_e}{10^{20}}\right)^{-1/2} \frac{1}{a} \ll 1$$

As can be seen from Figure 2.2 this requirement is not very stringent.

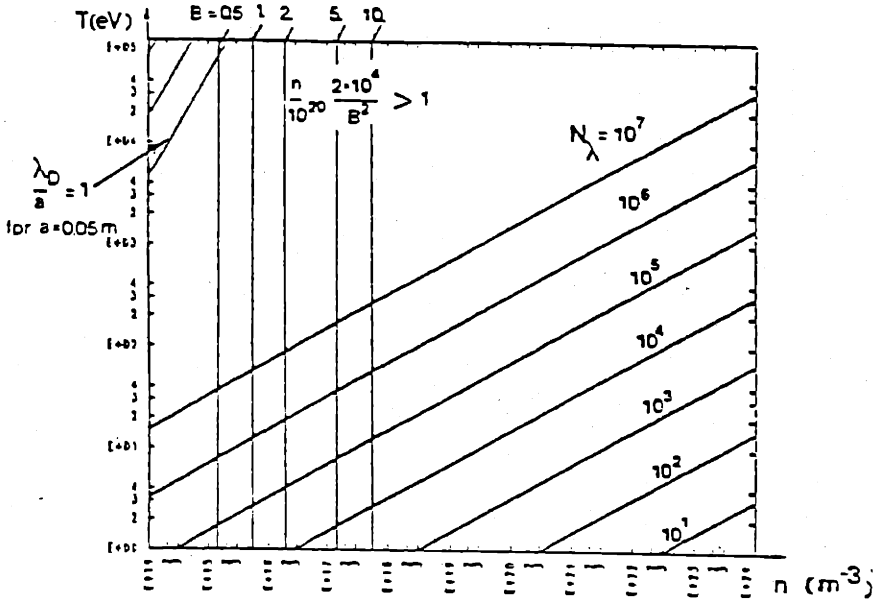

Figure 2.2 Limits corresponding to $\lambda_D \ll a$ and $\epsilon \gg 1$

Experiments on multipoles, at very low density and temperature have shown that under some conditions transport can be completely dominated by convective diffusion [13–15]. Similar connective cells were found in low density stellarators [16, 17]. While viscosity damp the convective cells [16] and the shear may reduce their size [18], reactor relevant regimes may still be influenced by convective cells. The important parameter is [15, 18]

$$\epsilon = 1 + \frac{\omega_{pi}^2}{\omega_{ci}^2} + \frac{\omega_{pe}^2}{\omega_{ce}^2}$$

which for reactor regimes fulfills $\epsilon \gg 1$. This corresponds to a regime where at least the ion larmor radius is larger than the radius of the Debye sphere. As for large ϵ, $\epsilon \sim \frac{n}{B^2} \sim \frac{1}{\nu K N_\lambda}$, this can again be expressed as some minimum value for N_λ for a particular choice of ν and K. Equivalently we can put some limits on n, with B as parameter on the n, T diagram. The limit is then given by (Fig. 2.2)

$$\left(\frac{n}{10^{20}}\right)\frac{2 \times 10^4}{B^2} \gg 1$$

This limit has to be fulfilled if we want to investigate transport processes in the plasma. To look at β limits it may be of less importance. If, in addition to not keeping N_λ constant, we also drop a second dimensionless parameter it is clear that the limits we have set for N_λ will still be applicable.

2.3.2. Dropping N_λ and β

Dropping a second dimensionless parameter gives us an second degree of freedom for which we can take a. If we drop β the scaling becomes

$$n \sim a^3 B^4$$
$$T \sim a^2 B^2$$

Again applying this to our example, and scaling from $a = 1.5m$, $B = 5T$ to $a = 0.15m$ and $B = 14T$ we obtain that properties related to transport (if dominated by collisional effects) would be similar in the scaled machine to the properties of plasma in a reactor if the density in the scaled machine varies as $6 \times 10^{17} m^{-3} < n_s < 6 \times 10^{18} m^{-3}$. The temperature range in the model should be

$$80eV < T_s < 800eV$$

Of course limits related to β will be drastically different. Indeed, β would be a factor $a^5 B^4$ lower in the scaled version compared to the reactor.

Dropping N_λ and β as dimensionless parameters corresponds to a plasma described by the Boltzman equation, assuming charge neutrality and fixed magnetic field (the magnetic field B is the imposed vacuum magnetic field and no longer self-consistently determined from Maxwell's equations). Under what conditions is this justified and what are the resulting constraints?

If one keeps ν, but does not keep β constant, the emphasis is usually to look at transport. However, there are strong indications that the β value may seriously influence transport. Because most toroidal systems rely on charge neutralisation by motion of the electrons along the field lines, transport may be affected if this process becomes ineffective.

According to [19] this happens when

$$\beta > \left(\frac{a}{R}\right)^2 \frac{1}{q^2} = \left(\frac{B_\theta}{B_\phi}\right)^2$$

Thus when

$$\beta_\theta > 1$$

Experimental evidence of the influence of β_θ on transport has been found recently. While some experiments invoke a strong temperature dependence of transport as the transport enhancing mechanism [20], others explain the effect by MHD instabilities [21] or resistive ballooning modes [22, 23]. The point we make here is that the value of β may definitely affect the transport mechanisms, and that to obtain relevant information on transport it is important to measure it at the appropriate β value.

2.3.3. Dropping N_λ and ν

If we choose to keep β and K constant the scaling becomes

$$n \sim a^{-2}$$

$$T \sim a^2 B^2$$

The emphasis would then be on an investigation of the β limits. Applying it again to the previous example, we can argue that the properties related to β limits are similar for a reactor at $a = 1.5m$ and $B = 5T$ as for a scaled experiment at $a = 0.15m$ and $B = 14T$, for densities $1 \times 10^{21} m^{-3} < n_s < 1 \times 10^{22} m^{-3}$ and temperatures $80eV < T_s < 800eV$, if we want to model the behavior in a reactor for densities varying between $10^{19} m^{-3} < n < 10^{20} m^{-3}$ and temperatures between $1keV < T < 10keV$. The collisionality in this case scales as $a^{-4} B^{-4}$ and will go up drastically, in the scaled version.

Dropping ν and N_λ corresponds to a plasma described by the Vlasov equation (collision operator = 0), and assuming charge neutrality. The magnetic field is derived self-consistently from Maxwell's equations. It seems that β limits are

little influenced by ν. While it may only seem so because β limits are often investigated theoretically using ideal MHD models that do not allow explicit inclusion of collisionality, there has been little experimental evidence that β limits may be influenced by the collisionality. Non ideal MHD modes would be different in the full scale machine and in the model if the collisionality is not kept constant between both.

2.3.4. Dropping N_λ and $\frac{\rho_\theta}{a}$

A third possibility to obtain two degrees of freedom is by keeping β and ν constant, while neglecting the influence of $\frac{\rho}{a}$ and N_λ. The scaling then is

$$n \sim a^{-1/3} B^{4/3}$$

$$T \sim a^{1/3} B^{2/3}$$

For the same example we obtain

$$8.5 \times 10^{19} m^{-3} < n_s < 8.5 \times 10^{20} m^{-3}$$

and

$$0.9 keV < T_s < 9 keV$$

There is however no theoretical justification (based on the equation modeling the phenomena) to keep those two variables constant and neglecting the others. The closest one can get is the resistive MHD model whose equation under transformation are invariant if β and $K^2\nu$ is kept constant. This would be another possible choice. The scaling of n and T would then be $T \sim a^{-1/2}$, $n \sim B^2 a^{1/2}$.

If we attempt to keep β and ν constant at the same time, we may model transport more appropriately than by keeping ν and $\frac{\rho}{a}$ constant, because as we have seen, there are strong indications that β does influence the transport. Under what conditions can we neglect the effect of $\frac{\rho}{a}$? In a reactorscale plasma $\frac{\rho}{a}$ is a small value. An upper limit on $\frac{\rho}{a}$ for experiments is usually set by the

heating method used. If the magnetic field is too low, $\frac{\rho}{a}$ may become so large for energetic particles that a large fraction of the injected power is lost. The value of $\frac{\rho}{a}$ should also be such that stabilizing influence due to finite larmor radius effects are present in the model to the same extent as they are in the full scale version. This depends very much on the magnetic geometry and the important parameter in this respect would be the ratio of ρ to the scale length for gradients (which may be much smaller than a , and independent of the size of the machine). Scaling with $\frac{\rho}{a}$ can be easily performed by varying a and B on a given machine, so that indications of the influence of this parameter could be gathered separately.

In this section, we have shown how we can increase our degrees of freedom by dropping one or more of the dimensionless parameters. We have also identified the constraints resulting from this first step. We have delineated the area in parameter space within which N_λ can be dropped as a parameter. In order to test β scaling, we could drop ν as a second parameter. For transport tests, dropping β may not be the appropriate choice. It is more justifiable to keep ν and β and drop $\frac{\rho}{a}$ as a second parameter.

Let us now discuss what constraints can arise from the second step : effects that were not included in similarity considerations : the neutrals and impurities.

2.4. Effects not included in the Similarity Scaling Laws

A widely accepted view is that the minimum size of an experiment is set by the requirement that a plasma be not dominated by plasma wall interaction. We want to investigate here in more detail whether those effects indeed set a minimum size.

Presence of neutrals and impurities in the plasma are interconnected because, at least for present machines, the mechanism of refueling, namely recycling at the wall/limiter involves interaction with wall/limiter just as much as impurity

production does. For the discussion we will try to separate both effects and rely on theoretical and experimental results to see what the constraints are. For both the neutrals and the impurities we will discuss their source (how they get into the plasma), what an acceptable level is (when can we neglect their effect on similarity scaling laws) and discuss some experimental results to find any additional constraints.

2.4.1. Neutrals

One of the mechanisms by which the idealized plasma we have used in our similarity scaling differs from a real plasma is by the presence of neutrals. The presence of neutrals in the plasma is a well known subject and we can rely on theoretical results to calculate their level. First the mechanism for the presence of neutrals in the plasma are reviewed. We then investigate what level is acceptable and constraints on temperature, density and size are derived to fulfill those conditions. Finally we discuss some experimental results related to recycling and refueling.

2.4.1.1. Source of Neutrals in the Plasma

In this section we will first calculate the level of neutrals in a plasma in complete thermodynamic equilibrium. We will then calculate this level for a plasma in coronal equilibrium. Next we will consider the penetration of neutrals from the edge, and finally the need for refueling.

Even in a plasma of infinite extent, and in thermal equilibrium, neutrals are present. This level can be derived from methods of statistical mechanics. The degree of ionization in a gas in thermal equilibrium can be calculated to be [24]

$$\frac{n_i}{n_n} = \frac{1}{n_e}\left(\frac{2\pi m_i T}{h^2}\right)^{3/2}\left(\frac{2\pi m_e T}{h^2}\right)^{3/2}\left(\frac{2\pi m_n T}{h^2}\right)^{-3/2} exp\left(\frac{-eV_i}{T}\right)$$

or

$$\frac{n_i}{n_n} = \frac{3\times 10^{27}}{n_e}\left(\frac{T}{e}\right)^{3/2} e^{\frac{-eV_i}{kT}}$$

This is the well known Saha equation and is shown in Fig. 2.3.

However a laboratory plasma is not in thermal equilibrium, its dimensions being too small for equilibrium with the radiation fields. In coronal equilibrium, the neutral density is a result of a balance between radiative recombination of electrons and ions, and ionization by electron and ion impact. The level of neutrals can be calculated from the steady state solution of the equations provided by Johnson and Hinnov [25], using their tabulated value of effective rate coefficients for ionization and recombination, and energy levels given by [26]. We will use here a simpler method and assume, as Goldston did [27] that the scale length for diffusion of the recombined neutrals is short under the conditions when we are led to consider recombination.

The local equilibrium density is then given as (we use rec as an index for recombination, iii for ion impact ionization, eii for electron impact ionization)

$$n_n = \frac{n_e n_i < \sigma v >_{rec}}{n_e < \sigma v >_{eii} + n_i < \sigma v >_{iii}}$$

For $< \sigma v >_{rec}$ we can use, if $T_e \leq 400eV$ the formula given by [28]

$$< \sigma v >_{rec} = \frac{1.27 \times 10^{-9} \left(\frac{13.6e}{T}\right)^{3/2}}{\frac{13.6e}{T} + 0.59} \frac{m^3}{s} \qquad (2.1)$$

and for $T_e \geq 400eV$, an analytical fit to their calculation

$$< \sigma v >_{rec} = 10^{-20} \left(\frac{T}{85e}\right)^{-1.365} \frac{m^3}{s} \qquad (2.2)$$

The values from $< \sigma v >_{eii}$ and $< \sigma v >_{iii}$ were calculated from formulas given in [29]. In Fig. 2.4 the values of $< \sigma v >$ are plotted for different processes.

Calculating now $\frac{n_n}{n_e}$ we obtain

$$\frac{n_n}{n_e} = \frac{< \sigma v >_{rec}}{< \sigma v >_{eii} + < \sigma v >_{iii}}$$

This is function of temperature only and plotted in Fig. 2.5.

Combining Fig. 2.3. (Saha) and Fig. 2.5. (Coronal) we can plot Fig. 2.6., giving the minimum level (neglecting transport and boundaries) of neutrals in a plasma, as a function of temperature and density.

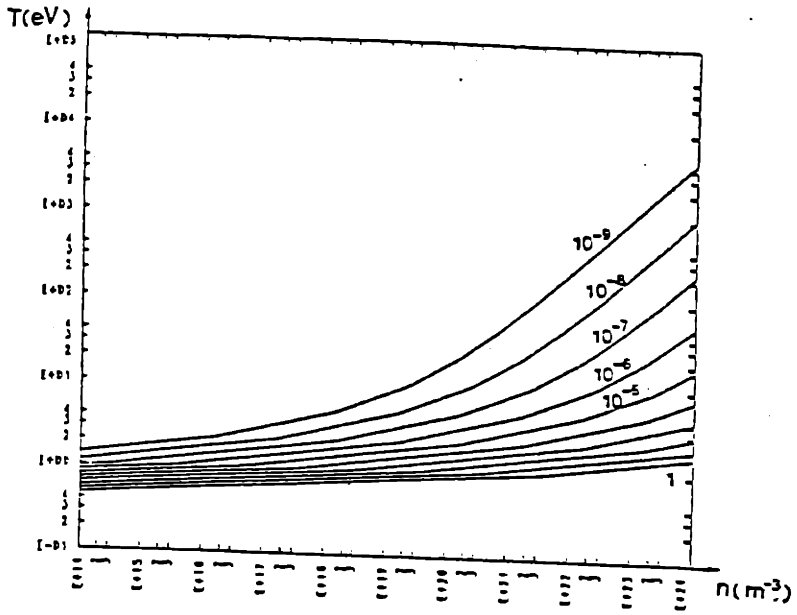

Figure 2.3 Neutral density from Saha equilibrium

There is however an additional mechanism for the presence of neutrals in the plasma namely their penetration from the edge. High levels of neutrals at the edge arise from several factors : the need to refuel the plasma, neutralisation of ions at the wall or simply because of the higher recombination rate at lower temperature.

Various authors have made extensive calculations of penetration depth neutrals into the plasma, either analytically [30–34] or numerically [35–37]. Numerical methods are based on Monte-Carlo algorithms or on neutron transport codes [38]. For a sufficient large plasma size and density the level of neutrals at the center is no longer influenced by the neutrals from the edge, the minimum then being the level calculated earlier (recombination). The penetration from neutrals from the edge, under the assumption $\lambda_{mfpcx} \ll \lambda_{mfpii}$ where

$$\lambda_{mfpcx} = \frac{< v >}{n_i < \sigma v >_{cx}} \tag{2.3}$$

is the mean free path for charge exchange and

$$\lambda_{mfpii} = \frac{< v >}{n_e < \sigma v >_{eii} + n_i < \sigma v >_{iii}} \tag{2.4}$$

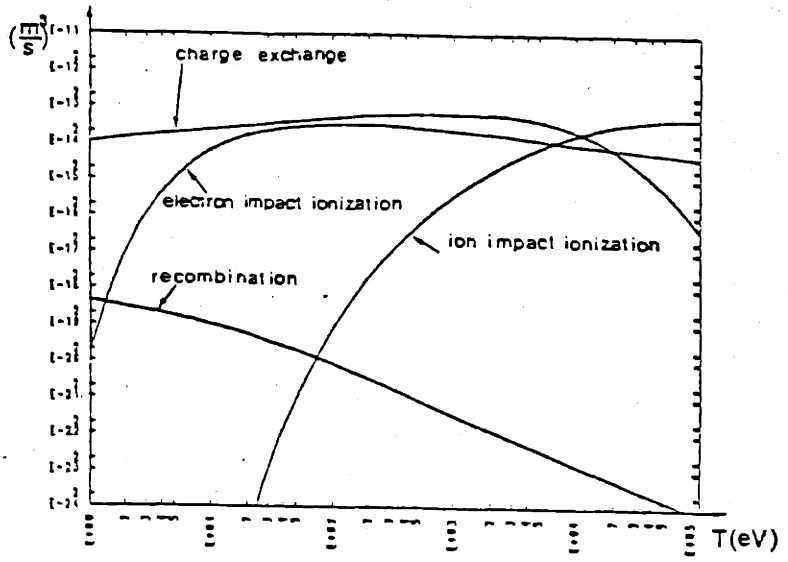

Figure 2.4 Cross section for charge exchange, electron and ion impact ionization and recombination for hydrogen

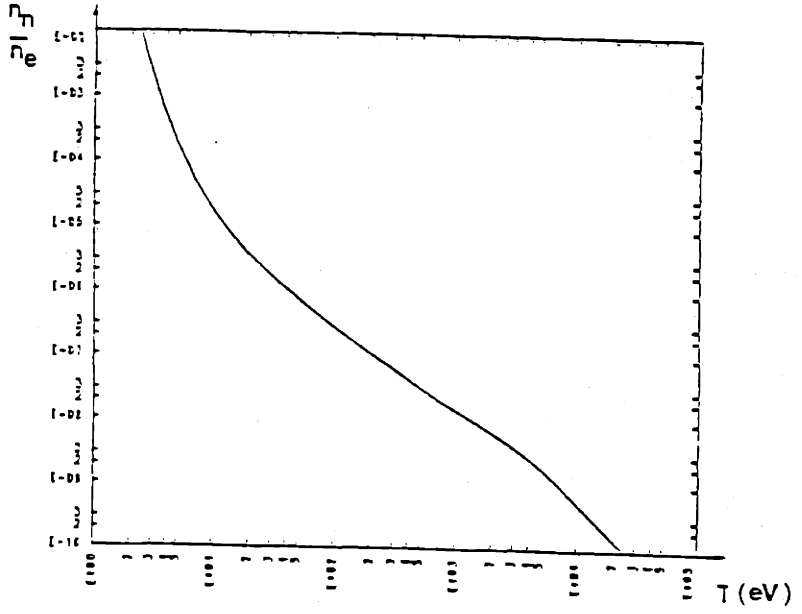

Figure 2.5 Neutral density obtained from balancing the ionization rate with the radiative recombination rate

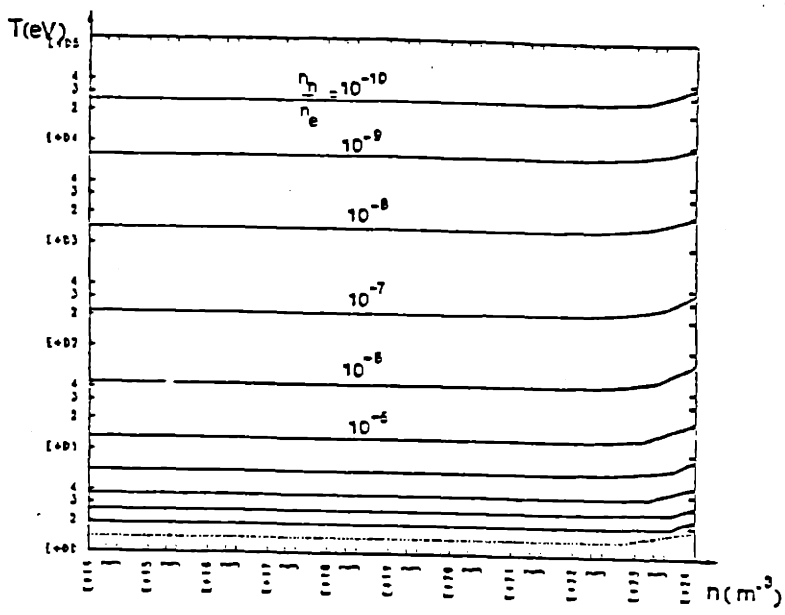

Figure 2.6 Neutral density as a function of density and temperature from coronal and Saha equilibrium. Note that the effect of the Saha equation only appears at very high density

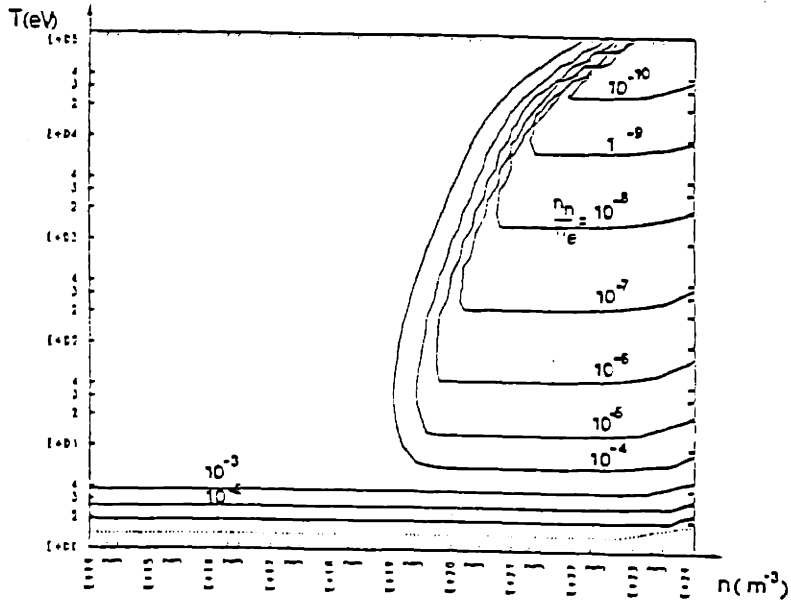

Figure 2.7 Levels of neutrals in a plasma for $a = 0.2m$, see text for assumptions with respect to neutral density at the edge

is the mean free path for impact ionization, can be treated as a diffusive process, governed by the equation [27]

$$\frac{\lambda_{mfpcx}}{3}\nabla^2 n_n - \frac{n_n}{\lambda_{mfpii}} = 0 \tag{2.5}$$

Taking a simple exponential variation for the density $n_n = e^{-x/L}$ (in slab geometry) we obtain that the thickness of the layer influenced by the neutral density at the edge is given by [27]

$$L = \left(\frac{\lambda_{mfpcx}\lambda_{mfpii}}{3}\right)^{1/2} \tag{2.6}$$

If the size of the plasma (minor radius a) is smaller than this scale neutrals will penetrate to the center. For $L < a$ one can assume the minimum level of neutrals at the center to be set by recombination.

To calculate the level of neutrals at the center, in the cases where $a < L$, we could use the numerical codes mentioned earlier. Their accuracy however is somewhat artificial. They are mostly used to interpret the measurements of the charge exchange flux. The neutral density at the edge is then not more than a parameter used to match the measured curve of charge exchange measured with the theoretical curve. Measurements of the neutral density at the edge is difficult and seldom performed.

That the accuracy may be somewhat artificial is further highlighted by the fact that for machines where the central density is set by recombination (and thus the "free" parameter at the edge is no longer useful), the codes are often not able to match the measured charge exchange flux. To calculate the level of neutrals at the center we will use a simple analytical formula. With the scale length L given in equation (2.6) we obtain the level at the center from a simple exponential decay [27]

$$n_n(o) = n_n(a)e^{-\frac{a}{L}} \tag{2.7}$$

To calculate L we have used the cross sections as given in Figure 2.3 and equations (2.1) and (2.2). An even simpler analytical formula, which immediately identifies the importance of the product na is given by Gordeev [28]

$$n_n(o) = n_n(a)\frac{1.23}{\sqrt{T_e}}exp(-\frac{6\times 10^{-18}na}{\sqrt{T_e}})$$

We have however chosen to take the value defined by equation (2.7). Using this formula it is straightforward to calculate the neutral density in the plasma, from the neutral density at the edge. Let us assume first that the particle confinement time is infinite, so that there is no need for the presence of neutrals at the edge of the plasma for refueling. Neutrals will then still be present there because of the higher recombination rate at lower temperature. Those edge neutrals will penetrate into the plasma through successive charge exchange, giving a level at the center, depending on size, density and temperature.

Let us take the neutral density at the edge to be the one arising from recombination assuming the plasma density at the edge to be 1/10 the plasma density at the center and the edge temperature to be $3eV$. The result for the neutral density is then shown for $a = 0.2m$ in Fig. 2.7 . Higher values of neutral density at the edge and thus at the center could result from the need to refuel the plasma.

We can estimate the impact of the need to refuel the plasma by the following simple model from Podesta and Engelmann [39] . Taking F_i to be the flux of ions leaving the plasma, F_h the flux of hot neutral particles leaving and F_c the flux of returning cold neutral particles, we can write down, for steady state, a balance of particle flux at the edge (see Figure 2.8)

$$F_i + F_h = F_c$$

as each particle lost (be it ion or fast neutrals) needs to be replaced by a cold neutral.

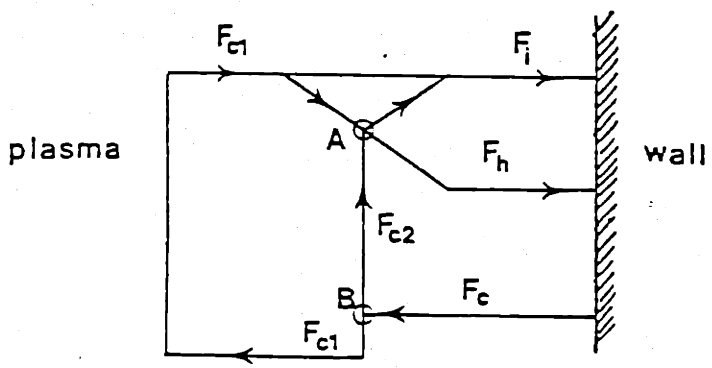

Figure 2.8 Simple model to calculate the influence of cold neutrals [39]. F_i is the flux of ions leaving the plasma, F_h the flux of fast hot neutral particles, and F_c the flux of cold neutral particles. In B, a fraction F_{c1} of the cold neutral particles undergo ionization, while in A, a fraction of the ions undergo charge exchange with the fraction F_{c2} of the cold particles.

Of the incoming cold neutrals a fraction F_{c1} will be ionized, while a fraction F_{c2} will undergo charge exchange with ions.

$$F_{c1} = \frac{< \sigma v >_{ii}}{< \sigma v >_{cx} + < \sigma v >_{ii}} F_c$$

$$F_{c2} = \frac{< \sigma v >_{cx}}{< \sigma v >_{cx} + < \sigma v >_{ii}} F_c$$

The process of charge exchange of the cold neutrals F_{c2} with the ions in A, does not change the number of ions so that $F_i = F_{c1}$. The number of hot neutrals corresponds to the number of cold neutrals that undergo charge exchange, giving $F_h = F_{c2}$. From those equations we can calculate

$$F_h = \frac{< \sigma v >_{cx}}{< \sigma v >_{ii}} F_i$$

The confinement time for charged particle is proportional to $\frac{1}{F_i}$, and the "energy confinement time" due to charge exchange is proportional to $\frac{1}{F_h}$.

We obtain for their ratio

$$\frac{\tau_{cx}}{\tau_p} = \frac{< \sigma v >_{ii}}{< \sigma v >_{cx}}$$

which is given in Fig. 2.9 as a function of the temperature. The inverse of this value can be considered as an enhancement factor that increases the energy losses due to particle loss.

The particle confinement time must be, for temperature between $30eV$ and 10^4eV, at least an order of magnitude larger than the energy confinement time, for us to be able to neglect charge exchange losses. The density of cold neutrals can then be estimated from

$$n_c \simeq \frac{1}{< \sigma_{cx} v > \tau_{cx}} \simeq \frac{1}{< \sigma_{ii} v > \tau_p}$$

The values of τ_p for which this yields a level of neutral density higher than our previously calculated values are shown in Fig. 2.10 for $a = 0.2m$.

In this section we have calculated the minimum level of neutrals resulting from Saha equation and coronal equilibrium. We have also shown how the level of neutrals can be higher than this minimum level in cases where $a < L$. The level of neutrals at the center will then be influenced by the neutral density at the edge. For this neutral density at the edge we have taken the level corresponding to the equilibrium recombination density for a temperature of $3eV$ and a plasma density 1/10 the central plasma density. The level of neutrals is then shown for $a = 0.2m$ as an example, in Figure 2.7. Even higher levels may result from the need to refuel the plasma.

2.4.1.2. Acceptable level

Setting an acceptable level of neutrals in the plasma for an experiment is a complicated question. The final configuration of the reactor with respect to fueling, presence of limiter or divertor, cold plasma blanket, neutral density at the edge, first wall design etc.. is not yet known. Thus we can not turn to a reactor design and deduce from it the level we could accept for an experiment, as we could do for values of β, ν, K, N_λ. One point that can be derived in

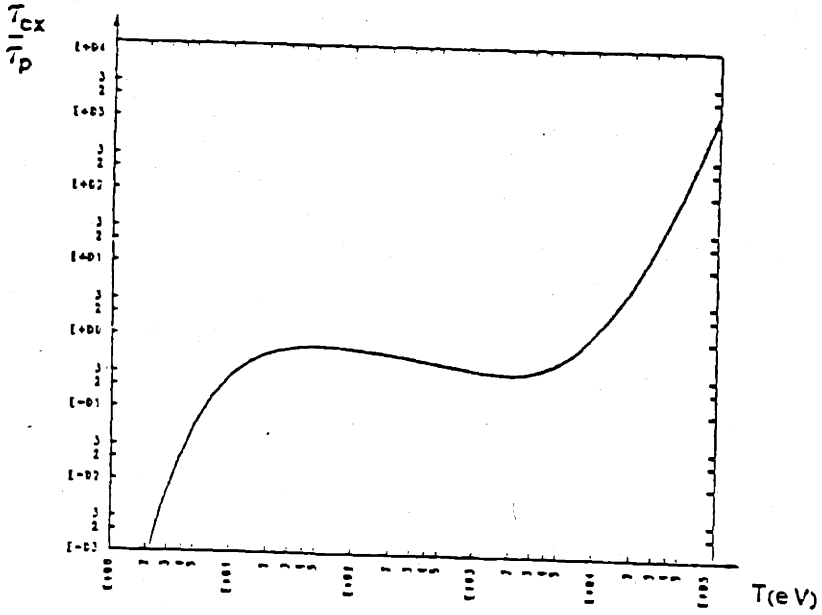

Figure 2.9 Ratio of energy losses (charged particles/ charge exchange)

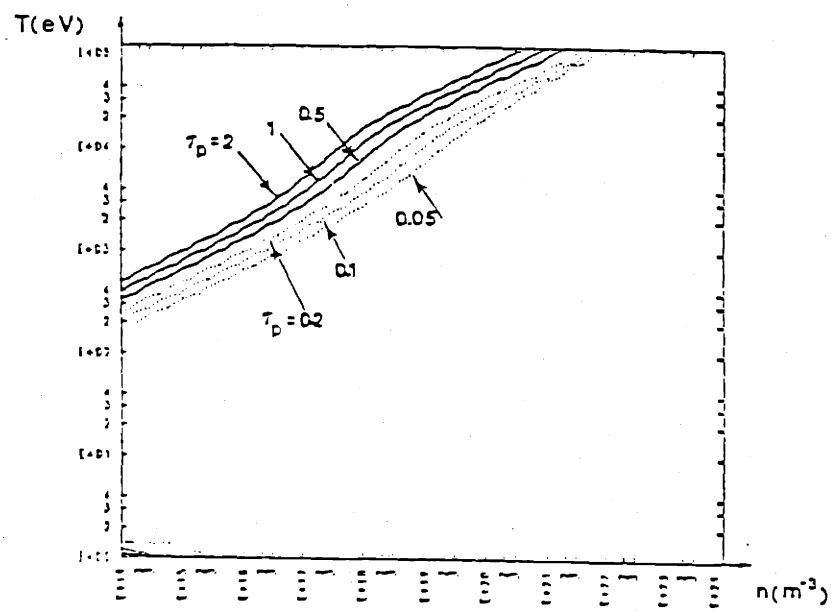

Figure 2.10 Values of τ_p the particle confinement time below which the need for refueling becomes an important effect for the level of neutrals in the plasma

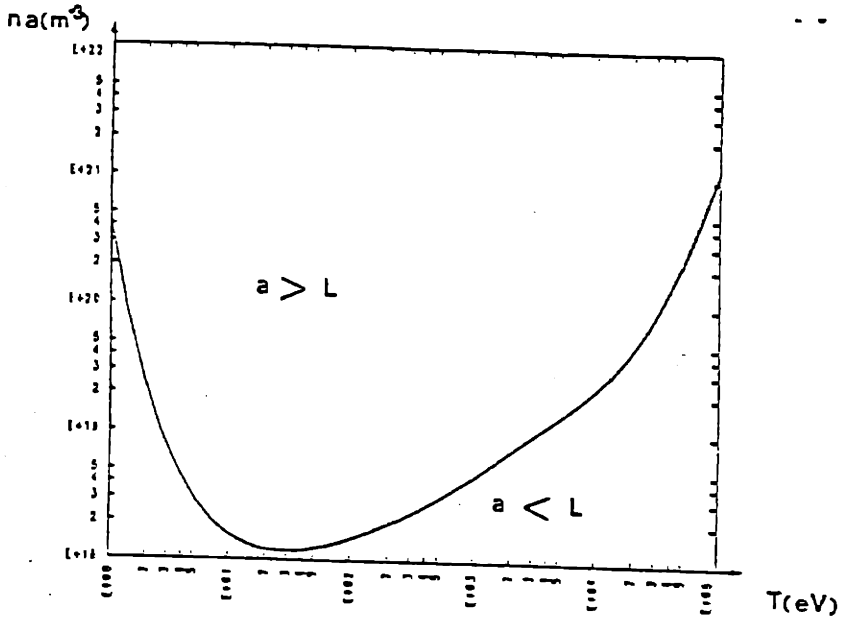

Figure 2.11 Constraint on na for $a > L$ as a function of temperature.

this way is that a reactor plasma is impermeable (in terms of $L < a$) to the neutrals from the edge. The neutral density at the center is thus set by radiative recombination.

If we view a reactor plasma as a core where neutrals do not play a significant role, an intermediate region (of size L) where the presence of neutrals may be an important effect and a scrape-off layer, and if we set the conditions that an experiment should model appropriately the different layers then we have the stringent condition that a minimum size on an experimental plasma is set by $a > L$. This rather stringent constraint can be translated in terms of a minimum na value as a function of temperature and is shown in Figure 2.11. It could be added, with a as a parameter to our previous constraints. For temperature between $30eV$ and $10keV$ a good analytical fit is given by

$$na = 1.6 \times 10^{17} \sqrt{\frac{T}{e}} m^{-2}$$

One also sees that below about $30eV$ the na limit again increases drastically, so that for an experiment there is little reason to work below $30eV$.

One of the design constraints used for ASDEX-U [40] was very precisely this condition. This impermeability constraint is rather well defined and experimentally proven [41].

Is it still possible to perform meaningful experiments in plasmas that do not fulfill this condition ? In order to answer this question we will have to look at the influence neutrals can have on an experiment, and obtain from this, limits on their levels so that their influence is minimized. The rest of this section looks specifically at plasmas in which the impermeability condition is not fulfilled.

Lehnert [42, 43] argues that for a plasma in the permeable regime, but approaching the critical limit above which it would become impermeable undergoes marked changes in pressure and density gradients. Those gradients would favor the development of ballooning instabilities, which would enhance transport and put an artificial limit of $\beta_p \simeq 1$. This ballooning instability limit would not occur for impermeable plasmas because of the much flatter density profile. Experimental evidence is scant. Alcator A and C have operated from the permeable into the impermeable regime without effect (except for the large decrease of neutral flux coming from the center [41]) but then again β is rather low in the machine. A sharp transition with improvement in energy confinement and flattening of the density profile has been observed in the so-called H-discharges of Asdex. This transition is accompanied with marked changes in the scrape-off layer and neutral density at the edge and neutral density in the divertor region. This seems to indicate that effect due to neutrals may indeed influence a discharge. If it were to be confirmed that such an important effect were due to the mechanism proposed by Lehnert, then indeed any future experiment related to β limits and transport near those limits should definitely be performed in the impermeable regime.

Transport of particles and energy can be affected by neutrals in multiple ways, in addition the possible effects related to β limits.

Neutrals can have a large impact on energy losses through charge exchange

losses. We have already shown that the particle confinement time must be much larger than the energy confinement time in order to be able to neglect losses due to charge exchange. It is in principle possible to take these losses into account by including the presence of neutrals when analyzing transport losses with a computer code. This is however often difficult to implement because the losses due to the cold neutrals depends very much on the edge neutral density and edge plasma temperature, neither of which are well known [44]. For a permeable plasma the best of all possible worlds with respect to levels of neutrals is when we have perfectly absorbing walls and a perfect vacuum at the edge. But then of course, unless the particle confinement time is infinite, the plasma density will decay and no steady state can be achieved. One could envisage using pellet refueling at the center to maintain the density even with a vacuum at the edge.

Another effect of neutrals is that they can enhance losses by radiation from impurities [45–47]. By charge exchange between neutrals and impurities the charge state of the impurities is lowered resulting in increased radiation losses. This is especially true in the case of high power neutral beam heating, but recent calculations have also stressed the importance of this effect for regular discharges [48]. Comparison of the rate coefficients for charge exchange recombination of ionized impurities with the ionization rates of those impurities can give values of the ratio of neutral density to plasma density above which this process can have an influence. Figure 2.12 shows the dependence of radiated power on the ratio of neutrals to plasma density and the temperature [49]. The acceptable influence of neutrals in this case would depend on the impurity level, and the power available.

High neutral levels in the center of the plasma should also be avoided because charge exchange with energetic ions provide a source of hot neutrals which bombard the wall. Those can eventually produce sputtering and cause impurities to come into the plasma [50].

In addition to affecting transport by the mechanism of charge exchange and

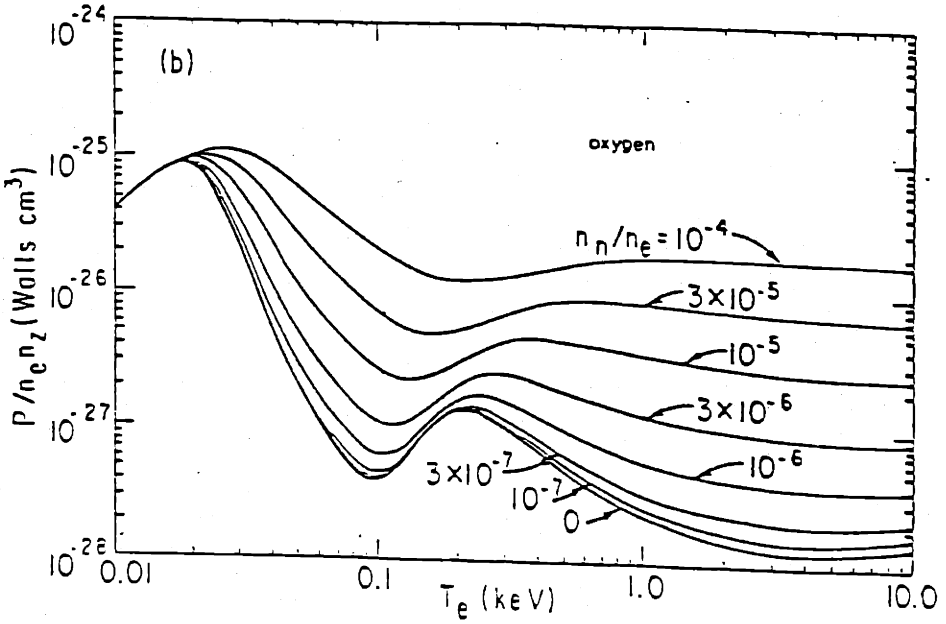

Figure 2.12 Enhanced radiation due to the reduced ionization degree of the impurities [49].

---

enhanced radiation losses, the presence of neutrals can also influence transport directly if their density is so high that particles collide more often with neutrals than with the charged particles.

To calculate the collision time of electron with neutrals we only include electron impact ionization [29] . In fact, below about $3eV$ elastic scattering [51, 52] starts to dominate. The ratio of neutral density to plasma density for which the electron-ion collision time τ_{ei} equals a fraction f of the electron-neutral collision time τ_{en} is shown in Figure 2.13. Similarly we can calculate the ion-neutral collision time and compare it to the ion-ion collision time. To calculate the ion-neutral collision time we have included charge exchange and ion impact ionization. The elastic collision cross section for protons with atomic hydrogen are much smaller [53], than the charge exchange cross section [29]. At high temperature ($> 10keV$) ion impact ionization dominates. Figure 2.13 shows the ratio of neutral density to plasma density for which $\tau_{ii} = f\tau_{in}$. Using the more stringent of the two conditions, and $f = 0.1$ we have delineated in Figure 2.14

the acceptable parameter space in the assumption that the only neutrals are those arising from recombination at the edge.

In this section we have shown that for the plasma to be impermeable to neutrals from the edge, there is a rather strict condition on the product of density and size. In the case of permeable plasmas we have to take multiple effects into account. Neutrals can have effects on β limits through influencing density profiles and will increase losses through charge exchange and enhanced radiation of impurities. Those effects could in principle be taken into account in large computer codes. In terms of applicability of similarity scaling we can request that the plasma behavior should not be dominated by collisions with neutral particles, this sets a maximum operating temperature.

2.4.1.3. Recycling and refueling

It is clear that in the regime of permeable plasma recycling and refueling at the wall are important effects. Some experimental results are reviewed here in order to investigate how this effect could be minimized. We also present a model that can explain some of the seemingly different behaviors between different machines and provides a helpful qualitative guide to minimize effects of the plasma wall interaction.

Several experiments have confirmed that recycling is the major way by which the plasma density is maintained. Hydrogen ions and neutrals that strike the walls are reflected or detrap absorbed hydrogen atoms. An equilibrium is attained where the number of particles gained is equal to the number of particles lost. Isotopic exchange experiments [54] in Dite, show that after numerous discharges in hydrogen, and a switch to D as filling gas, H is still present in the plasma in the first few discharges. While this recycling mechanism is useful in that the density is maintained, without the need of a large neutral density at the plasma edge, it has the disadvantage that controlling the density in the plasma is less easy. One could compare the situation with the method that was used to provide the equilibrium of the plasma in the early days of the tokamak. The

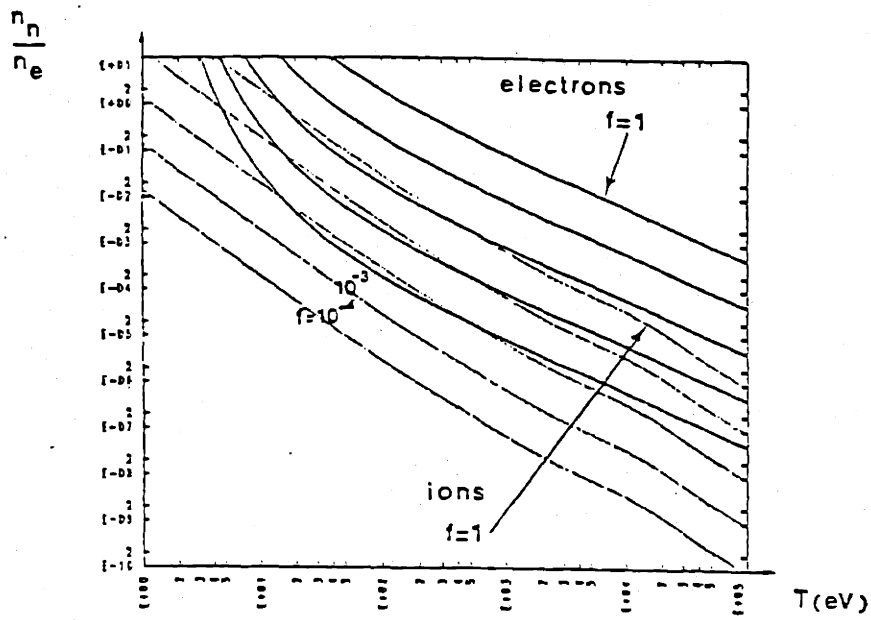

Figure 2.13 Acceptable ratio of neutral density to plasma density as a function of temperature, based on the collision times

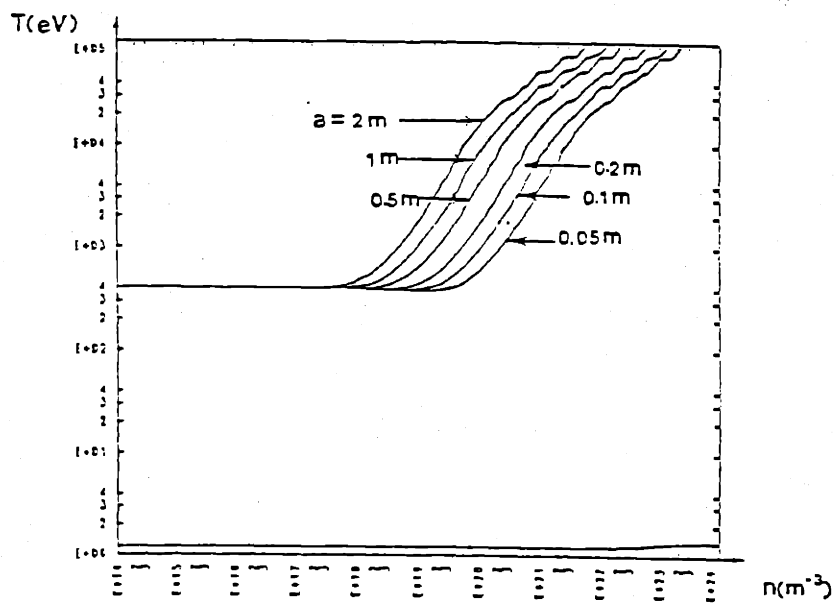

Figure 2.14 Limits in n, T diagram in relationship to collisions with neutrals

copper shell provided automatically equilibrium, but it was not until feedback methods were developed that the plasma could be better controlled.

An extremely enlightening series of experiments was performed on T-3 in 1971 [55]. Some conclusions are still valid, while reinterpreting a number of findings in view of recent information provides a better understanding. T-3 is particular [56] in that the chamber can be heated to 500 — 600°C. At this temperature all H is thermally desorbed [57]. Thus it can be assumed that no H is present on the walls of T-3. Another particular feature is the rather large plasma-wall distance because the radius of the limiter is comparatively small compared to the minor radius of the chamber. The series of experiments involved monitoring the H_β radiation at several locations, corresponding to ionization near the wall, near the limiter and near a pulsed gas injection port. Their conclusion, with respect to recycling is that the flow of neutrals from the limiter is approximately 10 to 20% of the total flow, and is proportional to the density of the plasma. An experiment using He injection confirmed that this flow from the limiter is due to neutralisation of the hydrogen ions reaching the limiter and desorption of the atoms formed and not of desorption by ion bombardment of H that would be present in the limiter. The remainder of the flow comes from the liner and consists of two parts. One part, dependent on the pressure of the working gas admitted to the chamber prior to the discharge, and only slightly dependent on the plasma parameters. A second part is associated with bombardment of the walls by plasma present in the shadow of the limiter. Distance between column boundary and wall changes the repartition of the flow.

Experiments on the effect of plasma wall distance have been performed on TFR [58]. In spite of increasing quantities of gas injected, the density decreased for increasing plasma wall distance from $7.4 \times 10^{-19} m^3$ for $a = 19cm$ to $4.8 \times 10^{-19} m^3$ for $a = 12.5cm$ (radius wall $r_w = 21.5cm$), confirming the role played by the wall in terms of recycling.

Experiments on other machines (TFR, Dite, Alcator) have shown similar or different behavior. Models have been set up based on one reservoir of particles

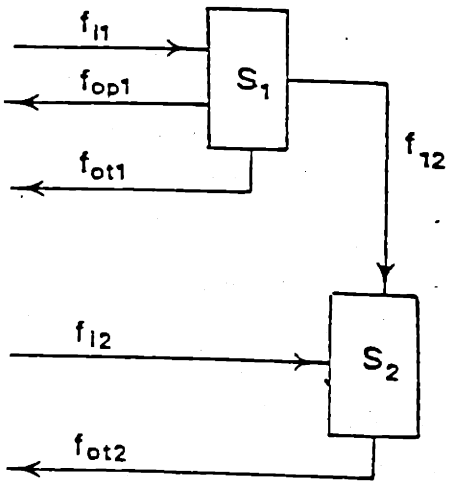

Figure 2.15 Two reservoirs model

in the wall, with fluxes of ions, hot or cold neutrals [59, 60]. One model has even be extended to include limiter interaction, a plasma transport model to calculate the fluxes and a wall diffusion model [60].

Those models are useful when trying to obtain the evolution of the density under particular conditions. Numerous constants within equations have to be estimated for the specific machine. It is then possible to get agreement between the model and the results. Our purpose here is to try to find the major factors affecting recycling and refueling and find the optimum conditions in terms of plasma behavior.

We have devised a simple model that explains qualitatively the behavior of wall interaction and especially the variation from one machine to another. We assume that there are in the wall two reservoirs of particles S_1 and S_2, that behave differently under different conditions, see Figure 2.15. Attention was drawn to fast processes in addition to slow processes by [61], the presence of two reservoirs is further confirmed by thermal desorption experiments conducted by Wilson [62] and by isotope exchange experiments by Blewer [63].

Assume the first "fast" reservoir S_1 to be filled by interaction with the plasma f_{i1}, while it can be emptied along three paths. One is a flux f_{0p1} proportional to f_{i1}, when S_1 is full, the second path is thermal desorption, the third is by "slow" transfer to S_2. The second reservoir S_2, is filled from reservoir S_1 and by more energetic ion and neutrals coming from the plasma. It desorbs by thermal effects. This model can be used both for the wall and the limiter. Different materials, at different temperature will behave differently, and this can be explained in terms of relative size of the reservoirs S_1 and S_2, and of the size of the fluxes f.

The relative contribution of limiter and wall is very much affected by the distance between plasma and wall. Other factors that affect recycling and vary from one machine to another are the choice of material for limiter and wall and prior conditioning of the wall, the number of limiters, and the temperature of the wall.

Recycling on the wall being due in part to the plasma in the shadow of the limiter, it will be affected by the number of limiters and errors in the magnetic field [64]. If field lines do not stay at a constant distance from the wall, a field line which is just not intercepted by a limiter may carry plasma along field lines quite far into the shadow of the limiter, and thus provide a mechanism for a high density plasma near the wall.

The usual choice for a wall has been stainless steel. Other choices have been quartz, gold plated stainless steel, with platinum diffusion barrier (Ormak), alumina (Petula), carbon (TM-G-Tokamak) and inconel (TFR, Textor). Stainless steel is the best documented. The saturation level of the surface increases with increasing energy of the impinging ions [63] and depends on microdamage of the steel [62]. Larger fluxes are needed to saturate the steel at lower temperature [65]. At low temperature ion induced release is the mechanism that detraps hydrogen. At room temperature, diffusion also plays a role.Total release cross sections at room temperature and at $77K$ [66] are about the same which confirms a reduction in the induced detrapping cross section at higher temperature. Clausing also

[65] found that recycling at higher temperature is greatly enhanced by thermal processes, while at $80K$ it is dominated by plasma induced processes.

Oxygen contamination of the surfaces was discussed in [61, 65]. It increases the amount of hydrogen retained on the surface and, while it does not affect the rapid recycling rate, it does increase the amount and the speed with which hydrogen is released over a longer time scale.

If we now translate this information into our model we have that at low temperature the flow f_{12} is shut off and only S_1 takes part in the process. The reservoir is large, which explains why the first Alcator discharges, without gas puffing have a large density drop [67]. It also explains why only a small number of discharges are necessary in Alcator to observe a complete switch over of the gas when performing on isotopic exchange experiments. While S_1 is large at low temperature, the change over is rapid and easy. At higher temperature the size of S_2 increases with respect to S_1, at the same time the fluxes f_{12} increases, as well as $f_{0:1}$ and $f_{0:2}$. The smaller reservoir S_1 is filled more rapidly, giving a lower density drop. For isotopic exchange experiments, when S_2 starts coming into play, more discharges are necessary to change the gas because the processes are slower. The T—3 result can be understood in the following terms. Because of the elevated wall temperatures there is good communication between S_1 and S_2, while the size of S_2 is relatively large compared to S_1. Ionization of the filling gas and poor confinement in the initial stage of the discharges fills S_1, and spills over in S_2. The first part of the flux identified in the experiment is the flow $f_{o:2}$, from S_2 proportional to the pressure of the filling gas. The second part, proportional to the plasma density is the flow f_{op1} which involves S_1. The model can also explain why, in experiments on ISX with neutral beam heating, the density drops. This is because fluxes to the wall are more energetic and thus penetrate to the reservoir S_2, from which the release is slower. The effect of oxygen on the walls at room temperature is to increase reservoir S_2 and increasing the flux f_{12}. It is thus similar to operating at higher temperature. No information is available on the influence of oxygen on trapping and detrapping

at low temperature but in terms of our model, results of Alcator seem to concur with the assumption that at low temperature only one "fast" reservoir exists. The use of Ti gettering is equivalent to having only a large and fast reservoir S_1. It is this in this respect completely similar to working with walls at liquid nitrogen temperature.

The two reservoir model can also be used on limiters. Because limiters operate at high temperatures, communication between S_1 and S_2 is very good. At high temperature S_2 is much larger than S_1, so that a large fraction of neutrals coming from the limiter come from S_2. For a graphite limiter S_2 is very large, which explains the difficulty of rising the density even with large gas puffing on Alcator C with a graphite limiter. It has even been shown [68] that even at room temperature 100% trapping is observed for fluxes up to 10^{18}atoms/cm^2.

The existence of two reservoirs, and their different behavior, could possibly be explained by the presence of two different mechanisms. The first reservoir would be linked to physical trapping of the atoms, while the second may involve chemical processes. The experimental results, together with the qualitative model we have developed suggest that operation with walls at liquid nitrogen temperature or with loaded titanium gettered walls result in rapid recycling of large quantities of H at the edge. This maintains the density of the plasma without the need of large neutral density at the edge. The rapid recycling cools the plasma edge, which is beneficial in terms of impurity production, but it also has effects on temperature and density gradients.

2.4.2. Impurities

In this section we intend to discuss the influence of impurities on the use of similarity scaling laws. We will follow the same pattern as for our discussion of the neutrals, although with slightly different emphasis. First we will discuss how impurities can get into the plasma. Contrary to the case of neutrals we can not calculate from theoretical grounds what their density is. We will therefore have to rely on the third part where we review some experimental results to obtain

more information. In the second part we discuss, as we did for neutrals, what an acceptable level is of impurities in order to be able to use similarity scaling laws.

2.4.2.1. Source of Impurities

In most cases impurities arise from the presence of a wall, and a limiter. Arcing, sputtering by ions and hot neutrals, evaporation are all possible mechanisms for dislodging some of the wall material or limiter, or of impurities absorbed on the wall/limiter. Distinguishing between interaction with wall and interaction with limiter is complicated by the fact that wall and limiter operate in quite different regimes. The large wall surface has a lower heat load than the limiter and is thus usually at lower temperature. While in some cases limiter and wall material are made of different material, which should allow us to pinpoint the source of impurities in the plasma, this is too optimistic because sputtered limiter material will cover the wall with a thin layer, making experiments inconclusive. Ionized particles can interact with the limiter by flowing down the field lines, while diffusion across the magnetic field is necessary to interact with the wall. Other sources of impurities can be the original gas composition in the chamber prior to filling, impurities introduced by the plasma formation scheme (plasma gun) or through the neutral beams used to heat the plasma.

No successful attempt has ever been made to calculate quantitatively the impurity level to be expected in a plasma based on the before mentioned influences. Even qualitatively the understanding is far from complete. We will thus have to rely more on experimental data.

2.4.2.2. Acceptable Level

The level from impurities from the point of view of application of similarity scaling laws is very small. Indeed, transport in a plasma is altered because ions (or electrons) will collide with impurities as well as with the other ions. Because the collision frequency of ions with impurities is proportional to $n_i n_z Z^2$ where n_z is the density of impurities, while the collision frequency of ions among

themselves is proportional the $n_i n_i$, it is clear that in order to have collisions between ions to be the dominant effect there is a rather stringent condition on the ratio $\frac{n_z Z^2}{n_i}$.

Using the definition of Z_{eff} ($n_e Z_{eff} = \Sigma n_i Z_i^2$), charge neutrality ($n_e = \Sigma n_i Z_i$) and the respective collision times, we can calculate the ratio $\frac{\nu_{iz}}{\nu_{ii}}$ as a function of Z_{eff}, for different values of Z (shown in Figure 2.16). In general we have

$$\frac{\nu_{iz}}{\nu_{ii}} = \frac{Z(Z_{eff} - 1)}{Z - Z_{eff}}$$

and

$$\frac{n_z}{n_i} = \frac{Z_{eff} - 1}{Z(Z - Z_{eff})}$$

Let us take Oxygen as the dominant impurity, assume it to be completely ionized (Z=8), and further take as limit of applicability of the similarity laws $\frac{\nu_{iz}}{\nu_{ii}} < \frac{1}{2}$. Even with this marginal constraint (we would rather set $\frac{\nu_{iz}}{\nu_{ii}} < \frac{1}{10}$) we obtain the stringent condition $Z_{eff} < 1.41$, $\frac{n_z}{n_i} < 0.8 \times 10^{-2}$.

The fact that theoretical scaling laws for τ_E based on similarity considerations did not agree with scaling laws derived by Hugill and Sheffield [69] from experiments was mentioned by Connor and Taylor [8]. The reason they give is the fact that radiation plays a dominant role and is not excluded from the calculation of τ_E.

Even though the data base used by Pfeiffer and Waltz [70] included only 14 out of 118 points where $Z_{eff} < 1.4$ (11 from Alcator, 2 from ATC, 1 for ST) they conclude it is possible to obtain scaling laws that are compatible with similarity scaling laws. Recently Zampaglione [71] found that the scaling laws for τ_E from machines with $Z_{eff} = 1$ agree with the theoretical constraints based on a collisional high β model.

In addition to influencing the transport, impurities can have other effects. A major one of course is radiation. It can mask or make very difficult to measure transport losses. Because of the large energy losses it restricts the parameter space available to perform experiments. Gibson [72] has pointed to impurities as

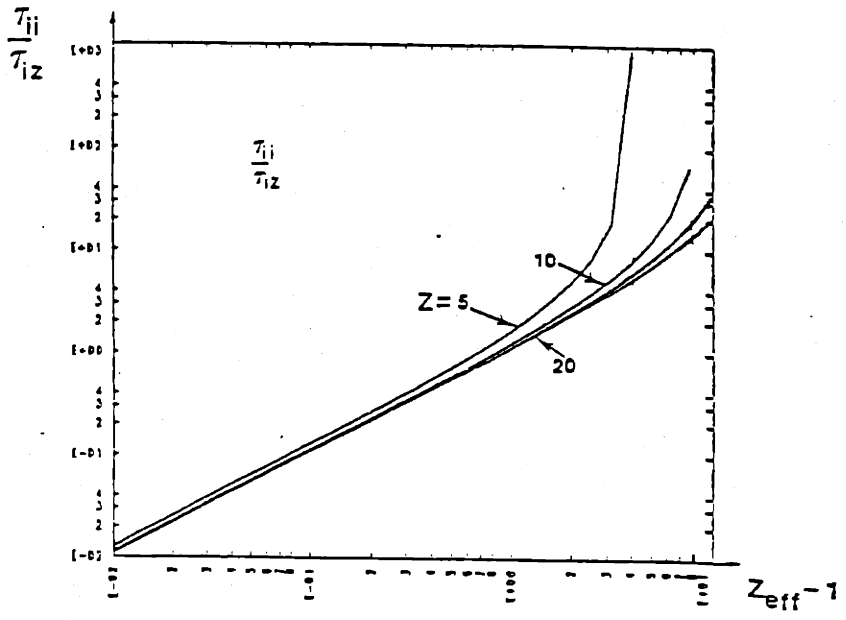

Figure 2.16 Ratio of collision frequency as a function of $Z_{eff} - 1$.

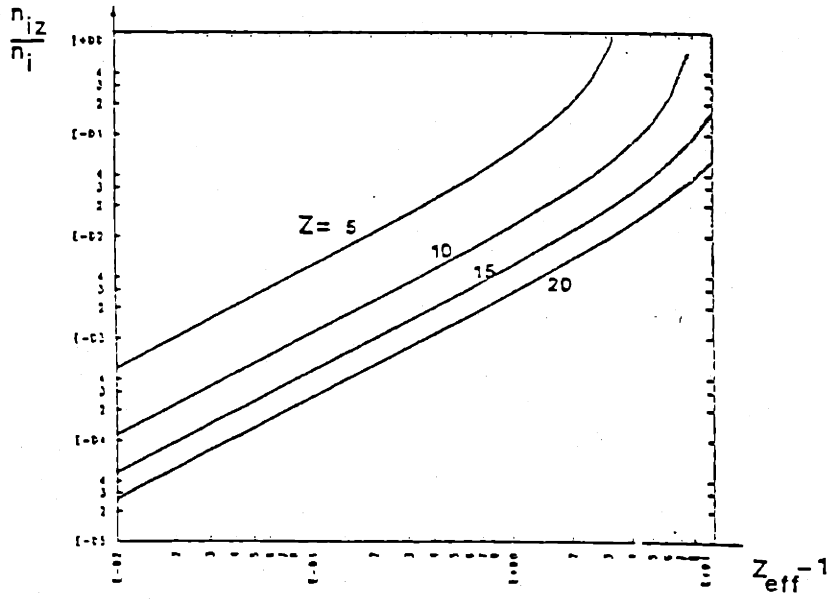

Figure 2.17 Acceptable level of impurities

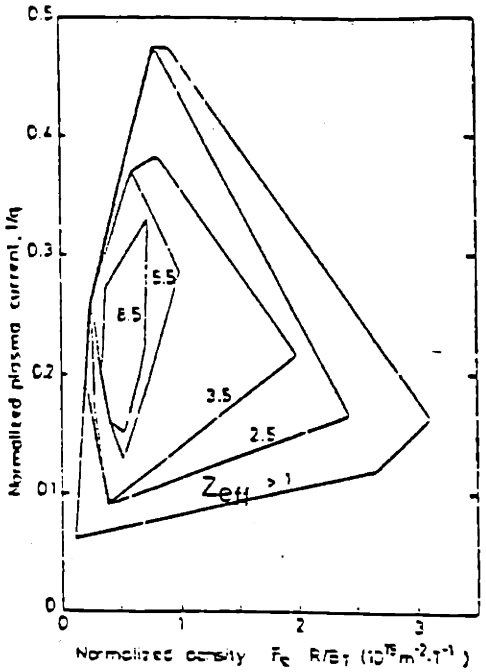

Figure 2.18 The operating space of tokamaks is reduced as Z_{eff} increases

a possible cause of the density limits. The diagram of Figure 2.18 summarizes the experimental results of numerous tokamaks [73] and shows how Z_{eff} reduces their operating space.

In Figure 2.19 and 2.20 we show the results of calculations for power losses in $\left(\frac{W}{m^3}\right)$, due to impurities for oxygen and iron, we have assumed coronal equilibrium [74], and an impurity density of 1% for oxygen and of 0.1% for iron.

Several caveats have to accompany those results.

A plasma may not be in coronal equilibrium, inward diffusion of impurities causing then to be in a lower charge state than one would expect from coronal equilibrium, thus possibly increasing the power radiated. Another mechanism already mentioned is the reduction in charge state of impurities due to charge exchange with the neutrals present in the plasma. The usefulness however of this simple approach is to readily identify regions of n, T parameter space that are certainly inaccessible. Comparing the power lost through radiation, with

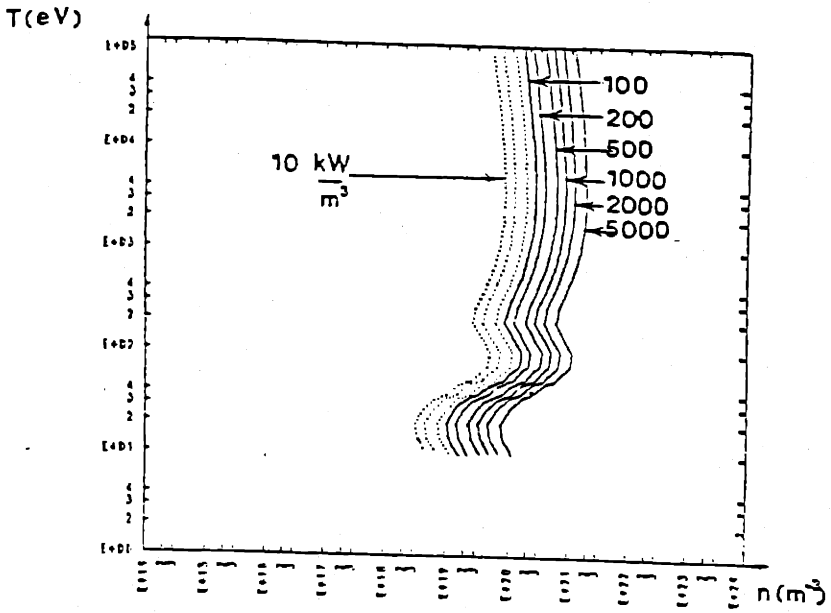

Figure 2.19 Radiation losses due to 1% oxygen impurity.

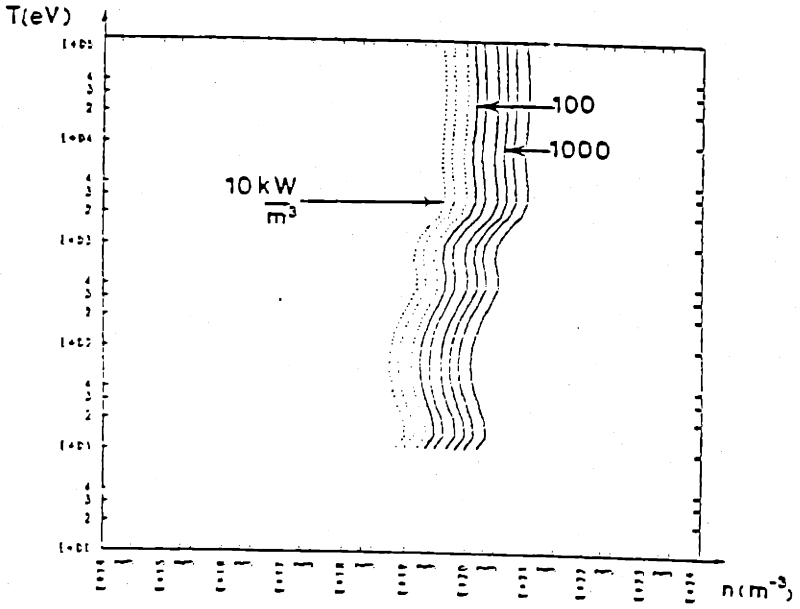

Figure 2.20 Radiation losses due to 0.1% iron impurity.

the power that can be deposited through ohmic heating would define the space within which tokamaks can certainly not operate. Machines in which a large major fraction of the energy is deposited by Ohmic heating are particularly sensitive to the presence of impurities. As the resistivity is proportional to Z_{eff} it can give localized increase in power deposited, and this changes the profiles. Similarly, large radiation levels have been responsible for inverted temperature profiles (lower at the center than at the edge). In view again of the temperature dependence of the resistivity it affects the current profile .

Only very low level of impurities are thus acceptable in a plasma if similarity scaling laws are to be applied. Additional constraints may arise from the large power losses and the sensitivity of current profiles to the presence of impurities. Let us now look at some experimental results to see whether size or magnetic field affect the impurity level.

2.4.2.3. Impurity Control

We have seen that, based on the applicability of similarity scaling laws, only very small amounts of impurities are allowed. The constraints are more stringent for heavy impurities than for light impurities. As the production mechanism and behavior in the discharge of heavy and light impurities is different, we will discuss them separately.

Heavy impurities are produced by arcing, evaporation and sputtering. Arcing has been shown to be more frequent on unclean surfaces, while it also shows a clear correlation with the edge temperature [75,76]. A low temperature at the edge is necessary to avoid arcing. Runaway electrons, or large thermal loads produce impurities by evaporation of local hot spots, usually at the limiter. Proper control of the discharge and a sufficient number of limiters are helpful to cure this problem. Sputtering is caused by the ions or neutrals colliding with and knocking out some of the atoms from the wall or limiter. There is a minimum energy necessary, depending on the mass of the sputtering particle and the material of the wall [77]. In this respect energetic neutrals, coming from

the center, because the plasma is not impermeable, are particularly damaging. High temperatures at the edge too result in efficient sputtering by ions because the ions may be accelerated by the sheath potential (of the order of three times the electron temperature). The process of selfsputtering, where the heavy ions of charge Z gain an energy ZT_e was shown to result in catastrophic increases of the impurity levels in the plasma [78]. Once again low temperatures at the edge are necessary in order to mitigate this problem. Heavy impurities will radiate strongly even at rather high temperature because they are incompletely stripped. Their behavior in the discharge is still not completely understood and it is still not clear whether they will accumulate in the plasma or not. Recent experiments on Alcator C [79, 80] have shown no accumulation in the center. An interesting difference was also revealed in the time behavior of heavy and light impurities, the reason being ascribed to the fact that light impurities (usually gases) are recycled at the wall while heavy impurities are not.

Light impurities are usually present as surface or bulk contaminants of the wall. Their introduction in the plasma arises from thermal desorption or particle induced desorption. The presence of oxygen on the wall influences the recycling of the hydrogen. It also affects the discharge in other ways. Effective radiation by oxygen at the edge lowers the edge temperature and results in a reduction of the sputtering of heavy impurities. The achievement of lower q values in T-10 compared to T-11 is attributed to the fact that the wall of T-10 are less clean than those of T-11. Better cooling of the edge, through oxygen radiation results in less heavy impurities, allowing flatter current profiles and thus lower q. The same effect was obtained by using Ne as radiator. In the case of oxygen however there may be an additional explanation. Experiments in which stainless steel was bombarded with 2 keV H have shown a strong dependence of the sputtering yield on the amount of oxygen on the surface [81]. Oxygen plays a peculiar role too in terms of the temperature of the wall. The oxygen/water cycle was reviewed in [82]. Marmar has shown that there is a distinctly different behavior for temperatures of the wall above or below the freezing point of water [67].

In terms of level of impurities is there an impact resulting from the size versus the magnetic field of a machine ? Accuracy of the magnetic field is important because errors can bring hot plasma, flowing along field lines nearer to the wall than would normally be expected. The absolute value of the magnetic field would only put constraints on the size in the case of very low magnetic fields, where we would have to request that the larmor radius of the impurity ion be small compared to a. In most cases the ratio $(\sqrt{mass}/charge)$ of the impurity ion is smaller than this ratio for a hydrogen ion so that the constraint on $\frac{\rho}{a}$ is more stringent for the hydrogen ions than for the impurities. If we want to avoid sputtering by fast neutrals the product na has to be sufficiently high for the plasma to operate in the impermeable regime. The presence of oxygen contamination may be helpful both directly and indirectly (by reducing the edge temperature) in reducing the sputtering of heavy impurities.

The amount of impurities in the plasma seems to bear little correlation with size or magnetic field. It does seem influenced by temperature at the edge, plasma wall distance, prior conditioning of the walls and by the vacuum system in general. That size and magnetic field have further little influence is confirmed by the fact that both Tosca and Alcator operate at $Z_{eff} = 1$. The wall preparation has a much larger impact : Alcator operates with walls at liquid nitrogen temperature. This seems to be an excellent method. The rapid recycling of a large reservoir of H on the wall keeps the edge temperature low. Possible oxygen contamination on the walls reduces the sputtering, while most of the oxygen that would be desorbed combines into H_2O that becomes fixed on the wall. Tosca uses gettering. This is an alternative method that however has the drawback of possible contamination with Ti.

2.5. Achieving the plasma parameters dictated by similarity

To achieve the plasma parameters obtained from similarity scaling laws we have to be able to produce the plasma and bring it to the required densities and temperatures. The constraints that can result from this are discussed here.

2.5.1. Plasma production methods

Several methods can be used for plasma production. The most widely used of course is breakdown by a strong DC electric field. This can easily be achieved when Ohmic heating is used, since the same coils are used. Other methods are microwave startup near electron cyclotron and upper hybrid resonances [83], and ICRF [84, 85].

Injection of plasma by washer-guns has often been applied to stellarators [17, 86], but can lead to a formation of convective cells. A more recent method has been the in-situ illumination with laser light of frozen pellets [87]. Sufficient flexibility exist in the choice of the startup method since little power is needed. More important constraints result from the methods that will be used to heat the plasma.

2.5.2. Plasma heating

Constraints can arise from the limitations on the methods that are used to heat the plasma. Our intention here is to review for each of the major heating methods some relations that may put constraints on size, magnetic field, density and temperature, thus restricting the parameter space in which one can operate.

2.5.2.1. Ohmic Heating

The use of ohmic heating sets a lower limit on a combination of density and temperature. The critical energy for runaway electrons is given by [88]

$$\frac{mv_{cr}^2}{2e} = \frac{e^2 n \ln \Lambda}{4\pi\epsilon_o^2 E} \tag{2.8}$$

The maximum power per unit volume that can be deposited is given by

$$P = \eta J^2 = \frac{E^2}{\eta}$$

Taking the resistivity to be

$$\eta = \frac{(m)^{1/2} Z e^2 \ln \Lambda}{3^{1/2} 12\pi\epsilon_o^2 T_e^{3/2}}$$

and the critical energy $\frac{mv_{cr}^2}{2}$ equal to the electron temperature T_e we obtain

$$P_{max} = \frac{n^2}{(\frac{T}{e})^{1/2}} \frac{\ln \Lambda}{Z} \frac{e^{7/2} 3^{3/2}}{4\pi\epsilon_o^2 m^{1/2}} = 9.1 \times 10^{-30} \frac{n^2}{(\frac{T}{e})^{1/2}} \frac{\ln \Lambda}{Z}$$

This restriction could be alleviated by the use of turbulent heating [89].

For specific concepts there will also be a constraint resulting from MHD stability. In a tokamak for example, the requirement that q on axis can not be much smaller than 1, results in a maximum current density.

$$J = \frac{1}{q} \frac{2B_\phi}{\mu_o R} < \frac{2B_\phi}{\mu_o R}$$

The maximum power that can be deposited then is

$$\begin{aligned} \eta J^2 &= \frac{(ne)^{1/2} Z e^2 \ln \Lambda}{3^{1/2} 12\pi\epsilon_o^2 T_e^{3/2}} \left(\frac{2B_\phi}{\mu_o q R} \right)^2 \\ &= 184 \times 10^6 \frac{1}{(\frac{T_e}{e})^{3/2}} \left(\frac{B_\phi}{qR} \right)^2 \end{aligned} \qquad (2.9)$$

Other concept may not be limited by this. It is not a constraint for a reverse field pinch for example. Concepts that have a rotational transform provided by external means can have a current density larger than given in formula (2.9) since the original rotational transform can be in the opposite direction as the one provided by the current. The need for coils providing the flux swing can put some constraints on the geometry and the method itself also results in a limited pulse length.

2.5.2.2. Electron cyclotron resonance heating

Electron cyclotron resonance heating will set constraints on density and magnetic field. The constraints are different depending on the heating mode considered [90]. Define ω_{ce} the electron cyclotron frequency, ω_{pe} the electron plasma frequency

and α the square of their ratio

$$\omega_{ce} = \frac{eB}{m}$$

$$\omega_{pe} = \left(\frac{ne^2}{\epsilon_o m}\right)^{1/2}$$

$$\alpha = \frac{\omega_{pe}^2}{\omega_{ce}^2} = \frac{m}{\epsilon_o}\frac{n}{B^2}$$

The constraints resulting from accessibility requirements are then [91]

$\alpha < 1$ for ordinary wave heating at $\omega = \omega_{ce}$

$\alpha < 2$ for extraordinary wave heating at $\omega = \omega_{ce}$, wave launched from high field region.

$\alpha < 2$ for extraordinary wave heating at $\omega = 2\omega_{ce}$

$\alpha < 4$ for the ordinary wave at $\omega = 2\omega_{ce}$.

In addition to accessibility we also have to consider whether the wave is being absorbed. The fraction of the wave absorbed in one pass through the cyclotron layer is given by

$$A = 1 - e^{-\Gamma}$$

The value of Γ is given by [90]

$$\Gamma_{1O} = \frac{\pi}{2}\frac{T_o}{mc^2}\alpha k R_o$$

for the extraordinary wave at the fundamental frequency.

$$\Gamma_{1X} = \frac{\pi}{2}\frac{T_o}{mc^2}\cos^2\theta\frac{1}{\alpha}[2 + \alpha(1-\alpha)]^2 k R_o$$

for extraordinary wave at the fundamental frequency.

$$\Gamma_{2X} = \frac{\pi}{2}\frac{T_o}{mc^2}\alpha k R_o$$

for the extraordinary wave at the second harmonic.

And

$$\Gamma_{2O} = \frac{\pi}{2}\left(\frac{T_o}{mc^2}\right)^2 \alpha k R_o$$

for the ordinary wave at the second harmonic. In those formulas R_o is the major radius of the device (for a tokamak; in general it is a measure of the gradient in the B field), k is the wave number at the resonance and T_o is the central temperature.

Note that the damping increases with the density (α) except for the extraordinary wave at the fundamental for which it is higher at lower density. The damping also increases with temperature and is rather small at low temperature for the ordinary wave at the second harmonic frequency.

2.5.2.3. Lower hybrid heating

The heating by lower hybrid waves is still not completely understood. The reason is that important effects result from non linear processes which are difficult to treat theoretically. We summarize here the constraints mentioned by Brambilla [92]. The lower hybrid frequency is of the order of the ion plasma frequency

$$\omega^2 = \omega_{LH}^2 = \frac{\omega_{pi}^2}{1 + \frac{\omega_{pe}^2}{\omega_{ce}^2}} \tag{2.10}$$

There is a low density cut off for slow waves. It is given by $\omega = \omega_{pe}$ or

$$n = 1.24 \times 10^{16}/m^3 \left(\frac{f}{1GHz}\right)^2 \tag{2.11}$$

For the resonance to be accessible the parallel index $N_\parallel = \frac{ck_\parallel}{\omega}$ has to be larger than a certain value given by

$$N_\parallel^2 > \left(1 + \frac{\omega_{pe}^2}{\omega_{ce}^2}\right)_{res} \tag{2.12}$$

Mode conversion and ion heating occurs for

$$N_\parallel \sqrt{\frac{T_i}{1000e}} = \alpha_1 \frac{\omega^2 - \omega_{LH}^2}{\omega_{LH}^2} \tag{2.13}$$

while electron Landau damping occurs for

$$N_\parallel \sqrt{\frac{T_e}{1000e}} > \alpha_2 \tag{2.14}$$

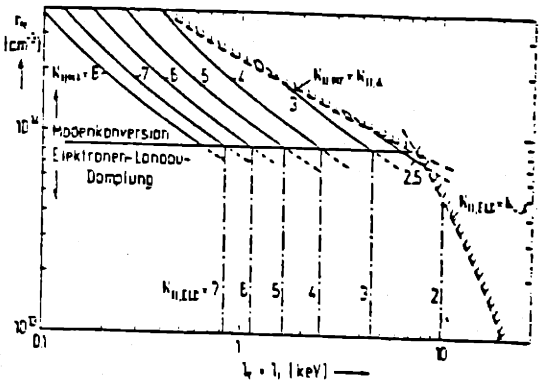

Figure 2.21 Constraints on density and temperature for lower hybrid heating [94]

Electron damping will be the prevailing mechanism when

$$\frac{\omega^2}{\omega_{LH}^2} > 1 + \frac{\alpha_2}{\alpha_1}\sqrt{\frac{T_i}{T_e}} \tag{2.15}$$

In a more recent paper [93] Brambilla gives $\alpha_1 = 6.7$ and $\alpha_2 = 6.4$. Combining the equations (2.13) with the accessibility conditions (2.12) will result in a maximum on the combination of density and temperature. Combination of equation (2.12) with the condition (2.14) result in a similar limit. Those limits are shown in Figure 2.21 [94] for the particular combination $B_o = 2.5T$, $f = 1.3GHz$ and D_2 gas. For lower hybrid heating we have thus a low density limit and a maximum on the combination of n and T. That this picture is far from complete is confirmed by the fact that on the ATC tokamak a threshold for the power was found, threshold which depended on the density [95]. For an average density of $1.8 \times 10^{19}/m^3$ the power threshold for heating was about $10kW$, while for an average density of $0.9 \times 10^{18}/m^3$, the power threshold was larger than $120kW$. This could be the result of poorly understood non-linear processes.

2.5.2.4. Ion cyclotron resonance heating

Different methods can be used to heat the plasma in the ion cyclotron range of frequencies. Heating at the second harmonic can only be efficient in high density, high temperature plasmas. Heating of a minority species at the fundamental with subsequent transfer of energy to the bulk through collisions provides absorption of the power in a single pass, but results in the production of an energetic tail which has to be confined. For a comparable concentration of two ion species mode conversion occurs at the ion-ion hybrid resonance layer. The wave energy is then damped through electron landau damping.

A common condition needed for propagation of the fast wave is given by

$$na^2 > 5 \times \frac{10^{17}}{m}\left(\frac{M}{M_H}\right)\left(\frac{\omega_a^2}{\omega^2}\right)$$

Confinement of the fast particles requires a minimum on $\frac{\rho_\epsilon}{a}$. Constraint on the size of an experiment can also result from the limited power density (about $500W/cm^3$) of the wave launching structures.

2.5.2.5. Heating by neutral beams

The use of neutral beams to heat the plasma result in a set of rather stringent constraints. A minimum for the product of density and size is set by the need to ionize a major fraction of the beam before it emerges again out of the plasma. An estimate is given by [94]

$$na = \frac{10^{18}}{m^2}\left(\frac{E}{1keV}\right)$$

for D tangential injection and

$$na = \frac{2 \times 10^{18}}{m^2}\left(\frac{E}{1keV}\right)$$

for H tangential injection.

On the other hand the energetic particles have to be confined. Details will depend on the geometry and injection method (counter or co-injection). As in the case of ICRH there will be the requirement that $\frac{\rho_\epsilon}{a}$ be smaller than a certain value.

2.6. Summary

In this chapter we have discussed the method of similarity, which argues that information obtained on models are applicable to full scale machines if some dimensionless parameters are kept constant. We have briefly reviewed two methods to derive the dimensionless parameters, each method having its particular advantages and drawbacks. Application of the method to plasma physics yielded the appropriate dimensionless parameters. In order to gain sufficient freedom in the choice of the parameters in the scaled version, we had to drop one or more of the dimensionless parameters. We have delineated under what conditions we can justify this. Departure of the model on which the similarity is based arises from the presence of neutrals in the plasma and from the presence of impurities. We have set limits on the level of neutrals and impurities that can be accepted in order to be able to continue to use the model. A major constraint arises if we request that the plasma be impermeable to neutrals. Level of impurities have little correlation with size or magnetic field. In a last section we have discussed the constraints we can encounter when we try to obtain the parameters dictated by similarity considerations.

3. Technical Constraints

3.1. Introduction

In this chapter we plan to investigate the technological constraints that may make some areas in the parameter space inaccessible. We will concentrate on obtaining relationships between the weight of the system (or a measure of its cost), its stored energy and energy requirements with size and magnetic field. Those two parameters were our possible degrees of freedom for the similarity scaling.

The weight of the coils depends on the size and the magnetic field, but also on current density limits and structural constraints. Those limits are different depending on the choices made for the coils. We thus investigate current density limits for water cooled, liquid nitrogen cooled and superconducting coils. For the structural constraints, we looked both at D shaped and circular coils. Using those constraints a general formula is set up that gives the mass of the system in terms of the size and the magnetic field.

Since the stored energy is also a function of size and magnetic field, we investigate whether there is a relation between stored energy and the mass of the coils

A sometimes stringent constraint, when going to small size and high magnetic field is access to the plasma for diagnostic and heating purposes. This aspect is

mentioned but depends strongly on the geometry. It is discussed in a later chapter specifically for the stellarator with helical magnetic axis. Power requirements can further restrict the choices one can make with respect to the design of an experiment. We show those requirements can be related to the stored energy, the pulse length and the mass of the experiment.

Let us now first turn to the investigation of current density limits.

3.2. Current Density Limits

3.2.1. Introduction

It is easy to see that current density limitations play an important role in the total weight of conductor that will be needed for an experiment. Indeed, take $W = Al\gamma$ where W is the weight, A is some characteristic cross section, l is the total length of the conductor and γ the density.

The cross section can be related to the current I and the current density J through $A = \frac{I}{j}$.

The weight of the current carrying conductor is then $W = \frac{I}{j} l\gamma$. Thus for a given size and magnetic field, the total weight of the conductor will go down, inversely proportional to the current density pointing to the reason why it is, from that point of view, necessary to go as high a current density as possible.

Limitations on the current density differ according to the type of conductor. Water cooled copper conductors have a maximum current density based primarily on the maximum allowable temperature rise and heat removal capacity of the cooling water. This is also the case for cryogenically cooled conductors. Superconducting coils have a current density limit because of safety and stability considerations. We will discuss each type of conductor separately. Since the current density in pulsed coils is related to the pulse length of the system, let us first address this issue.

3.2.2. The Equivalent Pulse Length

The pulse length of a system not only includes the experimental flat top time, but also a time related to the time it takes to ramp up and ramp down the fields, because resistive losses are also incurred during those times.

Let us, under some simplifying assumptions obtain an estimate for those losses. We will assume that the resistivity does not change (only true for water cooled coils, for lN_2 cooled coils the resistivity change is a very important effect and this will be considered when we calculate the current density) and that during each of the three phases (ramp up, flat top, and ramp down of the fields), the voltage is kept constant. During ramp up it is necessary to use a voltage higher than needed to sustain the flat top current. This reduces the time it takes to reach the nominal current and thus reduces the losses. In the same way, to decrease the current after the flat top reversing the voltage will bring down the current faster, reducing the energy deposited in the magnet.

If I is the nominal current, then we can define a "forcing constant" C_f for the voltage during ramp up as

$$\frac{V_u}{R} = C_f I$$

The time to reach nominal current is then

$$\tau_u = \tau \ln\left(\frac{C_f}{C_f - 1}\right)$$

with $\tau = \frac{L}{R}$ the time constant of the coils. The losses going up are then

$$E_{lu} = RI^2\tau\left[-C_f^2 \ln(1 - \frac{1}{C_f}) - C_f - \frac{1}{2}\right]$$

We can define an equivalent time for ramp up τ_{eu} as

$$E_{lu} = RI^2\tau_{eu}$$

giving

$$\tau_{eu} = \tau\left[-C_f^2 \ln(3.1 - \frac{1}{C_f}) - C_f - \frac{1}{2}\right]$$

If we take the time for ramp up equal to the time for ramp down, then we need the reversed voltage to be

$$\frac{V_d}{R} = -I(C_f - 1)$$

The losses going down will be

$$E_{ld} = RI^2\tau\left(-(1-C_f)^2\ln(1-\frac{1}{C_f}) - C_f + \frac{3}{2}\right)$$

Similarly, an equivalent time for ramp down is then

$$E_{ld} = RI^2\tau_{ed}$$

with

$$\tau_{ed} = \tau\left(-(1-C_f)^2\ln(1-\frac{1}{C_f}) - C_f + \frac{3}{2}\right)$$

The total energy deposited in the coils, during ramp up and ramp down is then given by

$$\begin{aligned} E_l &= E_{lu} + E_{ld} \\ &= RI^2\tau\left[(C_f^2 + (C_f-1)^2)\ln\frac{C_f}{C_f-1} - 2C_f + 1\right] \end{aligned}$$

This formula can be approximated by

$$E_l = RI^2\tau \quad \frac{2}{3}\frac{\tau_u}{\tau}$$

This is also what one would obtain assuming the current to ramp up and ramp down linearly.

The energy deposited in the coils is thus

$$\begin{aligned} E &= RI^2\tau_p + E_l \\ &= RI^2(\tau_p + \frac{2}{3}\tau_u) \\ &= RI^2\tau_e \end{aligned}$$

This now defines an equivalent pulse length τ_e, corresponding to a square pulse of length τ_e at the nominal current I. The value of τ_e is then

$$\tau_e = \tau_p + \frac{2}{3}\tau\ln\left(\frac{C_f}{C_f-1}\right)$$

with $\tau = \frac{L}{R}$, the time constant of the coils, τ_p the flat top time and C_f the voltage forcing constant during ramp up and ramp down. For experiment with very short flat top pulses τ_p, the equivalent time can be completely dominated by $\frac{2}{3}\tau \ln \frac{C_f}{C_f - 1}$.

3.2.3. Current Density in Water Cooled Copper Magnets

We have set up a model to calculate the maximum allowed current density based on the heat removal capacity of water cooling, both under steady state and pulsed conditions.

The model, the detailed calculations and more complete results are given in Appendix A. We found that the pulse length of an experiment puts it, from the point of view of current density/heat removal capacity in the conductors, rather unambiguously in one of two classes: pulsed mode or steady state. For a coolant velocity of $1m/s$ and a pulse length smaller than about 10 s, it is best to work in pulsed mode (i.e provide as much copper as possible to increase the thermal inertia of the system, while dimensioning the cooling passages for heat removal between pulses). The maximum current density is then given by $J = \sqrt{\frac{c_p \gamma}{\rho \tau_e}\,\Delta T}$ being $J \simeq 10$ kA/cm^2 $\sqrt{\frac{1s}{\tau_e}}$ maximum for $\Delta T = 50°$C and $\rho = 1.72 \times 10^{-8} \Omega m$. In this formula τ_e is the equivalent pulse length as defined in the previous section. For a pulse length larger than about 10 s, the steady state current density can be $J \simeq 2$ kA/cm^2. The value of $10s$ depends on the coolant velocity through a 0.8 power. At higher coolant velocity, the dividing line between pulsed and steady state system occurs at a lower value of the equivalent pulse length (for $v = 2m/s$, dividing line $\simeq 5s$) with corresponding increase ($\sim v^{0.4}$) in steady state current density.

3.2.4. Cryogenically Cooled Coils

The main purpose of using cryogenically cooled coils is to reduce the resistance of the copper conductor, allowing a longer flat top for the same energy dissipated as with room-temperature coils.

The limit on average current density is again the result of a limit on the allowable temperature rise. The transition of liquid nitrogen from nucleate boiling to film boiling at a temperature difference of about 13°C [96, 97] results in a drastic drop in heat transfer rate and thus much larger cooling times. See Table 3.1. At higher temperature, the initial advantage of lower resistivity is lost, so that little is gained for too high a temperature rise. Bitter type coils have a very uneven current density distribution, giving a local hot spot temperature rise much higher than the average. This local hot spot temperature increase, which can be up to 160°C, for an average increase of only 6°C [96], has to be limited in order to avoid approaching the annealing temperature of the copper (about 350°C). Cryogenically cooled coils only use copper hardened by cold drawing, eventually interleaved with steel for strength because copper alloys do not achieve the large reduction in resistance at cryogenic temperature. BeCu for example has a room temperature resistivity twice that of copper, and its resistivity only drops by a factor two at lN_2 temperature. Yield strength is $85kg/mm^2(850MPa)$. ZrCu has a room temperature resistivity 10% higher than copper at room temperature and

$\Delta T\,(°K)$	$Q/A\ w/cm^2$
Film Boiling	
300	5.5
250	3.5
200	3.0
150	2.0
100	1.5
60	0.9
Nucleate Boiling	
13	19
10	13
6	3.5
4	1.4
2	0.25

Table 3.1. Heat Transfer Rate for Liquid Nitrogen [96].

it decreases by a factor 4 at lN_2. Yield strength is $45kg/mm^2(450MPa)$. Using copper interleaved with steel, lower resistivity values are obtained at the same strength (assuming infinite resistivity for the steel, and plastic precompression of the copper as in Alcator C) : the gain in going to lN_2 for copper interleaved with steel, achieving a strength of $85kg/mm^2$, is a factor 5 compared to pure room temperature copper and about a factor 6.5 for a strength of $45kg/mm^2$ [96].

We derive briefly the formula for maximum current density based on maximum average temperature rise. Since the temperature changes over the pulse length, and both the resistivity and heat capacity are a strong function of temperature, we take this explicitly into account. Assuming an adiabatic temperature rise we have

$$\rho(T)J^2dt = \gamma c_p(T)dT$$

where $\rho(T)$ is the electrical resistance of the copper, being given by [98]

$$\begin{aligned}\rho(T) =& 1.57067 \times 10^{-8} + 0.545491 \times 10^{-10}T - 0.165573 \times 10^{-12}T^2 \\ & - 0.449932 \times 10^{-15}T^3\end{aligned}$$

in Ωm for $-200°C < T < 30°C$ and

$$c_p(T) = 379.87 + 0.21414T + 1.0255 \times 10^{-3}T^2 + 2.419 \times 10^{-5}T^3$$

in $\frac{Joule}{kg°C}$ for $-253°C < T < 25°C$ and γ is the density of the copper, taken to be $8.88 \times 10^3 \frac{kg}{m^3}$. The equation can be used to determine the temperature rise ΔT

$$\int_0^t J^2 dt = \int_{77K}^{77K+\Delta T} \gamma \frac{c_p(T)}{\rho(T)} dT$$

Putting the left hand side equal to $J^2\tau$, using an equivalent square wave pulse time it is possible to plot the temperature rise ΔT as a function of this parameter. The result is shown in Figure 3.1.

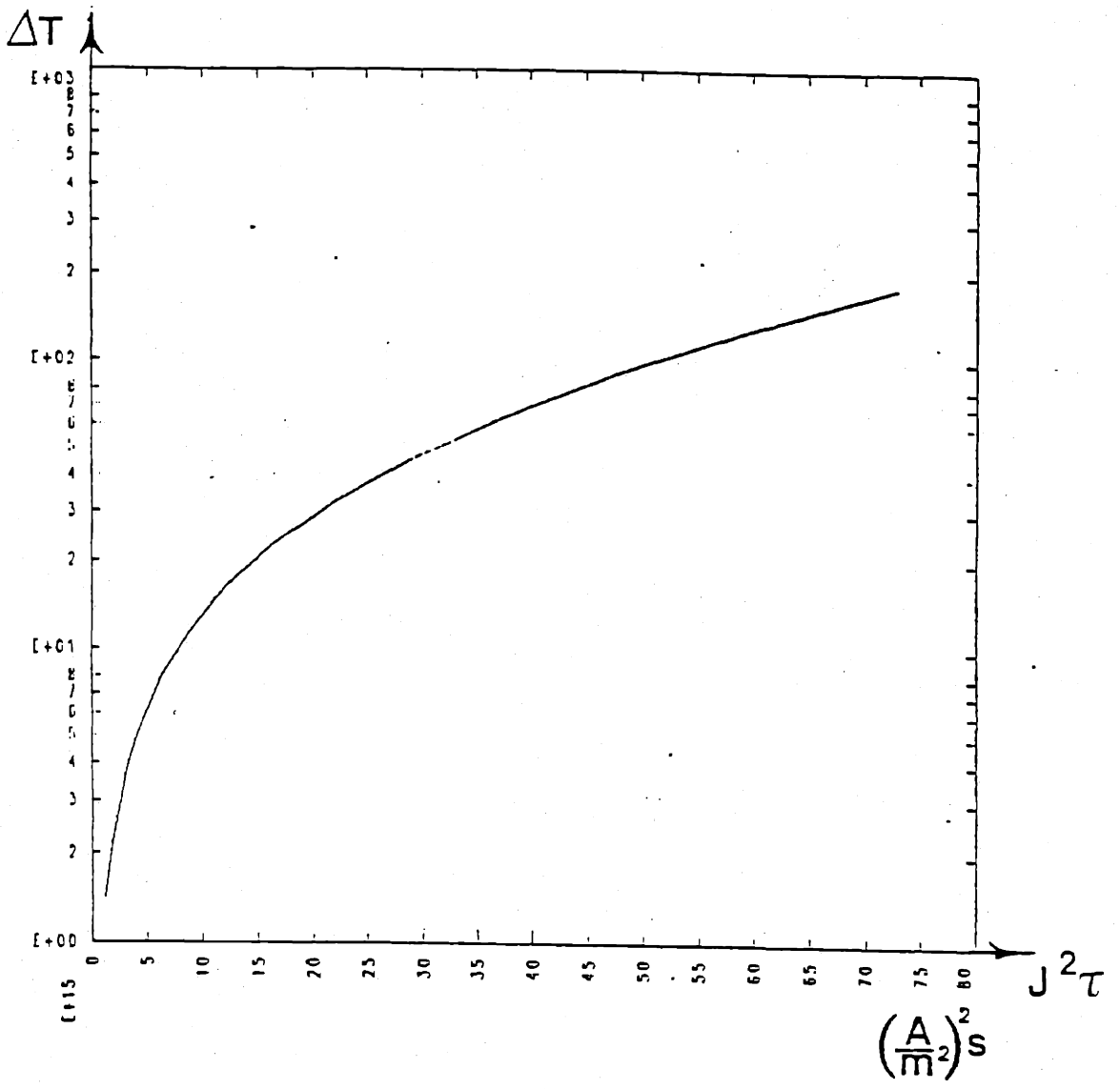

Figure 3.1 Temperature rise ΔT, as a function of equivalent square wave

Limiting ΔT to 15°C one obtains

$$J^2\tau = 10 \times 10^{15} \frac{A}{m^2 s}$$

giving for a 1 s equivalent square pulse a current density of $10^8 \frac{A}{m^2}$ or $10 \frac{kA}{cm^2}$. In Figure 3.2 we have also plotted the ratio of the resistance at the end of the pulse compared to the resistance at 77K.

We may also mention here that there is little advantage to use lN_2 cooled coils in steady state. Indeed, even though the heat deposited in the copper at $77K$ is a

factor 7 lower than at room temperature, the power needed to remove this heat at $77K$ is about 7.5 times the power deposited (carnot efficiency 0.35, assumed mechanical efficiency 0.4). The total power needed would thus be $\frac{1+7.5}{7} = 1.2$ the power needed for a room temperature system.

3.2.5. Superconducting Coils

Requirement of stabilization and protection set a limit both on the current density and the maximum current per conductor for large superconducting coils. We summarize here the results of reference [99]. Stability requires that

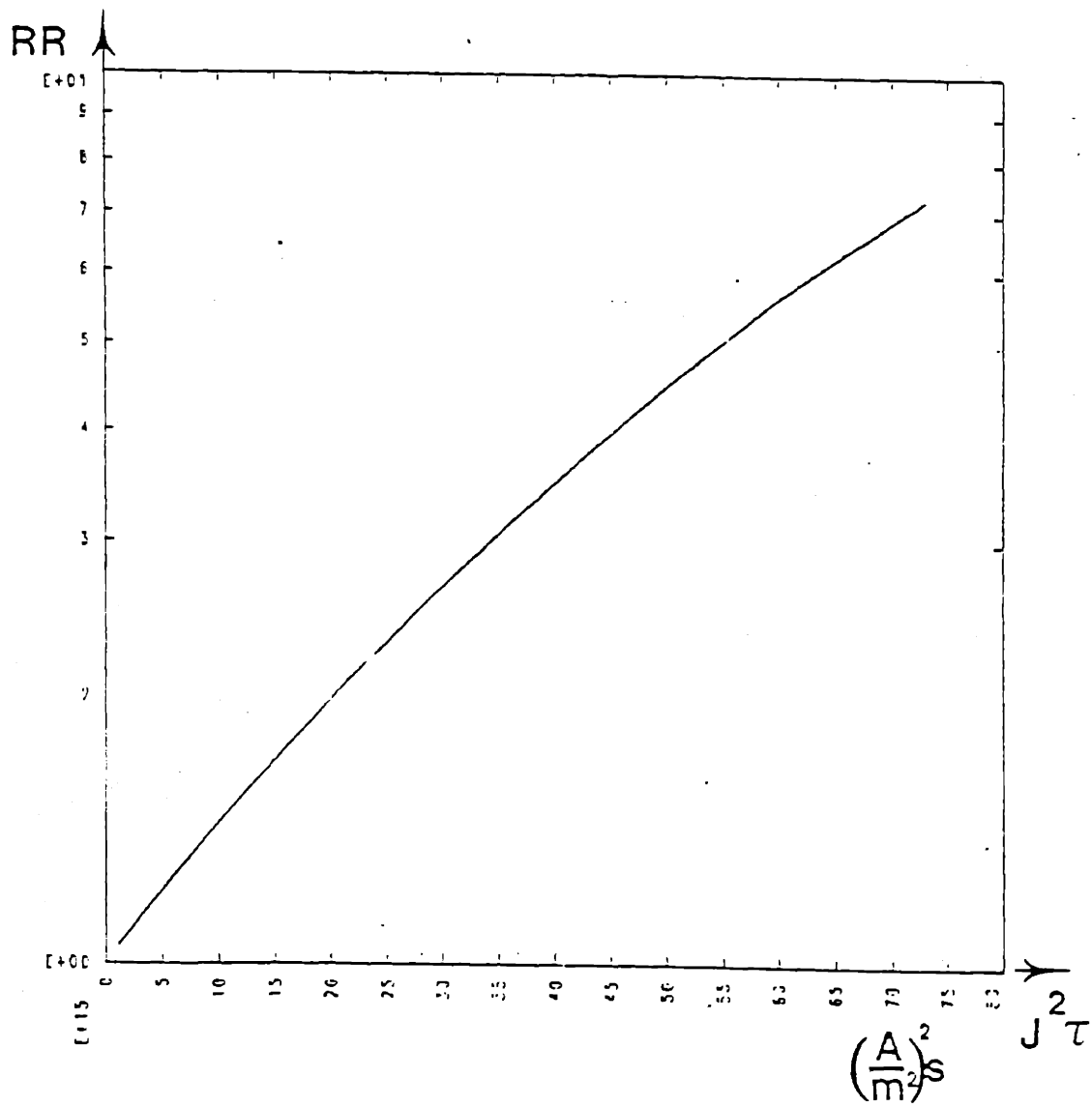

Figure 3.2 Resistance Ratio, as a function of equivalent square wave

if part of a superconductor goes normal, the disturbance will not spread, and the conductor will return to its superconducting state. This can be achieved if sufficient copper is provided around the superconductor. The current then will temporarily bypass the superconductor. If the heat dissipated in the copper is smaller than the critical heat flux, the conductor can cool down again and recover. Stability thus requires

$$\frac{\rho I^2}{A} < Q_c P$$

The wetted perimeter per unit length, P can be related to the area A using a dimensionless constant C in the following way

$$P = C\sqrt{A}$$

The current density then is limited to

$$J < \left(\frac{Q_c C}{\rho}\right)^{2/3} I^{-1/3} \tag{3.1}$$

Even though the superconductor may be fully stable it is always possible that a failure may drive the whole coil normal. An external dump resistor is used to discharge the coil current in this case. To save the coil one has to limit both the amount of heat deposited to avoid overheating, and limit the voltage to avoid breakdown. Choosing R, the resistance of the external dump resistor, such that the initial voltage at discharge is the maximum allowed voltage will discharge the superconducting coil the fastest. Thus

$$V_m = IR$$

Restricting the temperature rise in the coil during the discharge gives

$$\int_0^\infty J^2(t)dt = \int_{T_0}^{T_m} \gamma \frac{c_p}{\rho} dT$$

The left hand side can be written as $J^2\tau$ where J is the initial current density and $\tau = \frac{L}{R}$ is the time constant for the decay. The integral on the right hand side

depends on the stabilizers properties and the maximum allowed temperature rise. Let

$$f(T_m) = \int_{T_o}^{T_m} \left(\frac{\gamma c_p}{\rho}\right) dT$$

Values of $f(T_m)$ are given in figure 2 of reference [99] for various metals. Using further $E = \frac{1}{2}LI^2$ we obtain

$$J \leq \left(\frac{f(T_m)V_m I}{E}\right)^{\frac{1}{2}} \tag{3.2}$$

Equation (3.1) gives a maximum current density decreasing with the conductor current, equation (3.2) a maximum current density increasing with current. Combining both, we can obtain a optimum current density and current given by

$$J_{opt} = \left(\frac{f(T_m)V_m}{E}\right)^{\frac{1}{5}} \left(\frac{Q_c C}{\rho}\right)^{\frac{2}{5}} \tag{3.3}$$

$$I_{opt} = \left(\frac{f(T_m)V_m}{E}\right)^{\frac{3}{5}} \left(\frac{Q_c C}{\rho}\right)^{\frac{4}{5}} \tag{3.4}$$

For typical values of the parameters, namely

$$\begin{aligned} f(T_m) &= 1.5 \times 10^9 \frac{A^2}{cm^4} \text{ at } T_m = 300K \\ Q_c &= 0.3 \frac{W}{cm^2} \\ V_m &= 20\ kV \\ C &= 2 \\ \rho &= 3 \times 10^{-8} \Omega cm \end{aligned}$$

we obtain

$$\begin{aligned} J_{opt} &= \left[\frac{1.5 \times 10^9 \frac{A^2}{cm^4} \times 20 \times 10^3 V}{E}\right]^{1/5} \left[\frac{\frac{0.3W}{cm^2}}{3 \times 10^{-8} \Omega cm}\right]^{2/5} \\ &= 10 \frac{kA}{cm^2} \left[\frac{E}{10^6 J}\right]^{-1/5} \end{aligned}$$

In this section we have investigated the current density limits for various types of conductors in pulsed and steady state.

3.3. Structural Constraints

3.3.1. Introduction

Most toroidal concepts incorporate the use of toroidal coils. Those coils are usually the most stressed component of the experiment and account for a major fraction of its cost. We have therefore concentrated on constraints associated with the toroidal coils.

Often the current carrying conductor is not sufficiently strong by itself to carry the magnetic load, and reinforcing material is needed to support the load. The loads can essentially be subdivided into loads due to normal operating conditions and loads due to fault conditions, the latter being usually much larger than the former. Still we will restrict ourselves to the analysis of normal operating conditions because the magnitude of loads arising from fault conditions can depend a lot on the type of protection devised to detect the faults and to take appropriate steps to avoid the consequences. It is also more difficult to get general guidelines as the type of damage one could allow can vary widely from no damage at all to acceptance of the destruction of the faulty coil. We will thus restrict ourselves to calculating stresses in magnets due to magnetic loads in normal operating conditions. In addition we will only look at the interaction of the current with the self generated magnetic field thereby neglecting possible interactions like the load arising from other fields, as for example interaction of the vertical field with the current in toroidal field coils in tokamaks.

In order to be able to investigate several types of coils from a rather general viewpoint, and to obtain a formula sufficiently simple and versatile to be included later on in our weight and cost estimate, we show first that in the most general case of a coil subjected to forces in a plane and composed of copper and structural material, we can define an equivalent tangential force that will incorporate the regular tangential force and the bending moments and write a formula of the type,

$$\epsilon \overline{E} = \frac{T}{A_{coil}} = \sigma$$

Where T is the "equivalent" tangential force, that gives the same maximum stress or strain as the tangential force and moments together. In a next step we show that this "equivalent" tangential force can be written as

$$T = \frac{\mu_o N I^2}{4\pi} g_o$$

where g_o is a dimensionless constant depending only on geometrical factors. we further derive this geometrical factor for a number of coil geometries, namely a very long solenoid, D shaped coils and circular coils. Finally in this section we briefly discuss the limits on stresses and strains.

3.3.2. The Equivalent Tangential Force

Here we will prove that an equivalent tangential force can be defined, that gives the same maximum stress or strain as the sum of a regular tangential force and bending moments in a cross section composed of copper and steel.

First looking at the tangential force (we have used N_t to avoid confusion with N, the number of turns) :
For the tangential force, a fraction is taken up by the copper, a fraction by the steel, so that

$$\begin{aligned} N_t &= N_c + N_s \\ &= \sigma_c A_c + \sigma_s A_s \\ &= \epsilon_N E_c A_c + \epsilon_N E_s A_s \end{aligned}$$

thus giving

$$\epsilon_N \overline{E}_N A_{coil} = N_t$$

if we define

$$\overline{E}_N A_{coil} = E_c A_c + E_s A_s$$

Similarly, for the moment

$$\epsilon_M \overline{E}_M I_{coil} = M \frac{h}{2}$$

with

$$\overline{E}_M I_{coil} = E_c I_c + E_s I_s$$

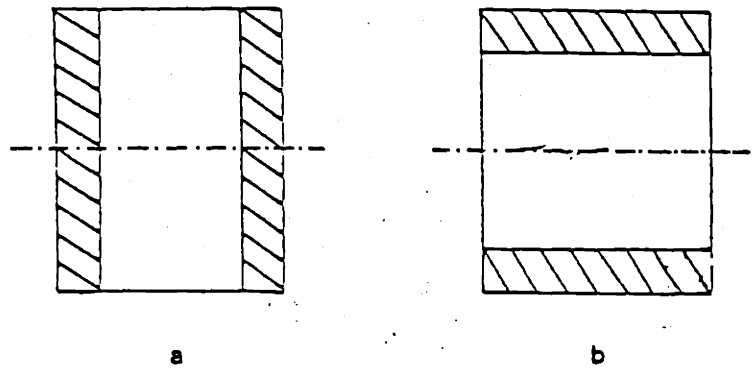

Figure 3.3 Two extreme possibilities for the distribution of the steel

---

Summing the strains we obtain

$$\overline{E}_N(\epsilon_N + \epsilon_M) = \frac{N_t}{A_{coil}}\left(1 + \frac{M\frac{h}{2}}{N_t}\frac{A_{coil}}{I_{coil}}\frac{\overline{E}_N}{\overline{E}_M}\right)$$
$$\overline{E}_N\epsilon = \frac{N_t}{A_{coil}}\left(1 + \frac{6M}{N_t h}\frac{\overline{E}_N}{\overline{E}_M}\right)$$

Using the definitions of $\overline{E}_N$ and $\overline{E}_M$ we can calculate the ratio $\frac{\overline{E}_N}{\overline{E}_M}$. Taking

$$\frac{A_s}{A_{coil}} = f_s$$

and

$$\frac{A_c}{A_{coil}} = 1 - f_s$$

the ratio $\frac{\overline{E}_N}{\overline{E}_M}$ is equal to 1 if the steel is concentrated as in Fig. 3.3a.

If the steel is concentrated as in Fig. 3.3b then

$$\frac{I_c}{I_{coil}} = (1 - f_s)^3$$
$$\frac{I_s}{I_{coil}} = 1 - (1 - f_s)^3$$

and

$$\frac{\overline{E}_N}{\overline{E}_M} = \frac{\frac{E_c}{E_s}(1 - f_s) + f_s}{\frac{E_c}{E_s}(1 - f_s)^3 + (1 - (1 - f_s)^3)}$$

for $0 \leq f_s \leq 1$ we have $0.83 \leq \frac{\overline{E}_N}{\overline{E}_M} \leq 1$ and we neglect the small variation of this ratio with f_s.

We obtain

$$\overline{E}_{N\epsilon} = \frac{N_t}{A_{coil}}(1 + \frac{6M}{N_t h})$$

Thus yielding

$$\overline{E}_{N\epsilon} = \frac{T}{A_{coil}}$$

where

$$T = N_t(1 + \frac{6M}{N_t h})$$

I have thus shown how an equivalent tangential force can be defined, yielding a general and simple formula. We will calculate this equivalent tangential force in terms of $\frac{\mu_o N I^2}{4\pi}$ and g_c the dimensionless geometrical quantity.

As a simple example, let us first look at a very long solenoid of length L (Fig. 3.4). We have

$$B = \frac{\mu_o N I}{L}$$

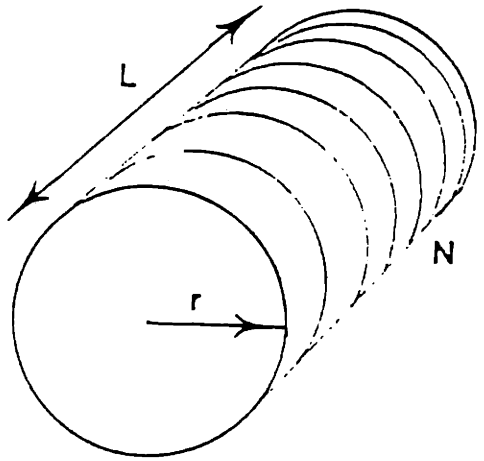

Figure 3.4 Long solenoid

The average pressure is given by

$$p = \frac{B}{2}\frac{NI}{L} = \frac{B^2}{2\mu_o}$$

The tension T on the current carrying conductor is

$$\begin{aligned} T &= \frac{B^2}{2\mu_o} \times \frac{L}{N} \times r \\ &= \frac{\mu_o N I^2}{2L} \times r \\ &= \frac{\mu_o N I^2}{4\pi}\left(\frac{2\pi r}{L}\right) \\ &= \frac{\mu_o N I^2}{4\pi} g_\sigma \end{aligned}$$

where $g_\sigma = \frac{2\pi r}{L}$

We will now see what g_σ is for constant tension coils or circular coils.

3.3.3. Stresses in D shaped Toroidal Coils

The formula for tension in D shaped toroidal coils is easily cast in the form

$$T = \frac{\mu_o N I^2}{4\pi} g_\sigma$$

Indeed according to [100] the tension can be approximated by

$$T = \frac{\mu_o N I^2}{4\pi}\frac{1}{2}\ln\left(\frac{R_2}{R_1}\right)$$

This gives

$$g_\sigma = \frac{1}{2}\ln\left(\frac{R_2}{R_1}\right)$$

3.3.4. Stresses in Circular Coils

For circular coils we have moments and tangential forces. The formula will thus have the general form

$$\overline{E\epsilon} = \frac{T}{A_{coil}}$$

with

$$T = N_t\left(1 + \frac{6M}{N_t h}\right)$$
$$= \frac{\mu_o N I^2}{4\pi} g_o$$

The complete analysis is given in appendix B. The results are summarized here. We find that the formula can be written as

$$T = \frac{\mu_o N I^2}{4\pi}\frac{r}{R}\left(1 + \left(\frac{h}{r}\right)_o \frac{r}{h}\right)$$

with the values for $(\frac{h}{r})_o$ given in Fig. B.18 and B.19. They depend on the aspect ratio, the stiffness of the structure and the way the reaction is taken up. For our purposes here we can use

$$\left(\frac{h}{r}\right)_o \simeq \frac{3\frac{a}{R}}{\xi}$$

with ξ varying between 3 and 20, depending on the stiffness of the structure and the way the reaction is taken up.

3.3.5. Limits on Stresses and Strains

Limits on stresses in conducting materials have been summarized in [101]. Tensile strength of full hard copper is in the range of 340 to 380 MPa. Reinforcing material (steel) can have maximum stresses up to 1500 MPa at room temperature, and 2300 MPa at liquid nitrogen temperature [102]. More commonly used design limits are 400 to 600 MPa [103].

The stresses in the conducting material are important limits when no reinforcement material is used. When reinforcement material is used the limit is usually the stress in the reinforcing material, or the strain (for superconductors).

A particular case is the Alcator type design where the yield of the copper under its initial loading cycle is used to prestress it. Assuming identical strains in the copper and the steel we can derive the following formula :

The maximum $\overline{E}\epsilon$ for the copper not to yield is

$$\sigma = \sigma_{cmax}[(1 - f_s) + f_s\frac{E_s}{E_c}]$$

If ones allows the copper to yield, then the limit is set by the ultimate strength of the steel.

$$\sigma = \sigma_{cmax}(1 - f_s) + \sigma_{smax}(f_s)$$

For

$$f_s > \frac{\sigma_{cmax}}{\sigma_{smax} - 2\frac{E_s}{E_c}\sigma_{cmax} + \sigma_{cmax}}$$

a more stringent condition (lower σ) follows from the requirement not to allow the copper to yield in compression. The limit is then

$$\sigma = 2\sigma_{cmax}\left((1 - f_s) + f_s\frac{E_s}{E_c}\right)$$

For superconducting materials a maximum limit of 0.2% is set for the strain because of degradation of critical current above this point.

3.4. Weight of the Toroidal coil system

In order to get a general idea of the cost of an experiment it is important to be able to estimate the total weight. If one can get this weight as a function of size and magnetic field, it is even possible to explore the parameter space as a function of the cost.

F.C. Moon [104] investigated the scaling of the weight of toroidal coils systems as a function of stored energy. He obtains one general scaling, both for superconducting and resistive water cooled magnets.

Within the range

$$10MJ < E(\text{stored energy}) < 2 \times 10^4 MJ$$

and

$$5 \times 10^3 kg < M(\text{mass}) < 10^6 kg$$

he obtains a simple scaling law, function of stored energy only. This scaling law is

$$\left(\frac{M}{10^3 kg}\right) = 1.37\left(\frac{E}{1MJ}\right)^{0.761}$$

A similar scaling law was obtained by Raeder et al., for the conductor mass of superconducting coils [94].

Several reasons have prompted us to investigate this in more detail.

1. constraints for resistive and superconducting magnets are different.
2. it is interesting to be able to separate copper (or current carrying) mass and steel (or supporting structure). The time constant of the coils system indeed is closely related to the copper mass.
3. the validity of the weight estimates of some reactor studies has been questioned [105].
4. the justification given by F.C. Moon for the $\frac{3}{4}$ power scaling law is not very convincing.

I plan to first obtain an expression for the mass as a function of size and magnetic field. In the next section the stored energy will be calculated and we will then be able to compare mass with stored energy, to see whether a simple law, relating mass to stored energy is justified.

I have looked both at circular and pure tension coils.

The total mass is taken as the sum of the current carrying mass and the load supporting mass. Both are calculated as a material density times a cross sectional area times a length.

The material density is taken to be $\gamma_c = 9\frac{kg}{dm^3}$ for copper and $\gamma_s = 7\frac{kg}{dm^3}$ for steel The cross section for copper is based on constraints related to current density (heat removal capacity, temperature increase, stabilization). The limits on current density have been investigated in more detail for water cooled coils, for cryogenic coils and superconducting coils.

The section for steel is assumed to enclose the copper and its dimensions are constrained by mechanical considerations (maximum stress, and for superconductors maximum strain).

Let us now first calculate the length of the coils, and then turn to the calculation of the cross section of copper and steel needed.

3.4.1. Length

The perimeter of one coil is easily calculated for the circular case.

$$l_c = 2\pi a$$

where

$$a = \text{ average radius of the coil}$$

For D shaped coils the length [100] is equal to

$$l_c = 2\pi R_o k[I_o(k) + I_1(k)]$$

where $k = \frac{1}{2}\ln\frac{R_2}{R_1}$ and $R_o = \sqrt{R_1 R_2}$ (see Fig. 3.5). Formulas for D shaped coils can be simplified if one relates some geometrical parameters to the dimensions of a circular coil, with major radius R and minor radius a, inscribed in the D shaped coil (Fig. 3.5). We have that

$$\begin{aligned} k &= \frac{1}{2}\ln\frac{R_2}{R_1} \\ &= \frac{1}{2}\ln\frac{R+a}{R-a} \\ &= \frac{a}{R} + \left(\frac{a}{R}\right)^3 + \left(\frac{a}{R}\right)^5 + \ldots \\ &\simeq \frac{a}{R} \end{aligned}$$

The length can be then approximated by

$$l_c = 2\pi a(1 + \frac{1}{2}\frac{a}{R})$$

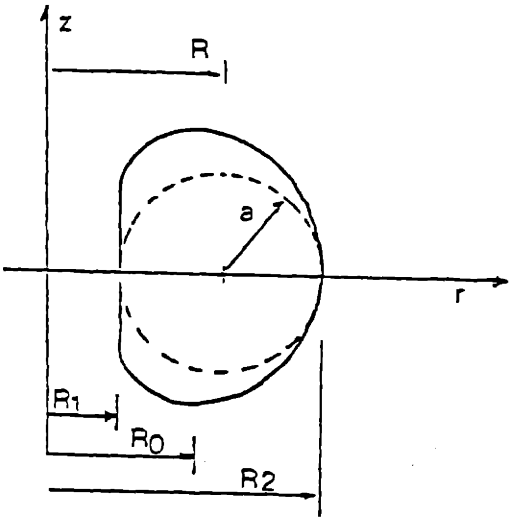

Figure 3.5 Relationship between the parameters of D shaped coil and inscribed circular coil.

Thus in general we can write the length as

$$l_c = 2\pi a g_l$$

where $g_l = 1$ for circular coils and $g_l = (1 + \frac{1}{2}\frac{c}{R})$ for D shaped coils.

3.4.2. Cross Section of Copper and Steel

The analysis is based in part on the calculation by Cain and Gray for the fraction of structural reinforcement needed [106] in constant tension coils. The calculation is carried further here to get an expression for the total weight. The general expression set up for stresses in coils also allows us to extend this derivation to circular coils.

Defining the steel cross section (Fig. 3.6) as

$$A_s = f_s h w = f_s A_{coil}$$

The cross section of copper, is A_c, while the section for copper, cooling passages and insulation is given by $(1 - f_s)hw$.

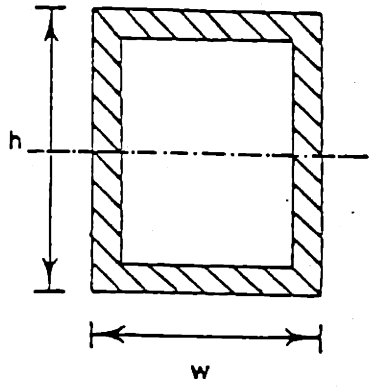

Figure 3.6 Cross section of a coil

Define the strain ϵ, using an average modulus of elasticity and the generalized tangential force T

$$\epsilon \overline{E} = \frac{T}{A_{coil}}$$

with $T = \frac{\mu_o N I^2}{4\pi} g_\sigma$.

Amperes law relates the current in the coil to the magnetic field with

$$B = \frac{\mu_o N I}{l_a}$$

where l_a is defined as $l_a = \frac{1}{B} \int B dl$. This gives us

$$A_{coil} \overline{E} = \frac{g_\sigma}{4\pi N \mu_o} \frac{(B l_a)^2}{\epsilon}$$

$$A_{coil} \overline{E} \left[\frac{\mu_o N}{B l_a} \right] = \frac{1}{4\pi} \frac{B l_a}{\epsilon} g_\sigma$$

With the average modulus of elasticity given by

$$\overline{E} A_{coil} = E_c A_c + E_s A_s$$

We obtain

$$(A_s E_s + A_c E_c) \frac{\mu_o N}{B l_a} = \frac{1}{4\pi} \frac{B l_a g_\sigma}{\epsilon}$$

$$A_s E_s \frac{\mu_o N}{B l_a} = \frac{1}{4\pi} \frac{B l_a g_\sigma}{\epsilon} - E_c \frac{A_c \mu_o N}{B l_a}$$

Using again

$$B = \frac{\mu_o N I}{l_a}$$

we can transform this into

$$A_s E_s \frac{\mu_o N}{B l_a} = \frac{1}{4\pi} \frac{B l_a g_\sigma}{\epsilon} - \frac{E_c A_c}{I}$$

or

$$f_s A_{coil} E_s \frac{\mu_o N}{B l_a} = \frac{1}{4\pi} \frac{B l_a g_\sigma}{\epsilon} - \frac{E_c}{j_c}$$

j_c being an average current density in the copper.

$$f_s = \frac{B l_a}{\mu_o N E_s A_{coil}} \left[\frac{1}{4\pi} \frac{B l_a g_\sigma}{\epsilon} - \frac{E_c}{j_c} \right] \tag{3.5}$$

This is a slightly more general expression of the formula obtained by Cain and Gray for the fraction of reinforcement needed. They have used their formula to derive maximum obtainable magnetic fields in toroids, subject to strain limitations. Indeed, for some combinations of B, ϵ, and j_c, f_s can exceed 100% leaving no room for copper. We will use our formula to derive the mass of copper and steel components.

Taking j as an average current density for the coil, cooling holes and insulation, we can write

$$(1 - f_s) A_{coil} = \frac{I}{j} \tag{3.6}$$

Combining (3.5) and (3.6) it is possible to solve for f_s and A_{coil}. We obtain

$$A_{coil} = \frac{B l_a}{\mu_o N} \left[\frac{1}{j} - \frac{E_c}{E_s j_c} + \frac{1}{4\pi} \frac{B l_a g_\sigma}{E_s \epsilon} \right]$$

$$f_s = \frac{\frac{Bl_c g_o}{4\pi\epsilon E_s} - \frac{E_c}{E_s j_c}}{\left[\frac{1}{j} - \frac{E_c}{E_s j_c} + \frac{1}{4\pi\epsilon}\frac{Bl_a g_o}{E_s}\right]}$$

We can now calculate the total volume of the material and using the densities of copper and steel calculate the total weight.

The volume can be calculated as $length \times N \times A_{coil}$. The total mass equals

$$M = l_c \times N \times A_{coil}[f_s(\gamma_s) + (1 - f_s)\gamma_c]$$

This in fact will slightly overestimate the weight of the copper as it assumes $\gamma_{insulation} = \gamma_{holes} = \gamma_{copper}$

We obtain

$$M = l_c \frac{l_a B}{\mu_o}\left[\left(\frac{1}{4\pi}\frac{Bl_a g_o}{\epsilon E_s} - \frac{E_c}{E_s}\frac{1}{j_c}\right)\gamma_s + \frac{\gamma_c}{j}\right] \tag{3.7}$$

The terms of this formula can be readily identified. The term with γ_s is the structural material and gives the reinforcement. Note that some fraction of the force is also taken up by the copper. Indeed, if

$$\frac{1}{4\pi}\frac{Bl_a g_o}{\epsilon E_s} < \frac{E_c}{E_s}\frac{1}{j_c}$$

or

$$j_c < 4\pi\frac{\epsilon E_c}{Bl_a g_o}$$

then the copper will be enough to take up the load and no structural material is needed.

The term with γ_c is the contribution due to the copper because of the need to carry current. Using the value for l_c the length of the coil, for l_a the length of the coil axis, and the values g_c, ϵ, j_c and j as derived in previous sections it is possible to calculate the total mass of the system.

3.5. Stored Energy

In this section we will briefly mention the formulas for stored energy in the two different types of coils I investigate, but also show that sufficient accurate results can be obtained by calculating the stored energy from $\frac{B^2}{2\mu_o} \times$ Volume

3.5.1. Circular Coils

Taking first a system of circular coils, as for a tokamak the formula for stored energy is given by [100]

$$\begin{aligned} E &= \frac{1}{2} L I^2 \\ &= \frac{\mu_o}{2} N^2 R \left(1 - \sqrt{1 - (\frac{a}{R})^2} \right) I^2 \end{aligned} \tag{3.8}$$

It is however easier, and more general to estimate the energy as a product of average energy per unit volume times a volume.

$$E = \frac{B^2}{2\mu_o} \times \pi a^2 \times 2\pi R \tag{3.9}$$

where B is calculated on the axis.

For $0 < \frac{a}{R} < 0.6$ the error made by using (3.9) gives values that are at most 10% lower than those obtained from (3.8).

Note that the formula, as (3.8) is for filamentary conductors. This overestimates the energy compared to the actual value when the thickness of the coil is taken into account [100]. Our estimate, which gives smaller values than the formula (3.8) is thus sometimes closer to the reality than we would by using the formula for filamentary conductors (3.8).

3.5.2. D shaped Coils

An exact formula also exists for the stored energy of filamentary coils of the Princeton D shape [100].

$$E = \frac{1}{2}LI^2$$
$$= \frac{1}{2}\frac{\mu_o R_o N^2 k}{2}[I_o(k) + 2I_1(k) + I_2(k)]I^2 \tag{3.10}$$

where

$$k = \frac{1}{2}\ln\left(\frac{R_2}{R_1}\right)$$

$$R_o = \sqrt{R_1 R_2}$$

Again we can estimate the stored energy instead, by using an average energy per unit volume times a volume. Calculating the B field at R_o and the volume to be the area times $2\pi R_o$ we obtain

$$E = B_o^2 \times 2\pi R_o^2 k[I_1(2k) - e^{-k}I_1(k)]2\pi R_o \tag{3.11}$$

By using (3.11) instead of (3.10) we are overestimating the stored energy by at most 5%. However, except for the fact that it confirms the accuracy of the calculation method *Volume* $\times$ *Average Energy Density* the formula (3.11) is not much simpler than (3.10).

The area of the D coil (A_D) can be written as a function of the area of the inscribed circular coil (A_c) as

$$A_D \simeq A_c(1+k) \simeq A_c(1+\frac{a}{R})$$

Rather than using the magnetic field at R_o as the average magnetic field we use the magnetic field at the center R of the circular coil. Calculating the volume then as

$$\pi a^2(1+\frac{a}{R})2\pi R$$

we can estimate the stored magnetic energy to be

$$E = \frac{B^2}{2\mu_o}\pi a^2(1+\frac{a}{R})2\pi R$$

This gives, for $0 < k < 0.6$ an error smaller than 15%.

3.5.3. Generalization

We can thus generalize the stored energy as

$$E = \frac{B^2}{2\mu_o} 2\pi R \pi a^2 g_E$$

with

$$g_E = 1 \text{ for circular coils}$$
$$= (1 + \frac{a}{R}) \text{ for D shaped coils}$$

3.6. Energy Requirements

The energy required for an experiment with pulse length τ_p is the sum of the stored energy $E = \frac{1}{2}LI^2$, the losses $RI^2\tau_p$ during the pulse length τ_p and the losses $RI^2\tau_{eu}$, where τ_{eu} is the equivalent time during ramp up of the field. When we looked at the equivalent time to get an expression for the total energy deposited in the coil, we had to include losses during ramp up *and* ramp down of the fields. The losses during ramp down are not to be included in the calculation of the total energy needed, because those losses are in fact a fraction of the energy stored in the fields. The total energy required is thus

$$P = \frac{1}{2}LI^2 + RI^2\tau_p + RI^2\tau_{eu}$$

Writing this as a function of the stored energy we obtain

$$P = E\left(1 + 2\frac{\tau_p}{\tau} + 2\frac{\tau_{eu}}{\tau}\right)$$

where $\tau = \frac{L}{R}$ is the time constant of the coils.

We found in a previous section the equivalent time during ramp up of the fields to be $\tau_{eu} \simeq \frac{1}{3}\tau_u$ where τ_u is the actual time it takes to reach the nominal current, and is given by

$$\tau_u = \tau \ln\left(\frac{C_f}{C_f - 1}\right)$$

I will now derive an expression for the time constant τ of the coils. We can write

$$\tau = \frac{L}{R} = \frac{2E}{I^2 R}$$

Using the expression for the resistance R

$$R = \rho \frac{N l_c}{A_c}$$

with the length given by

$$l_c = 2\pi a_c g_l$$

the stored energy

$$E = \frac{B^2}{2\mu_o} 2\pi R \pi a^2 g_E$$

and the magnetic field

$$B = \frac{\mu_o N I}{2\pi R}$$

this can be written in the form

$$\tau = \frac{\mu_o}{4\pi\rho\gamma_c} \frac{l_c A_c \gamma_c}{2\pi R} \frac{g_E}{g_l^2}$$

$$\frac{\tau}{1s} = 0.093 \frac{\left(\frac{Mc}{10^3 kg}\right)}{\left(\frac{R}{m}\right)} \frac{g_E}{g_l^2} \left(\frac{1.92 \times 10^{-8} \Omega m}{\rho}\right) \tag{3.12}$$

The accuracy of this simple formula can be judged by comparison with actual numbers.

For circular coils we take as example TFTR [107] with

$$R = 2.8m$$

$$W = 12800 \frac{kg}{coil} \times 20\text{coils}$$

we obtain

$$\tau = 0.093 \times \frac{12.8 \times 20}{2.8} \times \left(\frac{1}{1^2}\right) = 8.6s$$

The value is $\tau = \frac{L}{R} = 7.5s$

Calculating it for the D-shaped coils of JET [108] we obtain with

$$R = 3.05m$$

$$a = 1.93m$$

$$W = 12000\frac{kg}{coils} \times 32\text{coils}$$

we have

$$\tau = 0.093 \times \frac{12 \times 32}{3.05} \times \frac{1 + 0.6327}{(1 + \frac{1}{2} \times 0.6327)^2}$$
$$= 11.0s$$

The quoted value calculated from $L = 0.66H$ and $R = 61m\Omega$ is $\tau = 10.8s$.

Summarizing we can write the total energy needed for an experiment as

$$P = E(1 + 2\frac{\tau_p}{\tau} + \frac{2}{3}\frac{\tau_u}{\tau})$$

where τ_p is the pulse length of the experiment, τ the time constant $\frac{L}{R}$ and $\tau_u = \tau \ln\left(\frac{C_f}{C_f - 1}\right)$

For short pulse experiments the first and second term will dominate, both are independent of τ, for longer pulse experiment the second term becomes more important, pointing to the need to have a system with long time constant for long pulse experiment.

3.7. Relationship between Mass and Stored Energy

Having set up a formula that gives the mass as a function of the dimensions and the magnetic field as well as a formula for the stored energy in terms of the same parameters, we can now turn to the question of the relationship between the mass of the experiment and the stored energy.

It will be shown that different scalings of mass with stored energy are applicable, depending on the conditions. Recalling formula (3.7) we have

$$M = l_c \frac{l_a B}{\mu_o}\left[\left(\frac{1}{4\pi}\frac{B l_a g_o}{\epsilon E_s} - \frac{E_c}{E_s}\frac{1}{j_c}\right)\gamma_s + \frac{\gamma_c}{j}\right]$$

The structural mass is given by

$$M_s = \frac{l_c l_a B}{\mu_o}\left(\frac{1}{4\pi}\frac{B l_a}{\epsilon E_s} g_o - \frac{E_c}{E_s}\frac{1}{j_c}\right)\gamma_s \tag{3.13}$$

the mass of the conductor by

$$M_c = \frac{l_c l_a B}{\mu_o}\frac{1}{j}\gamma_c \tag{3.14}$$

If no structural material is needed, that is if $j_c < \frac{4\pi}{B l_a}\frac{\epsilon E_s}{g_c}$, then the mass will scale as the mass of the conductor only. The mass of the conductor depends on the current density.

For steady state operation ($\tau_e > 10s$) we had

$$j \simeq \frac{2kA}{cm^2}$$

giving a copper mass

$$M_c = \frac{l_c l_a B}{\mu_o}\frac{m^2}{2 \times 10^7 A} \sim aRB$$

thus not scaling as the stored energy.

For pulsed operation we had for the current density

$$j \simeq \frac{10kA/cm^2}{\sqrt{\tau_e}}$$

Let us write this as

$$j = J_{ss}\sqrt{\frac{25s}{\tau_e}} \tag{3.15}$$

with $J_{ss} = 2\frac{kA}{cm^2}$. The equivalent pulse length τ_e was given by

$$\tau_e = \tau_p + \frac{2}{3}\tau \ln\frac{C_f}{C_f - 1} \tag{3.16}$$

where τ is the time constant of the coils. The time constant τ itself depends on the weight of the coils through the formula (3.12). Using then the formulas (3.12), (3.14), (3.15) and (3.16) we can obtain a quadratic equation for the conductor mass.

The limiting cases are the most interesting. For short pulse length, short being defined as

$$\tau_p \ll \left(\frac{Ba}{J_{ss}\sqrt{25s\rho}} \frac{g_E}{g_l} \ln \frac{C_f}{C_f - 1} \right)^2$$

or

$$\frac{\tau_p}{1s} \ll 8.2 \left(\frac{Ba}{Tm} \right)^2 \ln^2 \frac{C_f}{C_f - 1} \left(\frac{g_E}{g_l} \right)^2 \left(\frac{2 \times 10^7 \frac{A}{m^2}}{J_{ss}} \right)^2 \left(\frac{1.92 \times 10^{-8} \Omega m}{\rho} \right)^2$$

the mass will scale as the stored energy

$$\left(\frac{M}{10^3 kg} \right) = 0.0625 \left(\frac{E}{1MJ} \right) \ln \frac{C_f}{C_f - 1} \left(\frac{2 \times 10^7 \frac{A}{m^2}}{J_{ss}} \right)^2 \left(\frac{1.92 \times 10^{-8} \Omega m}{\rho} \right)^2.$$

If the pulse length, together with a time related to ramp up and ramp down of the fields is sufficiently long, i.e. if

$$\frac{\tau_p}{1s} + 0.875 \left(\frac{Ba}{Tm} \right) \frac{g_E}{g_l} \ln \frac{C_f}{C_f - 1} \left(\frac{1.92 \times 10^{-8} \Omega m}{\rho} \right) \left(\frac{2 \times 10^7 \frac{A}{m^2}}{J_{ss}} \right) > 25$$

the conductor can be assumed in steady state. This means that even for extremely short pulse length, if $\left(\frac{Ba}{Tm} \right) \ln \frac{C_f}{C_f - 1} > 28$, so much heat is deposited in the coils during ramp up and ramp down of the fields that the experiment can be assumed steady state and the conductor mass will then scale as aRB.

If now structural material is needed then the scaling for the structural material will differ from the scaling of the conductor mass. Neglecting the term

$$\frac{E_c}{E_s} \frac{1}{j_c}$$

in formula (3.7), we have that the structural mass scales as

$$\frac{l_c l_c^2 B^2 g_\sigma}{\epsilon E_s} \sim \frac{aR^2 B^2 g_\sigma}{\epsilon}.$$

With g_σ constant, this scales as $aR^2B^2 \sim$ stored energy. We have discussed in Appendix B that in some cases (by changing g_σ), the scaling can go as B rather than B^2.

The conductor mass scales as

$$\frac{l_c l_a B}{j} \sim \frac{aRB}{j}$$

The combination of the structural mass scaling as aR^2B^2 and the conductor mass scaling as aRB can indeed give under certain limited conditions a scaling law as proposed by Moon, namely $(a^2RB^2)^{3/4}$.

The ratio of structural mass to conductor mass scales as

$$\frac{1}{4\pi}\frac{l_a B g_\sigma j}{\epsilon E_s}\frac{\gamma_s}{\gamma_c} \sim \frac{RBj}{\epsilon}$$

so that as we go to larger systems with higher magnetic field the structural mass term starts to dominate and we obtain a scaling as aR^2B^2, which for constant aspect ratio will be similar to a scaling with stored energy.

This increased dominance of the structural material for larger machines is somewhat slowed down for superconducting coils. Indeed for those coils we had that

$$j \sim \left(\frac{1}{E}\right)^{0.2}$$

so that

$$\frac{M_s}{M_c} \sim \frac{RB}{(a^2RB^2)^{0.2}} \sim \left(\frac{R}{a}\right)^{0.4} R^{0.4}B^{0.6}$$

For a pulsed system (liquid nitrogen cooled or water cooled) the dominance of the structural material can be enhanced, because the short pulse allows a higher current density in the copper and thus less conducting material. As in this case $j \sim \sqrt{\frac{1}{\tau_e}}$, where τ_e is the equivalent pulse length, we obtain

$$\frac{\text{structural mass}}{\text{conductor mass}} \sim \frac{RB}{\sqrt{\tau_e}}$$

3.8. Access and ripple

Lower limits on the size of an experiment are set by the need for access. That this is especially the case for the small high field experiments can be seen from the Alcator machines.

If we knew the depth of the coils, h, then it would be possible to calculate the available open area as

$$S = \left(1 - \frac{\text{Volume copper and steel}}{l_a l_c h}\right) l_a l_c$$

However, the choice of h can depend on a lot of factors, as for example structural constraints. It is also not necessarily true that a large h providing for a large open surface is optimum. Indeed, it may very much hinder the possibility of tangential injection. Access and ripple are very much interrelated and further depend on the particular geometry, the number of coils, the choice of the heating method etc... This issue has been addressed in more detail for the particular case of the helical axis stellarator. We should however keep in mind that it is a possible constraint on size and magnetic field of an experimental system.

3.9. Summary

In this chapter we have concentrated on investigating the technological constraints. We have also derived some useful scaling relationships (mass, stored energy, required energy) with size and magnetic field (the two free parameters we had from our similarity considerations). While it is usually straight forward to design an experiment once the general parameters as size, magnetic field, etc. are set, —computer programs have been written to do it [109, 110]— trade offs between size, magnetic field, pulse length, stored energy are seldom investigated in detail. More often than not they are picked as being a reasonable combination, without much justification.

In this chapter we have obtained for those parameters some general tendencies and interrelations providing a sounder basis for some basic choices.

Application of the methodology to the identification of the minimum scale for a stellarator with helical magnetic axis.

3.1. Introduction

3.1.1. Objectives

In this chapter we show how the methodology developed earlier can be applied. We will investigate the constraints specifically for the design of a stellarator with helical magnetic axis, and then find what the minimum scale is for this particular experiment. Consequently the emphasis is on two aspects: first we will investigate the geometry in detail to find the specific constraints resulting from the particular configuration, and then show how those constraints, together with the more general ones identified in the previous chapters (resulting from the three step method) can be applied to find a minimum scale for this machine.

Further in this introduction we briefly review the methodology described in the first chapter. In the rest of the chapter we will first give some background information on the stellarator with helical magnetic axis. We will then address the issue of the constraints resulting from the choice of experimental format, and use the material developed in the previous chapters to identify a design

window for a particular experimental objective. Within the design window the final choice can then be made, based on other considerations.

Because the methodology and the supporting work of chapter 2 and 3 is very general, not all of it will be used. On the other hand, since some constraints result from the peculiarities of the configuration chosen, and since those were not discussed in general, a large portion of this chapter is devoted to the identification and explanation of the constraints specific to this particular configuration. For a fixed geometry and a chosen experimental objective the constraints can be applied and within the design window a minimum scale can be found. Some choices have to be made along the way. Other choices could have been made, even resulting in a different end product. This however, does not affect our main purpose to show how the method is to be applied.

3.1.2. Methodology

In this section we will briefly review the methodology and show how we are planning to apply it to the stellarator with helical magnetic axis. For a given geometry, we have to decide, based on our experimental objectives, which dimensionless parameters we want to keep constant in our model. In chapter 2 we have discussed the important dimensionless parameters. We have shown that an obvious parameter, that we are allowed not to keep constant (within some limits) is N_λ. In order to test ideal MHD β limits, we could drop ν as second parameter. Non ideal modes would be affected by ν. In transport tests, dropping β, may not be the appropriate choice. Is is thus more justifiable, to keep β and ν, and drop $\frac{\rho}{a}$ as a second parameter. If we want two degrees of freedom (the size and the magnetic field), we can only fix two dimensionless parameters. For the particular geometry, and the value for the fixed dimensionless parameters, we can draw the constraints in a size versus magnetic field diagram. A special set of constraints is those that result from the particular geometry chosen. More general constraints are those that were discussed in the previous chapters and are the result of the three steps described in the introduction. The first step is to examine under which conditions we can drop the other dimensionless

parameters. The second step is to investigate under which conditions we can neglect effects related to neutrals and impurities. We will in this context apply the na limit. The presence of impurities, even within acceptable limits, may still have an effect on the power needed to heat the plasma. This is linked to the third step, the possibility of achieving the plasma physics parameters dictated by the similarity considerations. This last step requires us essentially to look at constraints resulting from heating methods and technological constraints. Constraints on a and B will result, for fixed β and $\nu*$, from the choice of the heating method (for example due to accessibility of the electron cyclotron resonance layer). Technological constraints, related to stresses and current density limits, can also reduce the design window in a a and B diagram. Having identified all the constraints, we can in this diagram make a choice based on other considerations, as for example cost, access, etc..

The method does not give guidance with respect to the choice of the concept to be investigated. Nor about the particular configuration chosen to embody the concept. External considerations usually fix those choices, and we were no exception. The choice of the helical axis stellarator, and some specifics of its configuration are merely the result of particular interests at the time a concrete example was needed to illustrate how one can go about finding a minimum scale. We have, however, investigated some variations on the geometry and we will justify the resulting choices that have been made.

3.1.3. Subdivision of the chapter

The chapter is subdivided as follows :

In section 2 we explain what a stellarator with helical magnetic axis is, give some possible variation of this type of concept, and present the particular configuration used here to apply the method.

In section 3 we discuss the geometry in more detail, present which variations we have considered, and how we went about making some choices.

The fourth section investigates the specific constraints resulting from the geometry at the same time using those constraints to finalize the geometry.

In section 5 we discuss in more detail the topic related to equilibrium, stability and to transport and collisionality. This is needed to make appropriate choices for the fixed dimensionless parameters, β and ν_*, but also to provide the necessary information in order to later make an estimate of the power requirements.
In section 6 we then apply the constraints resulting from the three steps described earlier, and also take into account the particular constraints resulting from the geometry.
The seventh and last section shows how, within the design window a final choice can be made.

3.2. The Stellarator with Helical Magnetic Axis

In this section we give some background information on the stellarator with helical magnetic axis. We first discuss the concept, and how it fits into the larger set of toroidal configurations. We then briefly discuss a number of particular configurations that can be classified under the name of helical magnetic axis stellarator. Finally we describe which particular one was chosen for this thesis.

3.2.1. Concept

A stellarator with helical magnetic axis is a particular type of toroidal configuration. Toroidal configurations have the advantage over open configurations that there is theoretically no loss of particles and energy along the field lines. They have a drawback, however : they are toroidal, which automatically implies that no absolute minimum B geometry can be constructed and that some way must be found to avoid possible charge separation resulting from drifts associated with the toroidal inhomogeneity of the magnetic field.

The large spectrum of concepts in toroidal geometry result in part from the different approaches that are used to avoid this charge separation.

The charge separating drifts can be canceled by modeling the magnetic geometry such that the drifts occur in the poloidal direction, as in an Elmo Bumpy Torus.

Radial electric fields can achieve the same result. A more standard method is to give the field lines a rotational transform, thus allowing charge cancellation by particles flowing along the field lines.

There are three ways of producing a rotational transform.

A rotational transform can be provided by a current along the magnetic axis as is the case in a tokamak. A second way is by making non circular magnetic surfaces and rotating them. This can be done by using helical windings as in a torsatron. The third way, and historically the first [111] by giving the magnetic axis a torsion. Figure 4.1 schematically shows how a torsion can produce rotational transform of the field lines [112].

The three ways can be combined and the total rotational transform on axis is then given by Mercier's formula [113]

$$\iota = \frac{1}{2}\int \frac{ds}{\cosh\eta}\left(\frac{\lambda}{2} + d'(s) - \frac{2}{\tau(s)}\right) \tag{4.1}$$

where

- ι is the rotational transform, measured from the normal,
- η is a measure of the ellipticity of the surfaces, defined as $\frac{a}{b} = e^{\eta(s)}$ with a, b being the large and small axis of the elliptical surface near the axis (Fig. 4.2).
  In terms of the excentricity ϵ defined as $\epsilon = \frac{a^2-b^2}{a^2+b^2}$ we can write $\frac{1}{\cosh\eta} = \sqrt{1-\epsilon^2}$,
- λ is defined as $\frac{\lambda}{2} = \frac{\mu_o J_{so}}{B_{so}}$,
  J_{so} being the current density on axis,
  and B_{so} the magnetic field there,
- $d(s)$ measures the rotation of the ellipse with respect to the normal,
- $\tau(s)$ is the radius of torsion.

In this formula the angle ι is measured from the normal. For concepts with a plane axis this fact is not crucial as the normal is always directed towards the axis of symmetry of the device. Measuring the angle with respect to the

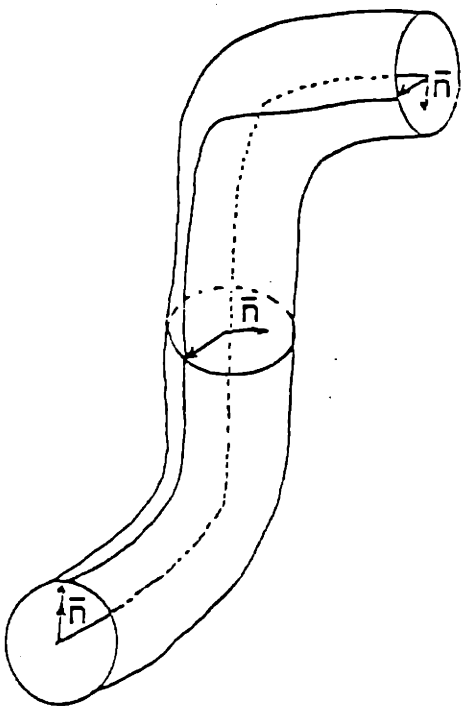

Figure 4.1 Rotational transform arising from torsion.

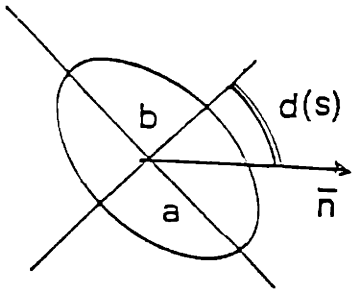

Figure 4.2 Definition of a,b and d for rotating elliptical surface

normal or to some fixed frame then does not make a difference. For the case of a non planar axis it is important to keep the difference in mind. Measuring the rotational transform from the normal is the most useful definition. Indeed, what matters is not the absolute motion of a field line, but its motion relative to the normal of the axis. It is the motion of the field line with respect to the normal that makes it sample regions of lower and higher magnetic field, and thus results in compensating drifts.

A stellarator with helical magnetic axis relies essentially on the third method to provide the rotational transform.

3.2.2. Different variations

A stellarator with helical magnetic axis can be built using helical coils, or using only circular coils .

A number of variations rely on helical coils to achieve their goal. A torsatron with $l = 1$ is such a configuration. Another possibility is a combination of a single, planar poloidal coil with helical coils: the Vintotron [114, 115]. Still another is the combination of helical conductors and toroidal coils forming a solenoid with helical magnetic axis, but plane-geometric axis (this is achieved by tilting the coils) [116].

The configuration can also be constructed using only circular coils. The first and most obvious choice is to place the (toroidal) coils perpendicular to the magnetic axis one would like to generate. Figure 4.3 shows some theoretically possible configurations from [117], at the same time defining n and m numbers. Figure 4.4 shows in more detail an $m = 1$, $n = 3$ system. Another proposal [118] keeps the center of the toroidal coil on a circular loop but gives the coils a tilt (Fig. 4.5). A third way is to combine a poloidal ring with toroidal coils. The toroidal coils are centered on a helical axis, but kept in $\phi = constant$ planes. A schematic vertical projection is shown in Fig. 4.6, while Fig. 4.7 gives

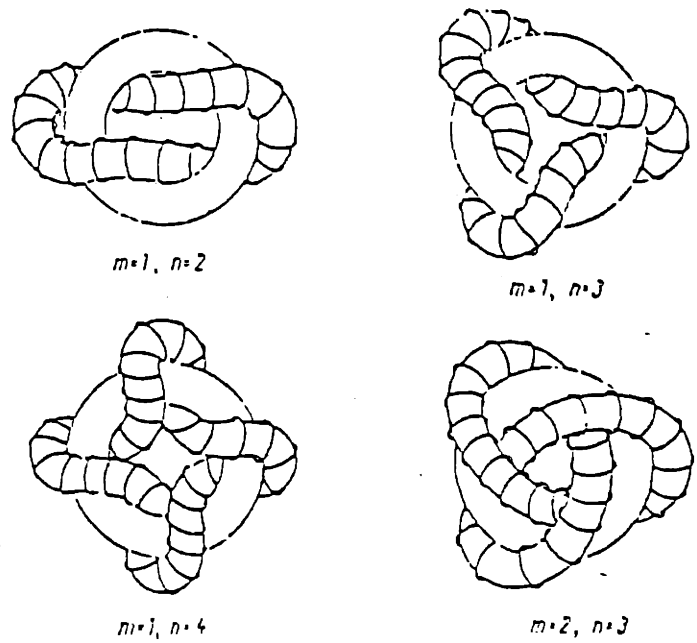

Figure 4.3 Possible configurations for stellarator with helical magnetic axis

a perspective drawing [119]. The coils can either link the poloidal ring or can be completely outside of it.

This last scheme is structurally especially simple, and allows some experimental flexibility because parameters associated with the magnetic axis can be changed by changing only the current in coils. This particular configurations, with no topological link between the toroidal coils and the poloidal ring was chosen as the configuration for further investigation and application of the method.

3.2.3. Definition of the parameters

Here we describe in more detail the particular choice and we identify the parameters that define the magnetic geometry. The basic components are shown in Figure 4.8.

A circular poloidal coil, of radius R_R carries a current I_R. The radius of its cross section is r_R. A pair of Helmholtz coils provide a vertical field B_v.

The toroidal coils, in $\phi = constant$ planes, have a radius a_c and are centered on a helical line with major radius R_c and minor radius r_c. While it is possible to

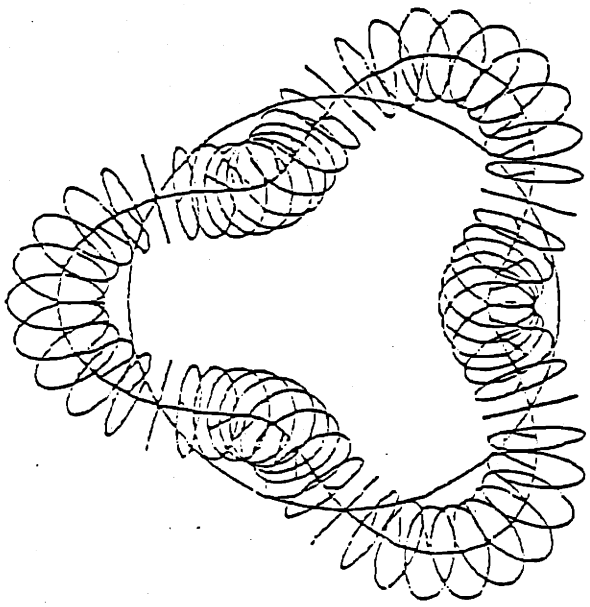

Figure 4.4 Stellarator with helical magnetic axis, obtained by placing the coils perpendicular to this magnetic axis. The figure is a vertical projection showing the coils and the circular loop (compare with Fig. 4.3).

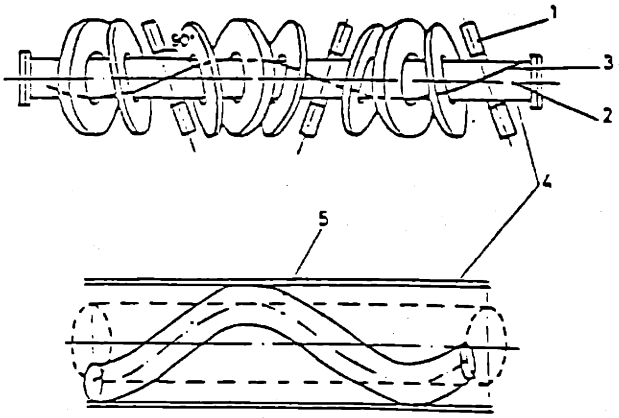

Figure 4.5 Stellarator with helical magnetic axis obtained by tilting the coils, straight version. The geometric center of the coils is a planar curve, but the tilt of the coils produces a spatial magnetic axis.

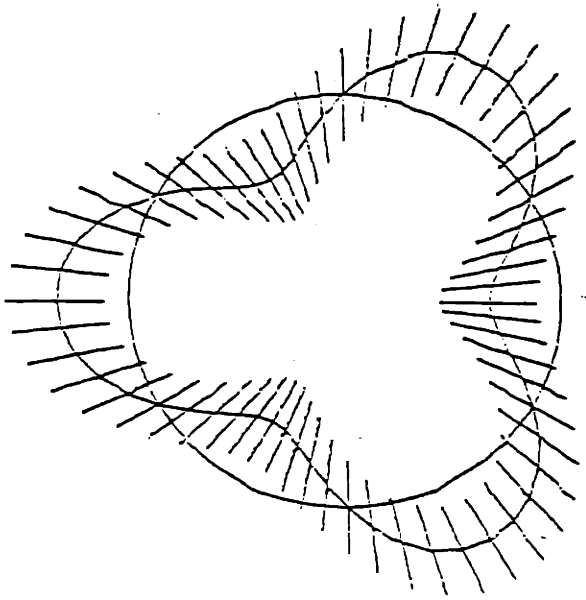

Figure 4.6 Helical stellarator obtained with coils in ϕ =constant plane, vertical projection showing the coils and the circular loop $m = 1, n = 3$.

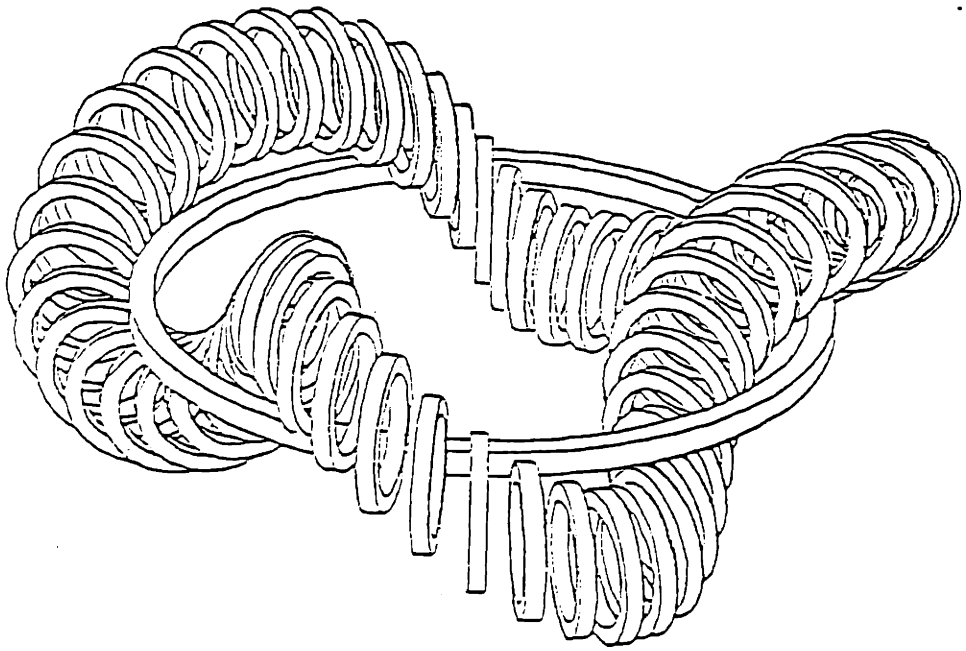

Figure 4.7 Stellarator with helical magnetic axis $m = 1$, $n = 3$ [119].

take $R_c \neq R_R$, and even to vary the radius r_c, so that the centerline of the coils would not lie on a torus with circular cross section (but rather, for example, on a torus with elliptical cross section), we have limited ourselves to the case where $R_R = R_c$, and $r_c = constant$. This particular choice was made because it results in toroidal coils, located at a *constant* distance of the toroidal ring, with obvious advantages in terms of standardization of the components and simplicity of construction.

The cross sectional dimension of the coils are $w_c \times h_c$ where w_c is the width (measured in the ϕ direction) and h_c the height. Their number is N and they carry a current I_c. The winding law of the helical line on which the coils are centered is defined as

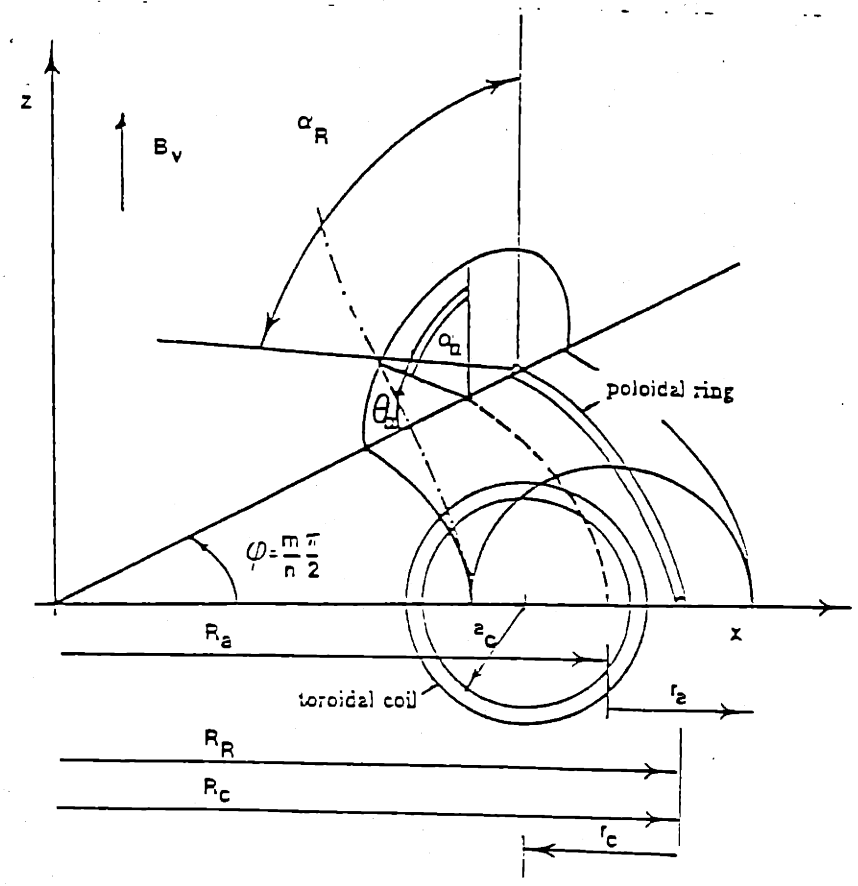

Figure 4.8 Parameters defining the geometry.

$$\frac{n}{m}\phi = \theta_c + \alpha_c \sin\theta_c \tag{4.2}$$

Those parameters are sufficient to uniquely define the magnetic geometry, including the position of the magnetic axis, shape of the surfaces etc... Let us, for the purpose of the discussion of the relation between the parameters introduce some additional definitions.

The magnetic axis is a helical line with major radius R_a, minor radius r_a and a winding law of the form

$$\frac{n}{m}\phi = \theta_a + \alpha_a \sin\theta_a \tag{4.3}$$

It is not obvious that the magnetic axis can be represented as a helical line with constant R_c, r_c and only a single harmonic for its modulation, but we will be show later that this is the case. The center for measuring the angle θ_c is the center of the ring ($R = R_c = R_R$), while the center for measuring the angle θ_a is $R = R_a$.

The angle α_c can be viewed as the angle $\frac{\pi}{2} - \theta_c$ at $\frac{n}{m}\phi = \frac{\pi}{2}$ (quarter period). Similarly, α_c can be viewed as the angle $\frac{\pi}{2} - \theta_c$ at $\frac{n}{m}\phi = \frac{\pi}{2}$. Define further α_R to be the angle of the magnetic axis at $\frac{n}{m}\phi = \frac{\pi}{2}$ measured from the ring center ($R = R_R$).

Let us also define a dimensionless parameter δ through $b_c = \delta r_c$, where b_c is the bore of the coil.

We have throughout used the index a to refer to properties related to the axis, the index c for properties related to the toroidal coils and an index R for properties related to the poloidal ring.

We have chosen here to define the geometry through dimensions, currents and magnetic fields. Alternatively one could use the more theoretical approach and define the magnetic geometry in terms of the position of the magnetic axis, shape of the surfaces, variation of the rotational transform etc... Different choices for the coil configuration could result in the same magnetic geometry. One could, for example, obtain the same magnetic geometry with helical coils. The reason

for first choosing the coil configuration, and investigating the geometry, is that it is easier to derive the theoretical parameters from real coil data than to infer actual coils from theoretical parameters. Other coil configurations, however, will result in other geometrical constraints, and those may even be less stringent For example, in order to obtain a helical axis stellarator with a large number of periods, the use of helical coils may be easier, at least for an experimental machine.

3.3. Geometry

3.3.1. Introduction

Having made a decision about the concept (stellarator with helical magnetic axis), and the particular coil configuration (toroidal coils, one poloidal ring, no topological link), we will want to address the constraints that arise from the particular geometry. From the start we have pointed out the importance of the magnetic geometry in performing scaling experiments, both in terms of its possible impact on the plasma parameters, and because of the existence of constraints specifically related to the geometry. However, as the geometry is different for each concept and as each concept needs a different number of parameters to be completely defined, we have not addressed the issue in general, but chosen to postpone the discussion and limit it to the particular concept and the particular configuration we used as an example. It is now time to tackle this aspect for the helical axis stellarator in the particular variation we have chosen.

It should be noted that while we have chosen a configuration for the helical axis stellarator consisting of toroidal coils, a poloidal ring with no linkage of the two sets of coils, we have not yet completely defined the geometry. To do this we could use two possible approaches.

The first approach would be to say that we want to model the geometry of a reactor exactly. One would have to rely on a reactor design to obtain

information on its geometry. Scaling it according to our parameters a and B, for fixed values of the dimensionless parameters β and ν_*, which we would also obtain from the reactor design, would give us the minimum scale experiment, after applying the constraints. This approach would be straightforward, if it were not for two problems. First there is no recent, well documented reactor design for a stellarator with helical magnetic axis (the adjective *recent* is added because, in fact, the first reactor design ever made, was a helical axis stellarator: the D-stellarator). Secondly, when we make a cursory calculation of what the geometry of such a reactor might look like, we note the need for a large number of periods in order to achieve large β values (the relationship between the number of periods and the β value will be discussed later). Unfortunately, however, the geometrical constraints, which will also be derived later, become more stringent when the number of periods increases. The resulting minimum scale experiment, because of this stringent geometrical constraint, together with high β values, would be very large. Those two problems essentially preclude the straightforward choice that the geometry be the reactor geometry.

We can then envisage a second approach. It is to keep our options open, and at first not completely fix the geometry. We can then investigate what the geometrical constraints are, for various geometries. The constraints resulting from the geometry are somewhat less stringent for particular choices of the geometry, and we might opt for a particular geometry where the constraints are the least stringent. This alternative approach to fixing the geometry is the one that was chosen here.

Any reactor design carried out today, would be based in part on the presently accepted, but untested relationship between the number of periods and the maximum achievable β. If we can test this theory under easier conditions (for example at a smaller number of periods), we could gain some confidence in the theory, and then, perhaps as the next step, build a model with reactor geometry.

Using this second approach for our particular case - i.e. choosing the geometry such that the geometrical conditions are the least stringent - we can not

choose the dimensionless parameters just by fixing them to the corresponding value in a reactor. Remember that the choice of the geometrical parameters has an influence on the achievable plasma parameters (for example there is a connection between β and the number of periods). The choice of the dimensionless parameters is now rather based upon the theory we want to test. The whole methodology however, namely 1) fixing dimensionless parameters, 2) taking a and B as the variables, 3) applying the constraints, and 4) choosing the final design within the design window, is still completely applicable. Indeed, the only difference is the following: if we had used the first approach (geometry =reactor geometry), the family of machines among which we choose the one which, within constraints, is the minimum scale member, contained also the reactor. Each member of the family (varying a and B) was similar to a reactor. Now we will choose the minimum scale member among a family which does not contain the reactor. Each member of the family however, is similar in that it will test the theory to the same extent. For a choice of β and ν_*, we will still have to apply the constraints resulting from the neglect of the other parameters (the members of the family must be truly similar), the constraints resulting from neutrals and impurities, and the constraints resulting from the ability to obtain the parameters required (constraints resulting from heating methods and technological constraints). Within the design window we can then choose the machine with the minimum scale, based on cost, access, etc...

3.3.2. How do we fix the geometry and find the resulting constraints ?

We have explained in the previous section how we are planning to fix the geometry: essentially by looking for the particular combination where the geometrical constraints are the least stringent. This will define the geometry and also identify the constraints specifically related to the geometry.

How do we find our way in this very large parameter space ? We will subdivide the parameters in "soft" parameters and "hard" parameters. The soft parameters are the easily changeable parameters, such as the current in the coils. The hard

parameters are the more permanent ones, those that are fixed once the machine is built. An example of a hard parameter is the number of periods.

Both the hard parameters and the soft ones affect the magnetic geometry. For example, it is clear that the shape of the magnetic axis depends on the number of periods. The position of the magnetic axis, within the toroidal coils also depends on the current in the toroidal ring.

Therefore we will first derive some relationship between those soft parameters (the current in the coils) and the magnetic geometry. Since the constraints we want to derive depend on the hard parameters and on the soft parameters, we then use the relationships that were developed (between soft parameters and magnetic geometry) and a particular choice of the geometry to make the constraints function of the hard parameters alone.

This then allows us to discuss the influence of the hard parameters on the constraints and choose them such as to make those constraints the least stringent. This finalizes the geometry and identifies the geometrical constraints.

Throughout this section we use dimensions, magnetic fields. It should be understood however, that in this section their absolute value is not fixed, since we will use R and B as scaling variables.

3.3.3. Discussion of the soft parameters

In this configuration a large number of parameters, associated with the magnetic geometry, can be changed by changing what we call soft engineering variables, the current I_R in the ring and the vertical field B_v. The modulation angle α_c of the winding law of the coils can be considered "semi-soft", as one could envisage the possibility to reposition those coils without too many problems. For those parameters it is necessary to have design values and sufficient freedom should still be maintained in order to be able to investigate easily the influence of their variation and the resulting variation of the well depth, rotational transform etc.., on plasma properties. Let us now discuss the influence of the soft variables

(the vertical field and the ring current) on the geometry. In Appendix C we give some basic information on spatial curves. We urge the reader to go through it carefully as an understanding of it is the basis of much of the further discussion in this chapter.

Extensive numerical calculations were performed by P.A. Politzer [120] in order to investigate the vacuum magnetic surfaces and the parameters associated with the magnetic axis, with variations of the vertical field, B_v, the ring current I_R and the winding law of the solenoid α_c. As there is no published record of them we briefly summarize the results here. A field line follower was used to trace out magnetic surfaces (puncture plots) and to calculate the magnetic properties. Coils were modeled by filamentary conductors. The calculations were performed for several combinations of I_R and B_v, for the particular case of $n = 3$.

We summarize here the results obtained for $R_R = 2m, a_c = 0.4m, r_c = 0.4m$ and $\alpha_c = \alpha_R$ (modulation angle for the winding law of the geometric center of the coils equal to the angle of the magnetic axis, as measured from the ring center).

1. The minor radius of the magnetic axis r_a depends on the ring current only, the dependence on the vertical field is extremely small (see Fig. 4.9).
2. The major radius R_a depends both on the ring current I_R and the vertical field B_v (Fig. 4.10).
3. While r_a and R_c vary when the angle of the solenoid is varied, the angle α_R varies little when the winding law of the solenoid is varied from $\alpha_c = 0$ to $\alpha_c = \alpha_R$ (in order to center the coils on the magnetic axis), as can be seen in Fig. 4.11.
4. The rotational transform depends only on I_R and decreases with increasing I_R (Fig. 4.12).
5. No magnetic surfaces are obtained from some combinations of B_v and I_R. Results pertaining to the well depth are shown in Fig. 4.13, and Fig. 4.14 shows an example of the shape of the flux surfaces.

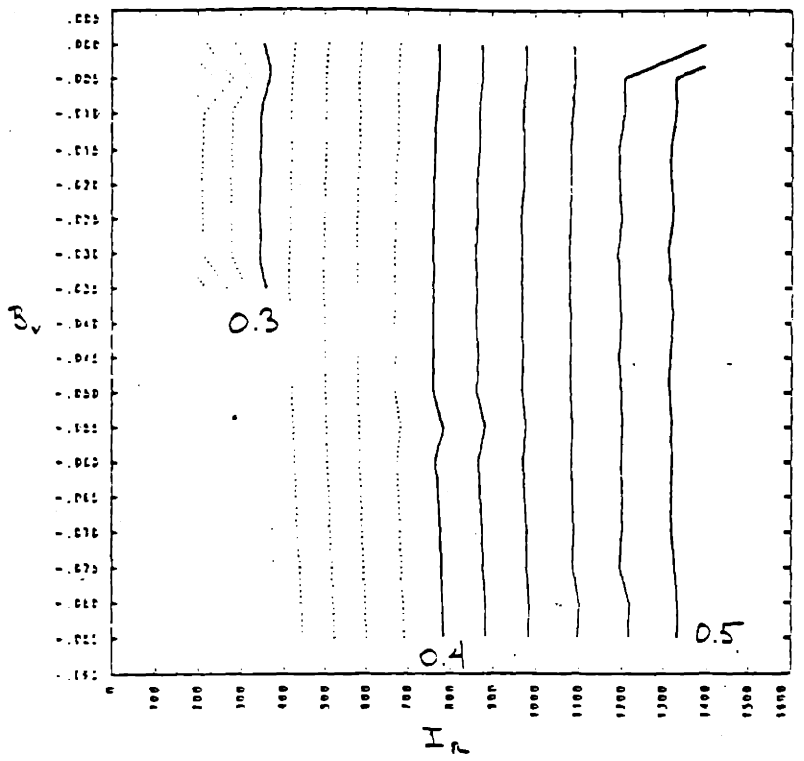

Figure 4.9 Minor radius r_c as a function of ring current I_R and vertical field B_v

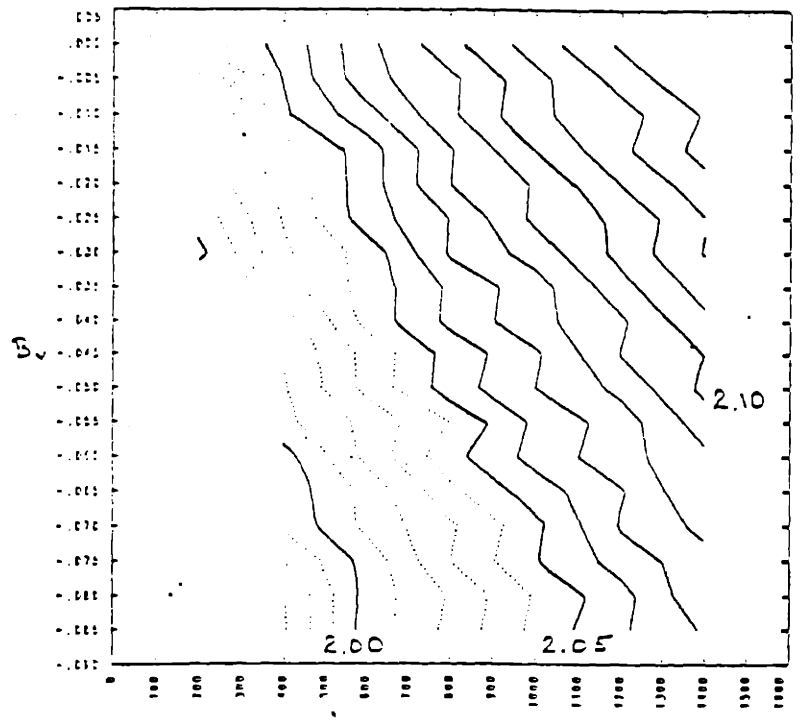

Figure 4.10 Major radius R_c as a function of ring current I_R and vertical field B_v. The waviness of the lines is the result of the fact that the values of were obtained for a finite number of combination I_R and B_v.

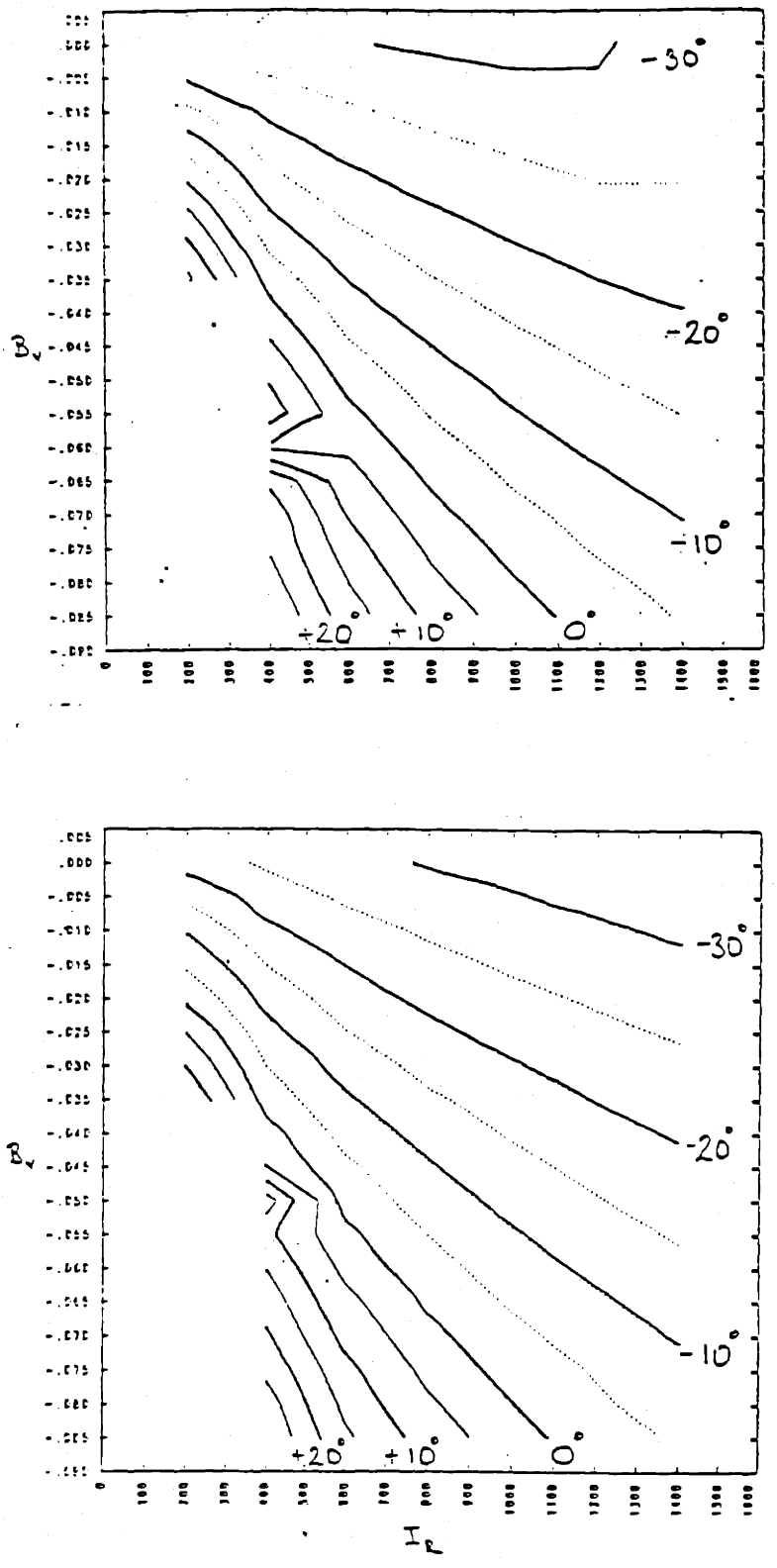

Figure 4.11 Value of α_R for $\alpha_c = 0$ (top) and $\alpha_c = \alpha_R$ (bottom)

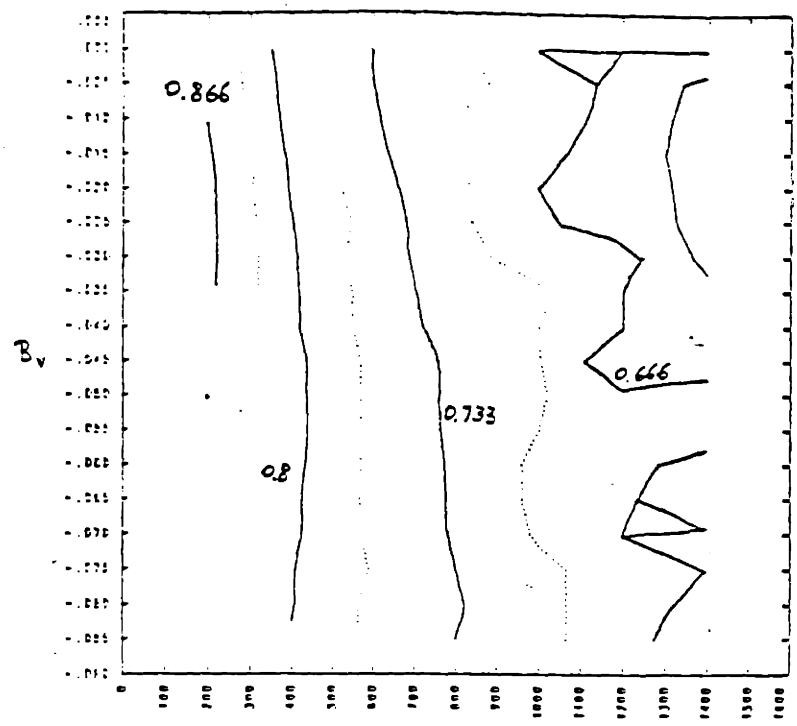

Figure 4.12 Normalized rotational transform ($\frac{\iota}{2\pi}$) per period.

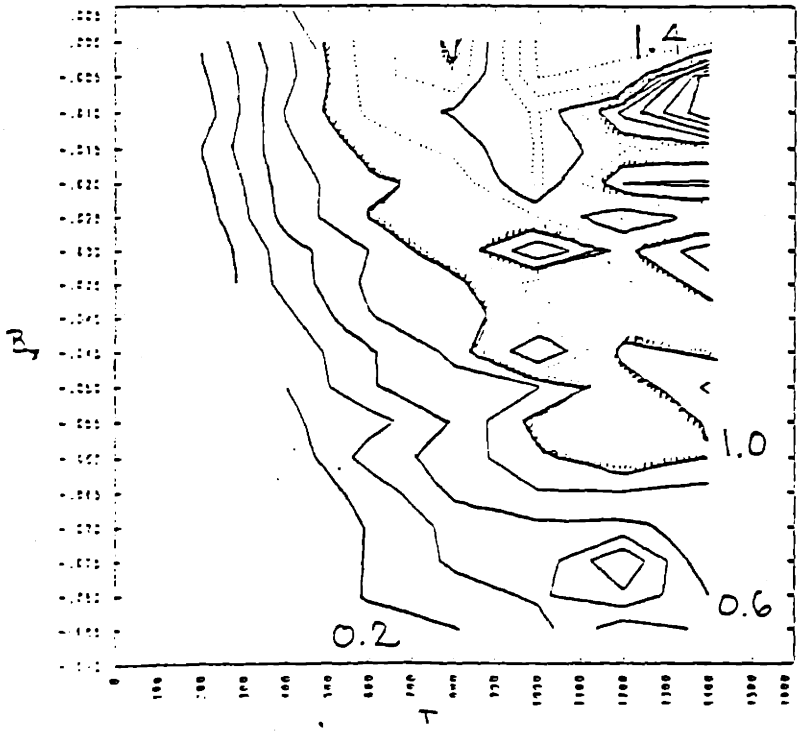

Figure 4.13 Well depth. $\frac{\Delta U}{U}(\%)$, where U is the specific volume defined as $U = \frac{dV}{d\Phi}$. Φ is the magnetic flux in the ϕ direction, within the magnetic surface ψ, and V is the volume enclosed in the surface ψ.

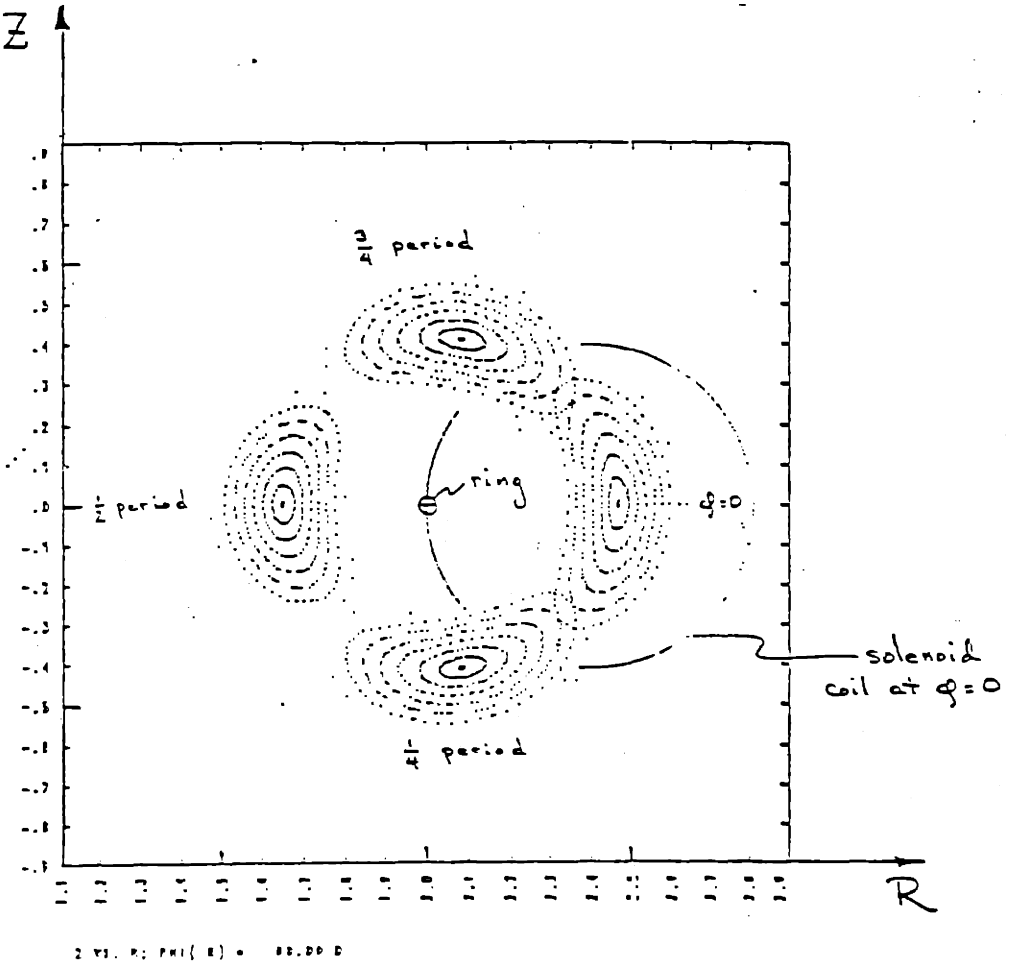

Figure 4.14 Shape of the surfaces for the case $R_R = 2m$, $\frac{r_c}{R_R} = 0.2$, $\frac{a_c}{R_R} = 0.2$, $\alpha_c = -12^o$, $I_R = 800kA$ and $B_v = -0.04T$

To obtain all the information (magnetic surfaces, well depth, etc...) on the final magnetic geometry there is no way around doing field line following. However in order to make choices with respect to the number of periods, major radius, minor radius (the hard parameters), it is important to be able to have some analytical or semi-analytical tools to narrow the parameter space that will be looked at numerically, and obtain relationships between the magnetic geometry and the soft parameters.

We have developed an simple analytical model which explains the parametric variations. A further refined numerical-analytical method obtains very easily and efficiently r_a, R_a, the angles α_c, α_R and the rotational transform and is in excellent quantitative agreement with the detailed numerical results. Approximate formulas are also provided for the ring current I_R needed to position the magnetic axis for a given minor radius, and for the vertical field B_v to obtain $R_a = R_R$. This is detailed in Appendix D.

3.3.4. Discussion of the hard parameters

In contrast to currents in coils, other engineering parameters are fixed or less easily changeable once the machine is built. They are the number of periods (n, m number); the ring radius (R_R), its cross section (πr_R^2); the number (N) of the toroidal coils, their radius (a_c), the bore of the coils (b_c), the displacement (r_c), and cross section ($h_c \times w_c$). The modulation angle (α_c) was considered semi-soft. Let us discuss how we can go about choosing those parameters.

The magnetic geometry and the geometrical constraints depend both on the choice of the soft parameters, and on the choice of the hard parameters. In order to make it a function of the hard parameters only, we will assume that the relationships developed in Appendix D are used to obtain the values of the soft parameters for each choice of the hard parameters. More explicitly, for each choice of the hard parameters, we will take for the ring current the value that will give for the magnetic axis a minor radius $r_a = r_c$. This particular value of ring current will further be called the design value of the ring current. Using the

vertical field, the magnetic axis can then be centered in the toroidal coils, giving also $R_a = R_R$. This then makes the geometry, and the constraints resulting from it, a function of the hard parameters only.

We will now show how we can reduce the number of hard parameters, so that we can concentrate on only five of them: n, the number of periods; r_c, the displacement of the coil; R_R, the major radius of the ring; b_c, the bore of the coil; and N the number of the coils.

Going back to Figure 4.3 where a configuration with $m \neq 1$ is shown, will easily convince us to take $m = 1$. A more solidly based argument is that taking $m \neq 1$ would increase the effects due to toroidality, compared to a machine with the same n and $m = 1$.

In view of the fact that this is to be an experimental machine, one appealing property of which is that the magnetic axis can be easily moved by changing currents in the coils, it is important to keep this flexibility and thus important not to take any steps that would, without reason, reduce the radius of the coil. Using the parameter Δ as defined in Figure 4.15, we can write in general $a_c = r_c - \frac{h_c}{2} - r_R - \Delta$. The coil radius a_c will be largest when $\Delta = 0$, and we thus opt for this choice. The result is also that the coils can be attached to the circular ring, with no additional stand off piece in between. We take thus always

$$a_c = r_c - \frac{h_c}{2} - r_R \tag{4.4}$$

We further have that there is, for a given configuration a relationship between the current in the toroidal coils, and the current in the ring. This is the relationship mentioned earlier and discussed in Appendix D.

Let

$$\frac{I_R}{I_c} = \lambda \tag{4.5}$$

This can also be written as

$$\frac{J_R \pi r_R^2}{J_c w_c h_c} = \lambda \tag{4.6}$$

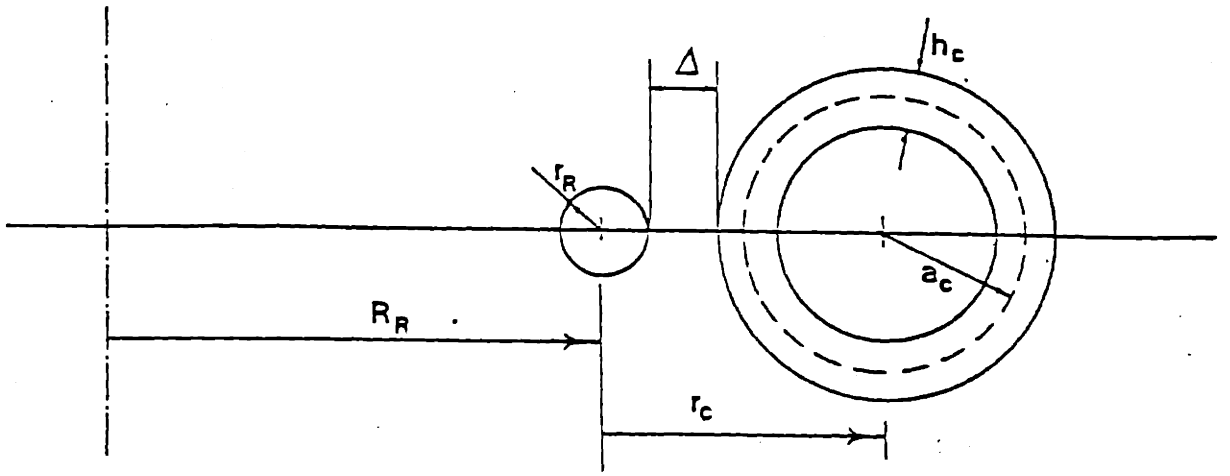

Figure 4.15 Position of the toroidal coils with respect to the ring

Requirements that the coils do not interfere in the center (see Fig. 4.17 for the definition of the variables) results in

$$R_i \Delta\phi = w_c \tag{4.7}$$

With

$$\Delta\phi = \frac{2\pi}{N} \tag{4.8}$$

and

$$R_i = R_R - r_c - a_c \tag{4.9}$$

the equation (4.7) can be written as

$$2\pi(R_R - r_c - a_c) = N w_c \tag{4.10}$$

We can further write a_c very simply in terms of b_c and h_c. Indeed, we have

$$a_c = b_c + \frac{h_c}{2} \tag{4.11}$$

The four equations (4.4), (4.6), (4.10), (4.11) can be used to express four variables as a function of the others. For example, we can express r_R, a_c, h_c and w_c as a function of the other parameters.

Having thus eliminated a_c, r_R, h_c and w_c we are left with: n the number of periods, R_R the ring radius, r_c the displacement of the coils, b_c the bore of the coil, and N, their number (and α_c the modulation angle of the winding law).

Remember that we still have the scale factor for the dimensions so that we can reduce the number of parameters by one by taking the ratio of the dimensions. The parameters are then n, $\frac{r_c}{R_R}$, $\frac{b_c}{r_c}$, N and α_c. Note that we have taken the ratio r_c with respect to the ring radius R_R, and the ratio of the bore b_c to the displacement of the coils r_c.

There are some qualitative indications on the choice of n, $\frac{r_c}{R_R}$, $\frac{b_c}{r_c}$, N. Those qualitative indications are given here only to give the reader some feeling for possible directions. We will address the issues quantitatively later on. A small value of n results in a simpler machine (see again Figure 4.3), but on the other hand helical symmetry is improved for a large number of periods. For the choice of $\frac{r_c}{R_R}$, one expects that increasing this value will give larger values of $\frac{a_c}{R_R}$ (for constant $\frac{b_c}{r_c}$) and thus possibly a larger plasma for the same overall size. A value of $\frac{b_c}{r_c} = 1$ gives the maximum coil radius for a given displacement of the coil. It is however a theoretical maximum as for $\delta = \frac{b_c}{r_c} = 1$ the ring has zero radius and the toroidal coils zero height (both are filaments). For a given size, the number of coils should be as small as acceptable, in order to increase access. The minimum will then be set by ripple requirements. The choice of α_c is not so crucial since it is a semi-soft parameter. In order to be able to investigate winding laws of the magnetic axis with both positive and negative winding angle, the choice of $\alpha_c = 0$ would give maximum flexibility. The choice of α_c could also be made such as to center the magnetic surfaces optimally in the coils ($\alpha_c = \alpha_R$). In a first configuration we would take $\alpha_c = 0$.

3.3.5. Summary

In this section we have introduced and defined the major parameters associated with the magnetic geometry of a stellarator with helical magnetic axis. We have divided the parameters in "hard" and "soft" parameters, and explained how we would go about finalizing the geometry and obtaining the geometrical constraints.

Results of numerical calculations were reported showing how parameters associated with the magnetic geometry can be changed by changing only the "soft" parameters, namely the vertical field and the ring current. A model was devised that gives the geometric data related to the magnetic axis and provides some simple analytical expressions relating the soft parameters to the geometry. This allows us to make the geometry function of the hard parameters only. We have further shown how we could reduce the number of hard parameters and briefly discussed qualitatively the choice of the remaining ones. Let us now turn to the quantitative discussion of those parameters.

3.4. Choice of the geometry and investigation of the related constraints

We will now discuss the issues more quantitatively. The choices will be dictated in part by geometric considerations (properties of the magnetic axis as a spatial curve, space constraints, ripple) and in part by required relations between ring current, coil current, number of periods and displacement of the coils. Optimization and trade-offs between plasma size and magnetic field, and properties related to MHD and transport also play a role in the choice of the parameters.

We have in the previous section explained how we take into account the dependence of the geometry on the soft parameters, and how we reduced the number of hard parameters to a manageable number. In what further follows we will often use a diagram of the number of periods n versus $\frac{r_c}{R}$, in which for

convenience n is treated as a continuous variable. It should however be clear that only integer values are of actual significance.

3.4.1. Constraints for the magnetic axis

The magnetic axis is a spatial curve whose position (R_a, τ_a) and winding law (α_a) are only slightly influenced by the details of how the toroidal coils are built. The only important parameters are then the number of periods n, the displacement of the coil $\frac{r_c}{R}$ and the winding law α_c. Taking here for the purpose of discussion here $\tau_a = \tau_c$, $R_a = R_c$ and $\alpha_a = \alpha_c$ we can derive a constraint, purely from geometrical consideration, on n, $\frac{r_c}{R_c}$ and α_c.

The constraint result from the fact that the normal to the magnetic axis can have two distinctly different behaviors. The minor radius curvature can always be dominant (with the normal thus always pointing towards the ring) or, at some points on the inside of the torus, the major radius can start to dominate (with the normal then pointing towards the center of the machine). If the major radius curvature starts to dominate on the inside of the torus, there is a discontinuity in the value of the rotational transform, because of the discontinuity in the behavior of the normal. Indeed, if the normal points towards the ring, it makes a 2π rotation per period. In the case the major radius starts to dominate, the net rotation after a period will be zero. Since the rotational transform is measured from the normal, there is a discontinuous change of 2π per period in the value of the rotational transform when the behavior of the normal changes (see also [121]). This discontinuous switch delineates thus two regions, one where we can truly speak of a stellarator with helical magnetic axis, and one where the minor radius curvature is no longer dominant. In this second region, the total rotational transform becomes zero in the limit of very small $\frac{r_c}{R}$, so that the charge separating drifts are no longer canceled. It is thus best to avoid this second region.

It is shown in appendix C that for the minor radius curvature to dominate we need

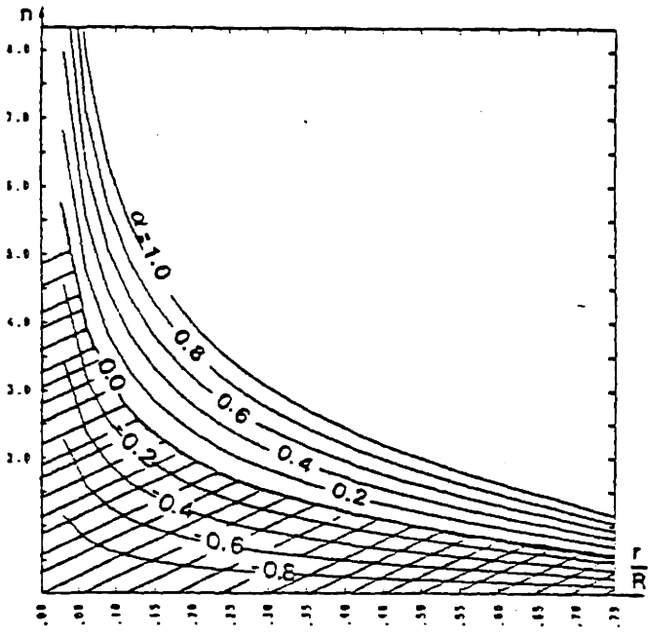

Figure 4.16 Regions in parameter space where the major radius curvature dominates.

$$\left(\frac{n}{m}\right)^2 > \frac{1-\frac{r_c}{R_c}}{\frac{r_c}{R_c}}(1+\alpha_c)^2 \tag{4.12}$$

Lines of constant α_c are shown in Figure 4.16. The allowable parameter space depends on α_c, but is in the direction of larger n, and larger $\frac{r_c}{R}$. For illustrative purposes we have hatched in the drawing the forbidden space for $\alpha_c = 0$.

3.4.2. Constraints from non-interference of the coil.

We have briefly used earlier the requirement that coils should not interfere on the inside, to obtain one relation that allowed us to eliminate a parameter. Here we will develop it in more detail because it also results in a maximum achievable value for $\frac{R}{R}$. The geometry is shown in Fig. 4.17.

The ring current I_R results, for a given current density, in a minimum radius r_R for the ring.

$$\pi r_R^2 J_R = I_R \tag{4.13}$$

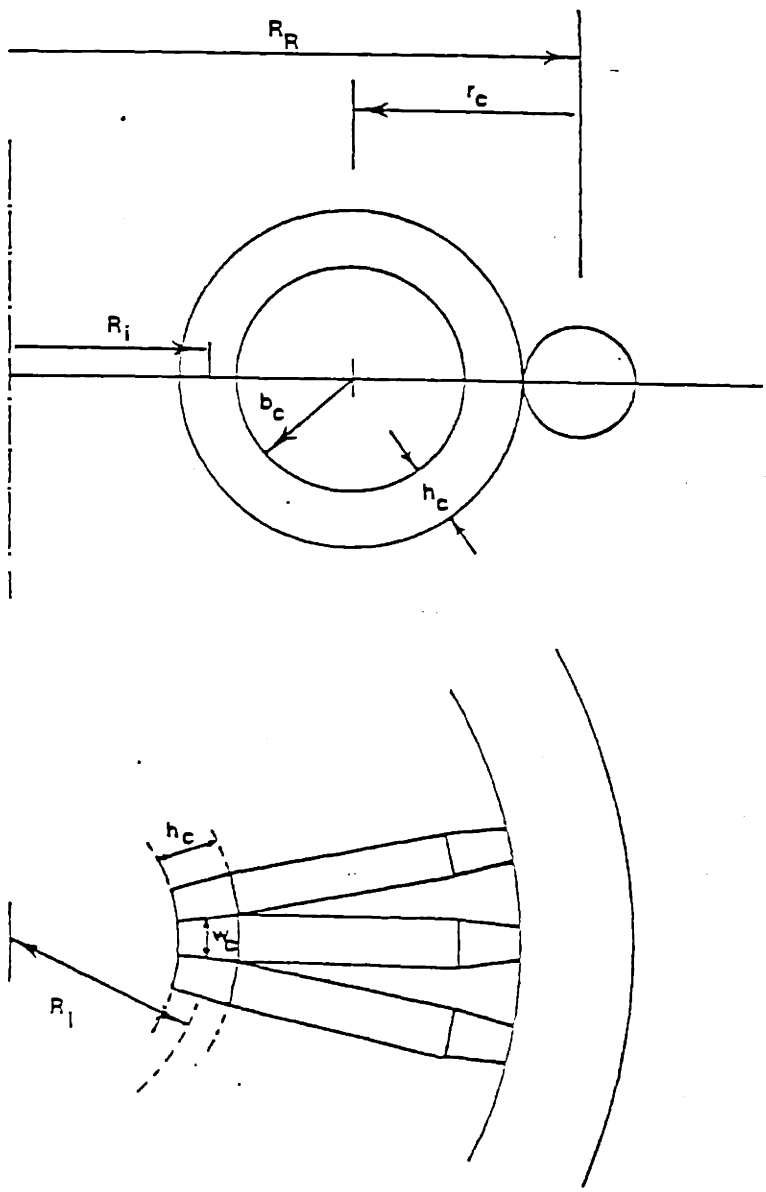

Figure 4.17 Definition of some coil dimensions.

Similarly the toroidal coils need a minimum area $w_c \times h_c$ to carry the current for a given density.

$$w_c h_c J_c = I_c \tag{4.14}$$

In order for the toroidal coils not to interfere at the inside (assuming the coil to be wedged) we request that

$$R_i \Delta\phi > w_c$$

where

$$\Delta\phi = \frac{2\pi}{N} \tag{4.15}$$

$$R_i = R_R - r_c - a_c \tag{4.16}$$

In principle w_c could get arbitrarily thin, the necessary area being provided by increasing h_c. However, increasing h_c decreases the bore of the coils. This trade-off will be considered later. To avoid the fact that the bore b_c would become too small, let us fix the ratio $\frac{b_c}{r_c} = \delta$ to some value $\delta = 0.5$.

The value of the ring current depends on the size, the number of periods, the winding law etc... This has been discussed earlier and in Appendix D. To eliminate this dependence on the soft parameters we will use what we have previously called the design value of the current (this corresponds to the current for a magnetic axis centered at $r_a = r_c$). The ring current is then given to a good approximation by

$$I_R = \frac{2\pi R B_\phi}{\mu_o} \frac{n}{m} \left(\frac{r_c}{R}\right)^2 \tag{4.17}$$

Let us further take as a first approximation for the current in the toroidal coils

$$B_\phi 2\pi R \sqrt{1 + (\frac{n}{m}\frac{r_c}{R})^2} = \mu_o N I_c \tag{4.18}$$

where B_ϕ is an average magnetic field, and $2\pi R\sqrt{1 + \left(\frac{n}{m}\frac{r_c}{R}\right)^2}$ is the length of the helical line in the center of the coils under the assumption of a straight helix.

From the set of equations (4.13 - 4.15) we can solve for $\frac{B_\phi}{RJ_c}$.

We obtain the quadratic equation

$$\frac{B_\phi}{RJ_c}\sqrt{1+\left(\frac{n}{m}\frac{r_c}{R}\right)^2} - \mu_o\left[1-\frac{r_c}{R}\left(\frac{3+\delta}{2}-\frac{1}{2}\sqrt{\frac{2B_\phi}{\mu_o R J_R}\frac{n}{m}}\right)\right]\left[1-\delta-\sqrt{\frac{2B_\phi}{\mu_o R J_R}\frac{n}{m}}\right]\frac{r_c}{R}=0 \tag{4.19}$$

Choosing values for

$$\delta = 0.5$$
$$J_c = 2\times 10^7 A/m^2$$
$$J_R = 2\times 10^7 A/m^2$$

We can solve this equation for $\frac{B}{R}$ in terms of $\frac{n}{m}$ and $\frac{r_c}{R}$. The result is shown in Fig. 4.18.

The lines in Fig. 4.18 delineate for a particular choice of $\frac{B}{R}$ the regions where the coils will not interfere. For small $\frac{r_c}{R}$ values we have wide coils, of small height, but for large $\frac{r_c}{R}$, as the coils increase in size, and thus crowd more and more the center, the width has to be reduced (with a corresponding increase in height). Figure 4.19 shows the variation of $\frac{B}{R}$ with $\frac{r_c}{R}$ for fixed $n=3$, as well as the relative distribution of the space between ring radius r_R, height of the coil and bore of the coil.

It is clear from Figure 4.18 that interference of the coils will put a rather stringent constraint on the value of $\frac{B}{R}$. Figure 4.18 was drawn for $J_c = J_R = 2kA/cm^2$ and $\delta = 0.5$. Changing the value of J_c, J_R or δ will change the value of $\frac{B}{R}$ but does not change the location of the maxima. In fact if we take $J_R = J_c$, Figure 4.18 can be normalized with respect to current density. The lines would then be lines of constant $\frac{B}{JR}$.

Since it is easier to relate to $\frac{B}{R}$ than to $\frac{B}{JR}$, we will, for the purpose of obtaining numbers, continue to use $J_R = J_c = 2kA/cm^2$. One should keep in mind however, that the geometrical constraint is on $\frac{B}{JR}$ rather than on $\frac{B}{R}$.

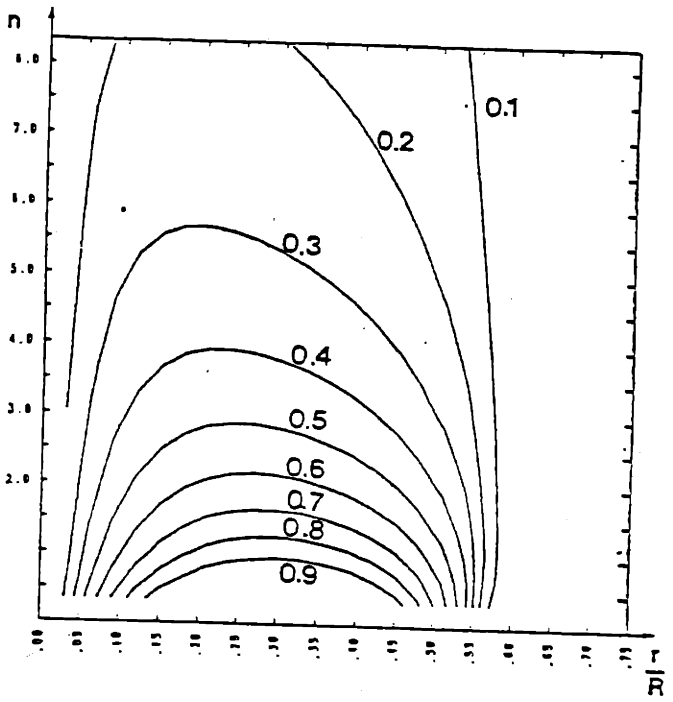

Figure 4.18 Maximum value of $\frac{B}{R}$ because of coil interference. We have assumed $J_R = J_C = 2 \times 10^7 A/m^2$ and $\delta = 0.5$. For small $\frac{r_i}{R}$ the value of $\frac{B}{R}$ decreases because below a certain point further decrease of $\frac{r_i}{R}$ and thus of $\frac{h_c}{R}$ can no longer be compensated by an increase in $\frac{w_c}{R}$. For fixed current density the current in the coil and the ring must decrease thus decreasing $\frac{B}{R}$. For large $\frac{r_i}{R}$ there is also a decrease in $\frac{B}{R}$ due to the fact that as the inner part of the coil gets closer to the center its width w_c decreases more rapidly than its height can increase.

Notice that combining Figure 4.18 (interference of coils), with Figure 4.16 (behavior of the magnetic axis) already gives us clear indication about the constraints on n and $\frac{r_i}{R}$ (for fixed values of δ), shown in Fig. 4.20.

We have in this section fixed the value of δ. In the next section we will discuss how things change when we allow δ to vary. Figure 4.20 will then change slightly

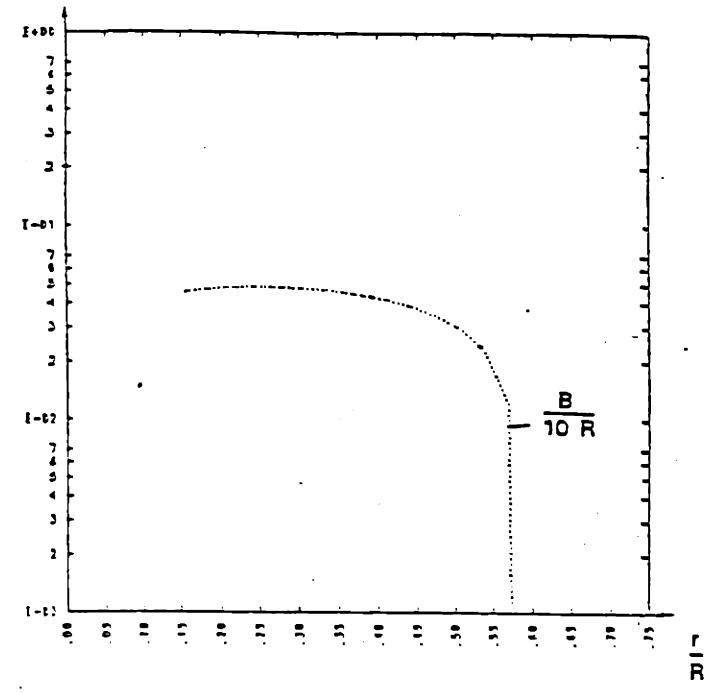

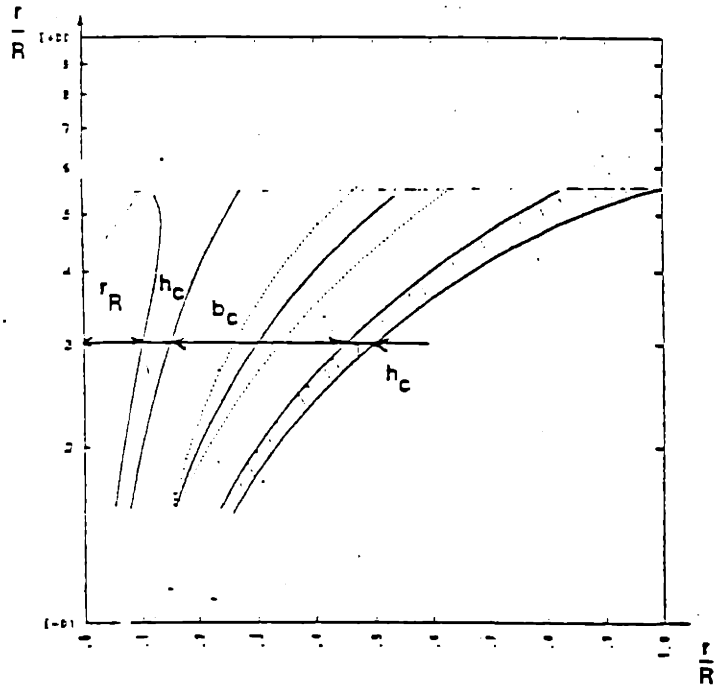

Figure 4.19 Maximum value of $\frac{B}{R}$ as a function of $\frac{r}{R}$ for $n = 3$, $J_R = J_c = 2 \times 10^7 A/m^2$ (top figure). Also shown is the relative fraction taken up by the ring and the toroidal coil as $\frac{r}{R}$ varies (bottom figure). We have assumed $\delta = 0.5$.

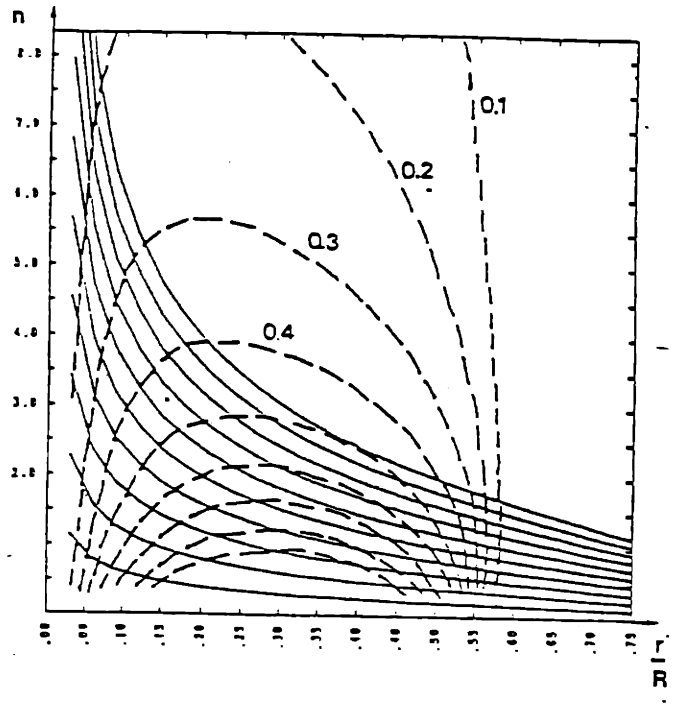

Figure 4.20 Combination of Figure 4.16 giving the regions where the minor radius curvature dominates with Fig. 4.18 giving the regions where the coils would interfere.

---

when we allow δ to change.

3.4.3. Effect of changing δ

In the previous constraints we have not addressed the issue of plasma size. By choosing the bore of the coil to be a certain fraction of the coil displacement ($\delta = 0.5$) we had assumed to have some room left for the plasma. When we allow δ to change we are faced however with a complicated trade-off. Increasing δ increases the bore of the coils and allows thus more space for the plasma, but will reduce the achievable magnetic field.

Influence on the magnetic field

Indeed, as δ increases, we have to decrease the height (h_c) of the coils. As the width w_c of the coils is set by interference near the center, the current in the toroidal coils has to go down if we fix the current density. The ring current,

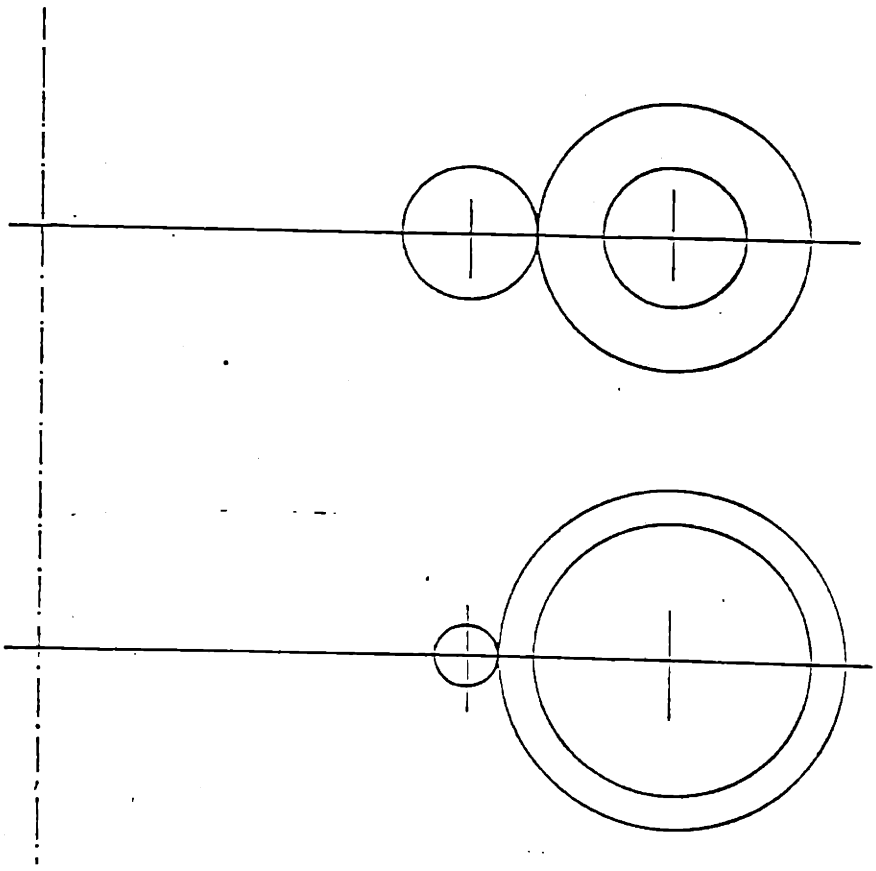

Figure 4.21 Effect of changing $\delta = \frac{b_c}{r_c}$ on the distribution of the space between r_R and h_c.

and thus the ring radius can then go down in the same proportion (Fig. 4.21). This also will influence the space available for the height of the coils. The exact distribution of the space $(r_c - b_c)$ between the coil (h_c) and the ring (r_R) is discussed in Appendix E. The net result, is that at constant current density and overall size, if we decrease δ, the magnetic field has to go down.

Influence on the plasma size

The actual increase of the plasma size when the bore of the coil increases can only be found exactly by running a computer code that gives the magnetic surfaces (puncture plots). It is however useful to identify the mechanisms that have an influence on the plasma size, and to obtain an approximate result. This will allow us to make a choice in the large parameter space n, $\frac{r_c}{R_R}$, $\frac{b_c}{r_c}$,

N, without having to scan this whole space numerically. There are three major factors.

The first is that we have to stay away a certain distance from the coils because of ripple considerations. We have taken here a simple, but quite accurate rule of thumb that surfaces of constant ripple are located at a distance Δ_{fc} from the coil, such that

$$\Delta_{fc} = \frac{\Delta_{ic}}{\xi}$$

where Δ_{ic} is the distance between the coils and ξ a ratio depending on the value of the ripple (Fig. 4.22). This rule of thumb was checked against a model given in [100] where, to calculate the ripple for a tokamak in the $z = 0$ plane, the toroidal coils are replaced by two infinitely long parallel straight current filaments, located at the position of the inner (r_1) and the outer (r_2) leg of the coil. The ratio $\xi = \frac{\Delta_{fc}}{\Delta_{ic}}$ calculated from their data at constant ripple is indeed independent of r_2 and r_1, and only slightly dependent on the number of coils. For 4 coils and a 2% ripple, we obtain $\xi = 2.25$, for 6 coils $\xi = 2.05$ and for 12 coils $\xi = 1.83$. The rule was also checked against published data about ripple surfaces in tokamaks (see Fig. 4.22).

Defining the plasma size through $a_p = b_c - \Delta_{fc}$, we introduce the ratio $\eta = \frac{a_p}{b_c}$. This ratio can be related to the parameters ξ, N, $\frac{r_f}{R}$ and $\frac{b_c}{r_c}$ through

$$\eta = 1 - \frac{Q}{\xi N}$$

where Q is a parameter defined in Appendix F. It depends on the number of periods n, the displacement of the coils $\frac{r_f}{R}$ and the bore of the coils $\delta = \frac{b_c}{r_c}$.

We have plotted in Figure 4.23 the value of $\eta = \frac{a_p}{b_c}$ as a function of the number of periods n and $\frac{r_f}{R}$ for $N = 60$ and $\xi = 2$ (corresponding to a 2% ripple). It is clear that for this choice of N and ξ there is a limit above which there is no area to the right of the center of the coil for which the ripple is smaller than 2%.

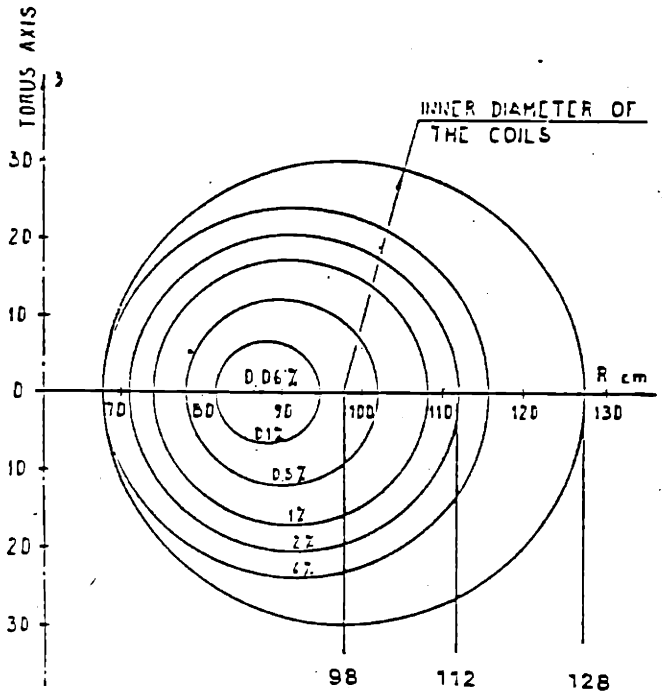

Figure 4.22 Surface of constant ripple for TFR [122]. The surface with ripple 2% at $z = 0$ is located at a distance $\Delta_{fc} = 128 - 112cm = 16cm$ from the inner side of the toroidal coil (at $R = 128cm$). TFR has 24 coils. The distance between the coils at $R = 128cm$ is $\Delta_{ic} = \frac{2\pi \times 128cm}{24} = 33.5cm$. For the ratio $\xi = \frac{\Delta_{ic}}{\Delta_{fc}}$ we obtain $\xi = \frac{\Delta_{ic}}{\Delta_{fc}} = \frac{33.5}{16} = 2.09$.

A second factor influencing the size of the plasma results from the fact that the plane of the coils is not perpendicular to the magnetic axis. The actual dimension of the plasma is related to the dimension of the plasma in the bore of the coil through the cosinus of the angle of the magnetic axis with the ϕ direction. This angle is the pitch angle given approximately in the general case (and exactly in the case of constant pitch winding law) by

$$\tan p = \frac{n}{m} \frac{r_a}{R_a}$$

Thus if we have an elliptical plasma with dimensions a_{p1} and a_{p2} in the bore of the coil at $\theta = \pi$, the actual dimension is a_{p1} and $a_{p2} \cos p$. This effect can be very large for large n and $\frac{r_a}{R}$. Shown in Figure 4.24 is the value of $\cos p$.

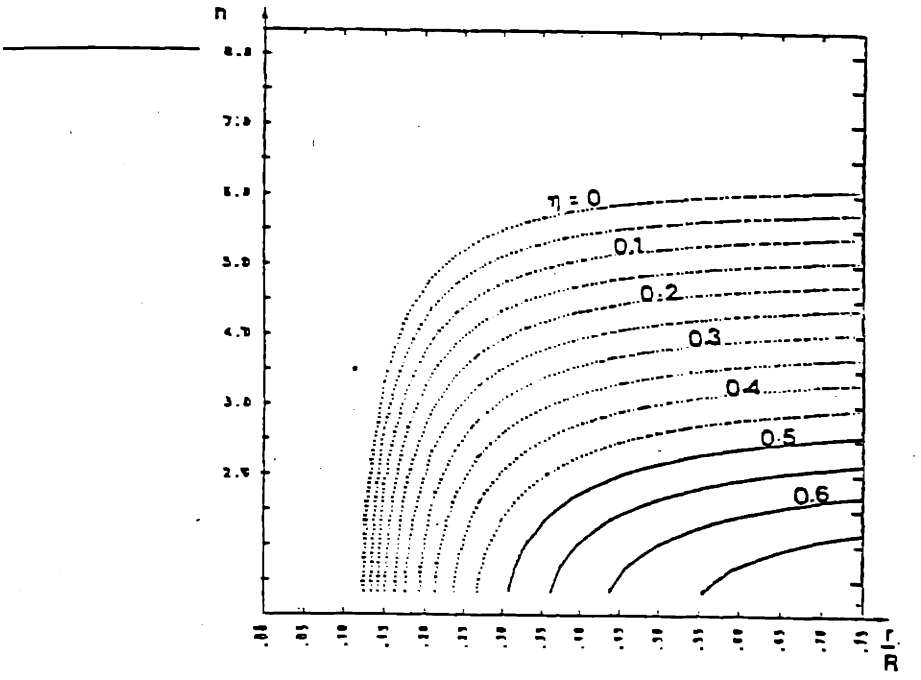

Figure 4.23 The parameter $\eta = \frac{a_p}{b_c}$ is a measure of the relative distance from the center of the coil to the radius where the ripple is 2%. The number of coils is $N = 60$.

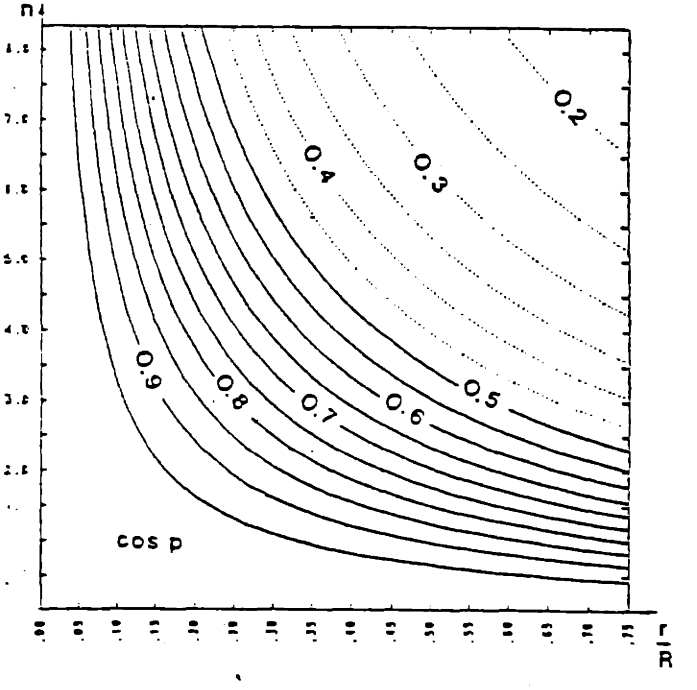

Figure 4.24 The value of cos p relates the actual size of the plasma to its size in the plane of the coils.

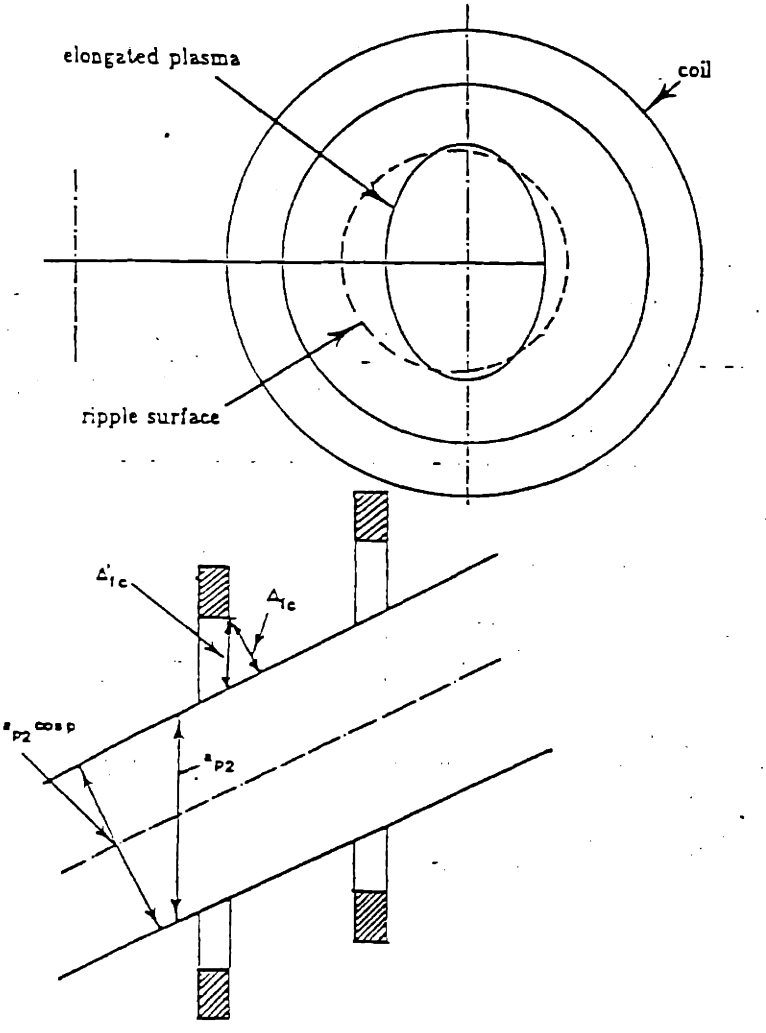

Figure 4.25 For a highly elongated plasma the limit may become the ripple at top and bottom. The fact that the coils are not perpendicular to the magnetic axis then also starts to play a role in calculating the distance (in the plane of the coils) one has to stay away from the coil.

A third effect can arise when the plasma is highly elongated. In this case the limit may not be set by the ripple on the outside, but at the top and the bottom (Fig. 4.25). One should also notice that in this case, the fact that the coils are not perpendicular to the magnetic axis also starts to play an effect in calculating the distance one has to stay away from the coils. With $\xi = \frac{\Delta_{fc}}{\Delta_{fc}}$ we have in fact to take $\Delta_{fcl} = \frac{\Delta_{fc}}{\cos p}$ if Δ_{fcl} is measured in the plane of the coils.

Trade-off between magnetic field and plasma size

Having briefly discussed in the first part of this section (and more at length in Appendix E) how the magnetic field changes as we change δ, the relative bore of the coils, and in the second part what factors affect the plasma size when δ changes we can now ask the question what effect this change has on our previous geometrical constraint (where we had taken $\delta = constant$) and how this affect the choice of the number of periods n and displacement of the coil $\frac{r_f}{R}$.

A computer model was set up that incorporates the variation with δ of $\frac{B}{R}$, and of the plasma size. The variation of $\frac{B}{R}$ with δ is included, as explained in Appendix E. To calculate the plasma size we take into account the ripple and the $\cos p$ effect. The effect of the elongation on the plasma size was not incorporated, since in order to know what the elongation is, we would need first to obtain puncture plots, and this would defeat the purpose of obtaining some tendencies in the larger parameter space without a prohibitively large numerical load. The resulting model is of course crude, but it will still give us some clear indication as to the choice of n and $\frac{r_f}{R}$.

The model was used to find for each combination of n and $\frac{r_f}{R}$ the value of δ that would optimize some criterion. Recall that increasing δ increases the plasma size but decreases $\frac{B}{R}$. We have looked at several possibilities, optimizing aB^2, aB or a^2B. The optimum choice for δ depend on what we optimize. But we found, interestingly enough, that for the optimum choice of δ, the area in the n, $\frac{r_f}{R}$ parameter space where aB^2, aB or a^2B was maximum, did not depend on whether we optimized aB^2, aB or a^2B.

To illustrate our model we refer to Figure 4.26. For the particular case of $n = 2$ and $\frac{r_f}{R} = 0.39$ we have plotted $\frac{B}{R}$ and $\frac{a_p}{R}$ as a function of δ. Recall that the variation is in fact on $\frac{B}{JR}$. We have assumed $J = 2kA/cm^2$ in the drawing, but scaling with J is straightforward. The figure shows clearly that when δ increases, the allowable value of $\frac{B}{R}$ decreases, while as δ increases, the plasma radius increases. The solid line gives the value of aB^2 and shows the presence of an optimum at $\delta = 0.45$. Finding this value of δ that optimize a^2B can be done for each n, and $\frac{r_f}{R}$ so that for each combination of n and $\frac{r_f}{R}$ we can identify an optimum δ, as well as a corresponding value of a^2B.

We show in Figure 4.27 for the case $n = 2$ and $n = 3$ how this optimum δ varies as a function of $\frac{r_f}{R}$. In the same plot is shown the value of $\frac{B}{R}$, the value of $\frac{a_p}{R}$ and the value of $\frac{a_p B^2}{R^3}$.

We see that aB^2 has a rather broad optimum around $\frac{r_f}{R} = 0.4$. If we were to have optimized aB or a^2B, rather than aB^2, the optimum value for δ would change resulting in different values for $\frac{B}{R}$ and $\frac{a_p}{R}$, but the actual position of the maximum of aB or a^2B for given n as a function of $\frac{r_f}{R}$ does not change much.

Similarly we obtain for $n = 3$ a broad maximum, independent again of whether we optimize aB^2, aB, or a^2B. It lies at slightly lower values of $\frac{r_f}{R}$, in the range $0.33 < \frac{r_f}{R} < 0.42$. It is however important to note that the values of the maxima for $n = 3$ is consistently about a factor 2 lower than the maxima for $n = 2$.

In terms of trade-off between plasma size and the constraint on $\frac{B}{R}$ we can conclude from this model that there is a region in n, $\frac{r_f}{R}$ space where the constraints on $\frac{B}{R}$ are the least stringent. In the case we optimize aB^2 the constraint on $\frac{B}{R}$, for the optimum choice is shown in Figure 4.28. Note that for low n the value of $\frac{B}{R}$ is larger in Fig. 4.28 than in Fig. 4.12. This is because the optimum δ is lower than 0.5 (which was assumed in Fig. 4.12). For large n the opposite is true ($\frac{B}{R}$ larger in Fig. 4.12), because the optimum δ is larger than 0.5. Had we optimized aB, the actual value of $\frac{B}{R}$ in Figure 4.28 would change. The shape of the curve however not. The constraints on $\frac{B}{R}$ would still be the least stringent

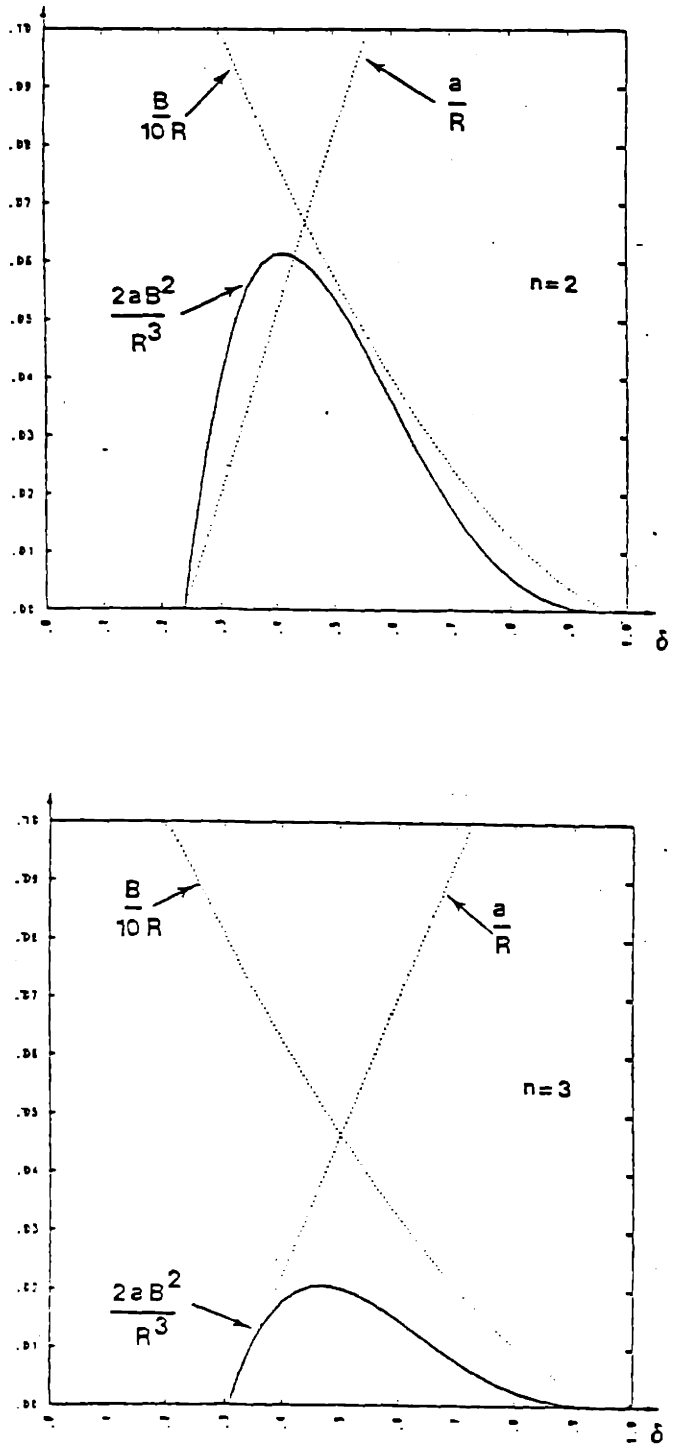

Figure 4.26 Variation of the plasma size $\frac{a_p}{R}$ and of $\frac{B}{R}$ with the relative bore of the coil $\delta = \frac{b_c}{r_c}$. Assumed $J_C = J_R = 2 \times 10^7 A/m^2$, $N = 60$ and $\xi = 2$.

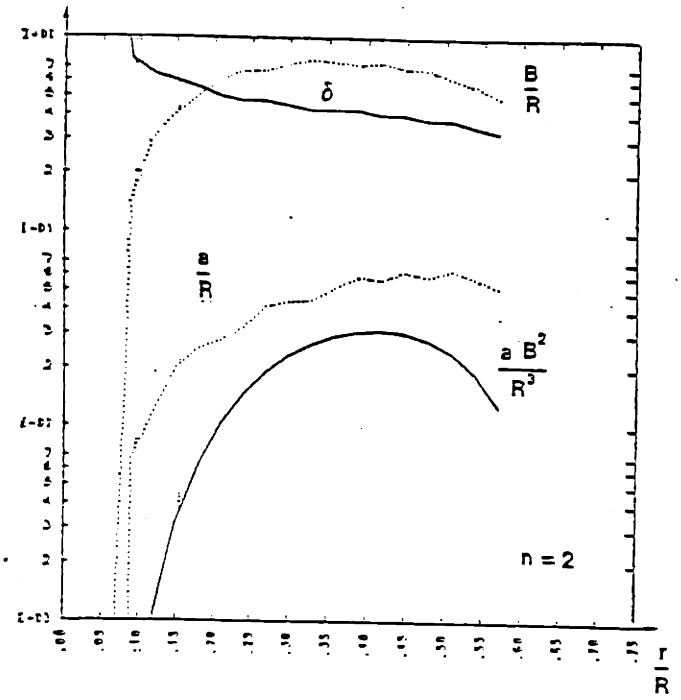

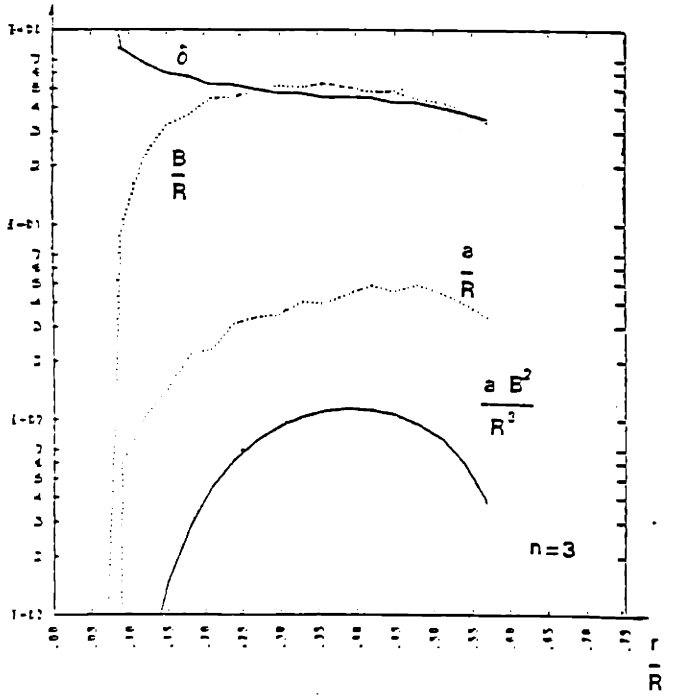

Figure 4.27 Variation of δ, $\frac{c}{R}$, $\frac{B}{R}$ and $\frac{aB^2}{R^3}$ with $\frac{r}{R}$ for $n = 2$ and $n = 3$.

for $n = 2$, $\frac{r_c}{R} \simeq 0.4$. Our model thus points to a choice of $n = 2$ and $\frac{r_c}{R} \simeq 0.4$. This choice would also be acceptable in terms of the first constraint, related to the avoidance of the region where the major radius curvature may start to dominate. This is shown in Figure 4.29.

Our model says that the constraints on $\frac{B}{R}$ are the least stringent in a certain region of the parameter space. In order to obtain the actual value of the constraint on $\frac{B}{R}$, and also in order to take into account some other constraints, we will resort now to more detailed numerical calculations. The computer code that makes the puncture plots and calculates parameters associated with the magnetic geometry was kindly provided by P.A. Politzer.

Numerical calculations

We report here the more detailed calculations in two cases. This will allow us to calculate the actual $\frac{B}{R}$ constraint, compare the results with our model and confirm the fact that the constraints on $\frac{B}{R}$ are the least stringent for $n = 2$, $\frac{r_c}{R} \simeq 0.4$. The two cases are one with $n = 2$ and $\frac{r_c}{R} = 0.38$ and one with $n = 3$ and $\frac{r_c}{R} = 0.33$.

In order to compare the numerical calculations with our model we also have to fix values of the ring current and the vertical field for the numerical calculations. Our simple model implicitly assumes $r_a = r_c$, $R_a = R_R$ and $\alpha_R = 0$, and we had taken for the ring current the value given by the approximate formula derived in Appendix D. The combination $r_a = r_c$, $R_a = R_R$ and $\alpha_R = 0$ is not achievable in practice. For our numerical calculations we have chosen, using the more refined model of appendix D, the current such that $r_a \simeq r_c$, and the vertical field such that $\alpha_R = 0$. We will then have that $R_a > R_R$, and the current I_R is slightly lower than the design value calculated from the approximate formula. The choice is shown in Figure 4.30.

For the fixed position of the coil, coil current and vertical field, we investigated how the area of good magnetic surfaces changed when the bore of the coil was

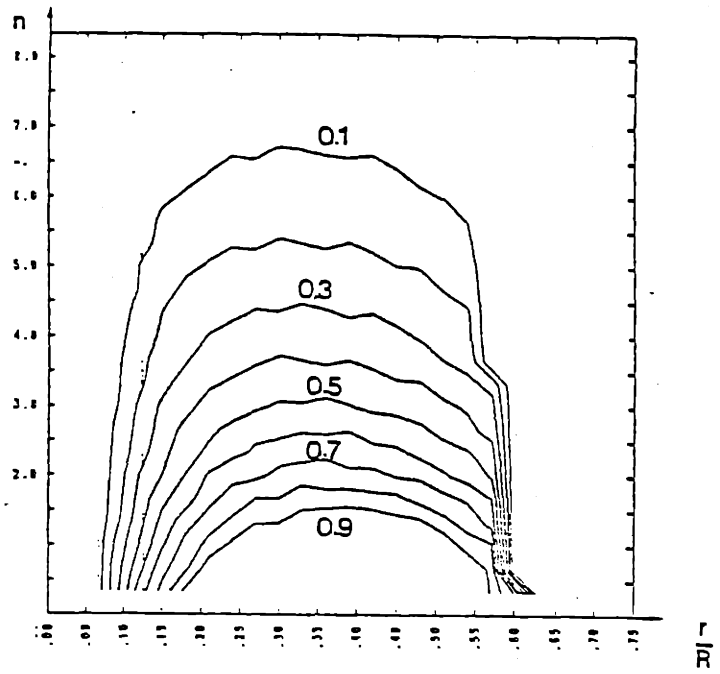

Figure 4.28. Values of $\frac{B}{R}$, when we allow δ to vary. The choice of δ is such that for each n, $\frac{r_f}{R}$, the value of aB^2 is maximized.

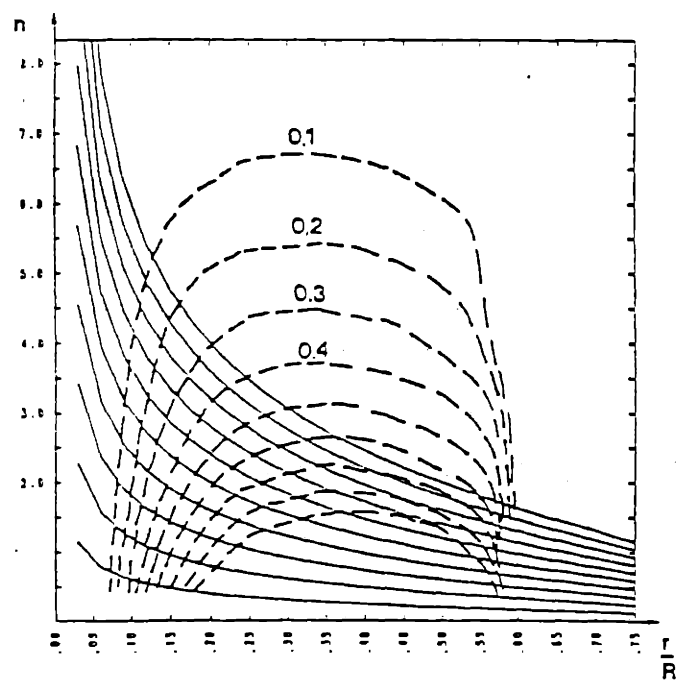

Figure 4.29. Constraints related to the behavior of the magnetic axis, and constraints on $\frac{B}{R}$

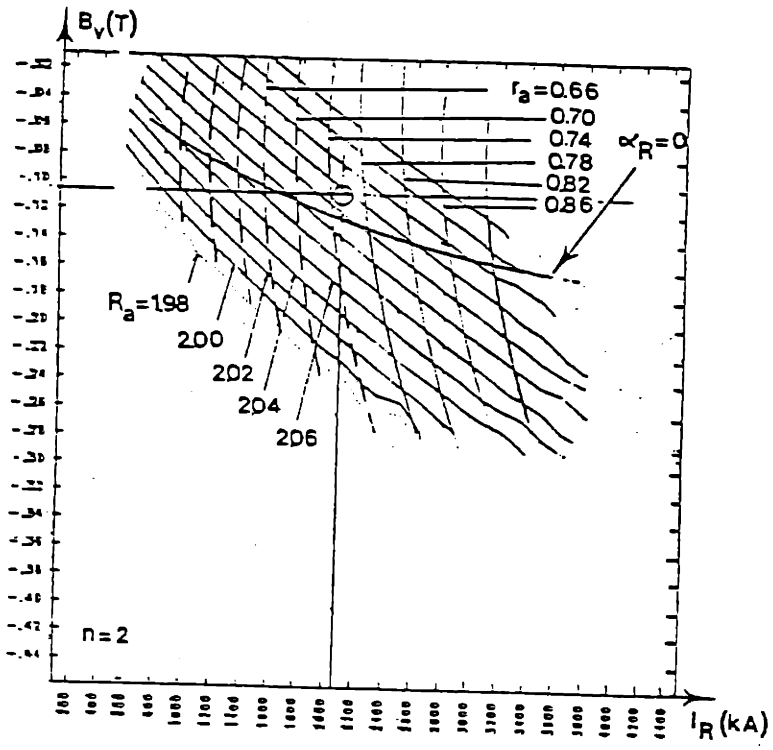

Figure 4.30 Choice of ring current I_R and vertical field B_v for $n = 2$, $\frac{r_c}{R} = 0.33$.

changed, and we calculated, using the method outlined in Appendix F, what values of $\frac{B}{R}$ could be achieved. Results are shown in Figure 4.31, for $n = 2$ and $\frac{r_c}{R} = 0.38$. Our model predicted lower values of $\frac{B}{R}$ and larger values of c_p. The reason for the higher values of $\frac{B}{R}$ is a result of the fact that for the numerical results we used a ring current of 2100 kA, lower than the ring current our approximate formula would give for $r_a = r_c$ (2680kA). Thus as the ring, dimensioned for this smaller current can be smaller, more room is available for the height of the coils for a given bore, resulting in a larger achievable $\frac{B}{R}$. The reason for the smaller size for c_p is that for our choice of B_v and I_R the plasma is slightly shifted outward ($R_a > R_R$), and not centered as assumed in our model, thus leaving less space for well formed surfaces. The agreement between the slope confirms the validity of our method to approximate the plasma size.

We have also seen that although the optimum value of δ predicted by our model depends on what was optimized, the region in n, $\frac{r_c}{R}$ space where we obtained

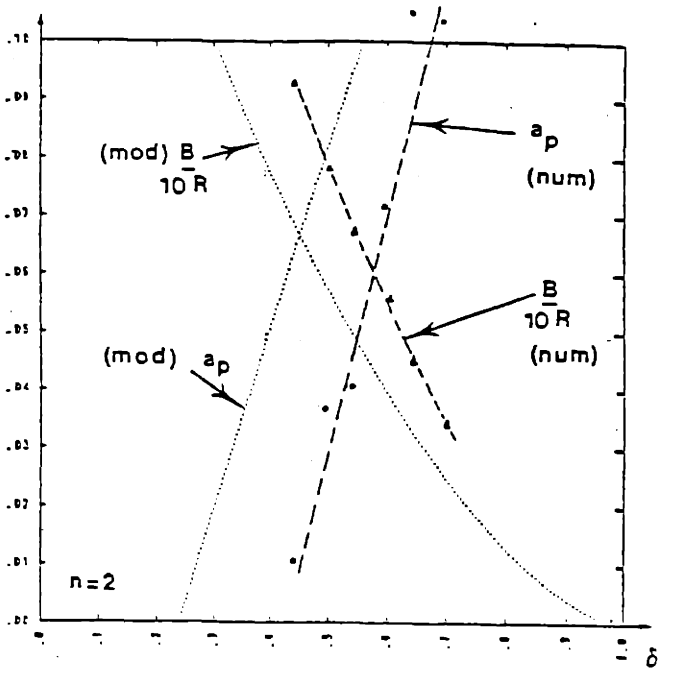

Figure 4.31 Value of $\frac{B}{R}$ and a_p from the simple model and from numerical calculations ($n = 2$, $\frac{r_c}{R} = 0.39$)

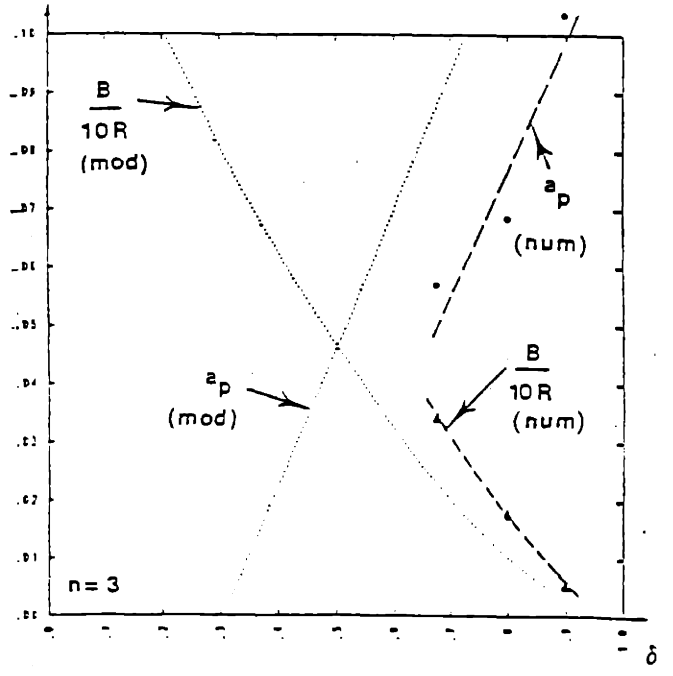

Figure 4.32 Value of $\frac{B}{R}$ and a_p from the simple model and from numerical calculations ($n = 3$, $\frac{r_c}{R} = 0.33$)

a maximum was insensitive to it. We can thus be reasonably confident that the model identifies properly the optimum region in the n versus $\frac{r}{R}$ space. We observe a similar agreement for $n = 3$ and $\frac{r}{R} = 0.33$ (Fig. 4.32). The detailed numerical calculations also confirmed that achievable values of aB^2 for example are lower for the $n = 3$ case than for the $n = 2$ case.

The underlying reasons for this advantage are : at the same value of $\frac{r_c}{R}$ the design current is smaller for lower n going as $n\left(\frac{r_c}{R}\right)^2$ giving thus a smaller cross section for the ring and thus more room for the height of the coils and a larger allowable $\frac{B}{JR}$. The length of the magnetic axis is also smaller ($l_a \sim 2\pi R\sqrt{1+\left(\frac{nr_c}{R}\right)^2}$) resulting in a larger B for the same current in the toroidal coils. For a fixed number of coils, and fixed major radius of the ring (R_R), the ripple is smaller for lower n, while the $\cos p$ term is larger ; those two effects allow a larger plasma radius. While at higher n values one would rather go to lower $\frac{r_c}{R}$ values, this also decreases the radius of the coils and thus the space for the plasma. The numerical calculations and our understanding of the underlying reasons make us confident that $n = 2$ and $\frac{r_c}{R} = 0.38$ would be a good choice for the geometry. Other considerations, to be discussed in the next section, will finalize the choice of δ and further confirm that the choice $n = 2$, $\frac{r}{R} = 0.38$ is also a good one on other grounds.

The final choice of $\delta = \frac{b_c}{r_c}$ and resulting constraint on $\frac{B}{JR}$ will be obtained from the numerical calculations from considerations related to well depth. This will be discussed now.

3.4.4. Constraints for the geometry resulting from MHD considerations

MHD equilibrium and stability is addressed here briefly, only in terms of its impact on the choice of the geometry. It will be addressed later in more detail to make a choice for the value of the dimensionless parameter β.

The numerical calculations provided information on the well depth. Strangely enough it was found that, for everything fixed, except the bore of the coil, the well depth measured at constant radius would decrease and even disappear as the

bore of the coil decreased. This effect was traced back to the fact that changing the bore of the coil has a slight effect on the position of the magnetic axis. Decreasing the bore of the coil decreases r_a and increases R_a. This results in a decrease in well depth. If we want to keep some well depth for the cases we have considered, the minimum δ for $n = 2$ and $\frac{r_c}{R} = 0.39$ is $\delta = 0.6$ corresponding to $\frac{a_p}{R} = 0.105$ and $\frac{B}{R} = 0.45$. For the case $n = 3$ and $\frac{r_c}{R} = 0.33$, the minimum is $\delta = 0.9$, corresponding to $\frac{a_p}{R} = 0.105$ and $\frac{B}{R} = 0.05$.

The situation for the well depth can be improved by taking $\alpha_c \neq 0$ or by reducing the design value of the ring current. Both measures reduce the flexibility of the machine, but still leave the advantage of the $n = 2$ system over the $n = 3$ system.

MHD equilibrium is discussed later in more detail. By limiting the pressure driven displacement of the plasma to some fraction of the bore of the coil, a value of β equilibrium can be found. It is function of n and $\frac{r_c}{R}$ and for each n, maximum for $\frac{r_c}{R} \simeq \frac{1}{n}$. The maximum value decreases with decreasing n. Shown in Figure 4.33 is the region where β equilibrium is maximum, as well as its actual value. In this respect a choice of large n would be best if we wanted to achieve the highest possible β. If the purpose however is to test theoretically predicted β limits, then a low value of β is not a disadvantage.

In view of our approach to choose the geometry such that the geometrical constraint is the least stringent, while still being able to test the theory, the choice $n = 2$ and $\frac{r}{R} = 0.38$ is acceptable.

3.4.5. Constraints on the geometry resulting from transport considerations

Transport in a helical axis stellarator is discussed later in more detail. Here we want to address specifically the influence of the geometry on the easiness of achieving low ν_* values. The collisionality is the ratio of the connection length to the mean free path. The connection length is related to the geometry, while the mean free path is related to the plasma parameters. Can we, through

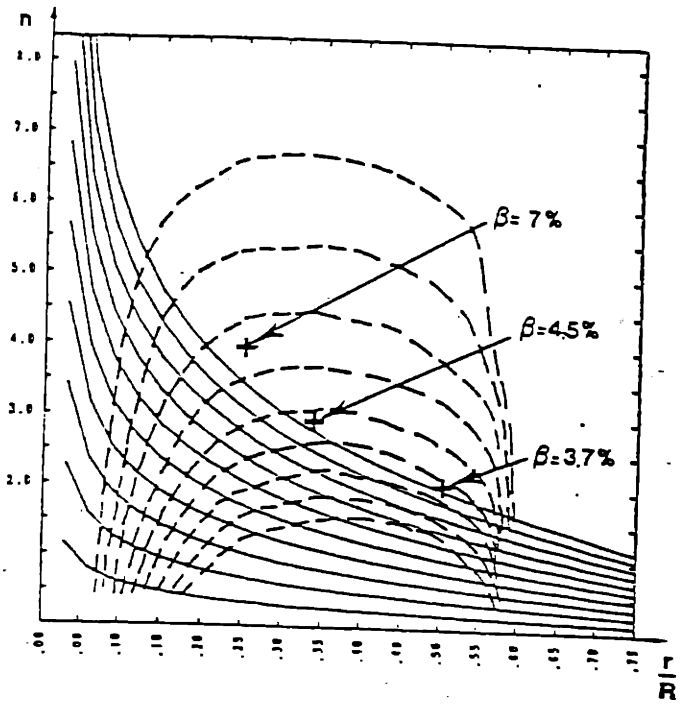

Figure 4.33 Region where β equilibrium is maximum

appropriate choices for the geometry, make it easier to obtain lower values of the collisionality ? In essence we are asking, can we, for fixed values of the plasma parameters, make the achievement of low collisionality easier by influencing the connection length.

As n and $\frac{r_p}{R}$ change, the connection length changes. The connection length is given by $\frac{1}{\kappa}$.where κ is the torsion. To first approximation we have used for the torsion the value for a straight helix. This is justified by the following argument: what matters in the end is an average over many periods. The integral of the torsion is the rotational transform and cross check with numerical calculations have shown that as long as we avoid the region where the major radius curvature starts to dominate, the rotational transform (calculated from the integral of the torsion of the magnetic axis) agrees within 20% with the numerical calculations. The integral of the torsion was also found to be little influenced by the actual winding law of the magnetic axis therefore we checked whether using the value for a straight system would be appropriate, and found that this was indeed the case.

Intuitively, it is clear that for a fixed size, the connection length decreases as $\frac{r_t}{R}$ decreases, and as the number of periods increases. This is shown in Figure 4.34, where we have plotted the value of the connection length (in arbitrary units, we are only interested in the relative measures). In order to get the smallest connection length, for fixed plasma parameters, one should go to high n number and low $\frac{r}{R}$. In this drawing we have assumed fixed overall size ($R_R = constant$). If, however, we compare machines of constant magnetic field we have to increase the size when we go to higher n (because of lower value of $\frac{B}{R}$ for higher n). This increases the absolute connection length for larger n machines. Taking this effect into account we obtain Figure 4.35, showing again, in arbitrary units, the connection length, now for constant B field. This drawing confirms that the choice $n = 2$, $\frac{r}{R} = 0.38$ is also, with respect to achieving easily a low collisionality, an appropriate choice.

3.4.6. Summarizing the section on the geometry

In the previous section we had introduced and defined the major parameters associated with the magnetic geometry of a stellarator with helical magnetic axis. We had divided the parameters as "hard" and "soft", and explained how we would go about finalizing the geometry and obtaining the geometrical constraints.

In this section we have discussed the choice of the hard parameters based on constraints associated with the magnetic axis, constraints related to the interference of the coils, and plasma dimensions. It was found that going to lower n and high value of $\frac{r_t}{R}$ would give an optimum choice, within the constraints. Further we have briefly discussed the choice of the geometry in terms of MHD equilibrium and stability. We have also shown how the geometry can influence the easiness with which one achieves low collisionality.

The intent of this section was to analyze and finalize the geometry of the experiment within a scale factor on size and magnetic field, and also to obtain the geometrical constraints. We succeeded in finalizing the geometry and have

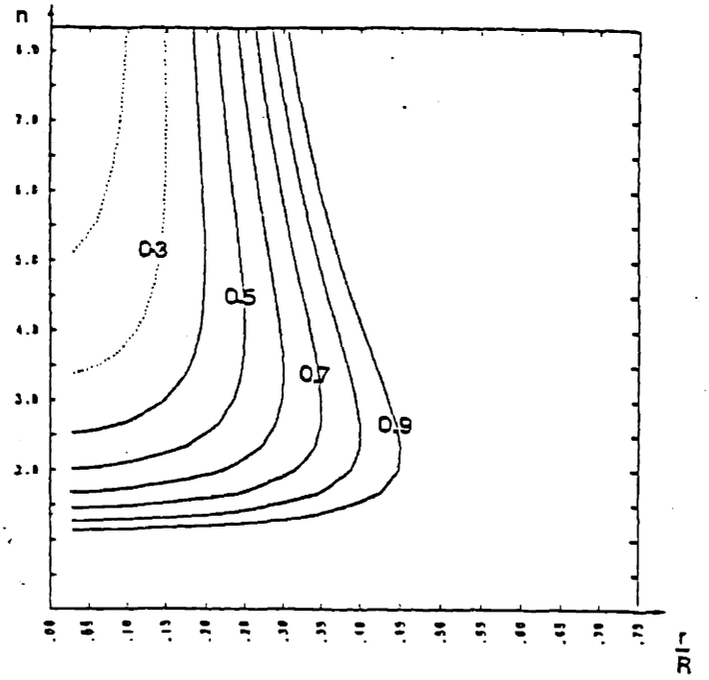

Figure 4.34 Measure of the connection length (in arbitrary units) as a function of n and $\frac{r}{R}$, for constant machine size.

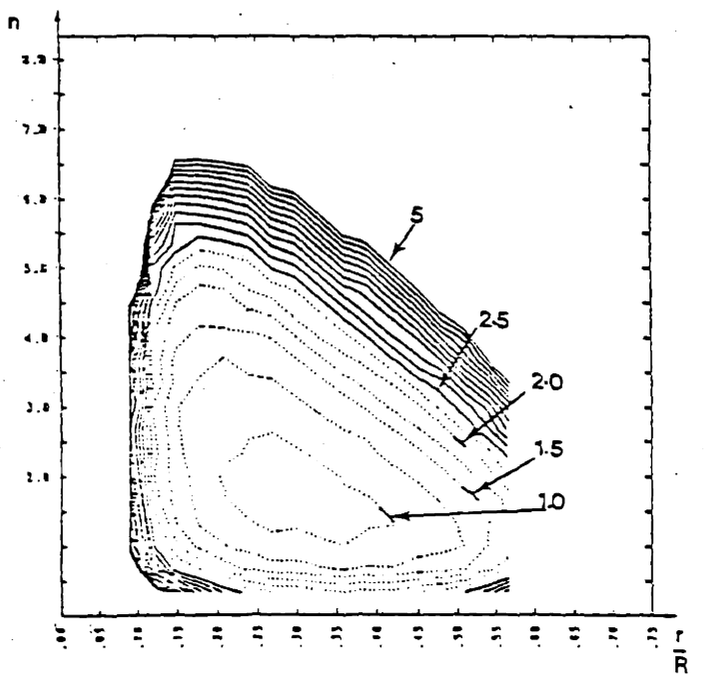

Figure 4.35 Measure of the connection length (in arbitrary units) as a function of n and $\frac{r}{R}$, for constant magnetic field. We have taken into account the fact that as n and $\frac{r}{R}$ increases the allowable $\frac{B}{R}$ decreases, thus resulting in the need to increase R for constant magnetic field.

chosen and justified the following parameters for the geometry : $n = 2$, $\frac{r_f}{R} = 0.39$, $\frac{b_f}{R} = 0.255$, $N = 60$. The value of other parameters can be calculated from this, and we obtain : $\frac{r_n}{R} = 0.08$, $\frac{h_f}{R} = 0.055$, $\frac{w_f}{R} = 0.0314$.

The other result from this section is the geometrical constraint: the magnetic field and the dimension cannot be chosen completely independently. They have, for our particular geometry, to fulfill the condition

$$\frac{(\frac{B}{1T})}{(\frac{J}{2\times 10^7 A/m^2})(\frac{R}{m})} \leq 0.45.$$

Note that a constraint on $\frac{B}{JR}$ is not particular to this geometry. The value of 0.45 however, is. Toroidal system that are limited by space constraints in the center (as for example tokamaks), will have a similar constraint. The value will depend on the particular choices made for the geometry, and especially on the slimness of the coil, but not on the scale of the machine.

Indeed, take I the total Ampere-turns, and let it be equal to Jp^2, where p^2 is a measure of the area occupied by the coils in the center. Then using $\int Bdl = \mu_o I$ we can calculate

$$\frac{B}{JR} = \frac{\mu_o}{2\pi}\left(\frac{p}{R}\right)^2$$

independent of the scale of the machine, but dependent on the square of the fraction of the major radius used to carry current. What is the value of $\frac{B}{JR}$ for some machines ? Alcator A has $B = 10T$, $R = 0.54m$, $J = 10.2 \times 10^7 A/m^2$, and this results in

$$\frac{(\frac{B}{1T})}{\left(\frac{J}{2\times 10^7 A/m^2}\right)\left(\frac{R}{m}\right)} = 3.63.$$

Alcator C with $B = 14T$, $R = 0.64m$, $J = 11.8 \times 10^7 A/m^2$ achieves

$$\frac{\left(\frac{B}{1T}\right)}{\left(\frac{J}{2\times 10^7 A/m^2}\right)\left(\frac{R}{m}\right)} = 3.9.$$

JET, with $B = 2.7T$, $R = 3.05m$, $J = 2 \times 10^7 A/m^2$ obtains

$$\frac{\left(\frac{B}{1T}\right)}{\left(\frac{J}{2\times 10^7 A/m^2}\right)\left(\frac{R}{m}\right)} = 0.88.$$

As pointed out, the reason for this smaller value is not that JET is much larger than the Alcator machines, but because its coils are much slimmer than the Alcator coils.

Let us now investigate in more detail the choice of the dimensionless parameters.

3.5. Choice of the dimensionless parameters

3.5.1. Introduction

This section focuses on the choice of the dimensionless parameters β and ν. We will discuss transport, and the different regimes that occur in this type of machine. From this we obtain a range of values of ν that we would like to investigate.
Similarly, MHD equilibrium and stability is reviewed to identify the possible β limits and be able to make a choice of β.

3.5.2. Transport and choice of ν

This section on transport is needed to identify the different regimes that occur in a stellarator with helical magnetic axis. It is also needed later as a basis to estimate the heating power required for a given experiment.

Different transport regimes occur because, at different degrees of collisionality, the ratio of the mean free path of particles between collisions to the length of magnetic field inhomogeneities can take different values. In a tokamak, the variation of the magnetic field along the field lines arises to first order because of the rotational transform and the $\frac{1}{R}$ variation of the toroidal B field. The inverse aspect ratio $\epsilon = \frac{r}{R}$ is a measure of the inhomogeneity while the connection

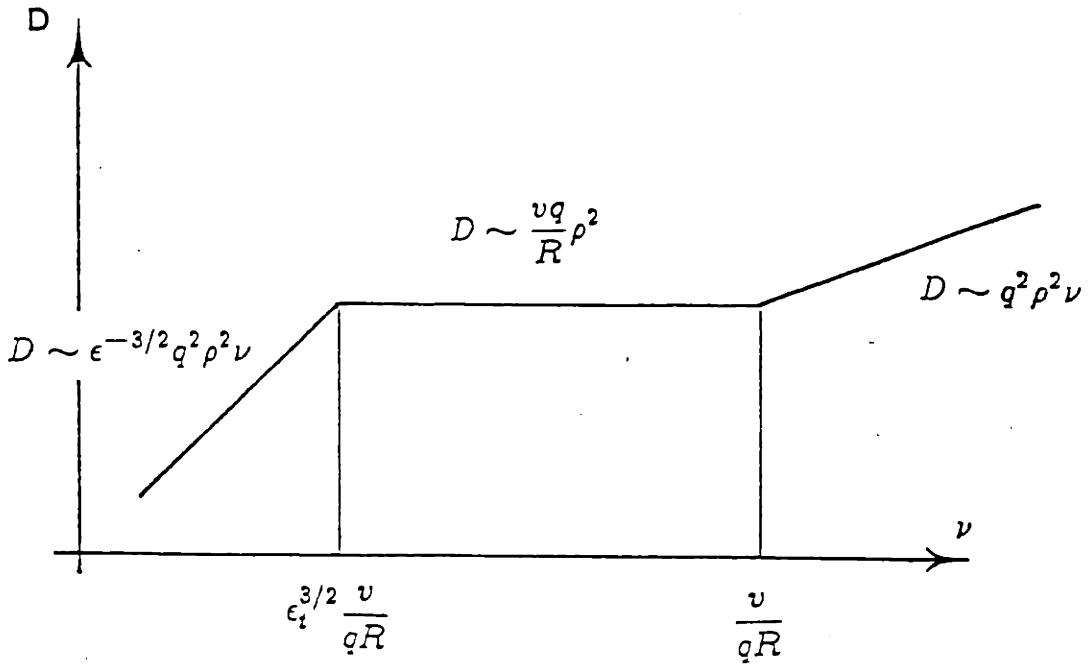

Figure 4.36 Tokamak neo-classical transport regimes

length is proportional to qR. The resulting transport regimes are the well known Galeev-Sagdeev regime, the plateau regime and Pfirsch-Schluter regime (Fig. 4.36).

To apply the same approach to a stellarator with helical magnetic axis let us first assume a straight helical solenoid. Even in a straight system the particles can be trapped in inhomogeneities of the magnetic field. Due to the rotational transform (the magnetic field lines lag with respect to the rotation of the normal to the magnetic axis) the magnetic field lines sample regions of high and low magnetic field. For a straight helical solenoid, the magnetic field on the magnetic axis is constant. The magnetic field away from the magnetic axis is modulated by a term $kr\cos\theta$ (similar to the term $\frac{r}{R}\cos\theta$ for the field modulation along a field line in a tokamak).

In this case the helical inhomogeneity takes the role of the toroidal inhomogeneity in a tokamak and one would expect intuitively that in the formulas for the different regions of tokamak transport, ϵ would be replaced by kr. Similarly

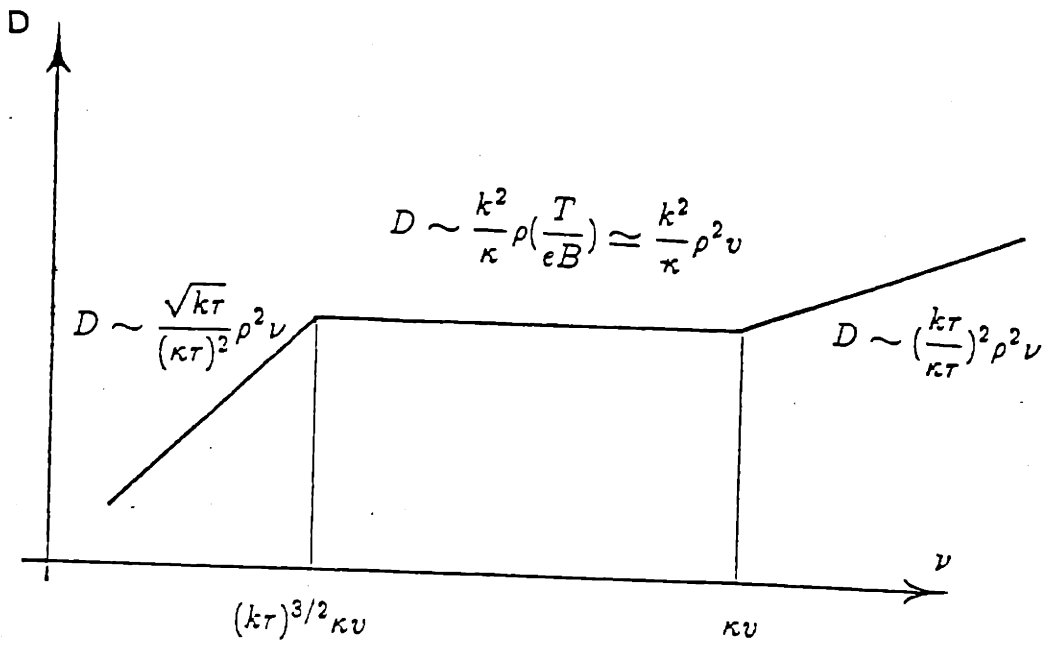

Figure 4.37 Neoclassical transport regimes for a straight helical axis stellarator

the role of the connection length qR in a tokamak is now replaced by $\frac{1}{\kappa}$. The transformation of the neoclassical formulas for a tokamak was obtained in a more rigorous fashion by Kalyuzhnyj and Nemov [123] for a straight helical system and for distances close to the magnetic axis ($k\tau \ll 1$, $\kappa\tau \ll 1$)

$$\epsilon \rightarrow k\tau$$

$$\frac{r}{qR} \rightarrow \kappa\tau$$

We thus obtain the same three regimes (Fig. 4.37). Those regimes are strictly valid only for a straight helical system.

The equivalence (in terms of drift orbits and transport) of a tokamak and a system having a helical symmetry, was proven in a much more general fashion (without the restriction $k\tau \ll 1$ and $\kappa\tau \ll 1$) by Boozer [124, 125]. Equilibria which have identical drift orbits and associated transport, are called by him isomorphic. He proves that all system with one periodicity (including the tokamak and straight helical systems) are isomorphic, and that their transport coefficient can be written in a general way.

If we now turn the system into a torus but still want to minimize the toroidal effects we need that the toroidal inhomogeneity must be much smaller than the helical inhomogeneity. If the displacement of the banana due to toroidal drift, during a trapped collision time, is much smaller than the banana thickness, then the toroidal inhomogeneity can be completely neglected. This requires [123]

$$\nu > \frac{r}{R}\kappa v_{th}\sqrt{kr} \tag{4.20}$$

$$\left(\frac{n}{m}\right)^2 \gg \frac{R}{r_a} \tag{4.21}$$

Under those conditions, the diffusion coefficient obtained for a straight helical system are also valid for a torus. Note however that the conditions are quite restrictive, and not valid on the magnetic axis.

If we now are in a regime where the drift of the bananas do start to play a role we have something analogous to the ripple diffusion and helical plateau of a stellarator. This was discussed by Nemov [126] and Kalyuzhnyj [127]. Turning a straight helical system into a torus has two important effects.

1/ The curvature and the torsion of the magnetic axis become modulated. For a low toroidality system $\left((\frac{n}{m})^2 \gg \frac{R}{r_c}\right)$ and constant $\frac{d\phi}{d\theta}$ the curvature and torsion are described by [126]

$$k = k_o + \mu k_1 \cos\theta$$

$$\kappa = \kappa_o + \mu \kappa_1 \cos\theta$$

where k_0, κ_o are the curvature and torsion for a straight system, and μ is the small parameter $\frac{R_c}{r_c}(\frac{m}{n})^2 \ll 1$. Further

$$k_o = \frac{\frac{1}{r_c}(\frac{nr_c}{mR_c})^2}{1+(\frac{nr_c}{mR_c})^2} \qquad \text{and} \qquad k_1 = k_o\frac{(\frac{nr_c}{mR_c})^2-1}{(\frac{nr_c}{mR_c})^2+1}$$

$$\kappa_o = \frac{\frac{1}{r_c}(\frac{nr_c}{mR_c})}{1+(\frac{nr_c}{mR_c})^2} \qquad \text{and} \qquad \kappa_1 = \kappa_o\frac{1+5(\frac{nr_c}{mR_c})^2+2(\frac{nr_c}{mR_c})^4}{1+(\frac{nr_c}{mR_c})^2}$$

2/ The second effect is that, even on the magnetic axis, there is a modulation of the magnetic field. Only the first effect was considered in those articles.

This facilitates theoretical treatment, but can also be achieved in practice by choosing appropriately the current in the toroidal coils. Coils on the inside of the torus would carry less current than those on the outside.

The ripple diffusion coefficient is then formally derivable from that of a toroidal stellarator by replacing $\epsilon_t \rightarrow \frac{r}{R}$ and $\epsilon_h \rightarrow k_o r$ and by multiplying the diffusion coefficient by a factor λ_c dependent on $\frac{nr_c}{mR}$. The factor λ_c can be found in [126].

Modulation of the angle of the magnetic axis in order to reduce the diffusion coefficient was also discussed by Kalyuzhnyj [127]. There is an optimal modulation of the magnetic axis given by $\theta = l\phi + d\frac{r}{R}\sin l\phi$ and $d = 3$, which reduces the diffusion coefficient by about 70% compared to the value for an unmodulated magnetic axis. He further shows that the value of $\frac{nr_c}{mR_c}$ close to unity is the worst choice with respect to diffusion because the diffusion coefficient is maximum at about this value (note that $\frac{n}{m}\frac{r_c}{R_c} = 1$ may be an optimum choice for MHD equilibrium).

Defining ν_* such that $\nu_* = 1$ at the transition from banana to plateau regime, we have that, for our geometry, the transition between plateau and P.S. regime occurs at $\nu_* = 100$. The requirement that the influence of toroidal effects can be neglected (4.20) translates into $\nu_* > 1$. If we thus want to investigate the theory, while not being influenced by the toroidal effects, we need $\nu_* > 1$. This puts us in the plateau regime. A maximum on ν_*, in order to stay in the same regime is $\nu_* = 100$. Note that this is higher than for a reactor, where $\nu_* \simeq 0.1$. A reactor, because of the higher number of periods, will not be influenced by toroidal inhomogeneity, even at this low value of ν_*. The actual choice of ν_* for the experiment, within the limits $1 < \nu_* < 100$, will be made later.

3.5.3. MHD equilibrium and stability, value of β

The equilibrium of a plasma in a toroidal magnetic field with non-planar axis has been treated by Shafranov [128, 129] and by Nagao et al [121, 130, 131]. The methodology adopted is to calculate the displacement of the magnetic axis resulting from the plasma pressure. The displacement has in general two

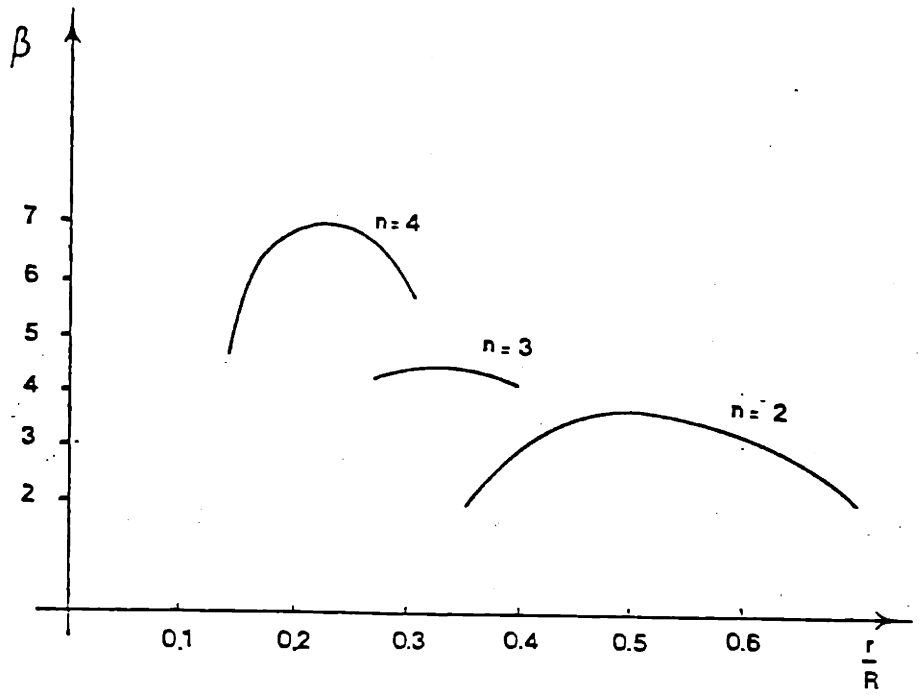

Figure 4.38 Values of β equilibrium as a function of n and $\frac{r_c}{R_o}$.

components, one along the normal (in the direction opposite to it) and one along the binormal. The value of β equilibrium is limited by requesting that the maximum displacement should not exceed a certain fraction of the bore of the coil. For a small number of periods, the displacement is minimum (and thus β equilibrium maximum) when $\frac{nr_c}{mR_o} = 1$. The actual values are shown in Figure 4.38 (adapted from [130]).

Zakharov [132] has addressed the question of stability of a plasma in stellarator with spatial magnetic axis. For a plasma without current, the stability against $m = 1$, $n = 0$ is guaranteed. For a low degree of shear, the plasma is weakly unstable against helical perturbations with $m \neq 0$ and $n \neq 0$ if the surfaces are circular. A D-shaped configuration of the magnetic surfaces can avoid this instability. Mond and Weitzner [133] have found that low shear systems with zero net current can be stable to interchange-like modes. They have also shown that for stability to be achieved, one needs

$$\alpha > \frac{\delta^2}{2(1-\delta^2)} \tag{4.22}$$

where δ is the amplitude of the helical magnetic field associated with the $l = 2$ harmonic

$$\psi = k[\frac{1}{2}r^2(1 + \delta\cos 2\phi) + ...]$$

and α is a measure of the pressure gradient. For a given helical magnetic field δ the system may be unstable when the pressure is slowly increased from zero until the pressure is large enough to fulfill the condition (4.22). A weak magnetic well would be sufficient to stabilize this mode until the pressure terms achieve the stabilizing effects. The increase in stability at higher plasma pressures was already mentioned earlier in [134, 135] and is a result of the deepening of the magnetic well because of the displacement of the magnetic surfaces under the influence of the plasma pressure.

As a summary of this section we can say that in the system we have chosen, the plasma should be in equilibrium for β values up to about 3%, while the presence of a slight magnetic well is sufficient to make it stable, a stability which is further improved by the presence of the plasma. The region of β we may want to investigate, is thus limited to $\beta < 3\%$.

3.6. Application of the constraints

3.6.1. The four dimensionless parameters

Let us now go step by step through the constraints. We have chosen, as discussed in Chapter 2, to take R and B as scaling variables. The dimensionless parameters were β, ν, N_λ and $\frac{\rho_t}{a}$ of which we will have to drop two in order to be able indeed to take R and B as scaling variables. Let us calculate of the dimensionless parameters.

The number of particles per Debye sphere is given by

$$N_\lambda = \frac{1.73 \times 10^2 (\frac{T}{e})^{3/2}}{(\frac{n}{10^{20}})^{1/2}} \qquad (4.23)$$

and the ratio of poloidal larmor radius to the size of the plasma radius is

$$\begin{aligned}\frac{\rho_\theta}{a} &= \frac{\rho}{\kappa\tau a_p} = \frac{\rho}{\kappa\frac{a_p}{2}a_p} = \frac{\rho 140}{R} \\ &= \frac{0.0144}{R}\sqrt{\frac{T}{e}}\frac{1}{B}\end{aligned} \tag{4.24}$$

The plasma β is given by

$$\beta = \frac{2nT}{\frac{B^2}{2\mu_o}} = \frac{8.06\times10^{-5}}{B^2}\left(\frac{n}{10^{20}}\right)\left(\frac{T}{e}\right) \tag{4.25}$$

and the collisionality by

$$\begin{aligned}\nu_* &= \frac{4}{3}\sqrt{\pi}n\frac{e^4}{(4\pi\epsilon_o)^2}\ln\Lambda\frac{qR}{\epsilon_t^{3/2}T_e^2} \\ &= 2.063\times10^{-16}\frac{n}{T^2}\frac{R}{\epsilon_t^{3/2}\frac{\iota}{2\pi}}\end{aligned} \tag{4.26}$$

For the geometry we had $\frac{r_t}{R} = 0.38$, $n = 2$, $\frac{c_p}{R} = 0.105$. We will further assume here $\tau_a = \tau_c$. We can evaluate the collisionality at half the plasma radius using the transformation of the formula as discussed in the transport section. We obtain

$$\nu_* = 1.45\times10^6\left(\frac{n}{10^{20}}\right)\left(\frac{T}{e}\right)^{-2}R \tag{4.27}$$

We will take B and R as the scaling variables and β and ν_* as the dimensionless parameters, to be considered as our experimental objective. From the previous section we had $1 < \nu_* < 100$ and $\beta < 3\%$. Fixing the choice of β and ν_* will give, for varying R and B, a family of similar machines (same experimental objective), among which the member with minimum scale can be found by applying the constraints.

Let us at first keep β and ν_* explicitly in the equations giving the constraints (rather than including a number), so that we can, for various values of β and ν_*, see which constraints are really of importance in our case. To obtain the

constraints on B and R, we need to solve the equations (4.25) and (4.27) for the density and the temperature in terms of β, ν_* and the scaling variables B and R, so that in the different constraints we can eliminate n and T. We obtain

$$\frac{n}{10^{20}/m^3} = 4.73\left(\frac{B^4}{R}\beta^2\nu_*\right)^{1/3} \tag{4.28}$$

$$\frac{T}{e} = 2.62 \times 10^3\left(RB^2\frac{\beta}{\nu_*}\right)^{1/3} \tag{4.29}$$

We will investigate the constraints resulting from the step by step method. We will express the constraints on B and R as a function of β and ν_*. To obtain a feeling for the importance of the constraint, we will insert the worst case values ν_* and β within the limits, $1 < \nu_* < 100$ and $0.3\% < \beta < 3\%$.

3.6.2. Constraints resulting from the first step

The first step was to consider under which conditions we could drop the two dimensionless constants N_λ and $\frac{\rho}{c}$. This is needed so that the devices we consider, for varying values R and B, are really similar.

Dropping N_λ

Using (4.28) and (4.29) we can calculate N_λ

$$N_\lambda = 1 \times 10^7\left(R^2B\beta\nu_*^{-2}\right)^{1/3} \tag{4.30}$$

The requirement $N_\lambda > 2500$ transforms (4.30) into

$$R^2B > 2.5 \times 10^{-12}\beta^{-1}\nu_*^2$$

Within the limits $1 < \nu_* < 100$ and $0.3\% < \beta < 3\%$ this constraint becomes the most stringent for $\nu_* = 100$ and $\beta = 0.3\%$. Even using those values it is not a very stringent requirement

$$R^2B > 8.3 \times 10^{-6}$$

Other constraints which we have discussed and result from properties that could be affected if we do not keep N_λ constant, were related to the ratio Debye length/size of the plasma, and Debye length/ion larmor radius. The Debye length had to be smaller than the size of the plasma

$$\frac{\lambda_D}{a} < \frac{1}{10}$$

With

$$\frac{\lambda_D}{a} = 1.75 \times 10^{-5}\left(RB^{-1}\beta^{-1}\nu_*^{-1}\right)^{1/3} < \frac{1}{10}$$

we obtain

$$\frac{R}{B} < 1.86 \times 10^{11}\beta\nu_*$$

Even with $\beta = 0.003$ and $\nu_* = 1$ this requirement is not stringent.

$$\frac{R}{B} < 5.6 \times 10^{8}$$

The ion larmor radius had to be larger than the radius of the Debye sphere. This resulted in

$$\frac{n}{10^{20}}\frac{2 \times 10^4}{B^2} > 1$$

or

$$B^2R < 1 \times 10^{15}\beta^2\nu_*$$

With $\beta = 0.003$ and $\nu_* = 1$ we obtain

$$B^2R < 4 \times 10^{7}.$$

We thus see that, even when using in each case the worst assumption with respect to the choice of β and ν_*, it is quite justifiable to drop N_λ as parameter.

Dropping $\frac{\rho_\theta}{a}$

Let us now look at the parameter $\frac{\rho_\theta}{c}$. We obtain

$$\frac{\rho_\theta}{a} = 0.74\left(R^{-5}B^{-4}\beta\nu_*^{-1}\right)^{1/6}$$

Setting the requirement $\frac{\rho_i}{a} = \frac{1}{2}$ we obtain

$$R^{5/6}B^{2/3} > 1.48\left(\frac{\beta}{\nu_*}\right)^{1/6}$$

with $\beta = 0.03$ and $\nu_* = 1$ we obtain

$$R^{5/6}B^{2/3} > 0.82$$

This is certainly a requirement we will have to take into account.

3.6.3. Constraints resulting from the second step

Neutrals

In terms of the influence of the neutrals we had the condition that the plasma must be impermeable for neutrals which resulted in

$$na > 1.6 \times 10^{17}\sqrt{\frac{T}{e}}$$

this translates into

$$B^2R > 0.027\beta^{-1}\nu_*^{-1} \tag{4.31}$$

a very stringent requirement. Taking for example $\beta = 0.003$ and $\nu_* = 1$ we obtain

$$B^2R > 9$$

If we did allow the plasma to be permeable to neutrals (which is however questionable), we then needed that the temperature should be sufficiently low that collisions between charged particles would dominate over collisions with neutrals. The requirement $T < 400eV$ translates into

$$B^2R > 3.5 \times 10^{-3}\beta^{-1}\nu_* \tag{4.32}$$

Since both are limits on B^2R we can see under which conditions one is more stringent than the other. Comparing (4.31) with (4.32) we can calculate that for $\nu_* > 2.77$ it is easier to fulfill the condition on na, while for $\nu_* < 2.77$ the condition on temperature would be less stringent, at least if we accept a permeable plasma.

Impurities

We have argued in chapter 2 that there does not seem to be a constraint on R or B from requirements related to impurities. The surface preparation and wall cleaning method is of much more importance. The presence of impurities will increase the power requirements and this will be taken into account later.

3.6.4. Constraints resulting from the third step

Here we investigate what constraints result from the actual possibility to achieve the parameters we want. We will look at two possible heating methods ECRH and ICRH, and also look at technological constraints related to current density and stress limits.

Constraints resulting from the heating method used

Let us now briefly look at the requirement for heating by ECRH. With $\frac{\omega_{pe}^2}{\omega_{ce}^2} < \alpha$ (where $\alpha = 1, 2, 4$ depends on which wave is launched and from which side) we obtain

$$\frac{0.097B^2}{\frac{n}{10^{20}}} > \frac{1}{\alpha}$$

This results in

$$B^2R > \frac{1.2 \times 10^5}{\alpha^3}\beta^2\nu_*$$

It is interesting to compare this to the $n\tau$ limit

$$B^2R > 0.027\beta^{-1}\nu_*^{-1}$$

For $\beta\nu_*^{2/3} > 6.15 \times 10^{-3}\alpha$ the limit set by accessibility of ECRH waves is more stringent than the constraint set by the impermeability requirement. Remember also that the use of ECRH may limit the maximum B, because gyrotrons with frequency higher than $100Ghz$ do not exist yet.

The accessibility limit for the ICRH fast wave can be translated into

$$B^{4/3}R^{5/3} > 0.026\beta^{-2/3}\nu_*^{-1/3}$$

which is not very stringent. A more stringent requirement will result from the need to confine the high energy tail. Another constraint when using ICRH is the result of the limited power density of the launching structure.

Let us now further investigate the necessary heating power. A small computer program was set up to calculate for the given geometry the losses from simple O-D equations. Several expressions for the confinement time can be used and the program also takes into account power lost by radiation (we have taken 0.1% Fe impurity and 1% Oxygen impurity). The expressions of the confinement time of a fast component (as for example an ICRH tail) can be chosen differently from the confinement time of the bulk particles. In the examples that follow we have taken for the bulk plasma a confinement time given by the Alcator scaling law, together with a neo-classical expression (Hinton-Hazeltine, appropriately translated for the helical axis stellarator) when this value is lower. For values of $\nu_* < 1$ we have taken the value at $\nu_* = 1$ (extended plateau).

In the case of ICRH heating we took a temperature of the tail 20 times the bulk temperature and an expression for the confinement time of the tail going as Hinton-Hazeltine with extended plateau. The power calculated from the confinement time of the bulk particles was corrected by an efficiency factor which we took to be

$$\frac{1}{1+\left(\frac{\tau_s}{\tau_f}\right)^5}\,\frac{1}{1+\left(\frac{\rho_\epsilon\sqrt{20}}{a}\right)^5}$$

to account for the fact that if the confinement time (τ_f) of the fast particles is less than their slowing down time (τ_s) they can not give energy to the plasma. For the slowing down time we used the expression given by Rose and Clark [11]. The second factor is to correct for the losses of the fast particles if their poloidal larmor radius is larger than the plasma size.

In the case of ECRH heating we have used an efficiency correction factor given by

$$\frac{1}{1+\left(\frac{\tau_{eq}}{\tau}\right)^5}\,\frac{1}{1+\left(\frac{\rho_\ell}{a}\right)^5}$$

where τ_{eq} is the electron-ion equilibrium time and τ is the bulk energy confinement time (for which we used the Alcator scaling law and Hinton-Hazeltine with extended plateau). The first factor takes into account that if the electron-ion equilibration time is much larger than the bulk energy confinement time, the temperature of the electron population will be much larger than that of the ions resulting in a regime quite different from a reactor regime. The second factor is a way to take into account the constraint on $\frac{\rho_\ell}{a}$.

It is clear that the values obtained for the power needed will only be approximate values. More detailed calculations are not warranted in view of large uncertainties in confinement times and scaling laws, especially for a machine as the helical axis stellarator. After all, one of the purposes of doing the experiment is exactly to obtain more information on the power needed.

Figure 4.39 shows for $R = 2m$, $\nu_* = 10$ the power needed as a function of B, with β as parameter (ICRH). Figure 4.40, for the same dimension and heating method, shows the power as a function of B for $\beta = 0.01$ with ν_* as parameter. The corresponding figures, in the case of ECRH are Fig. 4.41, Fig. 4.42.

Technological constraints

The geometrical constraint $\frac{\frac{B}{R}}{2\times10^{7}A/m^2\frac{B}{m}} < 0.45$, can be translated in a R versus B diagram into requirements for current density. This is shown in Figure 4.43. The current density limits depend on the mode of operation (steady state, pulsed). We have therefore also shown in Figure 4.43 what mode of operation is needed to obtain the particular combination of B and R.

Stresses are not an important problem in this type of machine. We know from the results of Appendix B, that in some cases, we can neglect the in plane moments of the toroidal coils. This is particularly so here because it is a large aspect ratio machine. The stresses resulting from in plane loads can then simply

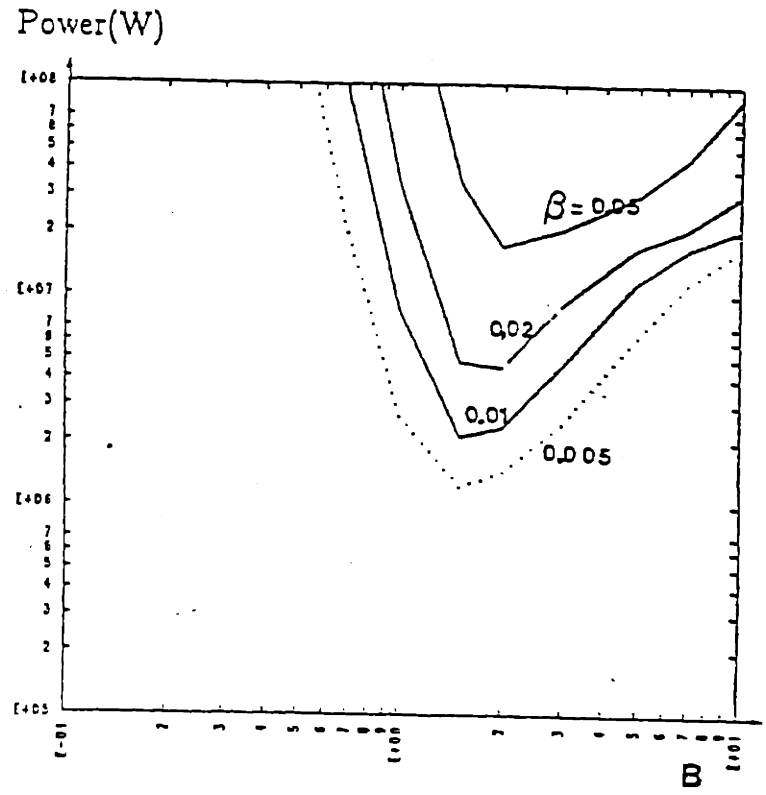

Figure 4.39 ICRH Power function of B, for $\nu_* = 10$

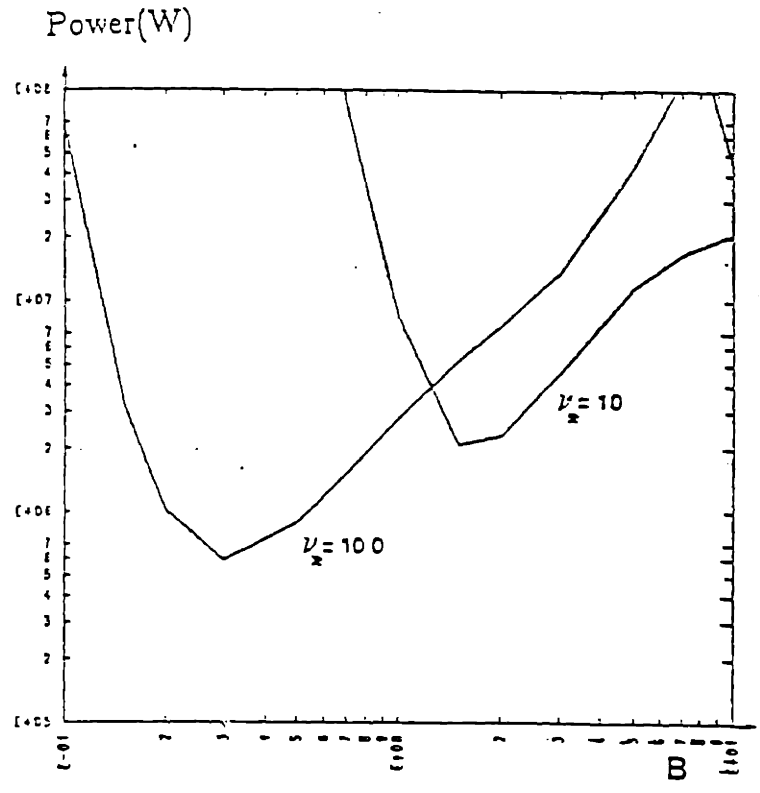

Figure 4.40 ICRH Power function of B, for $\beta = 0.01$

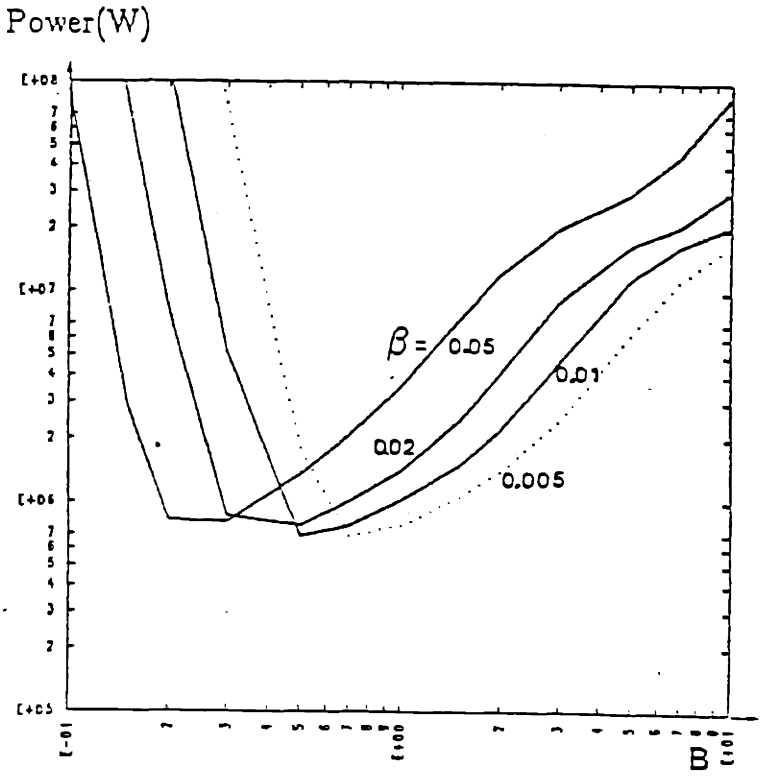

Figure 4.41 ECRH Power function of B for $\nu_* = 10$

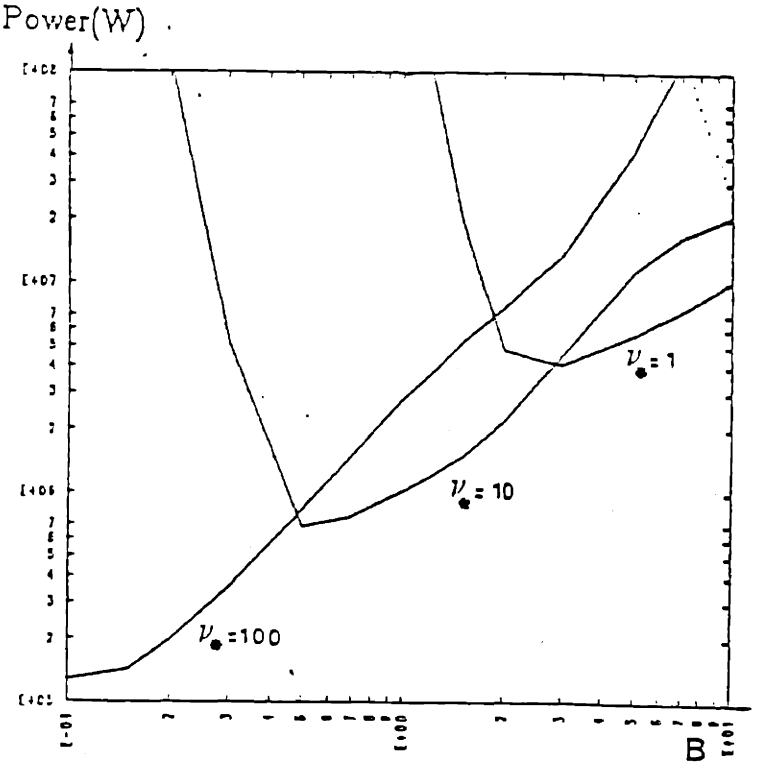

Figure 4.42 ECRH Power function of B for $\beta = 0.01$

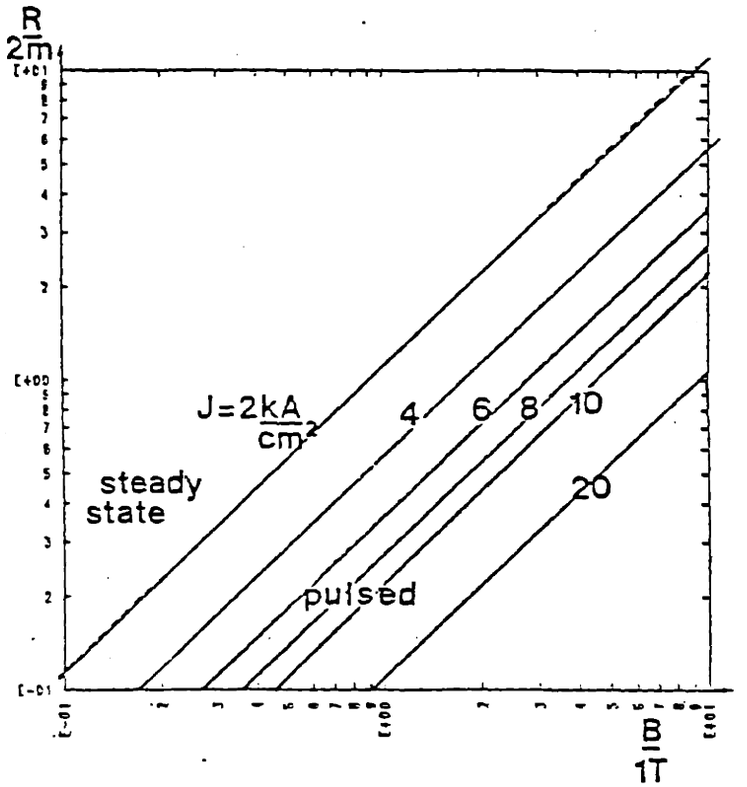

Figure 4.43 Current density requirements and corresponding mode of operation

be calculated from

$$\sigma = \frac{B^2}{2\mu_o}\frac{a_c}{h_c}$$
$$= 0.2 \times 10^7 N/m^2 \times B^2$$

For a limit of $\sigma = 340MPa$ full hard copper alone could take up the stresses up to $B \simeq 13T$.

Larger stresses however arise from the interaction of the current in the ring with the toroidal field coils, giving overturning moments. Taking a simple $\frac{1}{r}$ variation for the field due to the ring we obtain

$$B = \frac{\mu_o I_R}{2\pi r}$$

The force per unit length on the toroidal coils becomes

$$F = \frac{\mu_o I_R}{2\pi r} \times I_T$$

Using Fig. 4.44 we have

$$x = a_c \sin\theta$$

$$r = \sqrt{x^2 + (r_c - a_c\cos\theta)^2}$$

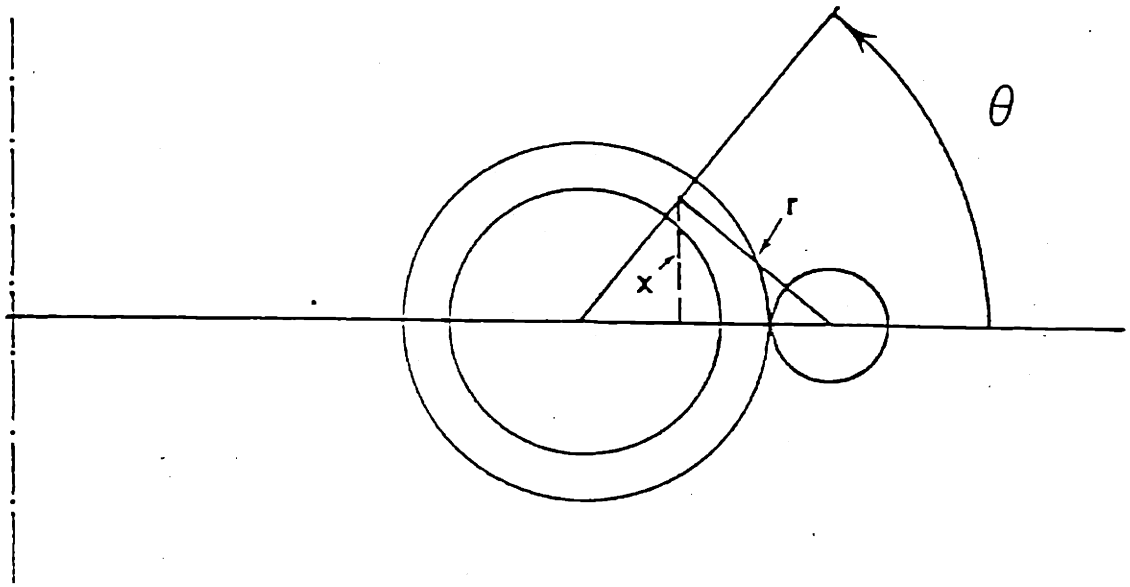

Figure 4.44 Calculation of the overturning moments on the toroidal coils.

We can then calculate the total overturning moment

$$\begin{aligned} M &= 2\int_0^{\pi} \frac{\mu_o I_R I_T}{2\pi r} \times a_c d\theta \times a_c \sin\theta \\ &= 2\int_0^{\pi} \frac{\mu_o I_R I_T a_c^2 \sin\theta d\theta}{2\pi\sqrt{(a_c\sin\theta)^2 + (r_c - a_c\cos\theta)^2}} \\ &= 8.4 \times 10^3 B^2 R^3 Nm \end{aligned}$$

This results in the midplane near the coil in a stress $\sigma = 46 \times 10^7 \times B^2 \quad N/m^2$ which for $B > 0.84T$ is too high for copper only. Thus at least in the area near the circular ring the coil will need, under certain conditions, some structural material to reduces stresses in the copper below acceptable levels.

3.6.5. Application of the important constraints to define a design window

We have, until now, purposely delayed to make a final choice for β and ν_*, which we consider our experimental objective. This for the simple reason that, making a choice, without being fully aware of the constraints, may have resulted in no design window at all in the R, B diagram, or unrealistic power requirements.

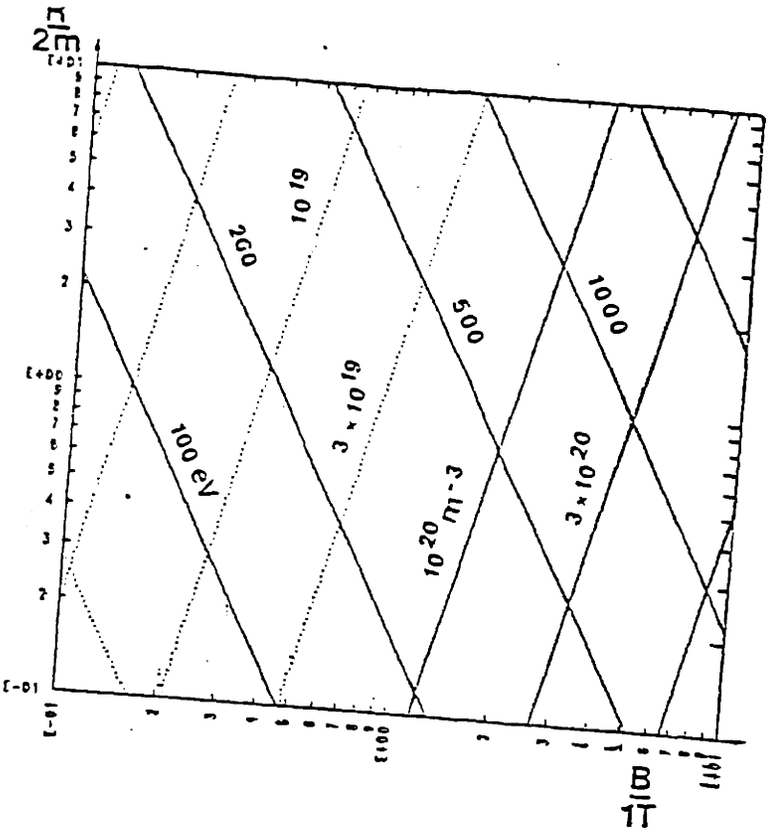

Figure 4.45 Values of temperature and density, as a function of size and magnetic field, for $\beta = 0.01$ and $\nu_* = 10$

Figure 4.39 and Figure 4.40 show that, to have, for a machine with $R \simeq 2m$, heating power requirements of the order of a MW, ν_* should not be much smaller than 10, while β not larger than 1%.

If we are willing to accept larger power requirements, other choices would have been possible. But we will take here, to obtain definite values for the design window, $\nu_* = 10$ and $\beta = 1\%$. With those values we can calculate what the density n, and the temperature T should be for similar machines. This is shown in Figure 4.45.

The power requirements can then be calculated as explained earlier, and result in Figure 4.46 for ICRH power and Figure 4.47 for ECRH power. The major constraints where the $\frac{\rho_i}{a}$ constraint, the na limit, the accessibility of the ECRH layer, the availability of gyrotrons. Constraints that have already been shown in Figure 4.43 are the combination of geometrical constraints and current density. The constraints on $\frac{\rho_i}{a}$ were implicitly included by correcting the power needed

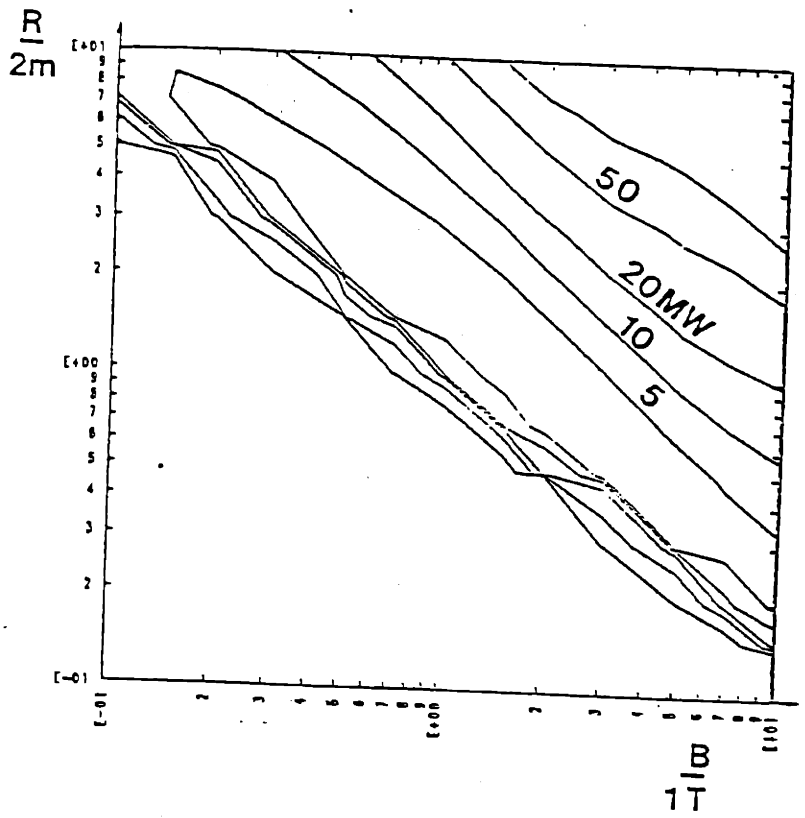

Figure 4.46 ICRH power as a function of size and magnetic field

by a factor that takes the losses into account if $\frac{\rho_t}{a}$ is too large. Shown in Figure 4.48 are the na limit, limits due to accessibility of the ECRH layer and the availability of gyrotrons (assumed $100GHz$).

It follows from Figure 4.48 that there are still choices possible with respect to the actual machine. Machine A ($R = 6m$, $B = 1.75T$) would be the minimum size machine if we used extraordinary wave at the second harmonic.
Machine B ($R = 1.2m$. $B = 3.5T$) the minimum size if we used the extraordinary wave at the fundamental. If in addition we want the machine to be able to operate in steady state, then the minimum size is machine C ($R = 4m$, $B = 1.8T$, with extraordinary wave heating at the fundamental).

The final design is chosen based on the cost of the machines and the heating power. Within the constraints we will try to find the minimum scale machine, based on the minimum of this total cost. If only the cost of the machine had to be considered (because for example the heating power is already available), another final choice for the machine might result. Or, if we had in addition

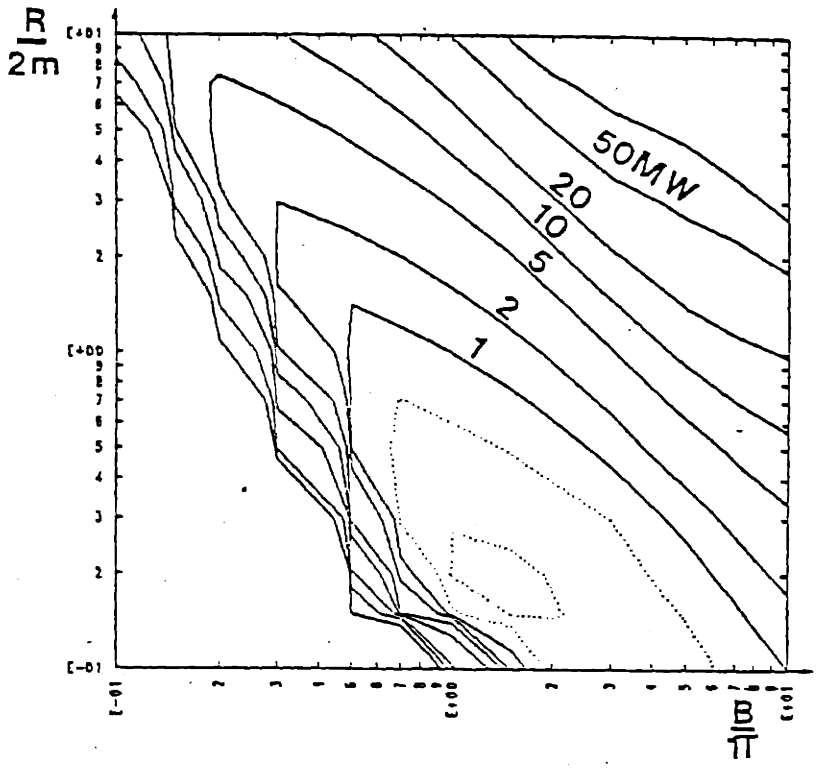

Figure 4.47 ECRH Power function of size and magnetic field

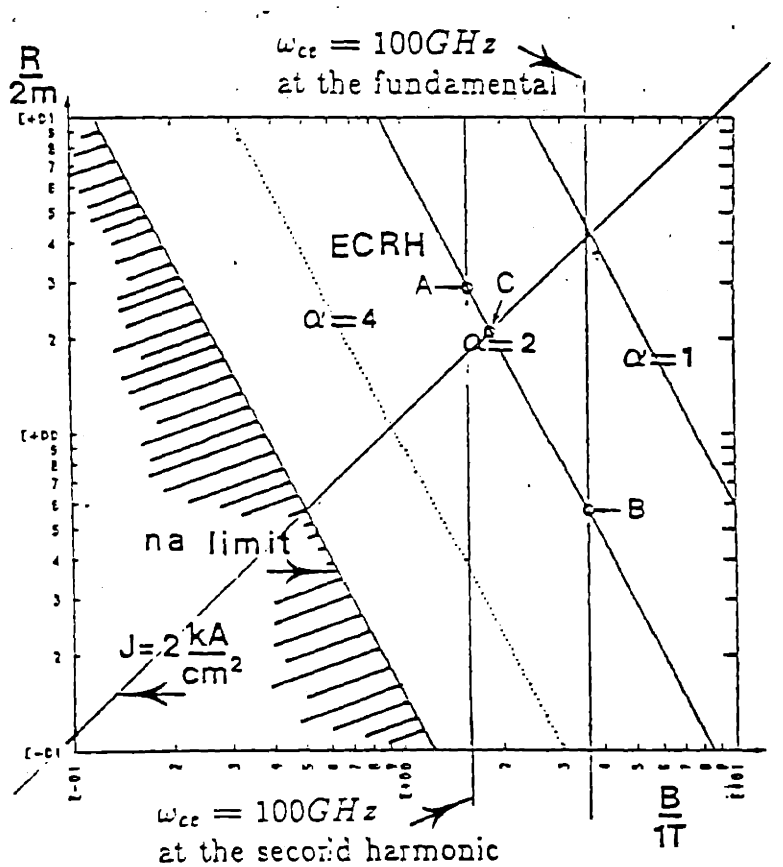

Figure 4.48 Impermeability constraint, and accessibility requirement for electron cyclotron heating

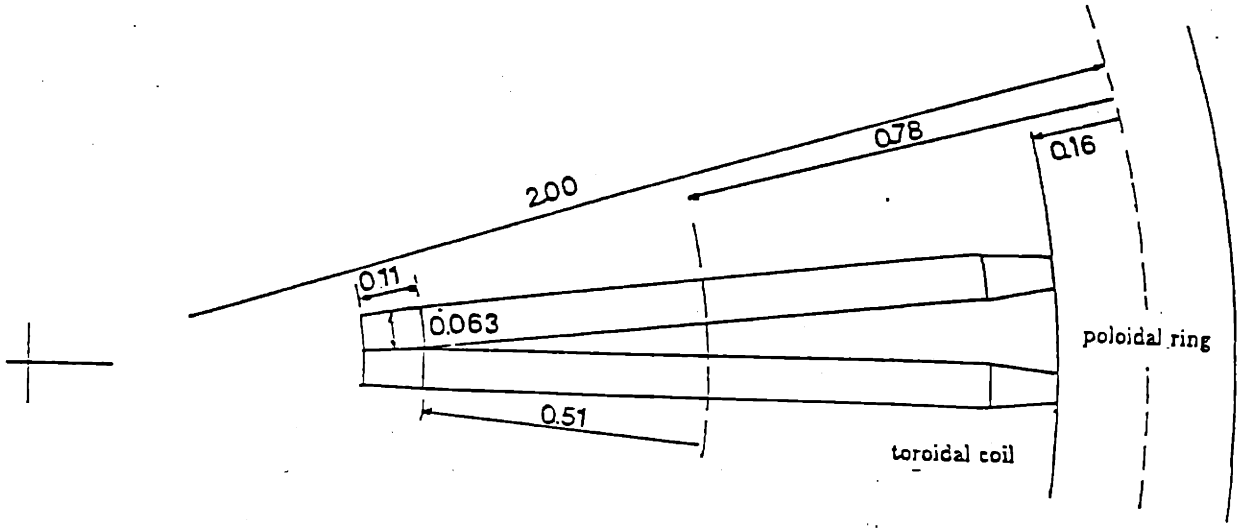

Figure 4.49 Dimensions reference case

to purchase the power supplies to energize the experiment, a different choice might result. The following section is an illustration on how we can, within the design window, make choices. We have assumed here on the one hand that the complete heating system has to be purchased. On the other hand we have assumed that sufficient energy is available on site (line, generator) that this is not an additional cost.

3.7. Final choice within the design window

In order to make the final choice, we will estimate the capital cost of the machine, and the heating power, both as a function of R and B. The final choice is then the machine which, within the constraints, minimizes this cost. The cost of the machine is estimated as follows. We have developed a reference design for $R = 2m$, $B = 1.14T$, $I_R = 2100kA$ and $B_v = 0.105T$. Figure 4.49 gives the dimensions. Figure 4.50 shows a perspective drawing of the full machine and Figure 4.51 shows a cutaway view (our thanks to P. Roemer for providing the program that generated those plots).

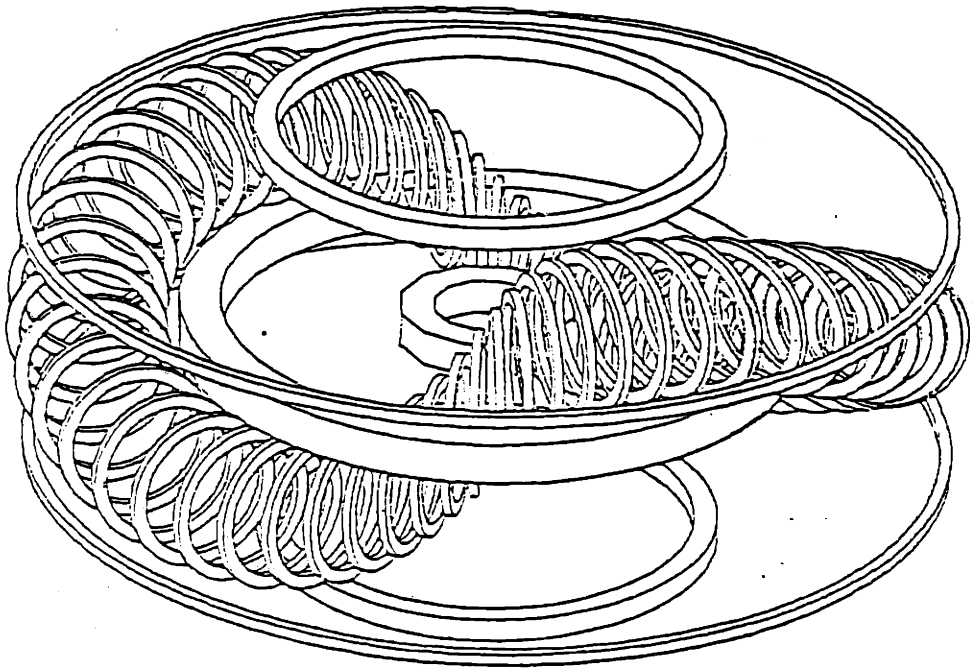

Figure 4.50 Perspective drawing of the $n = 2$ helical axis stellarator reference case

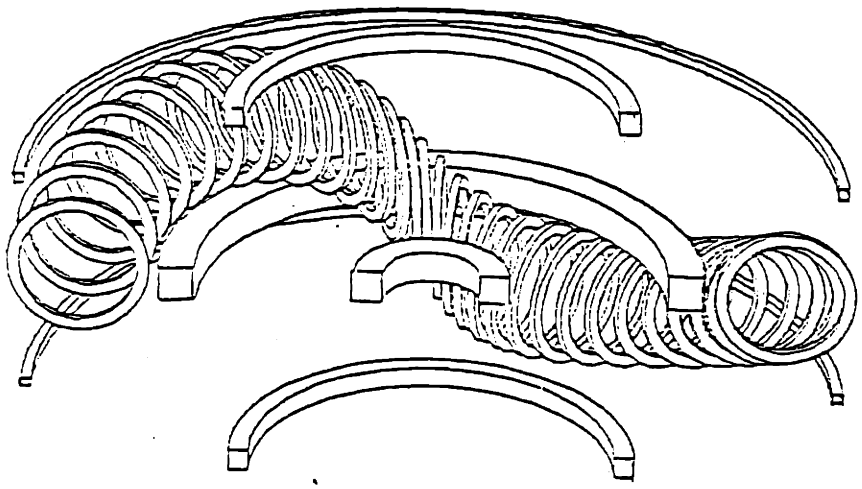

Figure 4.51 Cutaway view

The cost of this machine is estimated by calculating for this reference design the weight of the copper and the steel needed for the coils (based on current density), and then multiply the weight by a generally accepted cost per weight. The cost of the vacuum chamber is based on the cost for machines of similar size and complexity. The cost for machines other than this reference design (thus for other values of R and B), is obtained by scaling the cost of the components according to their weight as a function of size and magnetic field (using the relationship developed in chapter 3).

The current density needed to achieve $B = 1.14T$ and $R = 2m$ is $J = 2.5kA/cm^2$, in view of the constraint $\frac{\frac{B}{\mu_0}}{2\times10^7 \frac{A}{m^2}\, J} < 0.45$. An estimate of the cost of the toroidal field coils is then $1.61m^3 \times 9 \times 10^3 kg/m^3 \times 30\$/kg = 0.434 \times 10^6\$$. The vertical coils were positioned on a pentagon, and the current in them was calculated, using a program (SOLVE) provided by John Aspinal, so as to obtain the required vertical field and to null the flux linked to the poloidal ring. The currents are (Fig 4.47) $1.38MA$ in the central coil, $0.148MA$ in the top and bottom coil and $-44.5kA$ in the outer coils. Their resulting cost is $0.358m^3 \times 9 \times 10^3 kg/m^3 \times 30\$/kg = 0.096 \times 10^6\$$. The cost of the ring is given by $1.055m^3 \times 9 \times 10^3 kg/m^3 \times 30\$/kg = 0.285 \times 10^6\$$. The total cost of the coils is thus approximately $0.8 \times 10^6\$$.

For the structure we envisage a framework made of hollow circular beams, connecting the coils providing the vertical field to the central poloidal ring. (Fig. 4.52). The major load is the weight, and the cost of the total structure is estimated at $5.7m^3 \times 7kg/m^3 \times 10^3 \times 26\$/kg = 1 \times 10^6\$$.

For the vacuum chamber we would adopt circular bellows attached to rigid port sections. The rigid port sections would be located every fourth coil, and attached to the ring. This approach would allow, without major problems, to reposition the toroidal field coils, in order to change their winding law. An estimate, based on other machines of similar size and complexity is $1 \times 10^6\$$.

To scale those costs to machines of different size and field we have used for

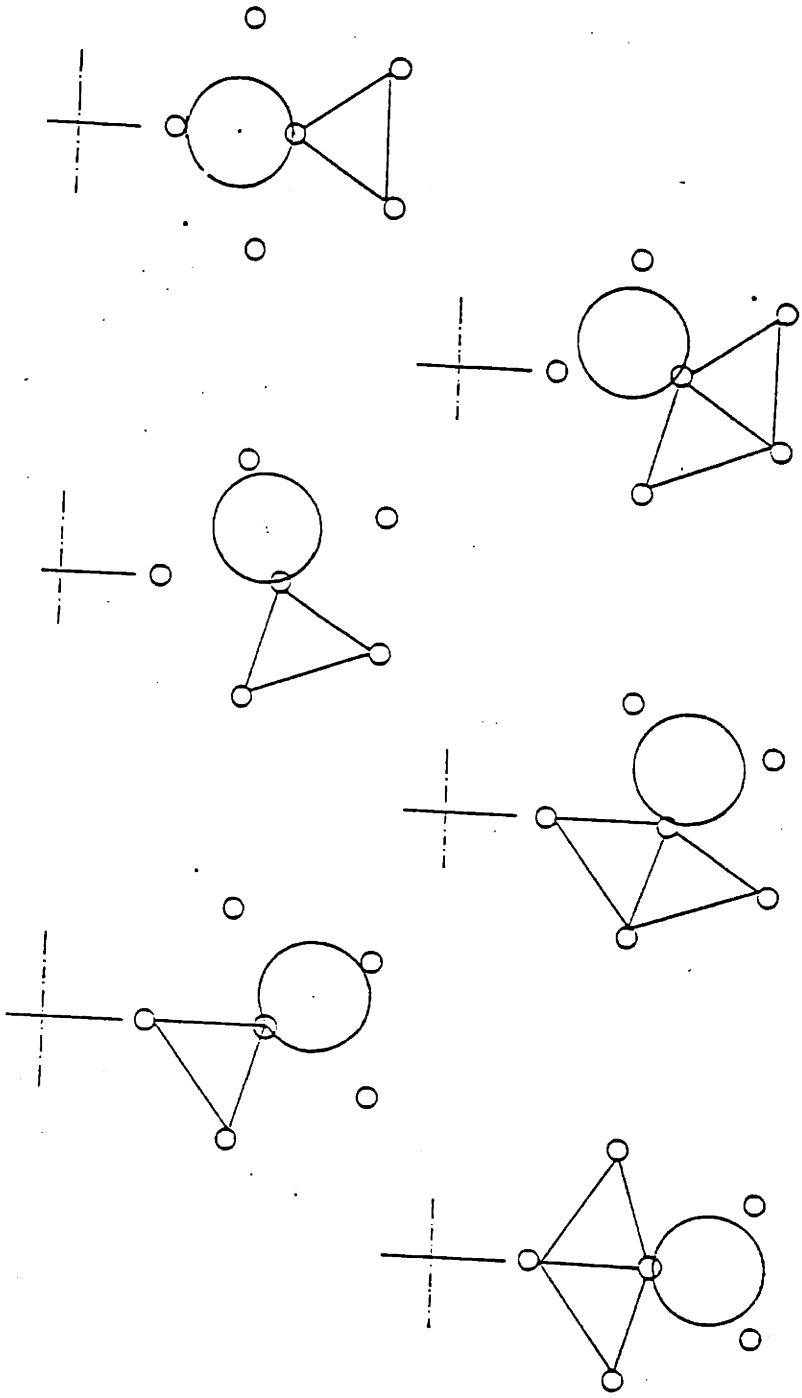

Figure 4.52 Structure, showing how the poloidal coils are connected to the central ring at intervals of 4 toroidal coils.

the coils $1.0 \times 10^6\$ \times (\frac{B}{1.14T})(\frac{R}{2m})^2$. For the structure we have taken that the section of the hollow beams should increase proportional to the weight of the coil system. Their length further increases linearly with the size. This gives us $1.0 \times 10^6\$ \times (\frac{B}{1.14T})(\frac{R}{2m})^3$. For the vacuum chamber we have taken a scaling going as the 3/4 power of the volume, thus giving $1 \times 10^6\$ \times (\frac{R}{2m})^{2.25}$. The scaling for the coils (and thus also of the structure) assumes constant current density. If the current density is increased from $2.5kA$ (which is necessary to achieve even higher $\frac{B}{R}$ values), the weight of the coils will go down. We have used the following scaling. If $\frac{B}{R} > \frac{1.14T}{2m}$ then the weight of the coils is reduced by $\frac{B}{R}\frac{2m}{1.14T}$, which is proportional to the increase in current density needed, above $2.5kA/cm^2$. For lower values of $\frac{B}{R}$, we have reduced the current density (and correspondingly increased the mass) down to a limit of $2kA/cm^2$.

For large values of B and R more reinforcement will be needed, and as shown in Chapter 3 the mass will then scale as R^3B^2. We have taken this into account by multiplying the mass of the coils and the structure by $\left(\frac{R}{2m}\frac{B}{1.14T}\right)$ for the case where $RB > 2m \times 1.14T$ (our reference design for which some structural material was needed for the coils). The resulting direct cost of the machine is shown in Figure 4.53.

The picture changes when we start taking into account the additional power. For ICRH we have taken a cost of 1\$/W and for ECRH a cost of 3\$/W.

Figure 4.54 shows the cost of the machine (capital and ICRH heating cost), as a function of size and magnetic field for $\beta = 0.01$, $\nu_* = 10$. To minimize the total cost, one would go to a small, high field machine. If we require that the space needed for the antenna structures to launch the power (at $4MW/m^2$) should not exceed 10% of the total area we obtain a minimum size of $R \simeq 1m$, and $B \simeq 4T$. The total cost does not vary markedly if we go to $R = 1.4m$ and $B = 2.5T$. Since this last machine has better access we opt for this choice. The corresponding density and temperature are $T \simeq 500eV$ and $n \simeq 10^{20}/m^3$ The current density needed is $8kA/cm^2$, a value which can be achieved using a

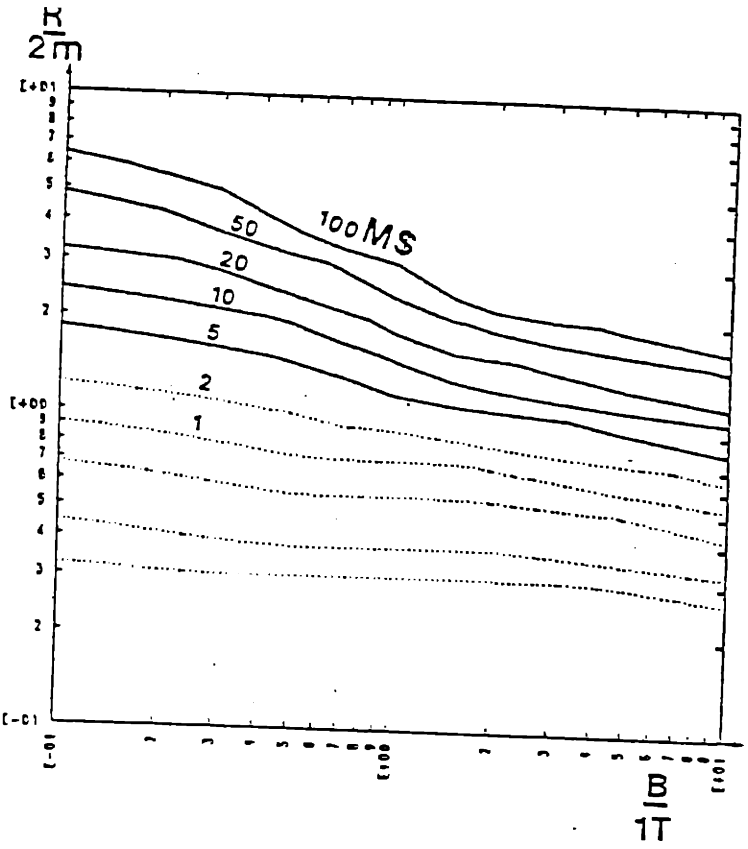

Figure 4.53 Direct cost of the machine, function of size and field

pulsed liquid nitrogen cooled system.

The machine takes on a different format if we assume ECRF heating. Figure 4.55 shows the total cost in this case, together with the limits. Since the absorption of the ordinary wave at the second harmonic frequency ($\alpha = 4$) is insufficient at low temperature we have little choice but to use the extraordinary wave at the fundamental (launched form the high field side), however with the caveat that the wave may still need multiple reflections to be completely absorbed. The choice is then $R = 1.2m$, $B = 3.5T$. The current density needed would be $13kA/cm^2$.

3.8. Summary

In this chapter we have shown how we could develop the methodology guidelines and formulas developed in the previous chapters to our particular case. We have investigated in detail the geometry of the helical axis stellarator and explained how we would go about fixing the geometry. We have shown what the influence

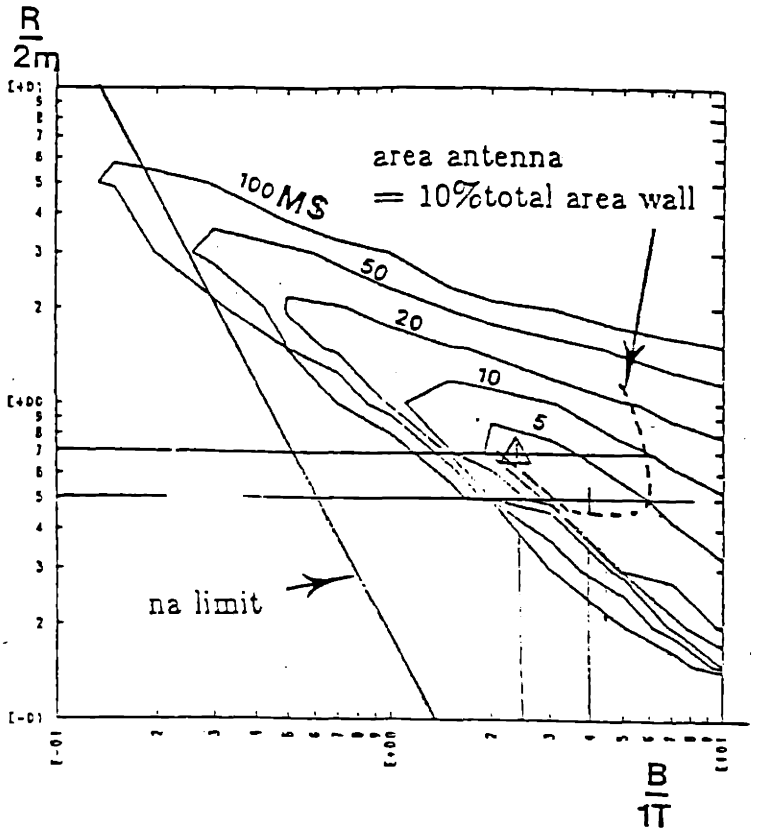

Figure 4.54 Total cost for ICRF heated machine

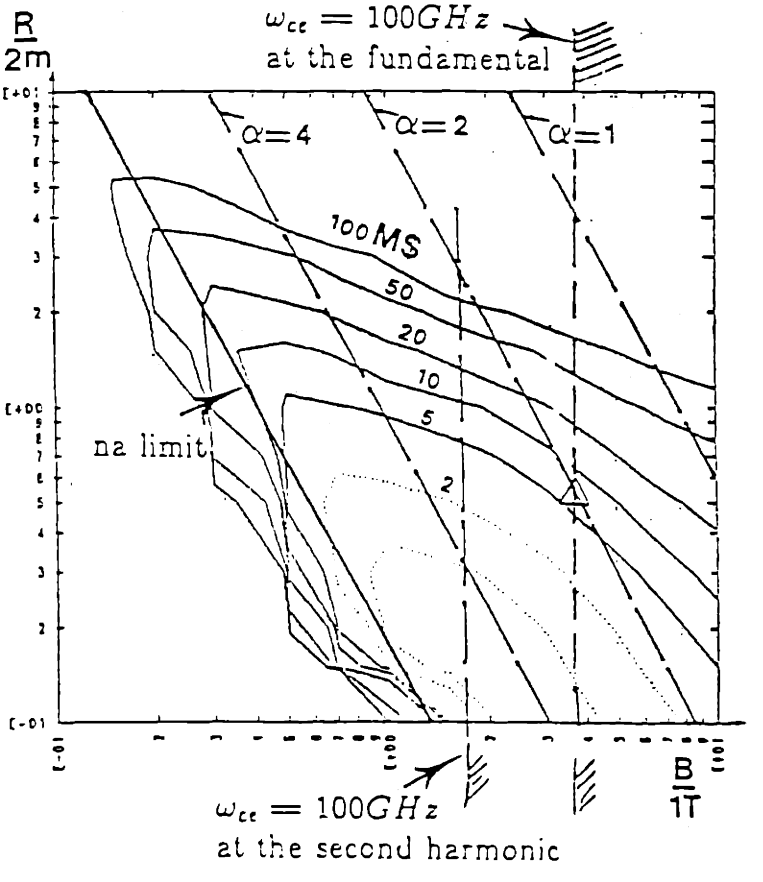

Figure 4.55 Total cost for ECRF heated machine

is of the current in the ring and of the vertical field on parameters associated with the magnetic axis. Relationships were developed so that the geometry could be made function of the hard parameters only. We have then investigated how we could choose those parameters (especially the number of periods and the displacement of the coils). This resulted in the definition of the geometry and a constraint on $\frac{B}{JR}$. Choosing then β and ν we could investigate the constraints imposed on size and magnetic field. By further applying the plasma physics and technological constraints developed in the earlier chapters we have identified two possible minimum cost machines. The choice between them would depend on the heating method used.

Let us briefly highlight where some basic choices have been made and what the resulting effects were. We have chosen from the start the particular configuration for the helical axis stellarator (circular toroidal coils, a poloidal ring, and no topological link between both). We have also taken the center of the toroidal coils to be located on a helical line with $R_c = R_r$ and $r_c = constant$. Those choices have resulted in a rather stringent geometrical constraint, pushing the machine to a larger size. The underlying reason is that size of the coils on the inside of the ring is constrained by non-interference requirements. The constraint, because of ripple requirement, is on the outside coils. For a tokamak the ripple problem can be solved by increasing the size of the coils, without a very large effect on the overall size of the system. In this case however, an increase in the size of the toroidal coils results immediately in an increase in the size of the whole system. This could be alleviated for example, by using helical coils to make the magnetic geometry. If one wanted to stick with circular coils, less stringent constraints would result from a number of other choices: we could allow a topological link between the ring and the toroidal coils, we could shift the toroidal coils outward ($R_c > R_R$), we could take larger toroidal coils on the outside (to reduce the ripple there) while keeping small ones on the inside (In order not to increase the overall size), we could decrease the spacing of the coils on the outside (again to reduce the ripple there). The choice of the machine configuration has a very

important effect on its minimum size.

Other choices that have been made were the experimental objectives ($\beta = 1\%, \nu_* = 10$) and the choice of the heating method. Further when we have minimized the total cost we have included the capital cost of the machine and the heating system. We would obtain other minimum size machines had we chosen a different experimental objective, or had we included the cost of power supplies etc.. The method we have developed allows us to obtain values for the minimum scale machine, for the particular choices made. The impact of making a different set of choices can easily be gathered by reapplying the method to this new set.

5. Summary

5.1. Introduction

This thesis addresses the question of the constraints that set a minimum scale for a toroidal fusion experiment. A method was developed that identifies those constraints. The resulting constraints have been investigated in general for any particular toroidal experiment. In a second part we address the issue specifically for a stellarator with helical magnetic axis, and find its minimum scale.

The starting point of this thesis was a question asked during a discussion about the the design of magnetic fusion experiments. "Why can't we build a 1 Gauss machine ?" And as some apparently simple questions usually do, it posed an important problem. What in fact are the constraints that set a minimum scale for an experiment ? The constraints on the scale of an experiment depend in part on what we want to achieve. We have chosen to concentrate on constraints for experiments investigating the plasma physics properties of toroidal concepts. The reason for this choice is threefold. One, the question of the constraints was specifically asked in this context. Two, the problem of investigating the plasma physics properties of some magnetic confinement concepts is particularly important and timely. It is important because fusion research should keep in mind the end product when assessing the potentiality of a concept as a

reactor candidate. Some concepts, possibly more reactor-friendly, but still in the earlier stage of their development are presently disadvantaged by the fact that little is known about their plasma physics properties. The problem is also timely ; we need to address the issue before we are definitively locked into the tokamak/mirror alternative. The third reason is that the question of the constraints that set a minimum scale is particularly relevant for those experiments. Other type of experiments do not need the construction of a new machine (one could use pure theoretical analysis, numerical analysis or perform the experiments on existing machines, because they address concept independent issues) or involve such a restricted and well-known set of constraints (for ignition experiments : the Lawson criterion) that they need not be addressed here. Construction of an experiment to test the plasma physics properties of a concept is presently the only approach possible to the problem. Identification of the constraints that set a minimum scale, in order to be able to perform the experiment at minimum cost is then a key issue.

If we look at what the minimum scale is for an experiment, it implicitly assumes that we can perform experiments that test the issues on a scale different from the full size machine. This implicit assumption underlies all present experimental effort. Indeed, no full scale reactor size machine exists yet.

Two approaches to investigate the plasma physics properties of a concept are possible:

The first one is to rely on experiments only. We can the try to model the plasma physics processes that occur in a reactor size experiment in a scale version. The issue of relevance of the results of scaled experiments is then answered in the same way that is used in other fields like hydraulics and aerodynamics : by the use of similarity. This method is widely applied in those fields to obtain from scaled versions (small models) results that can then be translated into results of significance for the full scale object. The relevance of the scaled experiment is justified based on the fact that, under some conditions, it models the same processes as in the large version, and thus allows us to obtain information on

them. Sometimes the requirements are so stringent that no small experiments could be build.

A second approach is then to rely partly on theory. Small experiments may be used to check certain aspects of a theory. If this results in less stringent constraints for the experiment than the first approach, it may be a first, confidence building, step towards a second, larger experiment that then would model the plasma physics processes of a reactor. For this second approach too, when we look at the minimum size, we have to compare machines that fulfill the goal to the same extend. This again can be done by using the method of similarity.

The difference in applying the method of similarity for the first and second approach is only in the following: the family of machines, among which we choose the one which, within constraints, is the minimum scale member contains also the reactor, if we use the first approach. Using the second approach, we choose the minimum scale member among a family which does not contain the reactor. Each member of the family however, is similar in that it will test theory to the same extend.

Applying the method of similarity to plasma physics experiments automatically result in the constraints and limits that set a minimum scale for an experiment.

Three steps are necessary :

-identify the parameter space in which one or more of the dimensionless parameters can be dropped so that we have indeed some freedom in making an experiment (if the number of dimensionless parameters we want to keep constant equals the degrees of freedom, then only one experiment can be build, and there is no point looking for a minimum scale).

-identify the constraints resulting from factors that are not included in the similarity scaling.

-identify the constraints and limits on the possibility of actually obtaining the parameters mandated by similarity considerations.

In the first part of this thesis we investigate in more detail the method of

similarity and the constraints resulting from those three steps. The dimensionless parameters are derived, and we show how in order to obtain two free scaling parameters (a scale factor on the linear dimensions and a scale factor on the magnetic fields) we need to drop two of the dimensionless parameters. The constraints resulting from the three steps are investigated in general in terms of plasma physics constraints and technological constraints. It entails some theoretical analysis, analysis of experiments performed on existing machines and the development of relationships between a number of parameters. Additional constraints which can result from the particular geometry of a concept are not investigated in general.

For fixed values of the dimensionless constants we can then plot in a size versus magnetic field diagram, the constraints resulting from the three steps described earlier. If a design window can be identified in this diagram, then we can make a further choice based on minimum cost, minimum heating power etc...

The second part of this thesis is an application of the method to the particular case of a helical axis stellarator. There we first address in more detail the constraints that arise from the geometry of the helical axis stellarator. The general method is then applied to identify the design window within the constraints and this finally results in a minimum scale for this particular experiment.

Let us now turn to the dimensionless parameters and plasma physics constraints.

5.2. Plasma physics considerations

5.2.1. Dimensionless parameters

We make the following assumptions: the plasma is fully ionized, consists of only two species : electrons and ions, is in steady state and at rest. Based on those assumptions we can construct eight dimensionless parameters, for which we choose

- ν_*, the collisionality defined as the ratio between the connection length and the

electron mean free path

-β, the ratio of the plasma pressure to the magnetic pressure

-$\frac{\rho_\theta}{a}$, the ratio of the ion larmor radius in the poloidal field to the minor radius of the plasma

-N_λ, the number of particles per Debye sphere

-$\frac{T_e}{T_i}$, the ratio of electron and ion temperature

-$\frac{n_e}{n_i}$, the ratio of electron to ion density

-$\frac{Z_i}{e}$, the ratio of ion charge to electron charge

-$\frac{m}{M}$, the ratio of electron mass to ion mass.

The ratio $\frac{T_e}{T_i}$ will be close to 1 for reactors as presently envisaged and should thus also be close to 1 for any experiment. Similarly, $\frac{n_e}{n_i}$ is always close to 1. Choosing hydrogen as the working gas, fixes $\frac{m}{M}$ and $\frac{Z_i}{e}$. This in fact leaves us with four dimensionless parameters to work with. Since we have only four degrees of freedom (size, magnetic field, plasma density and temperature), we have no freedom left in making a scaled experiment, if we want to keep the four dimensionless parameters constant. To have some additional freedom in making a scaled experiment, we will have to drop one or more of the dimensionless parameters. We then have to investigate what constraints result from not keeping one or more of the dimensionless parameters constant. This results in a first set of constraints.

5.2.2. Investigating the degrees of freedom by not keeping one or more of the dimensionless parameters constant

The number of particles per Debye sphere N_λ is related to the charge neutrality of the plasma. Not keeping N_λ constant is justified if its value is sufficiently large that charge neutrality can still be guaranteed. A quantitative value can be found by noting that the factor $\ln\Lambda$, in the formula for collision frequencies gives the dominance of the small angle collisions over the large angle collisions. The value of Λ is 9 times the number of particles per Debye sphere [11].

Setting a minimum of $\ln\Lambda = 10$, so that small angle collisions are at least 10

times more frequent than large angle deflections, we obtain $N_\lambda > 2500$. Other constraints, related to Debye shielding and Debye length are : $\frac{\lambda_D}{a} \ll 1$, the Debye length must be much smaller than the size of the experiment and $\frac{\rho_i}{\lambda_D} \gg 1$, the ion larmor radius is larger than the Debye sphere. Not keeping N_λ constant, while keeping it sufficiently large, can thus within certain limits be justified and gives us one degree of freedom. This is however usually not sufficient. As second parameter that we do not keep constant we can choose β, ν_* or $\frac{\rho_e}{a}$.

Not keeping β constant corresponds to a model where distortion of the vacuum fields by the presence of the plasma is neglected. Experiments however seem to indicate that this can have an important impact on transport. Not keeping ν_* constant would correspond to a model where we neglect the influence of collisions. It may be appropriate if we look at β limits and are only concerned about the investigation of equilibrium and stability that is not influenced by the resistivity of the plasma. It thus seems best to keep β and ν_* constant and drop $\frac{\rho_e}{a}$ as parameter. We can drop $\frac{\rho_e}{a}$ as parameter as long as the particles are indeed contained. This means $\frac{\rho_e}{a} \ll 1$. The influence of $\frac{\rho_e}{a}$ could also be gathered separately on an experiment by varying a and B for example within a limited range. In experiments that keep β and ν_* constant the scaling of density (n) and temperature (T) with the free parameters size (a) and the magnetic field (B) is

$$n \sim a^{-1/3} B^{4/3}$$

$$T \sim a^{1/3} B^{2/3}$$

For a given choice of β and ν we can thus plot in a a, B diagram the density and the temperature and already draw in this diagram the constraints resulting from the fact that we did not keep N_λ or $\frac{\rho_e}{a}$ constant.

5.2.3. Effects not included in similarity scaling laws

Two major effects, not included in the similarity scaling laws, have been considered here : the presence of neutrals and the presence of impurities. Neutrals are present in the plasma simply as a result of thermodynamic

equilibrium between the atoms in their ionized state and their bound state (Saha equilibrium). Because most laboratory plasmas are optically thin, they are not in complete equilibrium with their radiation fields and the minimum level of neutrals is a result of equilibrium between radiative recombination and collisional excitation (Coronal equilibrium).

Additional sources of neutrals are penetration of neutrals from the edge, the need to refuel the plasma and heating by neutral beams. In order for the center of the plasma not to be influenced by neutrals coming from the edge, we need that $na > 1.6 \times \frac{10^{17}}{m^2}\sqrt{\frac{T}{e}}$. There are strong theoretical [42, 43] and experimental [136] indications that neutrals from the edge have an important effect on β limits and transport. If this condition on na is not fulfilled then neutrals from the edge will penetrate to the center.

Assume as a minimum for the density of neutrals at the edge, the value arising from recombination for a plasma density one tenth the plasma density at the center and a temperature of $3eV$. We can then calculate the level in the center resulting from penetration. For collisions between charged particles then to be 10 times more frequent than the collisions between charged particles and neutrals, the plasma temperature should be below $400eV$ (the collision time between charged particles increases with temperature, while the collision time with neutrals is approximately constant).

The need to refuel the plasma may introduce even higher level of neutrals. A simple model based on work from Podesta and Engelmann [39] allows us to calculate their level and also shows that the charged particle confinement time must be at least one order of magnitude larger than the energy confinement time in order to be able to neglect the effect of losses due to charge exchange on the energy balance.

Recently an important effect of heating by neutral beams was discovered [45–47]. The lowering of the charged states of impurities in the center because of charge exchange with the fast neutral particles result in an increase in radiation losses.

In the case of permeable plasmas, for the effect of neutrals to be minimized, we thus have to work at sufficiently low temperature, and with plasmas of sufficiently long confinement times.

Since the presence and effects of neutrals are connected to recycling and refueling, we have analyzed experimental results and tried to explain some of the seemingly different behaviors observed in different machines. This resulted in a simple model that can explain qualitatively those difference.

The second effect not included in similarity scaling laws is the presence of impurities. Impurities can be present in the plasma through several mechanisms: arcing, sputtering by ions and neutrals, evaporation. They can also be introduced through the original gas composition of the chamber prior to filling, by the plasma formation scheme and through neutral beams used to heat the plasma.

Impurities can have an effect on particles transport. In order for the collision time between charged particles to be at least a factor 10 lower than the collisions with impurities, the requirement is that $Z_{eff} < 1.1$. Impurities also increases losses through radiation and can affect drastically q profiles when the plasma carries current. Since both Alcator (small high field tokamak) and Tosca (small low field tokamak) have operated at $Z_{eff} = 1$ there seems to be little correlation of the level of impurities with magnetic field. From their size we can also conclude that at least any size above $a = 0.1m$ is acceptable. The important factors are the temperature at the edge, and the wall conditioning. Rapid recycling of hydrogen at the wall result in a lower edge temperature, and thus less impurities. This can be achieved by Ti gettering (Tosca) or walls operated at lN_2 temperature (Alcator). Another method, that avoids the need of rapid recycling at the edge is the use of a divertor.

From this section we conclude that the effect of neutrals indeed may set a minimum on a combination of density and size of an experiment. Impurities however, do not directly put constraints on the size or magnetic field of an experiment.

5.2.4. Ability to obtain the parameters as dictated by similarity considerations

Several methods are available for plasma startup and it is always possible to find one that does not put any special constraints on size or magnetic field of an experiment. Heating methods however, do put rather stringent constraints.

Ohmic heating has a low density limit because of runaway problems, while for some concepts, there is some maximum on the combination of current, magnetic field and size because of MHD stability constraints (example $q > 1$ in a tokamak). Accessibility requirement for ECRH set a minimum magnetic field for a given plasma density. The actual relationship depends on which wave is used (ordinary, extraordinary). Condition for absorption of the wave are less stringent since multiple reflection on the chamber walls can result in complete absorption of the wave through multiple passes. At low density the equilibration time between electrons and ions may become so long that we obtain a plasma with very high electron temperature, but low ion temperature. Lower hybrid heating has a minimum cutoff density and a maximum for the combination of wave number temperature and density. ICRH has a minimum on density in terms of accessibility of the ion cyclotron resonance layer and because of the need to thermalize the ion tail that is produced. A minimum on the product of size and magnetic field is required because of the need to confine the fast particles before they thermalize. This last requirement is also valid for neutral beam heating. Thermalization of the fast particles will put some minimum on the product of density and size of the machine, while the need for tangential access too may put rather stringent constraints.

In this section on plasma physics constraints, we have, using the step by step method identified the three sets of constraints, and investigated from a general point of view their impact on the scale of an experiment. Other constraints arise from technological considerations and those are addressed in the next section.

5.3. Technological considerations

Two major technological constraints are current density limits and structural constraints. Other constraints can arise from the availability of stored energy, and the cost of the machine. In order to be able to address those issues in sufficient generality and obtain scaling laws with size and magnetic field (our two free parameters in the similarity method), we have developed a number of relationships between mass, stored energy and pulse length.

5.3.1. Current density limits

Current density limits depend on the choices made : steady state or pulsed, water or liquid nitrogen cooled or superconducting coils. The pulse length of an experiment (the equivalent pulse length, including ramp up and ramp down of the fields) puts it from the point of view of current density limits/heat removal capacity, for water cooled coils rather unambiguously in one of two classes : pulsed or steady state. For the pulsed mode ($\tau < 10 sec$), it is best to use as much copper as possible and to dimension the cooling passage for heat removal between pulses. The current density is then $J = 10 \frac{kA}{cm^2} \sqrt{\frac{1}{\tau}}$. For larger pulse length, the coil can be considered in steady state and larger cooling holes should be provided. The current density then is $J = \frac{2kA}{cm^2}$. The use of liquid nitrogen cooled coils is only justified in the pulsed mode. Limiting the temperature rise to 15°C the current density is then $J = 10 \frac{kA}{cm^2} \sqrt{\frac{1}{\tau}}$. Limits on current density for superconductors result from stability and protection requirements. A value that takes both constraints in account is given by

$$J = \frac{10kA}{cm^2} \left[\frac{E}{10^8 J} \right]^{-1/5}$$

5.3.2. Structural constraints

Structural constraints will set a minimum amount of reinforcing steel in cases where the copper is not sufficiently strong by itself to carry all the loads. The minimum fraction of steel needed for reinforcement of toroidal coils is given by

$$f_s = \frac{Bl_a}{\mu_o N E_s A_{coil}} \left[\frac{1}{4\pi} \frac{Bl_c g_c}{\epsilon} - \frac{E_c}{j_c} \right]$$

where B is the magnetic field at the geometric center of the toroidal coils, l_a is the length of the line that threads the geometric center of the coils, N is the number of coils, E_s, E_c are the elasticity modules of copper and steel respectively, A_{coil} is the cross sectional area of one coil, ϵ is the maximum allowable strain, g_σ can be considered as a geometric factor that depends on the shape of the coils and j_c is the average current density in the copper. This formula can then be used to calculate the total mass of the toroidal coils.

We have also investigated how the structural mass scales with magnetic field. One would expect it to scale as B^2. If, however, stresses in the coils are dominated by moments, then it is possible that the structural mass scales as B. Whether moments are dominant or not in toroidal coils depends on their loading, their shape, but also very much on the way they are supported. For the particular case of circular toroidal coils we have developed a simple method (based on Fourier expansion of the load), to analyze their stresses, including internal and external reactions and found that by proper distribution of the net reaction force we can minimize the moments in the coils.

5.3.3. Stored energy

The stored energy of a set of toroidal coils can be easily calculated as the volume times $\frac{B^2}{2\mu_o}$. In view of this simple formula it is tempting to look for a relationship between the stored energy in the coils and the mass of the system. Moon has proposed the scaling

$$\left(\frac{M}{10^3 kg}\right) = 1.37\left(\frac{E}{1MJ}\right)^{0.761}$$

The picture is however more complicated. In some limited, range the mass of the system can indeed scale as the stored energy. A system consisting mostly of current carrying copper will scale with a second power in the linear dimension and the first power of the magnetic field (aRB). The scaling of the mass of a pulsed system depends on the pulse length of the system as well as on the time constant of the coils. The time constant τ in turn depends on the copper mass

of the coils through a formula we derived

$$\frac{\tau}{1s} = 0.093 \frac{\left(\frac{Mc}{10^3 kg}\right)}{\left(\frac{R}{m}\right)} \frac{g_E}{g_l^2} \left(\frac{1.92 \times 10^{-8} \Omega m}{\rho}\right)$$

where R is the major radius of the coil set, ρ the copper resistivity, g_E and g_l geometrical factors depending on the shape of the coil. The problem of the mass of pulsed system can then be solved self-consistently and results for very short pulse length in a mass scaling as the stored energy while for longer pulses, the mass scales as aRB.

The technical constraints and scaling relationship derived in this section provide useful tools when we investigate the design window in a size versus magnetic field diagram. The second part of this thesis is the application of the method, and resulting constraints to find the minimum scale for a stellarator with helical magnetic axis.

5.4. Application to the design of a stellarator with helical magnetic axis

5.4.1. Definition of the concept

A stellarator with helical magnetic axis is a particular type of stellarator that relies essentially on the torsion of the magnetic axis to provide a rotational transform. Several variations are possible. The particular one chosen is shown in Figure 5.1

The toroidal coils are simple circular coils in $\phi = constant$ plane and they do not link the central poloidal ring. An additional set of poloidal coils provides a vertical field. Advantages of this concept are its experimental flexibility, its simple modular coils and possibly its potential of achieving high β values. Disadvantages are the highly complex geometrical form and the resulting constraints on the size and magnetic field.

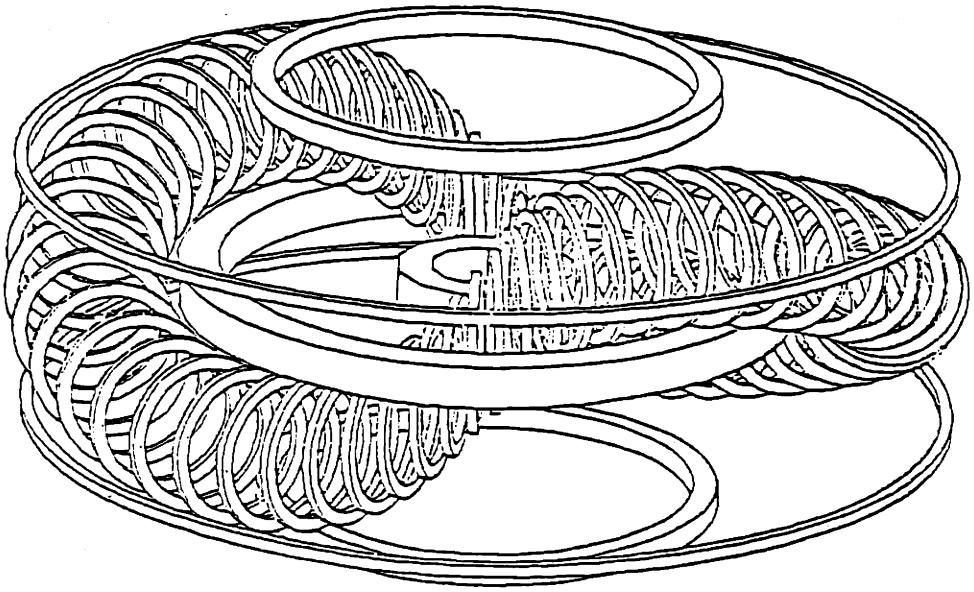

Figure 5.1 A stellarator with helical magnetic axis

5.4.2. Geometry

First of all the geometry has to be chosen. Two problems prevent us from taking the straightforward approach that we take the geometry to be the reactor geometry. The first one is that there is no recent detailed reactor design. The second one, more serious, is the following: if we make some estimates, based on the available theories for the geometry of a reactor, and take into account constraints, we would obtain for the experiment a rather large scale.

It was therefore felt that it would be more appropriate at first, to take the geometry such that those theories, upon which the geometry of a reactor would be based, could be tested under easier conditions. The approach to define the geometry has thus been to choose it such that the constraints resulting specifically from the geometry, would be the least stringent.

In order to achieve this, we have first divided the parameters upon which the geometry depend, on "soft" and "hard" parameters. The soft parameters being current in the coils, while the hard parameters are those that are less easily changeable once the machine is built (number of periods, ratio of coils size to

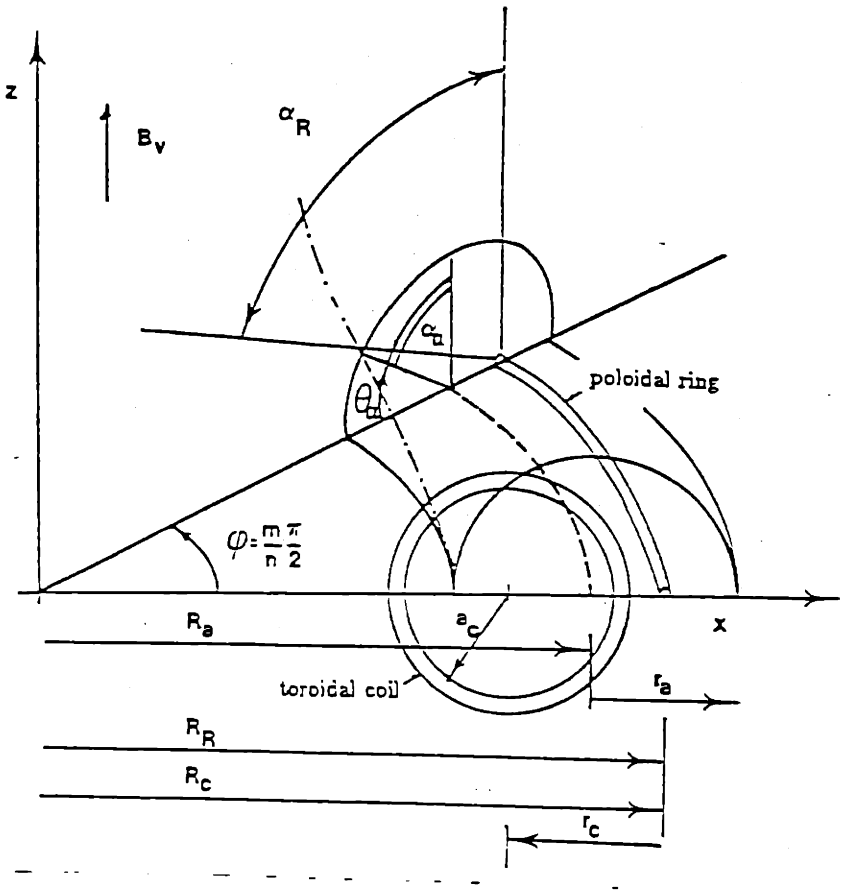

Figure 5.2 Definition of some geometric parameters

overall size, etc...). A relationship between the geometry and the soft parameters (current in the coils) was identified and used to make the geometry thus function of the hard parameters only. The choice of the hard parameters was then made such that the constraints resulting from the geometry were the least stringent.

The relationship between the soft parameters and the geometry is based on the assumption, confirmed by numerical calculations, that the magnetic axis is a helical line which can be defined as (Fig. 5.2)

$$r = r_a$$

$$R = R_c$$

$$n\phi = \theta + \alpha_c \sin\theta$$

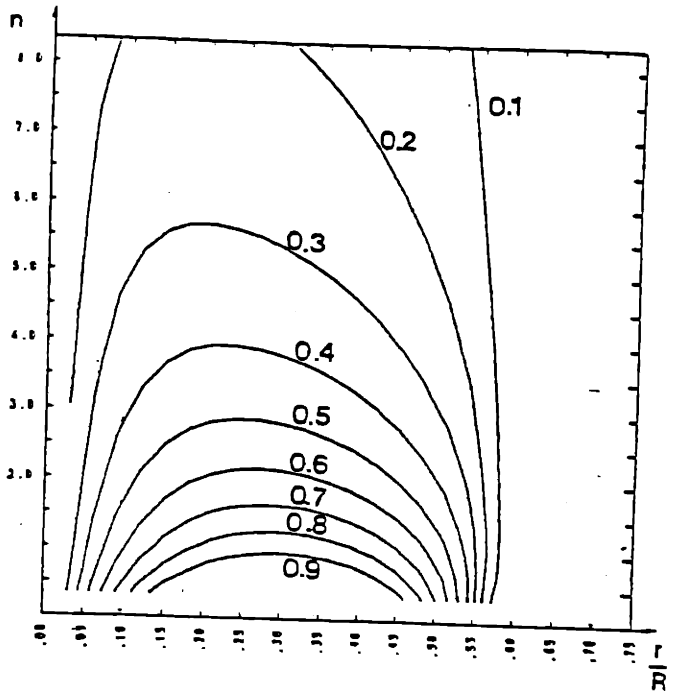

Figure 5.3 Constraints on $\frac{B}{R}$ for fixed bore of the coils and $J = 2kA/cm^2$.

We have developed a simple model that explains the variations of r_a, R_a, α_a with the ring current and the vertical field. The model also gives some simple analytical estimates for the ring current I_R and the vertical field B_v to obtain $r_a = r_c$ and $R_a = R_R$, namely,

$$I_R = \frac{n 2\pi B\phi}{\mu_o}\left(\frac{r_a}{R_R}\right)^2$$

$$B_v = -\frac{\mu_o}{2\pi}\frac{I_R}{R_c}$$

In a more refined version the model gives very accurately and efficiently the geometric parameters of the magnetic axis as a function of the ring current and the vertical field. Those relations allows us to make the constraints, specifically related to the geometry, function of the "hard" parameters only.

A first constraint is the following. In order to preserve as much as possible helical symmetry we need that the normal to the magnetic axis always points in the direction of the ring. This requires

$$\left(\frac{n}{m}\right)^2 = \frac{1 - \frac{r_c}{R_c}}{\frac{r_c}{R_c}}\left[1 + \sum \alpha_l\right]^2$$

Other constraints are set by requirements of non interference of the coils on the inside. For a fixed ratio of the bore of the coil to its displacement from the ring ($\delta = \frac{b_c}{r_c} = 0.5$), the limits are shown in Figure 5.3. Note that the value of $\frac{B}{R}$ drops drastically for low $\frac{r}{R}$ value because of the presence of the ring, while at large $\frac{r}{R}$ value the value drops too because of interference at the center. If we now allow the bore of the coil to vary and take into account the requirements of ripple on the outside, then the constraints become even more stringent.

The underlying reason is that size of the coils on the inside of the ring is constrained by non-interference requirements. The constraint, because of ripple requirement, is on the outside coils. For a tokamak the ripple problem can be solved by increasing the size of the coils, without a very large effect on the overall size of the system. In this case however, an increase in the size of the toroidal coils results immediately in an increase in the size of the whole system.

The size of the plasma is not only affected by ripple requirements, it is also affected by the angle between the magnetic axis and the plane of the coils. For a fixed value of $\frac{r_c}{R}$, four effects tend to favor a lower n number.

1. the ring cross section can be smaller, since the ring current is proportional to n. This gives more space for the toroidal coils and the plasma.
2. the toroidal magnetic field is larger, for the same number of coils and current in the coils since the length of the magnetic axis goes as $2\pi R\sqrt{1+(n\frac{r_c}{R})^2}$
3. the ripple is lower for the same number of coils at lower n number.
4. the angle between the tangent to the magnetic axis and the ϕ direction is smaller, providing a better utilization of the coil.

It is true that when we go to larger n, we have all incentive to go to lower $\frac{r}{R}$ so that those four effects are less marked. Going to lower $\frac{r}{R}$ however decreases the bore of the coils and thus the plasma size, for given overall size (R).

Those considerations, together with constraints related to MHD and transport result in a choice for the geometry $n = 2$, $\frac{r_c}{R} = 0.38$, $\frac{b_c}{r} = 0.255$. This finalizes the geometry. The constraint resulting from the geometry is the given by

$$\frac{\frac{B}{17}}{\frac{J}{2\times10^7 A/m^2}\left(\frac{R}{1m}\right)} < 0.45.$$

Keeping in mind this constraint relating B, R and J we have thus now a machine whose size and magnetic field we can vary in order to apply similarity scaling laws.

5.4.3. Choice of the dimensionless parameters

Based on an adaptation of the standard neoclassical theory we have that, for our geometry, $\nu_* = 100$ at the transition between plateau and P.S. (if we define $\nu_* = 1$ at the transition Banana-Plateau). In addition, in order to avoid effects due to toroidality, we need $\nu_* > 1$. MHD theory predicts, again for our geometry, a β equilibrium limit of about 3%. We will later choose ν_* and β within the range $1 < \nu_* < 100$ and $\beta < 3\%$. By fixing those values, and applying the three steps constraints, when we vary a and B to find the minimum scale, we are comparing equivalent machines, machines that would test the theory to the same extent.

5.4.4. Application of the geometrical, plasma physics and technological constraints

The geometrical constraint $\frac{\frac{B}{17}}{\left(\frac{J}{2\times10^7 A/m^2}\right)\left(\frac{R}{1m}\right)} < 0.45$, can be translated in a R, B diagram into requirements for current density. In view of actual limits for the current density, this will set the possible mode of operation (if we want $\frac{B}{R} > 0.45$, then we need $J > 2kA/cm^2$, and only pulsed operation is possible). This is shown in Figure 5.4.

With β and ν_* as dimensionless parameters ; R and B as our degrees of freedom, we can express the density n, and the temperature T as

$$\frac{n}{10^{20}} = 4.73\left(\frac{B^4}{R}\beta^2\nu_*\right)^{1/3}$$

$$\frac{T}{e} = 2.62\times10^3(RB^2\frac{\beta}{\nu_*})^{1/3}$$

It can be easily shown that, within the range $1 < \nu_* < 100$, $0.3\% < \beta < 3\%$, dropping N_λ as parameter does not result in stringent constraints on R, B. Dropping $\frac{\rho_e}{a}$ as parameter however result in the constraint.

$$R^{5/6}B^{2/3} > 1.48(\frac{\beta}{\nu_*})^{1/6}$$

The na limit (related to avoidance of a regime that may be dominated by neutrals from the edge) translates into

$$B^2R > 0.027\beta^{-1}\nu_*^{-1}$$

Heating methods will further narrow the design window. We have investigated two cases : the use of ECRH and the use of ICRH. Accessibility of ECRH waves requires $B^2R > \frac{1.2\times10^5}{\alpha^3}\beta^2\nu_*$, where $\alpha(= \frac{\omega_{pe}{}^2}{\omega_{ce}{}^2} = 1, 2, 4)$ depends on which wave is launched.

Based on estimates of power requirement, we have chosen the values $\nu_* = 10$ and $\beta = 1\%$ for the dimensionless parameters. Power requirements for those values of β and ν_* are shown in Figure 5.5. The design window for a machine heated by ECRH is then shown in Figure 5.6. It follows from this figure that

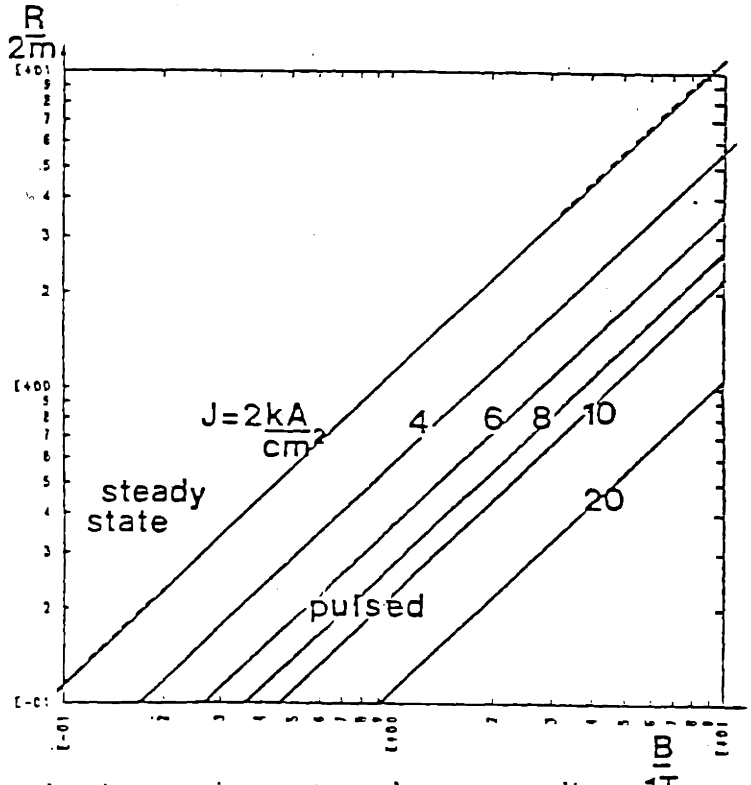

Figure 5.4 Current density requirements and corresponding mode of operation.

there are still choices possible with respect to the actual machine. Machine A ($R = 6m$, $B = 1.75T$) would be the minimum size machine if we used extraordinary wave at the second harmonic.
Machine B ($R = 1.2m$. $B = 3.5T$) the minimum size if we used the extraordinary wave at the fundamental. If in addition we want the machine to be able to operate in steady state, then the minimum size is machine C ($R = 4m$, $B = 1.8T$, with extraordinary wave heating at the fundamental).

5.4.5. Finalizing the choice

In order to finalize the choice within the design window, we estimated the capital cost of the machine, and the cost of the heating system. The capital cost of the machine was calculated, for a reference design, from the weight of the components, and an accepted cost/weight factor. For other machines the cost was estimated by scaling the weight of the components appropriately with B and R. The cost of the heating system was taken for ECRH to be $3\$/W$.

The total cost of the machine is then shown in Figure 5.7. Within the constraints, the minimum cost machine would then be $R = 1.2m$, $B = 3.5T$, $n = 2.5 \times 10^{20}/m^3$, $T = 650eV$ and about $2MW$ of ECRH power.

Other choices could have been made, for example if we also had to include the power supplies for the machine, or if we wanted a steady state machine. A similar approach for a machine heated by ICRF results in $R = 1.4m$, $B = 2.5T$.

5.5. Recommendations

We have seen that concept specific geometrical constraints play an important role in the minimum scale of an experiment. It is tempting to think of a work that would concentrate on identifying those constraints for all the different concepts to complement our work. In our work we have concentrated on the method and looked mainly at concept independent constraints. The method we

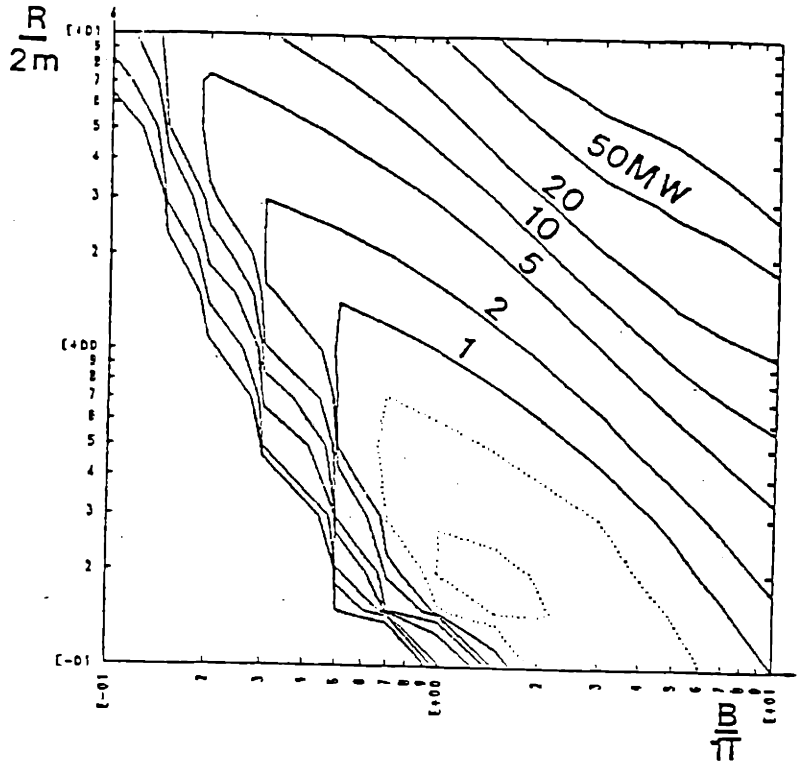

Figure 5.5 Power requirements for a helical axis stellarator heated by ECRF waves as a function of size and magnetic field.

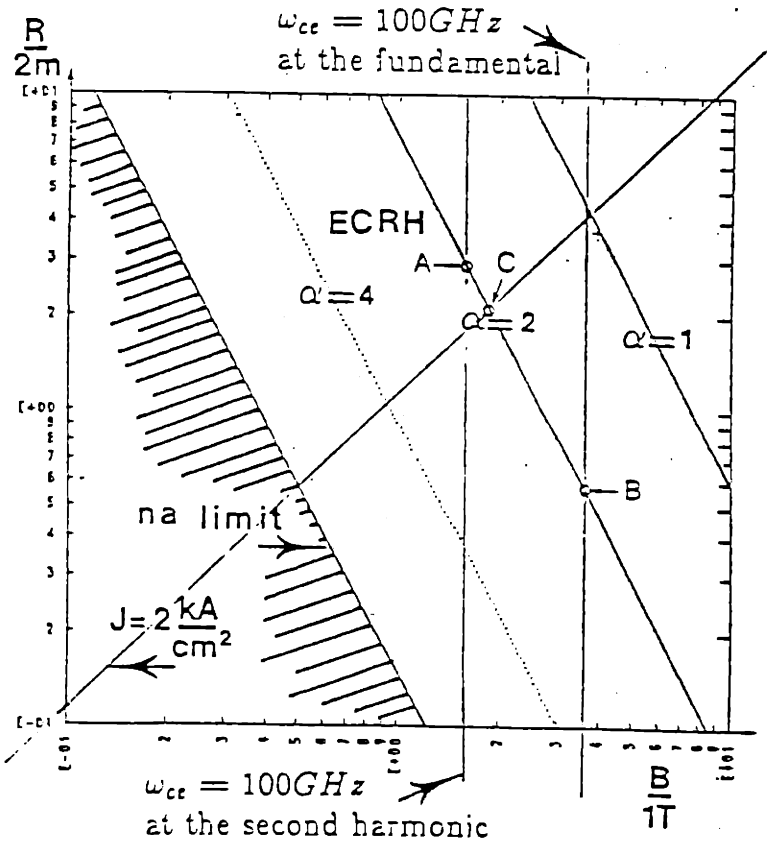

Figure 5.6 Design window for ECRH heated machines

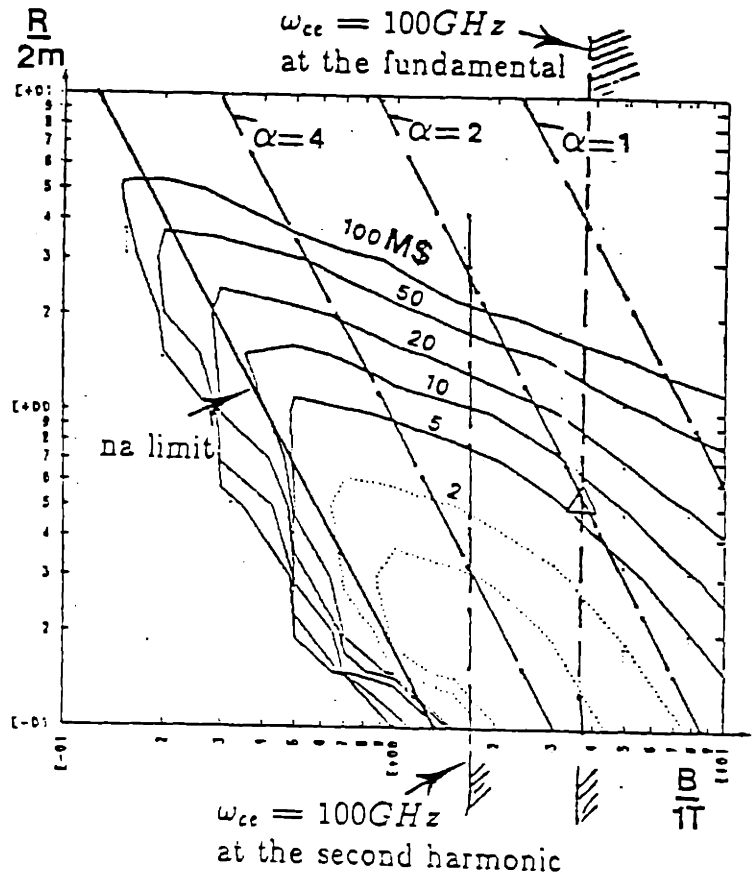

Figure 5.7 Capital cost (machine and heating power) for a helical axis stellarator heated by ECRF waves as a function of size and magnetic field.

---

have developed, together with all the constraints, could then provide a complete design methodology for any toroidal experiment.

More in particular for the configuration we have chosen for the helical axis stellarator (circular toroidal coils, a poloidal ring, no topological link between both) may be the configuration one would prefer for a helical axis stellarator reactor. For an experiment however, one may be better advised to produce the magnetic configuration by using helical coils, or, if one still wanted to avoid using helical coils, consider the possibility of linking the toroidal coils with the

poloidal ring. The resulting geometrical constraints would be less stringent than those we obtained.

Appendix A. Current Density in Water Cooled Coils

We have set up a model to calculate the maximum allowed current density based on the heat removal capacity of water cooling, both under steady state and pulsed conditions.

Model

We consider a square conductor of dimensions L, with an internal cooling channel, diameter d (Fig. A.1). We further define $\ell = 1/2(L - d), \ell$ being the distance from a side to the cooling channel. The heat generated within the copper per unit volume can be written as ρJ^2. The heat will increase the temperature of the copper and be removed by the cooling water.

Writing down a heat balance equation for the volume shown in Fig. A.2 we obtain

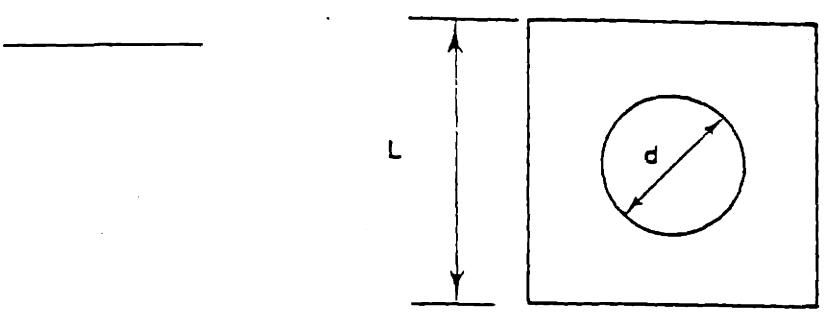

Figure A.1 Model of Conductor used

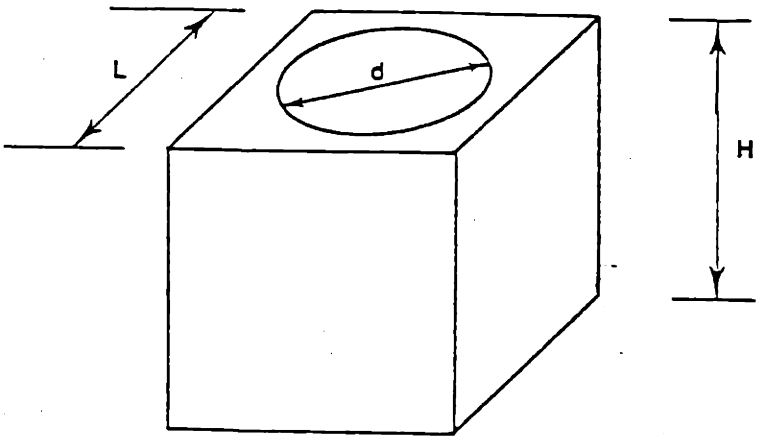

Figure A.2 Volume on which heat balance equation is written down.

$$\rho J^2\left(L^2-\frac{\pi d^2}{4}\right)H = c_p\gamma\left(L^2-\frac{\pi d^2}{4}\right)H\frac{dT_{\text{copper}}}{dt}+\left(T_{\text{wall}}-T_{\text{coolant}}\right)h\pi Hd \tag{A.1}$$

where

c_p	is the heat capacity of copper in J/°C kg,
γ	is the density of copper in kg/m^3,
T_{copper}	is an average copper temperature,
$T_{\text{wall}}-T_{\text{coolant}}$	is the temperature drop at the copper-coolant interface,
h	is the heat transfer coefficient in W/m^2°C for water (turbulent flow) in round tubes.

The heat transfer coefficient h can be approximated by [101]

$$h = 0.14\left(1+1.5\times 10^{-2}\ T_{\text{coolant}}\right)\frac{v^{0.8}}{d^{0.2}}$$

where v is the fluid velocity in m/s, d is the cooling passage diameter in m, and T_{coolant} is the average water temperature in degrees centigrade. The

temperature rise in the copper is given by [1]

$$\Delta T_c = \frac{W_v \, \ell^2}{2k} \tag{A.2}$$

where W_v is the local heat input density in watt/m^3, k is the thermal conductivity of copper (3.86×10^{-2} W/m°C), and ΔT_c is the temperature rise at the hot spot in °C and is approximately equal to $T_{\text{copper}} - T_{\text{wall}}$.

Defining λ = Area copper/Total area = $\frac{L^2 - \pi\ell^2}{L^2}$ we obtain

$$\lambda \rho J^2 = \lambda c_p \gamma \frac{dT_{\text{copper}}}{dt} + (1-\lambda)\frac{4}{d}\left(T_{\text{wall}} - T_{\text{coolant}}\right)h \tag{A.3}$$

$$T_{\text{copper}} - T_{\text{wall}} = \frac{\lambda \rho J^2 \ell^2}{2k} \tag{A.4}$$

This can be combined into

$$\frac{dT_{\text{copper}}}{dt} + \frac{T_{\text{copper}}}{\tau} = \frac{\rho J^2}{c_p \gamma}(1+\epsilon) + \frac{T_{\text{coolant}}}{\tau} \tag{A.5}$$

$$T_{\text{wall}} = T_{\text{copper}} - \frac{\rho J^2}{c_p \gamma}\,\epsilon\tau \tag{A.6}$$

where

$$\epsilon = (1-\lambda)\frac{4h}{d}\frac{\ell^2}{2k} \tag{A.7}$$

$$\tau = \frac{\lambda}{1-\lambda}\frac{d}{4h} c_p \gamma \tag{A.8}$$

The meaning of the two parameters ϵ and τ is as follows: ϵ can be thought of as the ratio of temperature drop ΔT_{copper} and $(T_{\text{copper}} - T_{\text{coolant}})$ in steady state. Indeed equating $\Delta T_{\text{copper}} = \epsilon(T_{\text{copper}} - T_{\text{coolant}})$ we obtain $\epsilon = (1-\lambda)\frac{4h}{d}\frac{\ell^2}{2k}$ as defined.

In Fig. A.3 we have plotted the regions in which ϵ can be neglected. For a given fluid velocity the value of ϵ is given as a function of the dimensions of the conductor in Fig. A.4.

If we assume $\rho, c_p, \epsilon, \tau$ to be independent of the temperatures and taking cycles where during a time t_1, J is constant, while during a time t_2, J is equal to zero, we can solve for the maximum temperature

$$T_{\text{copper}} = T_{\text{coolant}} + \frac{\rho\tau J^2}{c_p\gamma}(1+\epsilon)\frac{1-e^{-t/\tau}}{1-e^{-\frac{t_1+t_2}{\tau}}} \qquad (A.9)$$

or we can calculate the maximum allowable average current density as a function of the other parameters.

$$J = \sqrt{\frac{c_p\gamma}{\rho\tau(1+\epsilon)}\left[T_{\text{copper}} - T_{\text{coolant}}\right]\frac{1-e^{-\frac{t_1+t_2}{\tau}}}{1-e^{-t/\tau}}} \qquad (A.10)$$

In view of the results of Figs. A.3 and A.4 it is completely justified to neglect ϵ.

The pulsed or steady state nature is contained in the factor $\frac{1-e^{-\frac{t_1+t_2}{\tau}}}{1-e^{-t_1/\tau}}$. We have plotted this as a function of t_1 and t_2 in Fig. A.5. Five regions can be readily identified and are indicated in the figure. It is clear that a major parameter, to decide whether an experiment in this respect is steady state or not, is τ. Recalling from Eq. (A.8)

$$\tau = \frac{\lambda}{1-\lambda}\frac{d}{4h}c_p\gamma \qquad (A.8)$$

Substituting the value for $h = 0.14(1 + 1.5 \times 10^{-2}T_{\text{coolant}})\frac{v^{0.8}}{d^{0.2}}$

we obtain

$$\tau = \left(\frac{\lambda}{1-\lambda}\right)\ \frac{c_p\gamma}{0.56\left(1+1.5\times10^{-2}T_{\text{coolant}}\right)}\ \frac{d^{1.2}}{v^{0.8}} \qquad (A.11)$$

If we take $T_{\text{coolant}} \approx 30°\text{C}$ then $1 + 1.5 \times 10^{-2}T_{\text{coolant}} \simeq 1.5$. Further with $c_p\gamma \simeq 3.97 \times 10^6$ J/m^{3}C, we can investigate the independence of τ on v, d, L (through λ). This is shown in Fig. A.6 for $v = 1$ m/s. Increasing the fluid velocity will decrease the value of τ (Eq. (A.11)) with a 0.8 power.

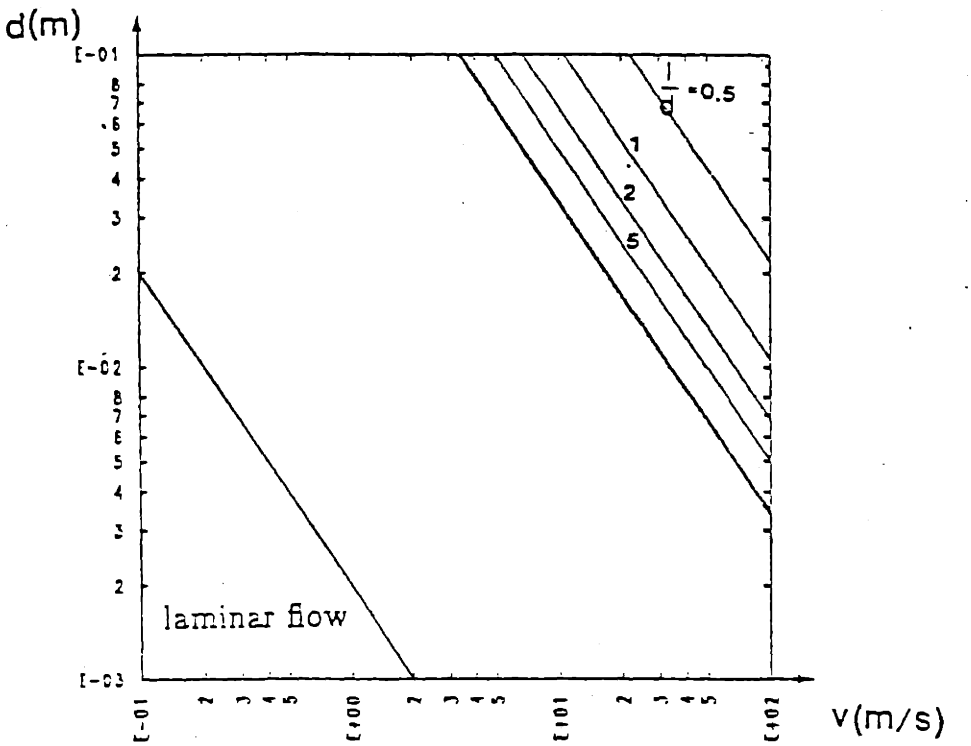

Figure A.3 Region where ϵ can be neglected. The lower left corner is the region of laminar flow. In the center region the temperature drop wall fluid always dominates the temperature drop in the copper. In the upper right region the values of $\frac{l}{d}$ are shown for which the temperature drop wall-fluid equals the temperature drop in the copper. For smaller $\frac{l}{d}$ the wall-fluid temperature drop dominates.

In steady state ($t_2 \ll t_1$) the current density is given by

$$J = \sqrt{\frac{c_p \gamma}{\rho \tau}\left(T_{\text{copper}} - T_{\text{coolant}}\right)} \qquad (A.12)$$

This value is plotted in Fig. A.7 again for $v = 1$ m/s assuming a maximum

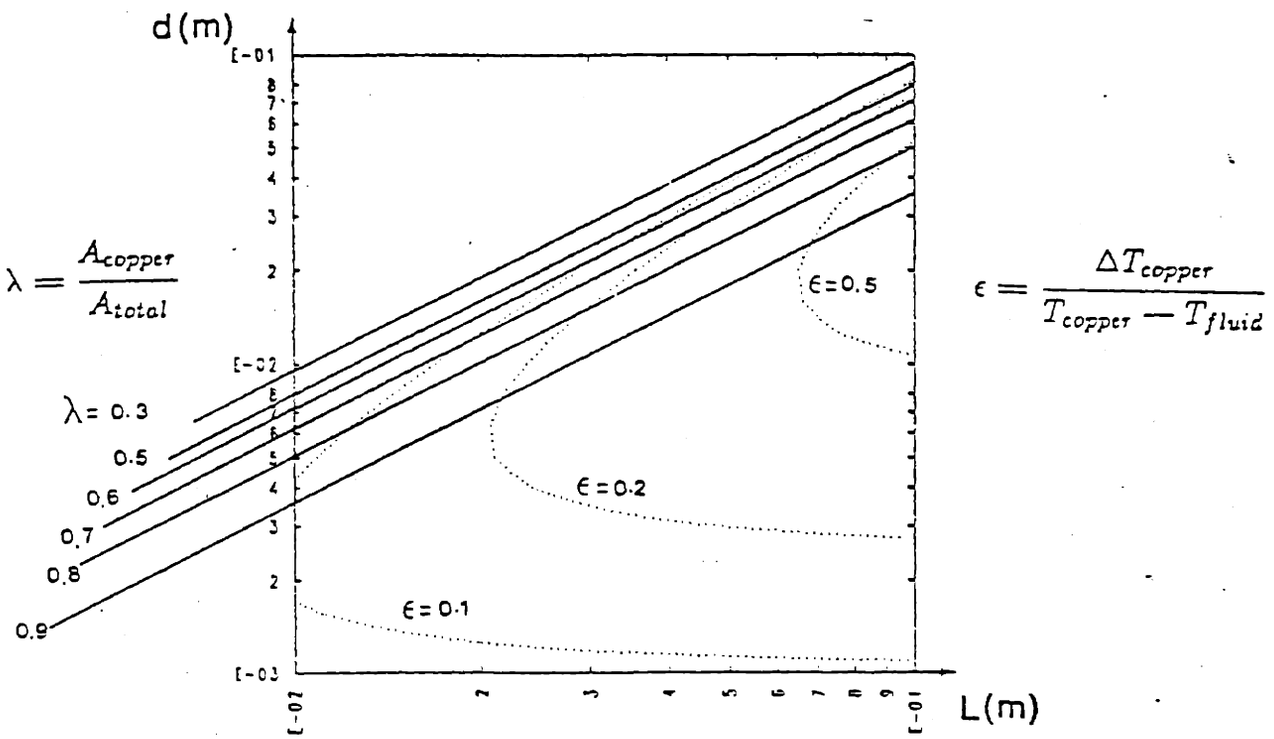

Figure A.4 Values of ϵ for $v = 2$ m/s. For v smaller the value of ϵ becomes even smaller, so that the temperature drop $T_{\text{copper}} - T_{\text{fluid}}$ always dominates the temperature drop in the copper.

$T_{\text{copper}} - T_{\text{coolant}}$ of 50°C and with $\rho = 1.72 \times 10^{-8} \Omega m$. The dependence on velocity is a 0.4 power. Under pulsed conditions the current density can be increased by a factor

$$\sqrt{\frac{1 - e^{-\frac{t_1+t_2}{\tau}}}{1 - e^{-t_1/\tau}}}$$

Combining Fig. A.7 with the square root of the values given in Fig. A.5 allows us to calculate the current density for arbitrary conditions. A question one may ask is the following: assuming an experiment of given t_1, is it more interesting to choose a small τ (small L, large d) in order to increase $J \sim \sqrt{\frac{1}{\tau}}$, and work steady state $t_1 \gg \tau$, or to take a larger value of τ, so that although the steady state value of J is smaller, one can take advantage of the increase of

$$\sqrt{\frac{1 - e^{-\frac{t_1+t_2}{\tau}}}{1 - e^{-t_1/\tau}}}$$

To investigate this we have plotted in Fig. A.8 the value

$$J = \sqrt{\frac{c_p \gamma}{\rho \tau} \Delta T \left(\frac{1 - e^{-\frac{t_1+t_2}{\tau}}}{1 - e^{-t_1/\tau}} \right)}$$

for $t_2 \to \infty$ and $t_1 = 10$ s.

If $t_1 \gg \tau$ this will give us the steady state value, if $t_1 \ll \tau$ it will give us the maximum allowable value, assuming only one pulse and infinite cooling time. It can be seen that for sufficient large L it is indeed more interesting to decrease d, thus increasing τ and work in a pulsed mode. For small τ the opposite is true (it is better to work steady state by increasing d, thus reducing τ).

In Fig. A.9 we have plotted the local current density (in copper only). This is a measure of how efficiently the copper is used, and using this criterium it is always better to go to steady state. The choice of $t_1 = 10$ s for the pulse length is intermediate between two extremes and thus also gives the two possible

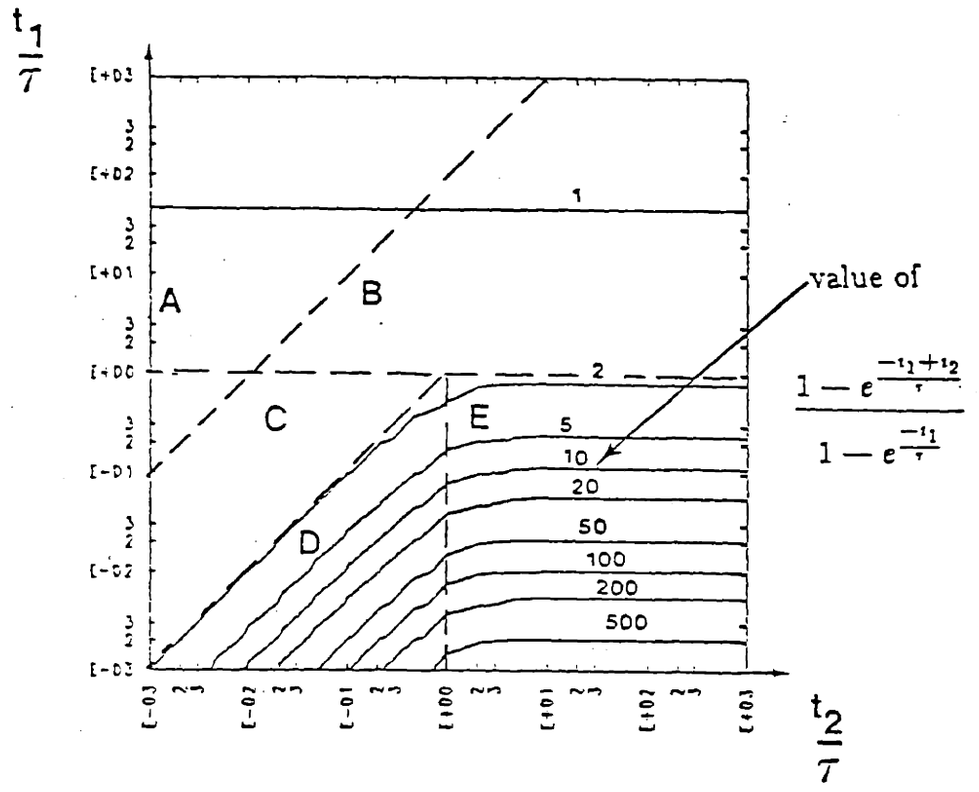

Region A $t_2 \ll t_1 \rightarrow$ steady state

Region B $t_1 \gg \tau \rightarrow$ steady state

Region C $t_1 < \tau, t_2 < \tau$ and $t_2 < t_1 \rightarrow$ steady state

Region D $t_1 < \tau, t_2 < \tau$ and $t_2 > t_1 \rightarrow$ quasi steady state

Region E $t_1 < \tau, t_2 > \tau$ pulsed operation

Figure A.5 Region of pulsed and steady state operation.

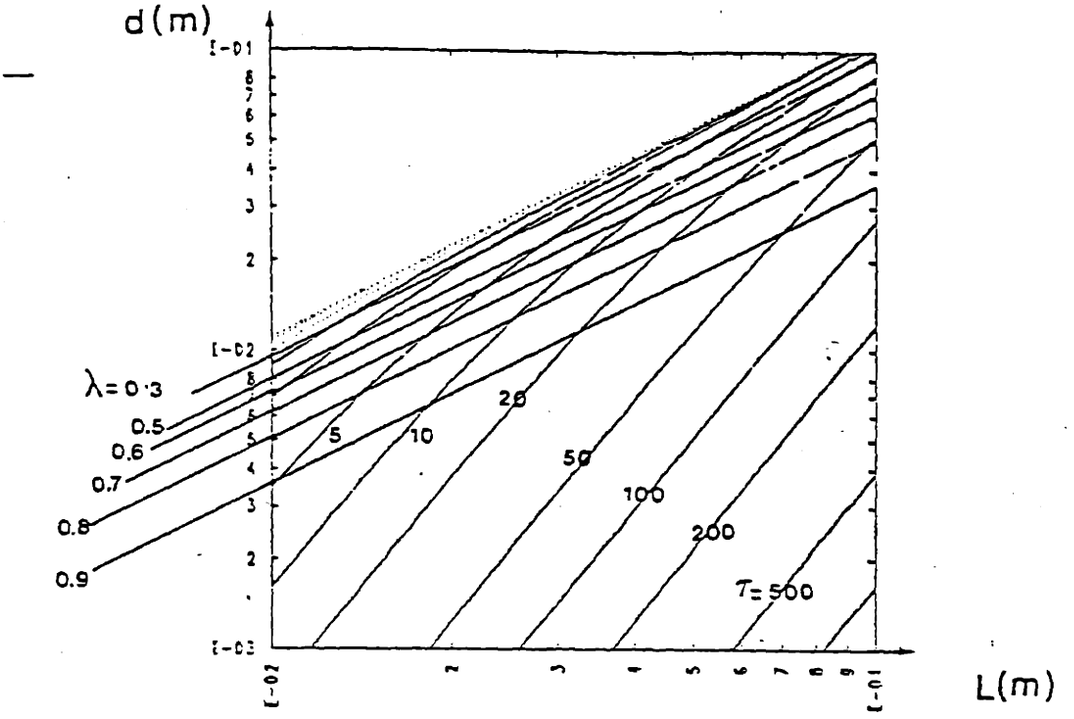

Figure A.6 Value of the parameter τ for a fluid velocity of 1 m/s.

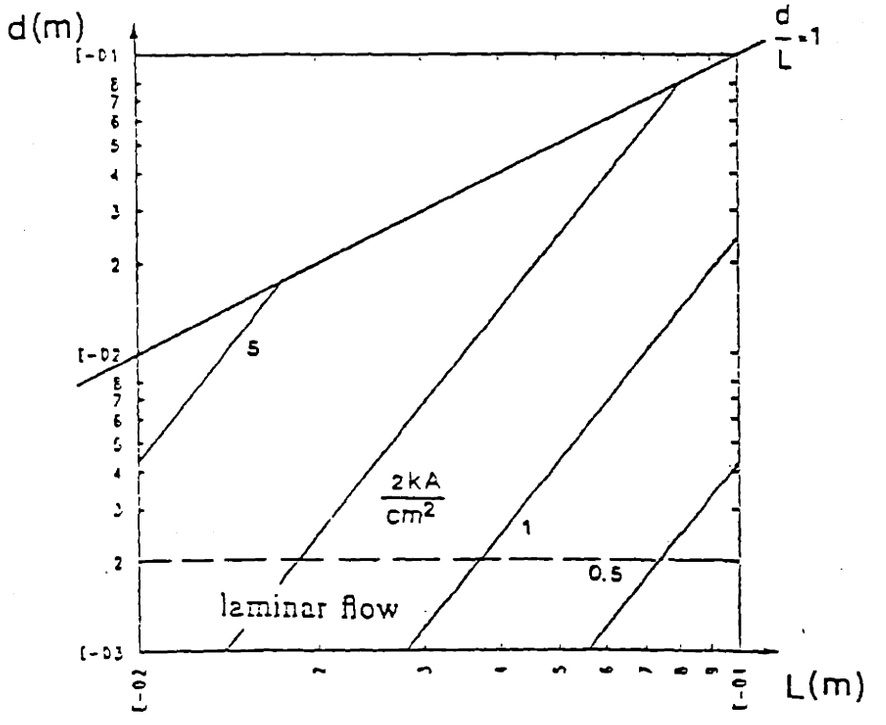

Figure A.7 Maximum average current density under steady state condition for $v = 1$ m/s.

solutions, either steady state or pulsed. For $t_1 = 100$ s one can see from Fig. A.10 that it is always interesting to go to steady state for a given L. However, one can obtain the same average current density in pulsed mode by decreasing L and d (i.e., $d = 3$ cm, $L = 5.5$ cm, steady state gives 2 kA/cm^2 just as $d = 0.2$ cm, $L = 2$ cm will in pulsed mode). It can be seen from Fig. A.11 that the local current density goes down drastically in pulsed mode.

For $t_1 = 2$ s, Fig. A.12 shows that for given L it is more interesting to go to pulsed mode. The local current density indeed is nearly independent of L and d (Fig. A.13) and thus increasing d/L only brings down the average current density.

Increasing the fluid velocity decreases the value of τ (with $v^{-0.8}$) and thus tends to favor the steady state option at lower values of t_1.

Conclusion

The pulse length of an experiment puts it, from the point of view of current density/heat removal capacity in the conductors, rather unambiguously in one of two classes: pulsed mode or steady state. For a pulse length smaller than about 10 s, it is best to work in pulsed mode and the maximum current density is given by $J = \sqrt{\frac{c_p \gamma}{\rho t_1}}\,\Delta T$ being $J \simeq 10$ kA/cm^2 $\sqrt{\frac{1\text{s}}{t_1}}$ maximum for $\Delta T = 50°$C and $\rho = 1.72 \times 10^{-8} \Omega m$. For a pulse length larger than about 10 s, a steady state current density of $J \simeq 2$ kA/cm^2 is a reasonable value for a conductor size of 5 cm $\times$ 5 cm.

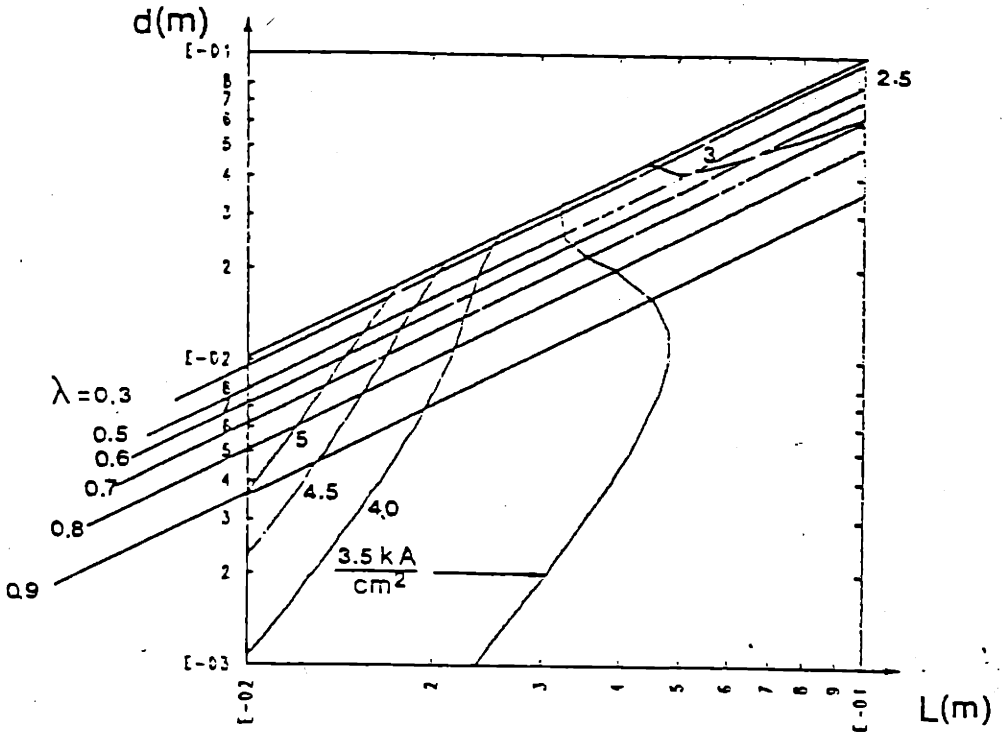

Figure A.8 Maximum average current density (including upgrading when pulsed). $t_i = 10$ s, $v = 1$ m/s.

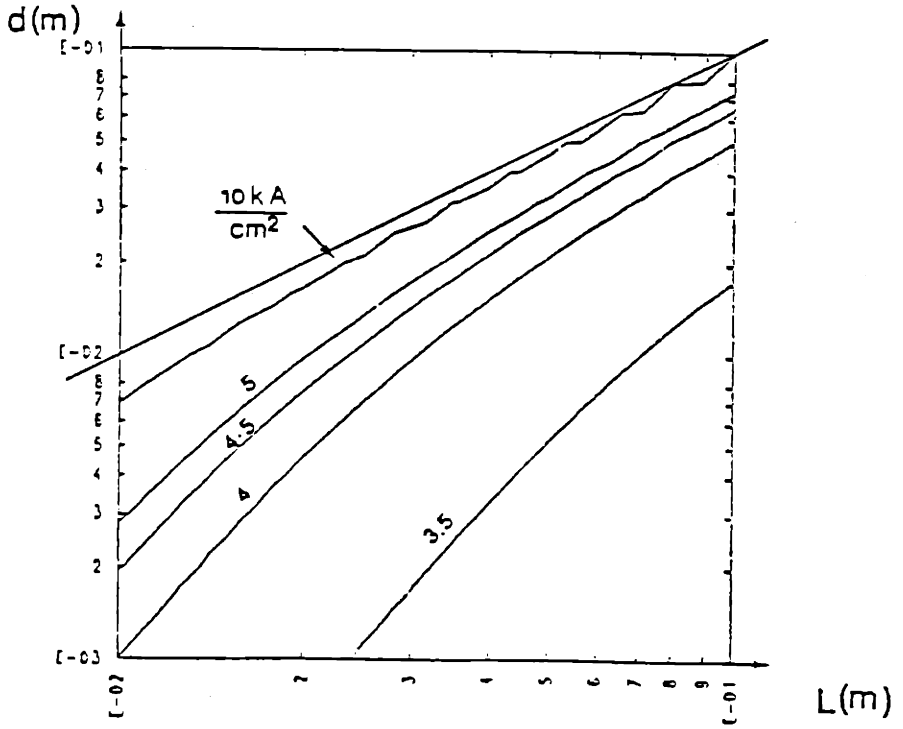

Figure A.9 Maximum local current density (including upgrading when pulsed).

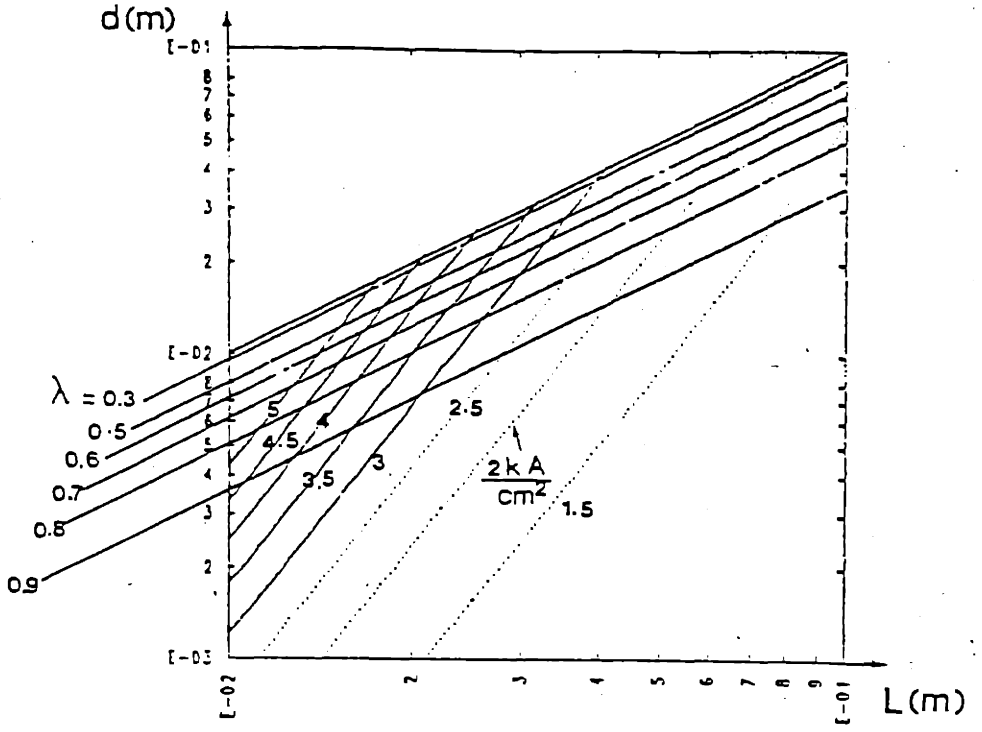

Figure A.10 Maximum average current density (including upgrading when pulsed). $t_1 = 100$ s, $v = 1$ m/s.

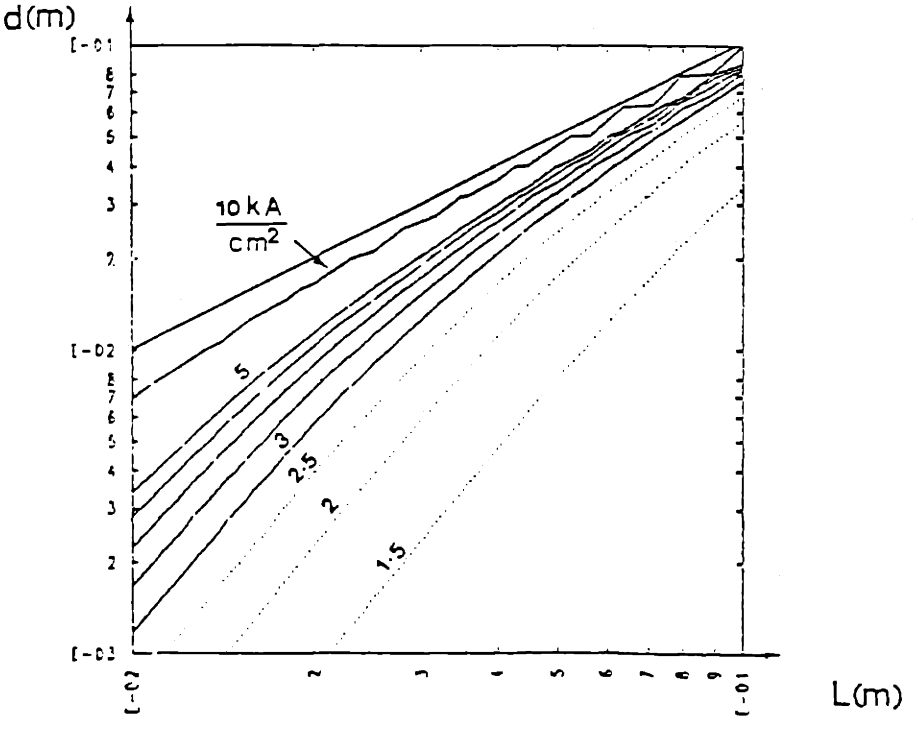

Figure A.11 Maximum local current density (including upgrading when pulsed).

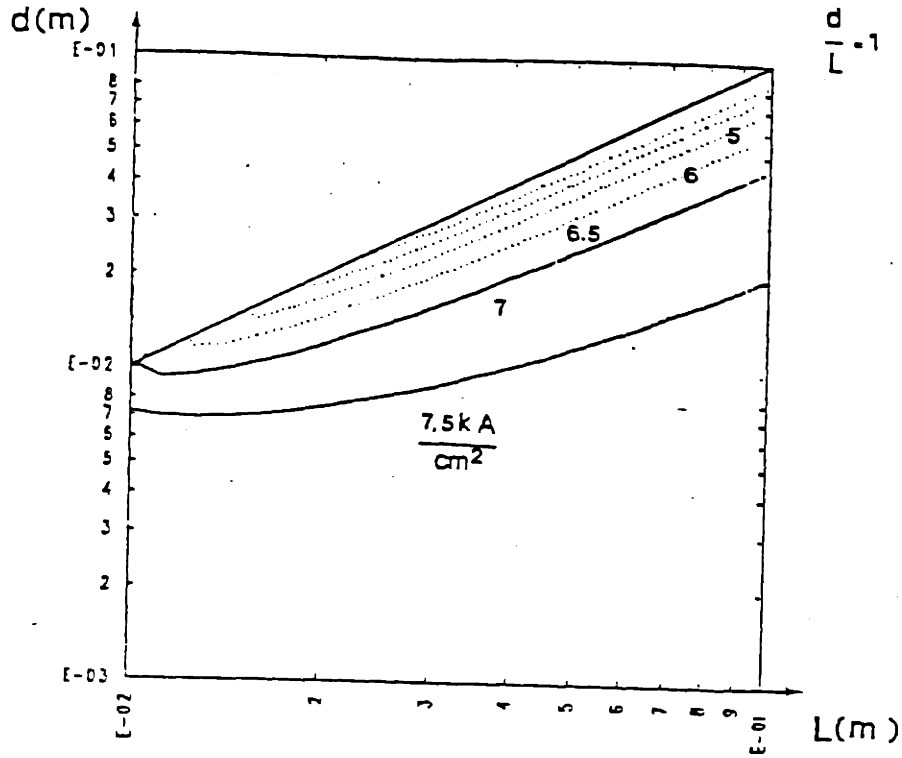

Figure A.12 Maximum average current density (including upgrading when pulsed). $t_1 = 2$ s, $v = 1$ m/s.

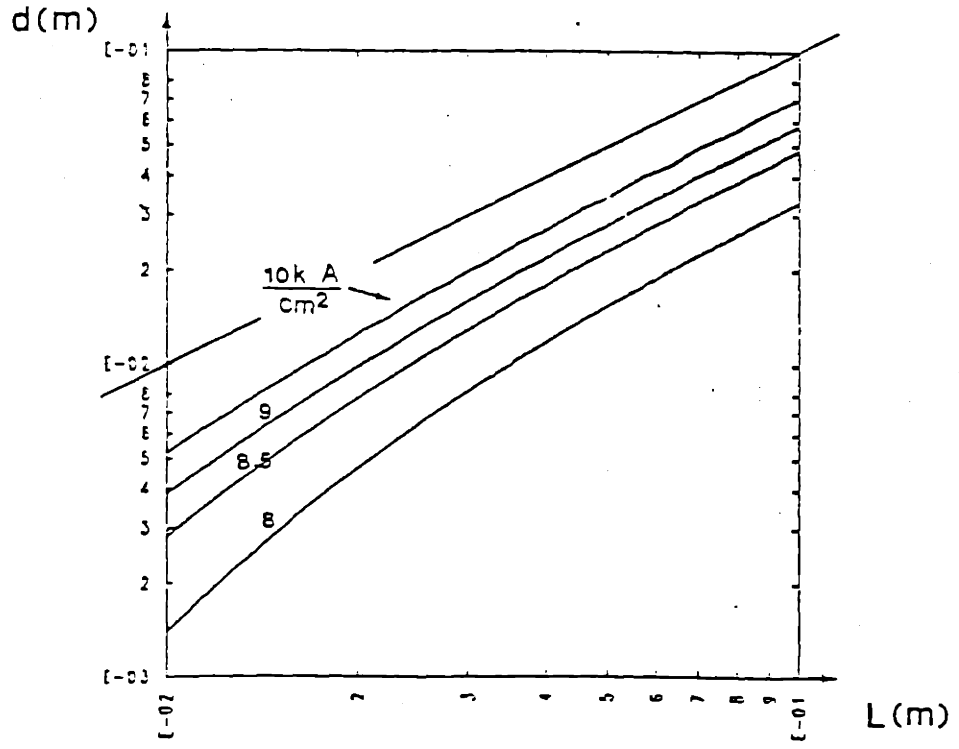

Figure A.13 Maximum local current density (including upgrading when pulsed).

Appendix B. A Model for Stresses in Circular Toroidal Magnets

Introduction

Except for some notable exceptions, like the spheromak and the torsatron most toroidal systems have, as one of their basic components, magnetic coils that provide the main toroidal field. This analysis was set up to calculate stresses in circular coils, as needed in Chapter 3. The model is kept sufficiently simple to investigate a wide range of possible structural support systems and the influence of the aspect ratio. We also wanted to clarify two points :

1. for some of the published reference designs, using circular coils, the structural weight scales as B, not B^2 [103]. Since in chapter 3 and 4 we use a relationship between mass and magnetic field, it was important to understand why these reference designs give $Mass \sim B$.

2. there has been some debate on the advantages and disadvantages of circular coils and "moment-free" D-shaped coils. The moment-free, D-shaped were found not to be moment free, while circular coils turned out not be dominated by bending stresses.

Since the toroidal coils make up a rather large fraction of the total system cost, both the conductor and magnet structure being significant cost items, large efforts have gone into optimizing their design.

There have been basically two approaches.

One approach considers the coils separately, neglecting the out of plane structure, and optimizes the shape of the magnet to reduce bending moments. The first

analysis by File, Mills, and Sheffield [137] which used a filament in a simple 1/R field, supported by a central cylinder, was later further refined by taking into account the finite thickness of the coils [138] and the ripple in the toroidal field [137, 139]. An attempt to consider not only the coil shape as the primary design parameter but also proper design of the center support structure in order to minimize in plane bending stresses, was presented by Ojalvo and Zatz [140].

A second approach has been to model the coils, together with the out of plane structure as a continuous rotationally symmetric shell. Gray, et al. approximated the shell by a membrane [141]. Bobrov and Schultz [142] used Reissner shell theory to analyze orthotropic shells of finite thickness and pointed out that choosing the shape of the coils so as to minimize bending stresses may not be the optimum strategy. The reason is that the additional circumferential length needed to give the coil its bending free shape may more than outweigh the material savings resulting from its bending free properties.

Because of the intrinsic difference in the two approaches, each approach has tended to concentrate on a different way to support the net inward force resulting from the magnetic load. A central column is necessary to take the net force when the coils are considered separately while the shell approach is easiest when one assumes this force to be completely taken up internally. The importance to distribute appropriately the load between both a shell structure and a central cylinder was evident from the design of the toroidal field coils for TFTR [143]. Montgomery [144] has pointed out that the natural bending free shape depends strongly on the way the coil is supported. It is thus important to have a model that can include both the effect of the out of plane structure as well as the reaction of a central column in taking up the net inward force.

The model presented in this appendix can achieve this. The coils are considered separately, but the effect of the out of plane structure is included by modeling the coils as beams on elastic foundation. The model is thus more complete than the first approach, and contrary to the second, allows us to give different properties to the coil and the out of plane structure.

Model

The coil is considered as a circular ring of isotropic properties, with an applied load given by the interaction of the coil current I and the toroidal magnetic field B, for which we take a simple 1/R variation

$$p(N/m) = \frac{BI}{2} = \frac{1}{2}\,\frac{\mu_o N I^2}{2\pi R}\,.$$

In this formula N is the number of coils. With $R = R_o + a\cos\theta$, where R_o is the major radius of the geometric center of the ring and a its radius (Fig. B.1), we can write this as

$$P(\theta) = \frac{1}{2}\,\frac{\mu_o N I^2}{2\pi\, R_o}\,\frac{1}{1+\frac{\epsilon}{R_o}\cos\theta}$$

or

$$p(\theta) = p_o\,\frac{1}{1+\epsilon\cos\theta} \qquad (B.1)$$

with

$$p_o = \frac{1}{2}\,\frac{\mu_o N I^2}{2\pi\, R_o} \text{ and } \epsilon = \frac{a}{R_o}\,.$$

The fact that the coil is part of a three dimensional structure is taken into account by assuming a reaction force on the coil proportional to its displacement

$$f(N/m) = ky \qquad (B.2)$$

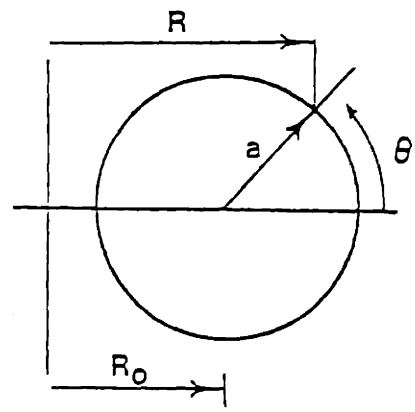

Figure B.1 Model for a toroidal coil.

where f is the reaction force per unit length and y the displacement in the minor radial direction. The reaction constant k can be chosen appropriately to model a very strong interaction (Alcator Bitter plates) or a very weak one (coils not interconnected). Note that here k is assumed to be constant. Two different models are used for the central column, either a concentrated force or a distributed force. The distribution of the reaction between the elastic foundation, modeling the out of plane structure, and the central cylinder can be varied continuously.

The solution is derived from the known solutions of a circular ring on an elastic foundation, subjected to a concentrated force P (Fig. B.2).

From [145] we have

$$y = \frac{Pr^3}{4\alpha\beta EI}\left(\frac{2\alpha\beta}{\pi\eta^2} - A\cosh\alpha\phi\cos\beta\phi + B\sinh\alpha\phi\sin\beta\phi\right)$$

$$M = -\frac{Pr}{2}\left(\frac{1}{\pi\eta^2} + A\sinh\alpha\phi\sin\beta\phi + B\cosh\alpha\phi\cos\beta\phi\right)$$

$$Q = -\frac{P}{2}[(\alpha A - \beta B)\cosh\alpha\phi\sin\beta\phi + (\beta A + \alpha B)\sinh\alpha\phi\cos\beta\phi]$$

$$N = \frac{P}{2}\left(\frac{\eta^2 - 1}{\pi\eta^2} - A\sinh\alpha\phi\sin\beta\phi - B\cosh\alpha\phi\cos\beta\phi\right)$$

where

$$\eta = \sqrt{\frac{r^4 k}{EI} + 1}$$

$$\alpha = \sqrt{\frac{\eta - 1}{2}}$$

$$\beta = \sqrt{\frac{\eta + 1}{2}}$$

$$A = \frac{\alpha\cosh\alpha\pi\sin\beta\pi + \beta\sinh\alpha\pi\cos\beta\pi}{\eta\left(\sinh^2\alpha\pi + \sin^2\beta\pi\right)}$$

$$B = \frac{\alpha\sinh\alpha\pi\cos\beta\pi - \beta\cosh\alpha\pi\sin\beta\pi}{\eta\left(\sinh^2\alpha\pi + \sin^2\beta\pi\right)} \qquad (B.3)$$

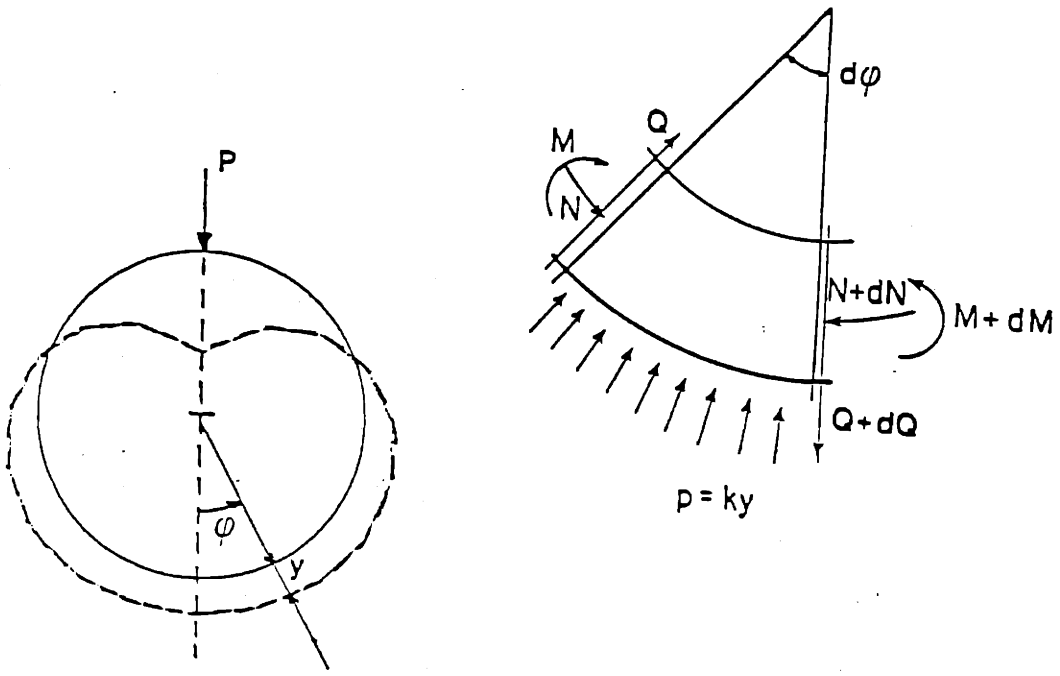

Figure B.2 Definition of angles, moments and forces. Also shown is the displacement y for a point force P.

These results, which give $y(\phi)$ for a force applied at $\phi = \pi$, can also be considered as the displacement y at π for a force at ϕ (Fig. B.3). If we take the force to be $P = \ell(\phi)\ r d\phi$ and perform the integration we can find the displacement at $\phi = \pi$ for a distributed force $\ell(\phi)$. It can further be generalized by making the reference axis not vertical, but at an angle ψ (Fig. B.4). Still measuring ϕ from this reference axis we can get the displacement at an arbitrary location, for an arbitrary distribution of the force, and more particularly for

$$P = -p(\theta) r d\phi = -p_o \frac{r d\phi}{1 + \epsilon \cos(\pi + \psi + \phi)}.$$

We thus have

$$y(\psi) = \int_{-\pi}^{\pi} \frac{-p_o}{1 + \epsilon \cos(\pi + \psi + \phi)} \times \frac{r^4}{4\alpha\beta EI}$$
$$\times \left(\frac{2\alpha\beta}{\pi\eta^2} - A \cosh \alpha\phi \cos \beta\phi + B \sinh \alpha\phi \sin \beta\phi\right) d\phi$$

In order to perform the integration we expand $\frac{1}{1+\epsilon\cos\theta}$ in Fourier series as follows.

First use

$$\frac{1}{1+\epsilon\cos\theta} = 1 - \epsilon\cos\theta + \epsilon^2\cos^2\theta - \epsilon^3\cos^3\theta + \epsilon^4\cos^4\theta \ldots$$

then write the powers of $\cos^n\theta$ in terms of $\cos n\theta \ldots$ to obtain

$$\frac{1}{1+\epsilon\cos\theta} = \frac{a_o}{2} + \sum_{n=1}^{\infty} a_n \cos n\theta$$

with

$$a_n = \sum_{i=0}^{\infty}(-1)^n \frac{\epsilon^{n+2i}}{2^{n-1+2i}} C\binom{n+2i}{n+i} \qquad (B.4)$$

The series to calculate the coefficients a_n (summation over i) converges rapidly each term being a factor

$$\frac{\epsilon^2}{4}\frac{(n+2i+1)(n+2i+2)}{(n+i+1)(i+1)}$$

smaller than the previous one.

For the Fourier series also, only a few terms are necessary as the leading coefficient of a_n is $\frac{\epsilon^n}{2^{n-1}}$. Performing then the integration term by term finally

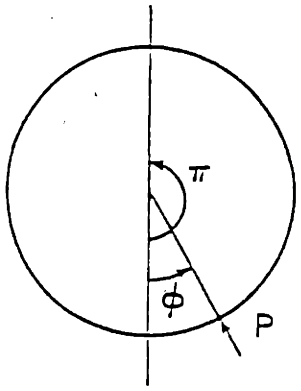

Figure B.3 Solution at π for force P at ϕ.

yields

$$y(\psi) = -\frac{p_o r^4}{4\alpha\beta EI}\left(\frac{2\alpha\beta}{\pi\eta^2} \times \frac{a_o}{2} \times 2\pi - Achc(\psi) + Bshs(\psi)\right)$$

$$M(\psi) = \frac{p_o r^2}{2}\left(\frac{1}{\pi\eta^2} \times \frac{a_o}{2} \times 2\pi + Ashs(\psi) + Bchc(\psi)\right)$$

$$Q(\psi) = -\frac{p_o r}{2}\left((\alpha A - \beta B)chs(\psi) + (\beta A + \alpha B)shc(\psi)\right)$$

$$N(\psi) = -\frac{p_o r}{2}\left(\frac{\eta^2 - 1}{\pi\eta^2} \times \frac{a_o}{2} \times 2\pi - Ashs(\psi) - Bchc(\psi)\right) \qquad (B.5)$$

where

$$chc(\psi) = \int_{-\pi}^{\pi} \cosh\alpha\phi \cos\beta\phi\left[\frac{a_o}{2} + \sum_{n=1}^{\infty} a_n \cos n(\pi + \psi + \phi)\right] d\phi$$

$$= \sum_{n=0}^{\infty} a'_n\left[\frac{1}{[\alpha^2 + (\beta - n)^2]}\left((\beta - n)\cosh\alpha\pi \sin\beta\pi \cos n\psi + \alpha\sinh\alpha\pi \cos\beta\pi \cos n\psi\right)\right.$$

$$\left. + \frac{1}{[\alpha^2 + (\beta + n)^2]}\left((\beta + n)\cosh\alpha\pi \sin\beta\pi \cos n\psi + \alpha\sinh\alpha\pi \cos\beta\pi \cos n\psi\right)\right] \qquad (B.6)$$

I have defined

$$a'_n = a_n \text{ for } n \neq 0$$

$$a'_n = \frac{a_n}{2} \text{ for } n = 0.$$

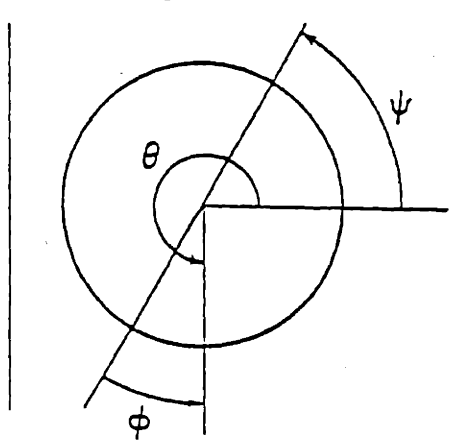

Figure B.4 The reference axis now becomes tilted at an arbitrary angle ψ.

Similarly

$$shs(\psi) = \int_{-\pi}^{\pi} \sinh \alpha\phi \sin \beta\phi \left[\sum_{n=0}^{\infty} a'_n \cos n(\pi + \psi + \phi)\right]$$

$$= \sum_{n=0}^{\infty} a'_n \left[\frac{1}{[\alpha^2 + (\beta - n)^2]} \left(\alpha \cosh \alpha\pi \sin \beta\pi \cos n\psi - (\beta - n) \sinh \alpha\pi \cos \beta\pi \cos n\psi\right)\right.$$

$$\left. + \frac{1}{[\alpha^2 + (\beta + n)^2]} \left(\alpha \cosh \alpha\pi \sin \beta\pi \cos n\psi - (\beta + n) \sinh \alpha\pi \cos \beta\pi \cos n\psi\right)\right] \tag{B.7}$$

$$shc(\psi) = \int_{-\pi}^{\pi} \sinh \alpha\phi \cos \beta\phi \left[\sum_{n=0}^{\infty} a'_n \cos n(\pi + \psi + \phi)\right]$$

$$= \sum_{n=0}^{\infty} a'_n \left[\frac{1}{[\alpha^2 + (\beta - n)^2]} \left(-(\beta - n) \sinh \alpha\pi \cos \beta\pi \sin n\psi + \alpha \cosh \alpha\pi \sin \beta\pi \cos n\psi\right)\right.$$

$$\left. + \frac{1}{[\alpha^2 + (\beta + n)^2]} \left(+(\beta + n) \sinh \alpha\pi \cos \beta\pi \sin n\psi - \alpha \cosh \alpha\pi \sin \beta\pi \cos n\psi\right)\right] \tag{B.8}$$

$$chs(\psi) = \int_{-\pi}^{\pi} \cosh \alpha\phi \sin \beta\phi \left[\sum_{n=0}^{\infty} a'_n \cos n(\pi + \psi + \phi)\right]$$

$$= \sum_{n=0}^{\infty} a'_n \left[\frac{1}{[\alpha^2 + (\beta - n)^2]} \left(-\alpha \sinh \alpha\pi \cos \beta\pi \sin n\psi - (\beta - n) \cosh \alpha\pi \sin \beta\pi \sin n\psi\right)\right.$$

$$\left. + \frac{1}{[\alpha^2 + (\beta + n)^2]} \left(+\alpha \sinh \alpha\pi \cos \beta\pi \sin n\psi + (\beta + n) \cosh \alpha\pi \sin \beta\pi \sin n\psi\right)\right] \tag{B.9}$$

These formulas completely solve the problem for the loading forces. For the reaction forces we have investigated two cases.

1. A single reaction force applied at $\theta = 0$ or $\theta = \pi$ (Fig. B.5). For this the formulas (B.3) can be used directly.

2. In order to model the reaction of a central column we have chosen a force distributed as $\sin^8 \frac{\theta}{2} \cos\theta$. The 8th power for the sin term is a compromise. A higher power would give too peaked a distribution which would then not be significantly different from a single force. For too low a power we obtain that the effect on the outer section, between $\theta = -\frac{\pi}{2}$ and $\theta = \frac{\pi}{2}$ becomes important so that we would not appropriately model a column in the center. This distribution is plotted in Fig. B.6. In order to get the formulas for this case we have followed the same procedure and expanded $\sin^8 \frac{\theta}{2} \cos\theta$ according to

$$\begin{aligned}\sin^8 \frac{\theta}{2} \cos\theta &= -1 + 6\cos^2 \frac{\theta}{2} - 14\cos^4 \frac{\theta}{2} + 16\cos^6 \frac{\theta}{2} - 9\cos^8 \frac{\theta}{2} + 2\cos^{10} \frac{\theta}{2} \\ &= -0.2187 + 0.3828\cos\theta - 0.2500\cos 2\theta + 0.1133\cos 3\theta \\ &\quad - 0.03125\cos 4\theta + 0.004\cos 5\theta \qquad (B.10)\end{aligned}$$

Again term by term integration is performed and in fact the earlier formulas (B.5) - (B.9) apply, limiting the sum to $n = 5$ with a_n taken from (B.10).

The magnitude of the reaction force (be it the single force or the distributed force) is varied with a parameter $frac$ that measures what fraction of the total net inward force, due to the magnetic loading, is taken up by the reaction, the other fraction being taken up by the overall structure. The net inward force is given by

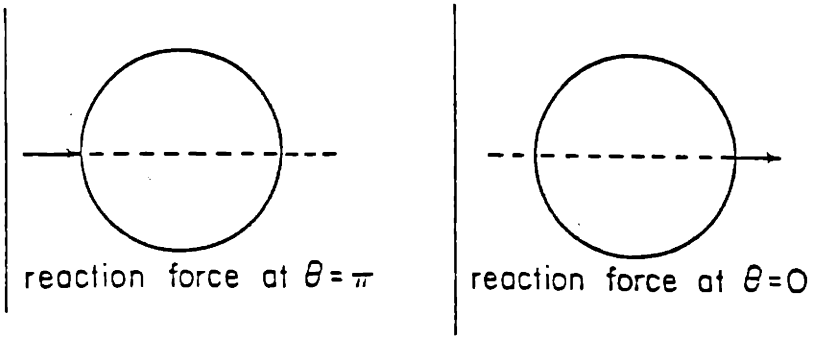

Figure B.5 Position of the concentrated reaction.

$$F_i = \int_{-\pi}^{\pi} \frac{-p_o \cos\theta}{1+\epsilon\cos\theta} r\,d\theta$$

$$= 2\pi r p_o \frac{1}{\epsilon}\left[\frac{1}{\sqrt{1-\epsilon^2}} - 1\right] \qquad (B.11)$$

For the single reaction force we apply

$$F_r = frac \times 2\pi r p_o \frac{1}{\epsilon}\left[\frac{1}{\sqrt{1-\epsilon^2}} - 1\right]$$

to the circular ring at $\theta = 0$ or $\theta = \pi$.

For the distributed force

$$p_r = frac \times \frac{256}{49} p_o r \frac{1}{\epsilon}\left[\frac{1}{\sqrt{1-\epsilon^2}} - 1\right] \sin^8\frac{\theta}{2}\cos\theta,$$

where the coefficient of $\sin^8\frac{\theta}{2}\cos\theta$ is such that for $frac = 1$, the net outward force exactly equals the net inward magnetic force.

Results

Displacements, moments, transverse and tangential forces have been calculated for varying values of η (related to the stiffness of the structure k through

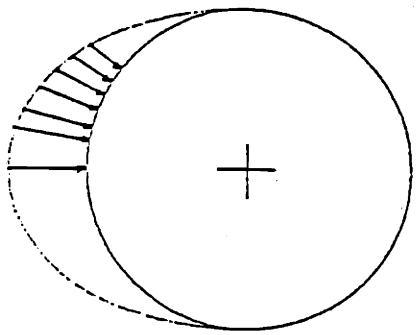

Figure B.6 Distributed reaction force.

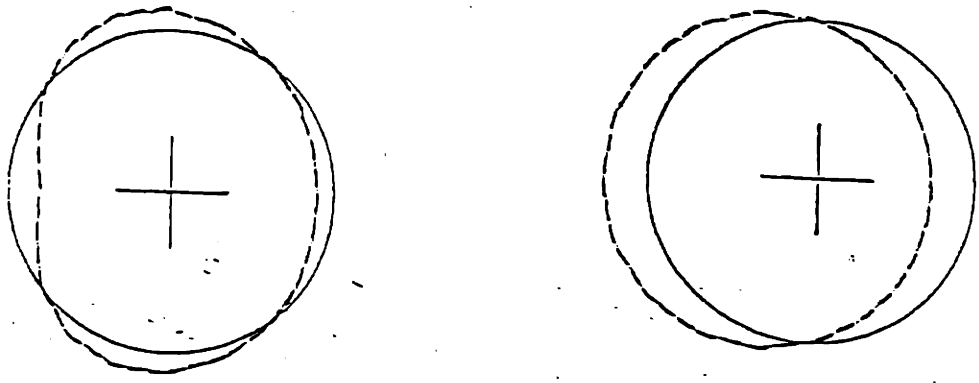

Figure B.7 Single force on the inside $\eta = 2$ $\epsilon = 0.45$ $frac = 1, frac = 0.25$.

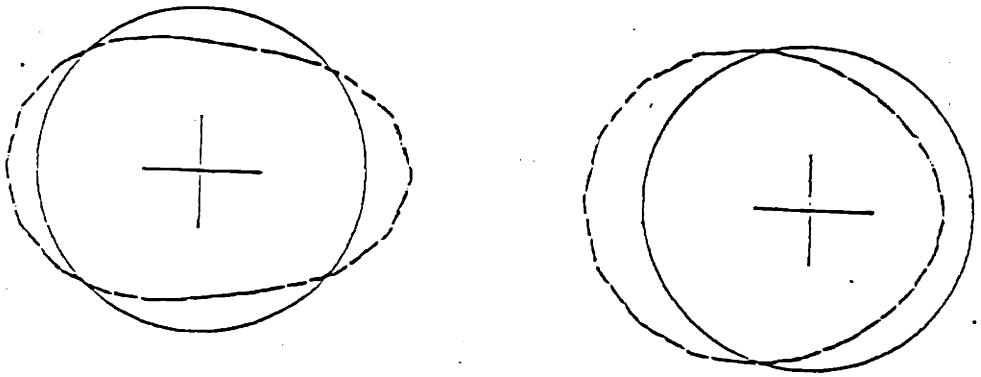

Figure B.8 Single force on the outside $\eta = 2$ $\epsilon = 0.45$ $frac = 1, frac = 0.25$.

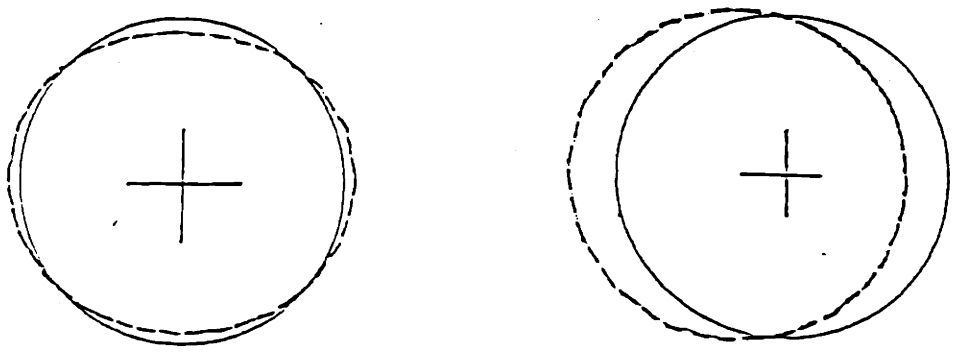

Figure B.9 Distributed force on the inside $\eta = 2$ $\epsilon = 0.45$ $frac = 1, frac = 0.25$.

$\eta = \sqrt{\frac{r^4 k}{EI} + 1}$), and ϵ (inverse aspect ratio $\frac{a}{R}$). Some deformed shapes are shown in Figs. B.7 - B.9.

Except in such extreme cases as where more than 50% of the net centering force is balanced by a single point force on the inside or on the outside, the transverse force Q is always less than 30% of the tangential force so that in our discussion we concentrate on moment and tangential force only. It is helpful to calculate the sum of the tangential force acting on both legs of the coil in the horizontal midplane, as in Fig. B.10. The value of $N_1 + N_2$ is equal to

$$F_z = \frac{\mu_o N I^2}{4\pi} \log\left(\frac{1+\epsilon}{1-\epsilon}\right).$$

If there were no external force, and the coil had to take the total bursting force acting on it internally with hoop stresses then the theoretical minimum for N_1 would be

$$N_1 = \frac{\mu_o N I^2}{4\pi} \; \frac{1}{2} \log\left(\frac{1+\epsilon}{1-\epsilon}\right)$$

To within less than 10% (for ϵ smaller than 0.5) this is equal to

$$N_1 = \frac{\mu_o N I^2}{4\pi} \; \frac{r}{R_o}$$

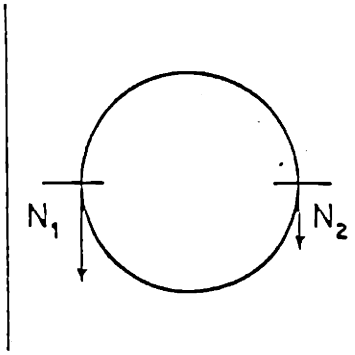

Figure B.10 Tangential forces of the horizontal section.

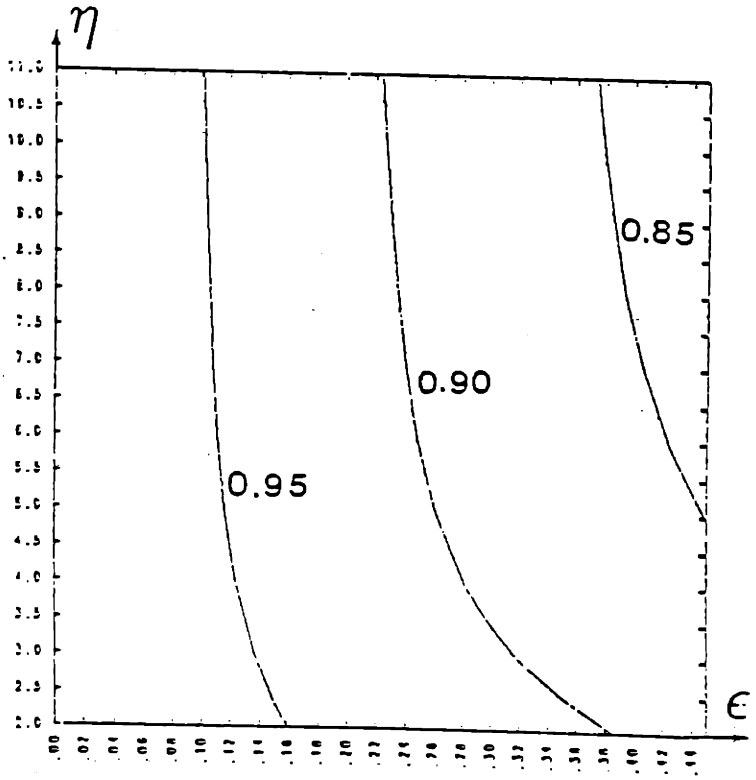

Figure B.11 Normalized N for a distributed reaction.

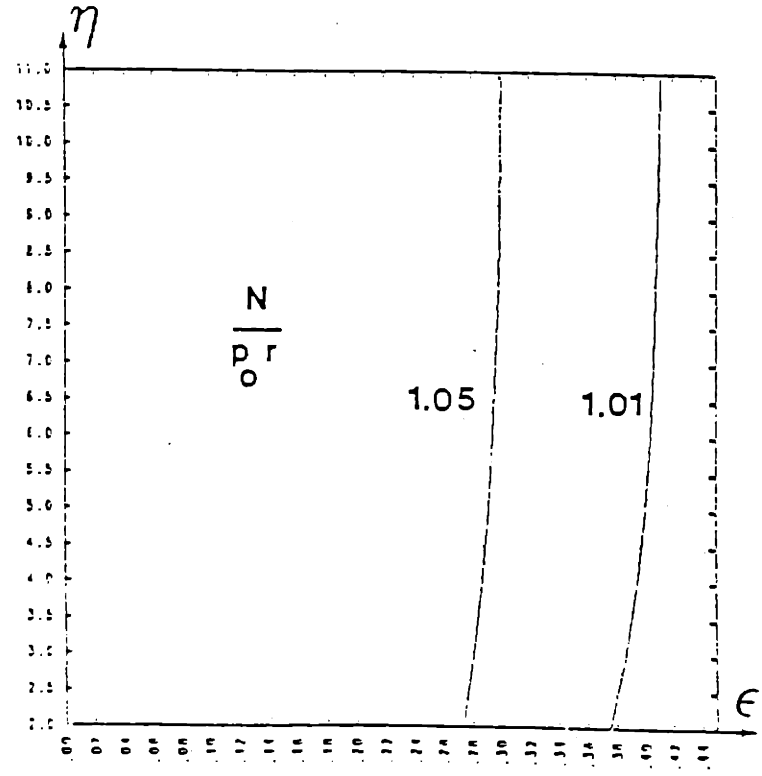

Figure B.12 Normalized N for no external reaction.

which is the value one would obtain assuming a uniform pressure calculated from the current in the coil and half the magnetic field at the center.

The value of N normalized for the case where the total reaction is taken up by a central cylinder (distributed force), is shown in Fig. B.11. If the net centering force is taken up internally we obtain the results of Fig. B.12. Except for the cases where more than 50% of the net centering force is taken up by a single force on the outer leg, the value of $N_1 \Big/ \frac{\mu_o N I^2}{4\pi} \frac{r}{R_o}$ is always within 25% of 1.

The variation of moments is somewhat more complicated, as it is much more sensitive to ϵ, η and the fraction of the force taken up by an external reaction. Typical values of $M/\frac{p_o r^2}{2}$ as a function of η and ϵ for the case of a bucking cylinder taking the total net centering force are shown in Fig. B.13. Figure B.14 assumes no bucking cylinder. The variation between no bucking cylinder and a bucking cylinder taking up all the net centering force is shown in Fig. B.15, for fixed ϵ and η. Figure B.16 gives the same for a single force. Some conclusions can be drawn for the variation of the moments. First, there is an optimal distribution of the net centering force between the reaction of the cylinder and the part taken up by the internal structure. The smaller the aspect ratio, the larger the optimal fraction is that should be taken up by a bucking cylinder. The moments are usually smaller for a larger aspect ratio, while a stiffer structure always gives smaller moments for any aspect ratio. By properly choosing the fractions taken up and the stiffness of the structure, it should be possible to keep $M/\frac{p_o r^2}{2}$ well below 0.02.

As both N and M vary (even though N only varies slightly) we are interested in what the variation of the stresses will be once they are combined. Will stresses due to moments dominate or need the structure be designed essentially for stresses due to N?

It is important to make the distinction between stresses due to tangential force and stressed due to moments because they scale differently. And so will the total

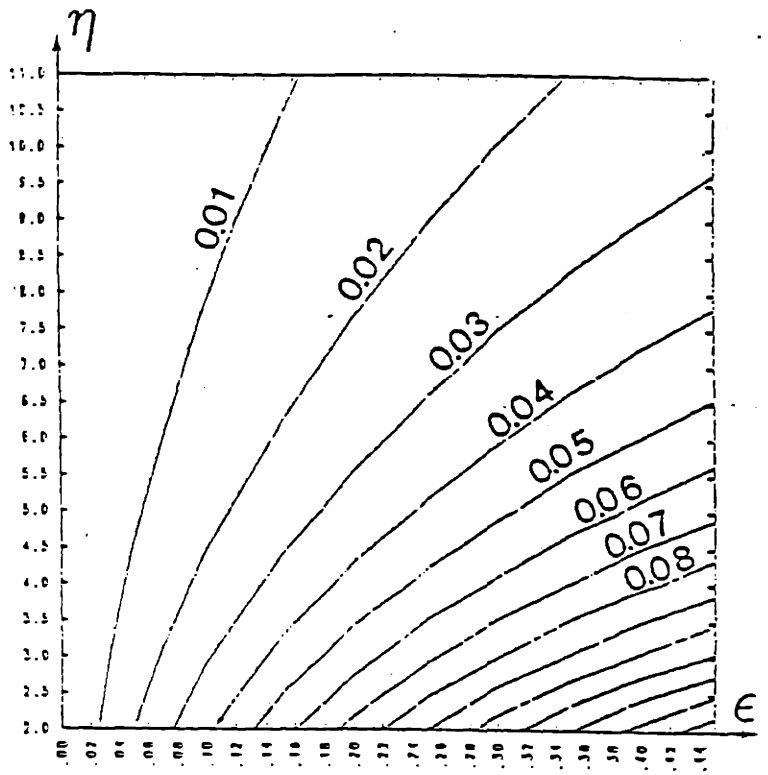

Figure B.13 Normalized absolute value of the maximum moment for the case of a distributed reaction.

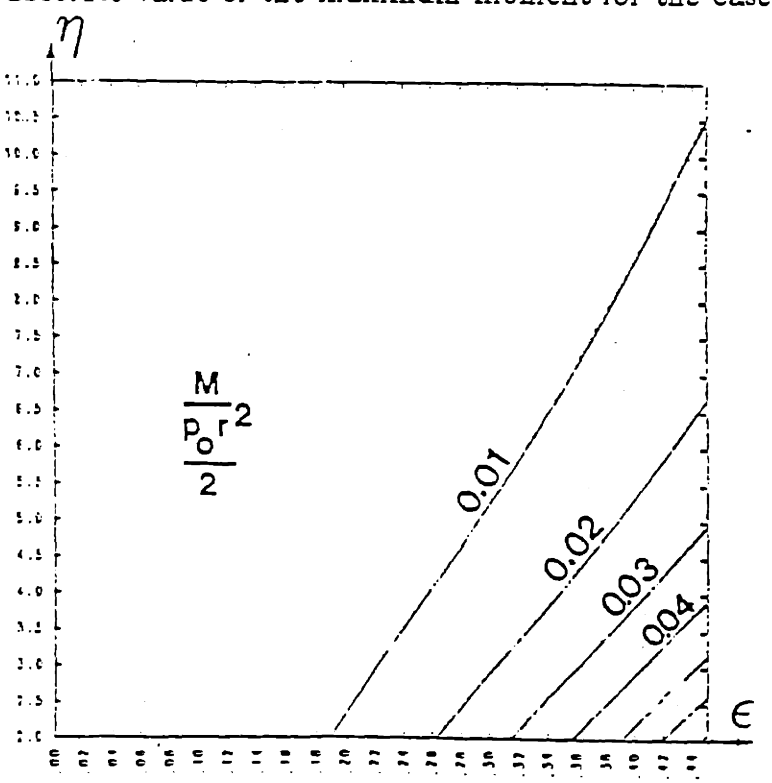

Figure B.14 Normalized absolute value of the maximum moment for the case of no external reaction.

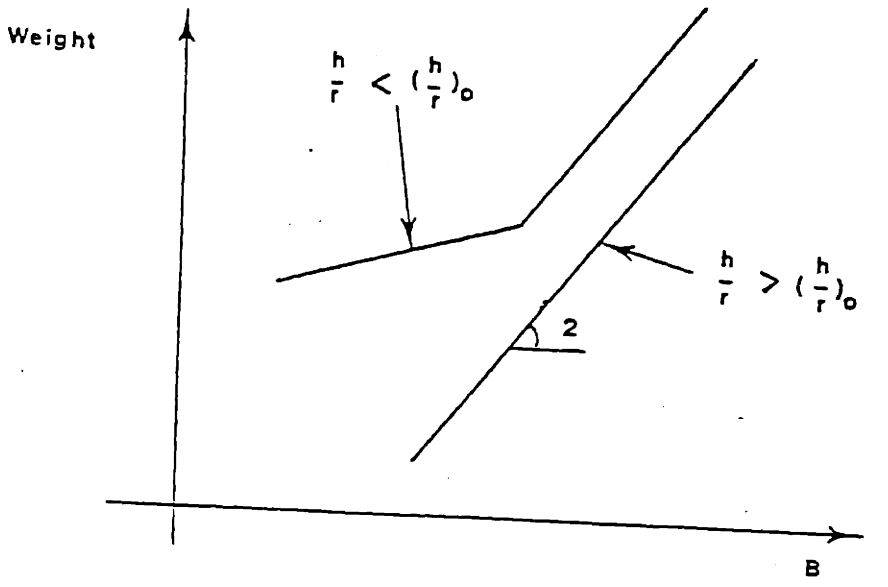

Figure B.17 Scaling of the weight with B, shown schematically.

amount of structural material necessary, depending on whether it is dimensioned for bending or tangential stresses.

For a tangential force, if the load quadruples (for a doubling of the magnetic field), the cross section and thus the weight have to quadruple if the maximum allowable stress stays the same. The structural material thus scales as B^2.

For moments, as $\sigma = \frac{6M}{bh^2}$ (where $h \times b$ are the dimension of the section of the coil, h being measured in the radial direction), if the load quadruples the amount of material does not necessarily have to quadruple. By increasing h, keeping b constant it is possible to keep the same maximum allowable stress with only twice as much material. The structural material in this case scales as B.

One way of distinguishing between dominance of tangential force or moments is by comparing the actual built $\frac{h}{r}$ of the coil with $\frac{6M}{Nr}$.

Indeed let

$$\begin{aligned}\sigma_{max} &= \frac{N}{A} + \frac{6M}{bh^2} \\ &= \frac{N}{A}\left(1 + \frac{6M}{Nh}\right) \\ &= \frac{N}{A}\left(1 + \frac{6M}{Nr} \cdot \frac{r}{h}\right).\end{aligned}$$

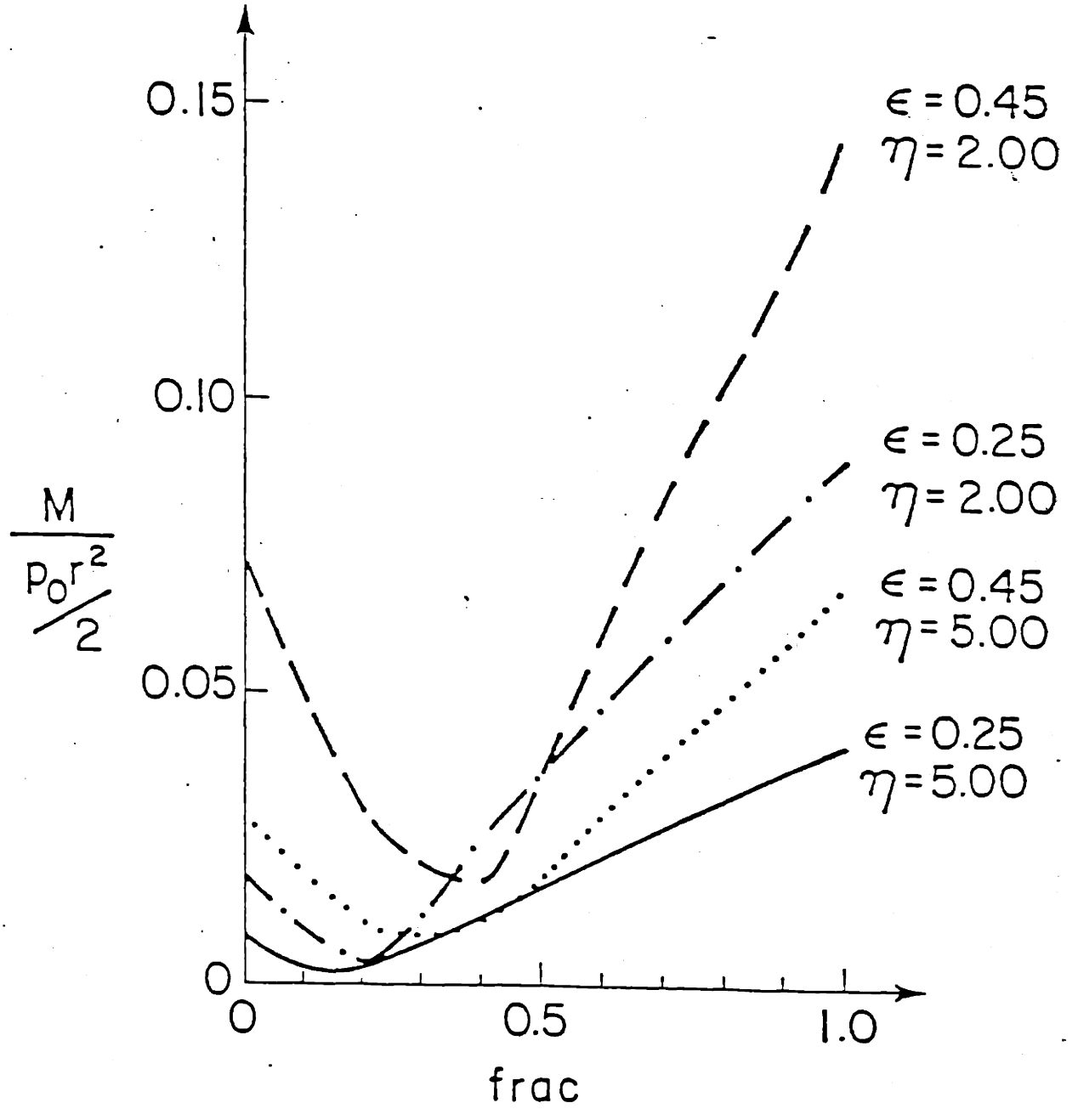

Figure B.15 Normalized moment as a function of the fraction taken up by a distributed reaction.

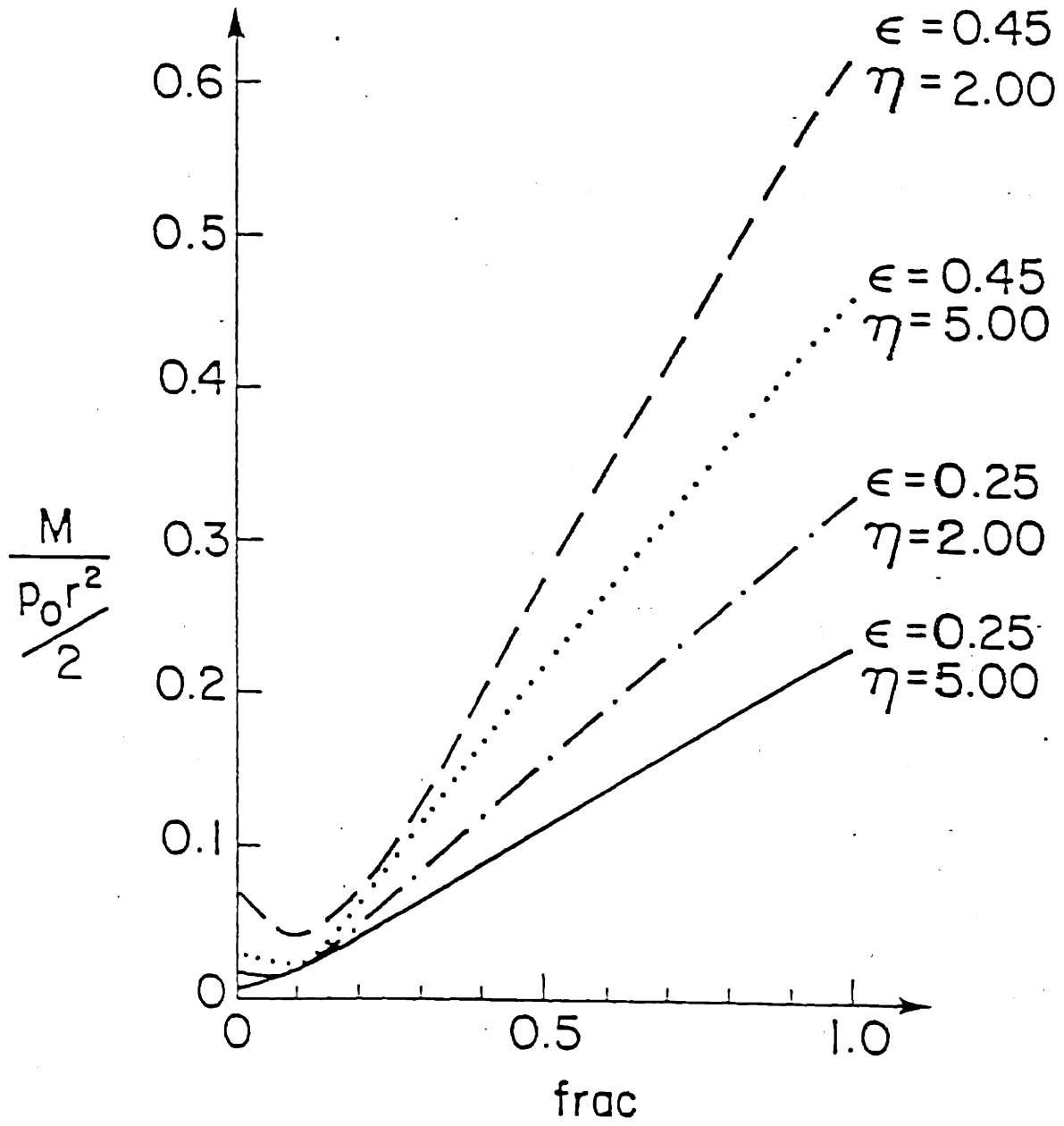

Figure B.16 Normalized moment as a function of the fraction taken up by a point reaction.

If we call $\frac{6M}{N\tau} = (\frac{h}{\tau})_o$, then if $\frac{h}{\tau} > (\frac{h}{\tau})_o$ it means that the normal force dominates, thus giving a structural material weight scaling as B^2. If $\frac{h}{\tau} < (\frac{h}{\tau})_o$, the moment dominates and by increasing $\frac{h}{\tau}$ it is possible to have the structural material weight scale as B. Of course this increase of $\frac{h}{\tau}$ will be beneficial up to $\frac{h}{\tau} = (\frac{h}{\tau})_o$ at which point the weight will start to scale as B^2. It is also possible that for reasons of access, or of power dissipation one would rather not increase h. Then of course weight will scale as B^2. This can be represented schematically in Fig. B.17. Values of $\left(\frac{h}{\tau}\right)_o$ are given in Figs. B.18 and B.19. The negative values of $frac$ are for a single reaction force at $\theta = 0$ in both figures. Positive values of $frac$ are for a single force at $\theta = \pi$ in Fig. B.18, and for a distributed force in Fig. B.19. For most present machines, the reaction force is provided by the wedging action of the nose of the coil or by a bucking cylinder. If the wedging action of the nose of the coil is considered as taking up the forces internally in a very local manner on the inside, then our model is not applicable because we have assumed that the reaction constant k is really constant along the periphery of the coil. Alternatively, we can view the vault of the coil casings on the inside as a central cylinder that provides a distributed central reaction on the coils. The model is then applicable and we are thus somewhat in between the case of a single central force ($frac = 0.4 \rightarrow 1.0$ of Fig. B.18) and a distributed central reaction ($frac = 0.4 \rightarrow 1.0$ of Fig. B.19). The radial build of the coil is usually not larger than $h/\tau = 0.3$. Thus in general we have $\frac{h}{\tau} < (\frac{h}{\tau})_o$ and moments dominate. If however most of the centering force is taken up internally by a well distributed out of plane structure, without central reaction force or bucking cylinder, $(\frac{h}{\tau})_o$ becomes small so that $\frac{h}{\tau} > (\frac{h}{\tau})_o$ is easily satisfied, and the structure has to be dimensioned essentially for the tangential force.

Our analysis thus shows that a more solid distributed intercoil structure would be beneficial. It could take a larger fraction of the inward force thereby reducing the moments in the coil. We can write down for $M/\frac{p_o\tau^2}{2}$ at the minimum approximately $M/\frac{p_o\tau^2}{2} < \frac{\epsilon}{20}$. Since we had $\frac{N}{p_o\tau} \sim 1$ we can write $\left(\frac{h}{\tau}\right)_o = \frac{6M}{\tau N} < \frac{3\epsilon}{20} = 0.15\epsilon$. Thus for $\left(\frac{h}{\tau}\right) > 0.15\epsilon$, the coil is not dominated by bending stresses.

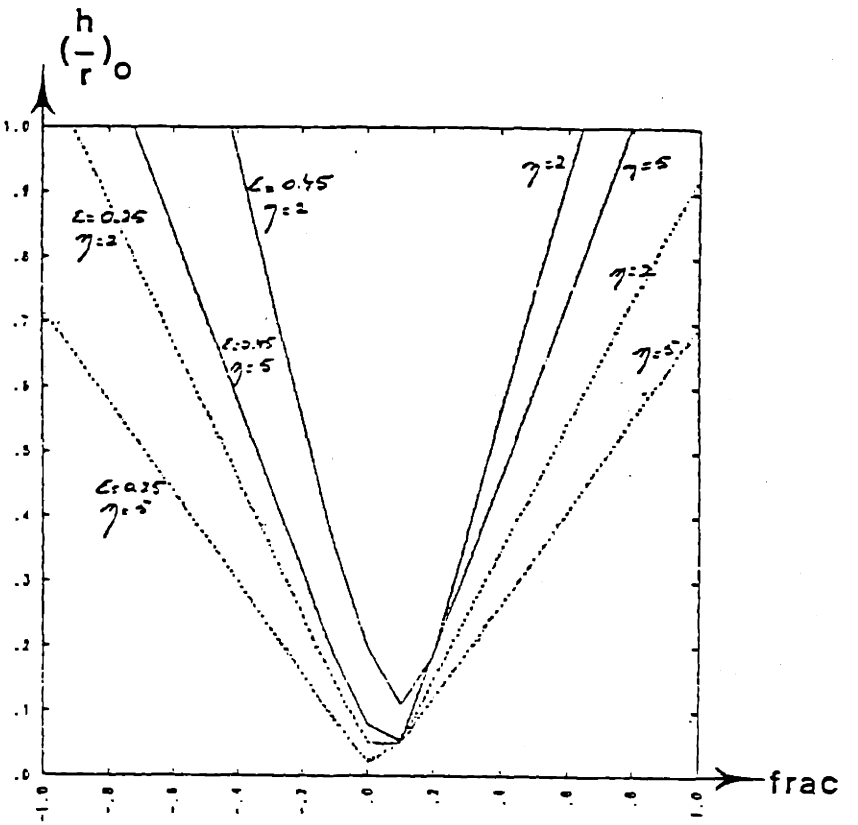

Figure B.18 Value of $(h/r)_o$ as a function of *frac* for a single force.

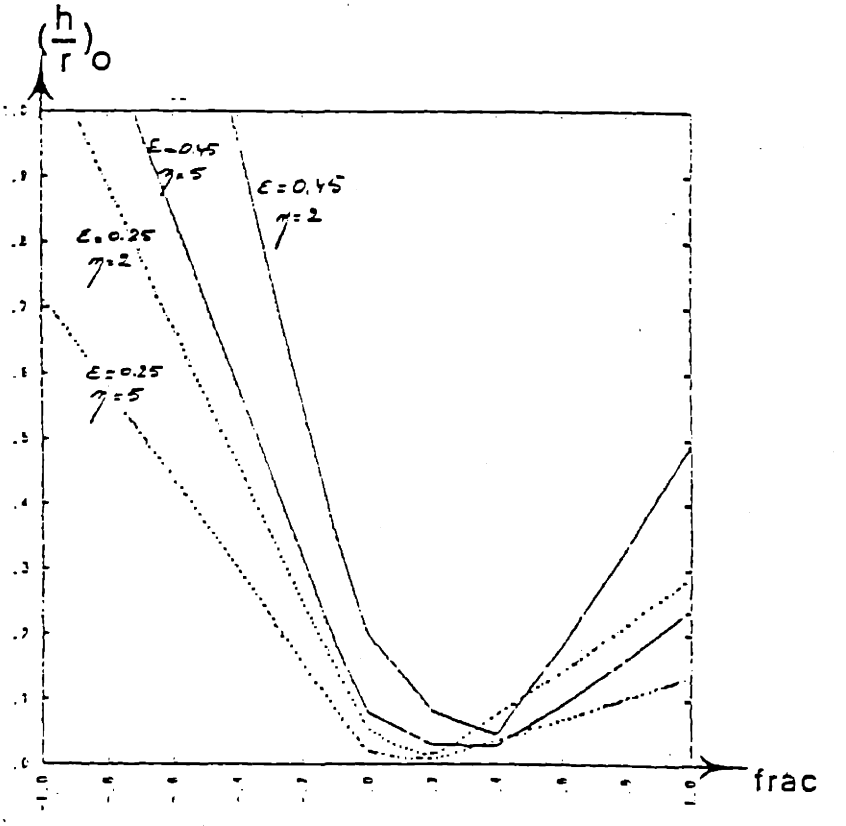

Figure B.19 Value of $(h/r)_o$ as a function of *frac* for a distributed force.

Presently most of the net centering force is taken up by a bucking cylinder or by wedging of the nose of the coils only and $M/\frac{p_o r^2}{2} \simeq \frac{\epsilon}{3}$ so that $\left(\frac{h}{r}\right)_o \simeq \epsilon$. In order for the coil not to be dominated by bending stresses it is necessary that $\frac{h}{r} > \epsilon$, which is not fulfilled in most present cases.

It is interesting to note that our model confirms the fact pointed out by Bobrov and Schultz [142] that circular coils, when taking into account the structure that supports out of plane stresses, are not necessarily moment dominated. In their model no additional reaction force was included. This model goes further, in that it shows how circular coils may become moment dominated if most of the reaction force is taken up by an external reaction (single force or distributed force). It also shows that there is an optimum in the distribution of the centering force between the out of plane structure and a central bucking cylinder. This optimum, however, contrary to present practice, lies for circular coils in the direction of having a large fraction of the force being taken up by the out of plane structure. As of now the purpose of the out of plane structure is mainly to take up torques and overturning moments resulting from the interaction of poloidal coils with the current in the toroidal coils. Its usefulness in taking up the net centering force should be recognized.

The fact that the addition of a small central reaction reduces the bending moment in the coils can be understood qualitatively in the following way. Assume an infinitely rigid circular coil subjected to the magnetic forces without central support. The net inward force will be taken up through the elastic foundation by a rigid shift of the coil. It is easy to show that the net load on the coil then has a $\cos^2\theta$ dependence meaning that the coil tries to deform into an oblong shape. The moment at $\theta = \pi$ is such that it tries to reduce the radius of curvature there. Adding a small outward central reaction has the opposite effect, thus decreasing the total moment. Recall further that in our analysis we have assumed k, the reaction due to the out of plane structure, to be constant. A continuous rotationally symmetric toroidal shell would have a larger k (stiffer) near $\theta = \pi$ than near $\theta = 0$. How much larger depends on the aspect ratio. The

deformation of the toroidal shell is toward a D shape. The moment at $\theta = \pi$ is then such that it tries to increase the radius of curvature. This is already past the optimum as the addition of a central reaction would increase this moment.

Conclusion

A simple method has been devised for the analysis of circular beams on elastic foundations subjected to an arbitrary distribution of in plane loads. By expanding the load distribution in Fourier components, the method can be applied to any particular case. Using this method to analyze the magnetic load on toroidal coils we have shown that under certain circumstances circular coils can be dominated by bending stresses. It is then possible for the structural mass to scale with B rather than B^2. We also have shown that the moments in the coils can be reduced by an appropriate distribution of the net centering force between a external reaction force (as from a central cylinder) and internal reaction (provided by the out of plane structure that makes from the toroidal coils assembly a torus).

Appendix C. Insight in the behavior of normal and binormal for a helical line wound on a torus

For a spatial axis given by $\bar{r}(s)$ the Frenet formulas define and relate the tangent, normal and binormal as follows, (Fig. C.1).

Tangent $\bar{t}$

$$\bar{t} = \frac{d\bar{r}}{ds} \tag{C.1}$$

Normal $\bar{n}$, radius of curvature ρ

$$\frac{1}{\rho}\bar{n} = \frac{d\bar{t}}{ds} \tag{C.2}$$

Binormal $\bar{b}$

$$\bar{b} = \bar{t} \times \bar{n} \tag{C.3}$$

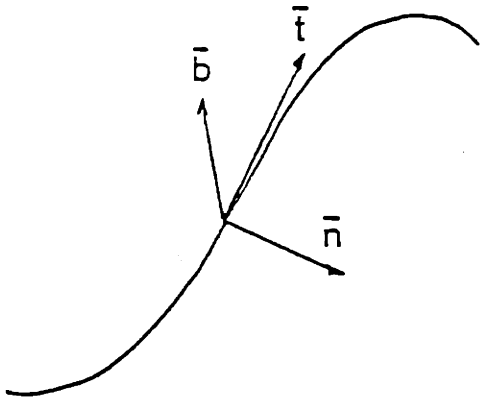

Figure C.1 Tangent, normal and binormal for a spatial curve

Torsion $\frac{1}{\tau}$

$$-\frac{1}{\tau}\bar{n} = \frac{d\bar{b}}{ds} \tag{C.4}$$

As we further have

$$\frac{d\bar{n}}{ds} = -\frac{1}{\rho}\bar{t} + \frac{1}{\tau}\bar{b} \tag{C.5}$$

it is possible to view ρ as a measure of the rate of rotation of the tangent in the $\bar{t}, \bar{n}$ plane, while τ would then be a measure of the rotation of the normal in the $\bar{b}$, $\bar{n}$ plane. It is important to understand the development further along to be able to visualize certain parameters. A helical line wound on a torus is a particular case for which those formulas apply.

R_a is the major radius, r_a the minor radius. The toroidal angle is ϕ, while the poloidal angle is θ.

The geometrical parameters are given by [117] for an arbitrary winding law $\phi(\theta)$. Defining $h(\theta)$ as follows

$$R_c \frac{d\phi(\theta)}{d\theta} = \frac{h(\theta)}{1 - \frac{r_c}{R_a}\cos\theta} \tag{C.6}$$

it is possible to calculate the radius of the curvature $\rho(\theta)$

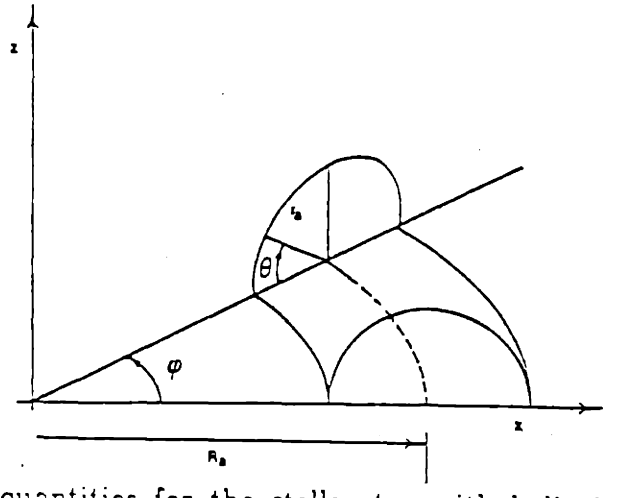

Figure C.2 Geometrical quantities for the stellarator with helical magnetic axis

$$\frac{1}{\rho(\theta)} = \left(r_a^2 + h^2\right)^{-3/2}\left(r_a^4 + r_a^2\left(\frac{dh}{d\theta}\right)^2 + 2r_a\frac{\left(r_a^2 + h^2\right)h\frac{dh}{d\theta}\sin\theta}{R_a - r_a\cos\theta}\right.$$
$$+ \frac{r_a^2(r_a^2 + R_a^2 + 2r_a^2\cos^2\theta - 4r_aR_a\cos\theta)h^2}{(R_a - r_a\cos\theta)^2}$$
$$\left. + \frac{\left[r_a(r_a\cos^2\theta + 2r_a - 2R_a\cos\theta) + h^2\right]h^4}{(R_a - r_a\cos\theta)^2}\right)^{1/2} \qquad (C.7)$$

and the torsion

$$\frac{1}{\tau(\theta)} = \left[r_a^2\frac{d^2h}{d\theta} + \frac{\left(r_a^3\sin\theta + 3r_a\cos\theta h\frac{dh}{d\theta}\right)\frac{dh}{d\theta} - r_ah^2\frac{d^2h}{d\theta}\cos\theta}{R_a - r_a\cos\theta}\right.$$
$$+ \frac{r_a^2(R_a^2 - r_a^2)h + r_a(3R_a - r_a\cos\theta)h^2\frac{dh}{d\theta}\sin\theta}{(R_a - r_a\cos\theta)^2}$$
$$\left. + \frac{r_a(2r_a^2 - R_a^2 + h^2)\cos\theta - r_a^2R_a}{(R_a - r_a\cos\theta)^3}h^3\right] \qquad (C.8)$$
$$\left[r_a^4 + r_a^2\left(\frac{dh}{d\theta}\right)^2 + 2r_a\frac{(r_a^2 + h^2)h\frac{dh}{d\theta}\sin\theta}{R_a - r_a\cos\theta}\right.$$
$$+ \frac{r_a^2(R_a^2 + r_a^2 - 4R_a\cos\theta + 2r_a^2\cos\theta)h^2}{(R_a - r_a\cos\theta)^2}$$
$$\left. + \frac{(r_a^2\cos^2\theta + 2r_a^2 - 2r_aR_a\cos\theta + h^2)h^4}{(R_a - r_a\cos\theta)^2}\right]^{-1}$$

Insight in the motion of the normal can be gained by tracking the variation of certain angles which I define now. The tangent $\bar{t}$ lies always in the plane defined by $\bar{e}_\theta$ and $\bar{e}_\phi$. The angle of $\bar{t}$ with $\bar{e}_\phi$ is called the pitch angle and is equal to

$$\tan p = \frac{\frac{r_c}{R_c}}{\left(1 - \frac{r_c}{R_c}\cos\theta\right)\frac{d\phi}{d\theta}} \qquad (C.9)$$

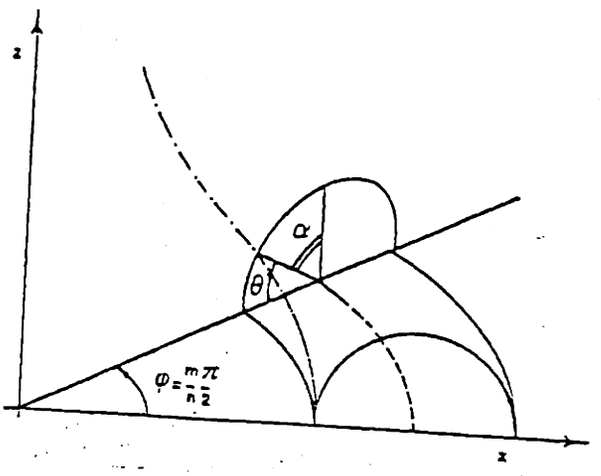

Figure C.3 Geometrical representation of the winding law angle α

The complement of this angle, which I call q is the angle of the tangent $\bar{t}$ with $\bar{e}_\theta$. Note that a "constant pitch" winding law requires

$$\frac{d\phi}{d\theta} \sim \frac{1}{1 - \frac{r_a}{R_c}\cos\theta} \tag{C.10}$$

The proportionality constant can be obtained from a closure condition

$$\int_0^{2\pi} \frac{d\phi(\theta)}{d\theta} d\theta = \frac{m}{n} 2\pi \tag{C.11}$$

so that one obtains

$$\frac{\phi}{2} = \frac{m}{n} \tan^{-1} \sqrt{\frac{1 - \frac{r_a}{R_c}}{1 + \frac{r_a}{R_c}}} \tan\frac{\theta}{2} \tag{C.12}$$

The constant pitch is then given by

$$\tan p = \frac{n}{m}\frac{r_a}{R_a} \tag{C.13}$$

A simple winding law is given by

$$\phi = \frac{m}{n}\theta \tag{C.14}$$

We can generalize it by introducing the winding law angle α, as follows

$$\frac{n}{m}\phi = \theta + \alpha \sin\theta \tag{C.15}$$

The angle α, can to first order be seen as the angle between $\bar{e}_r$ and $\bar{e}_z$ at $\frac{n}{m}\phi = \frac{\pi}{2}$, (this is a quarter period), as shown in Fig. C.3.

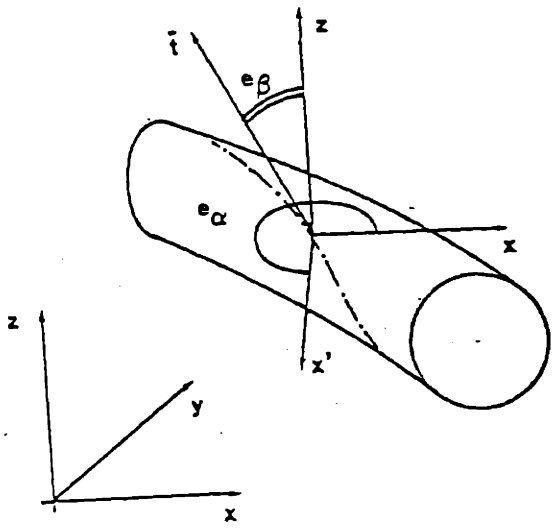

Figure C.4 Definition of the Euler angles e_α and e_β

The direction of the normal is completely defined by its Euler angles e_α and e_β.

The angle e_α is the angle a vector starting out parallel to the x axis has to rotate around the z axis to become perpendicular to the plane containing the tangent $\bar{t}$ and the z axis (Fig. C.4). The angle e_β then, is the angle a vector parallel to the z axis has to rotate around the x' axis to end up parallel to the tangent.

It is sometimes easier to visualize the angles c and d (Fig. C.5). The angle c is the angle between $\bar{e}_r$ and the normal $\bar{n}$. As it is easy to know the direction of $\bar{e}_r$ at each point, the knowledge of c gives a good indication of the direction of the normal. The angle d is roughly a measure of how much the plane containing n and $\bar{e}_r$ deviates from being a $\phi = constant$ plane.

Having defined those parameters, let us now assume a winding law of the form

$$\phi = \frac{m}{n}(\theta + \alpha \sin\theta) \qquad (C.16)$$

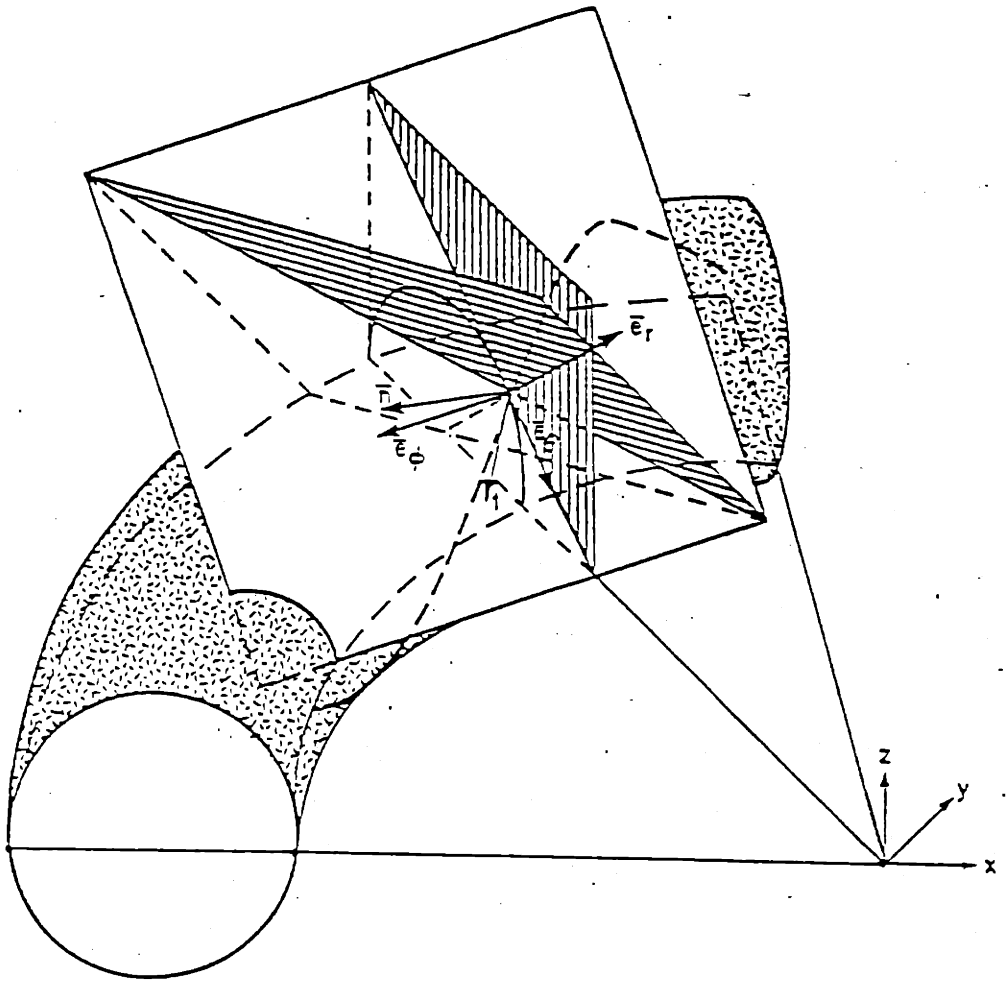

Figure C.5 Definition of the angles c and d. The figure shows three intersecting planes and the torus. Plane A (unshaded), contains the vectors $\bar{e}_\phi$ and $\bar{e}_\theta$, and thus also the tangent $\bar{t}$. Plane B (shaded vertically) is a $\phi = constant$ plane, and thus contains $\bar{e}_r$ and $\bar{e}_\theta$. The plane C (shaded diagonally) is perpendicular to the tangent $\bar{t}$ and contains $\bar{e}_r$ and $\bar{n}$. The angle c is the angle between those two vectors $(\bar{e}_r, \bar{n})$. The angle d, defined as $\epsilon_a - \phi$ is also a measure of the angle between plane B and C, measured in the $z = 0$ plane.

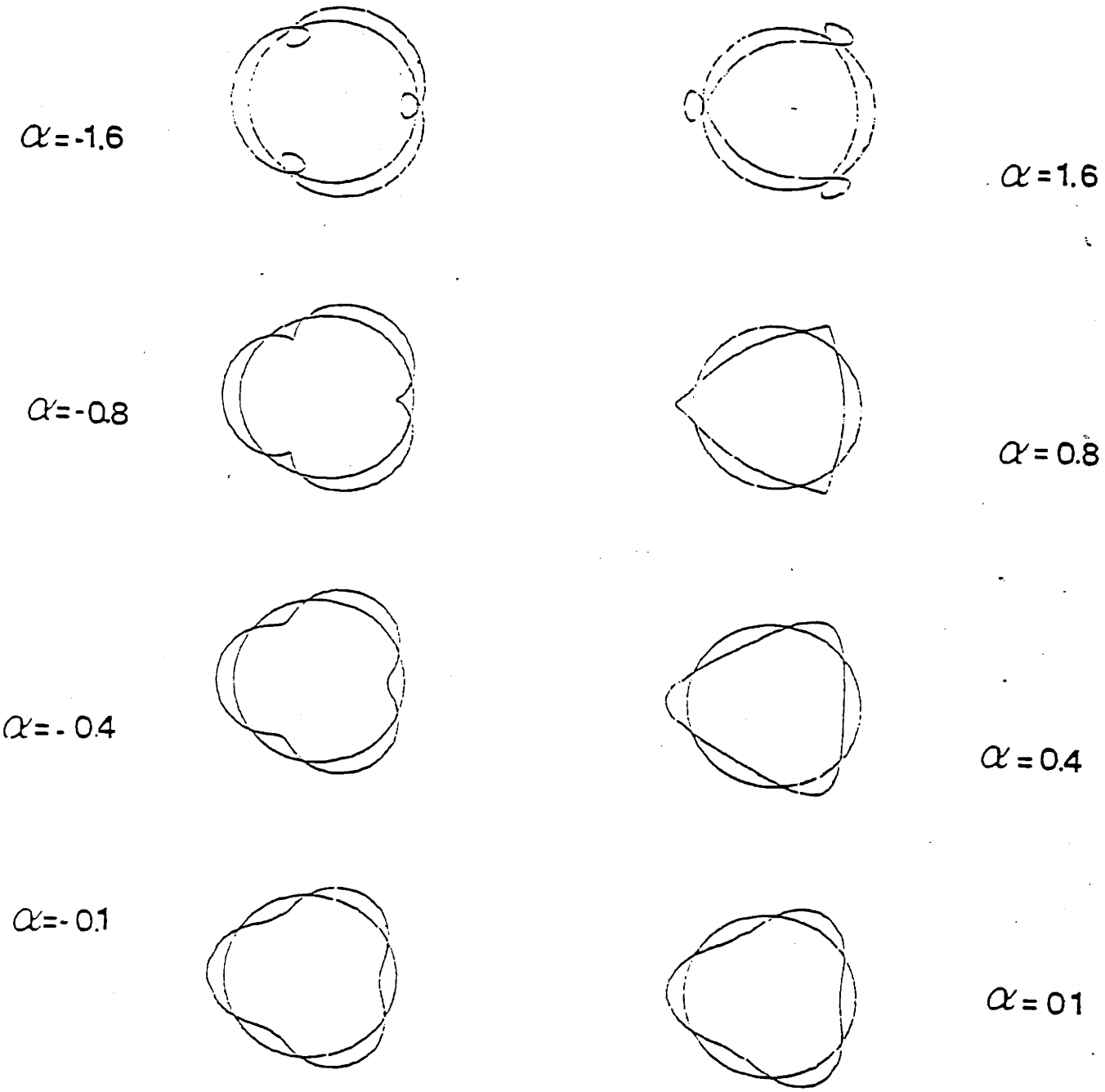

Figure C.6 Projection of the winding law for different values of α

Fig. C.6 shows a projection on the x, y plane of the winding law for different values of α.

From those drawings we can see that one of the constraints on the winding law will be $|\alpha| < 1$.

This can be generalized for a winding law of the type

$$\phi = \frac{m}{n}\left(\theta + \sum\left(\frac{\alpha_\ell}{\ell}\right)\sin \ell\theta\right) \qquad (C.17)$$

by requiring that $\frac{d\phi}{d\theta} > 0$ for all θ.

Figure C.7 shows the variations of the normalized curvature $\frac{1}{\rho}$ and normalized torsion $\frac{1}{\tau}$ as a function of the angle θ for various values of α. The normalization factors used, are the values for a straight helix.

$$\frac{1}{\rho_o} = \frac{1}{r_a\left(1 + \left(\frac{mR_c}{nr_c}\right)^2\right)} \qquad (C.18)$$

$$\frac{1}{\tau_o} = \frac{\frac{mR_c}{nr_c}}{r_a\left(1 + \left(\frac{mR_c}{nr_c}\right)^2\right)} \qquad (C.19)$$

The variation of the angle q, which is the complement of the pitch angle, the angles c and d are shown in Figure C.8.

One can notice a marked difference between the behavior of the angle c between the cases $\alpha = 0.3$ and $\alpha = 0.6$. Recalling that the angle c is the angle between the normal $\bar{n}$ and $\bar{e}_r$ in the plane perpendicular to the tangent I have shown schematically in Figure C.9 what the difference is between the two cases.

In one case, at $\theta = 0$ the major radius curvature dominates, while in the other case, it is always the minor radius of curvature which dominates.

In one case the normal makes a complete 2π rotation, in the other not. The "dividing line" between the two possible behaviors depends on $\frac{n}{m}$, $\frac{r}{R}$ and the

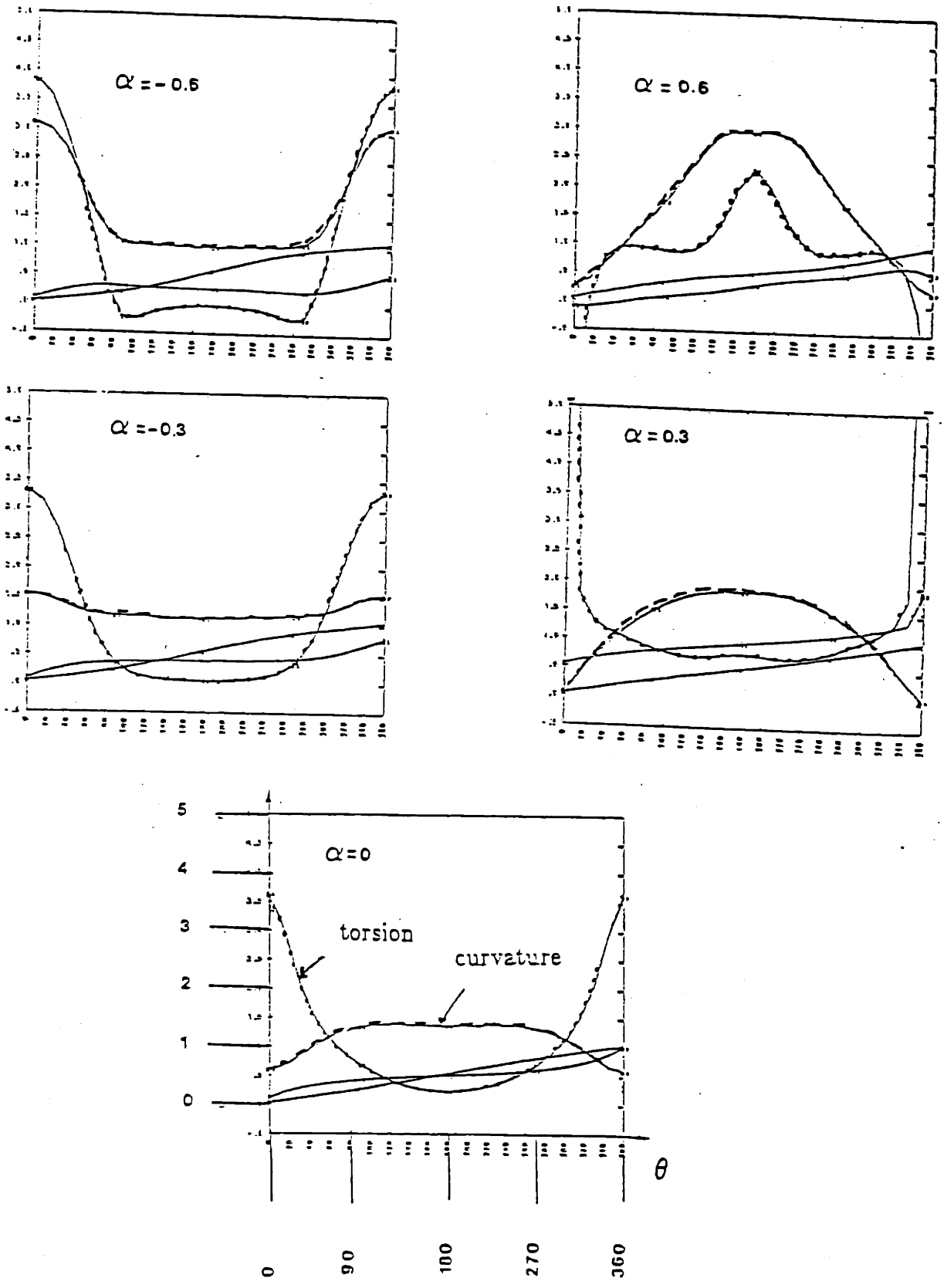

Figure C.7 Variation of the curvature and the torsion. Both are normalized to the value for a straight helix

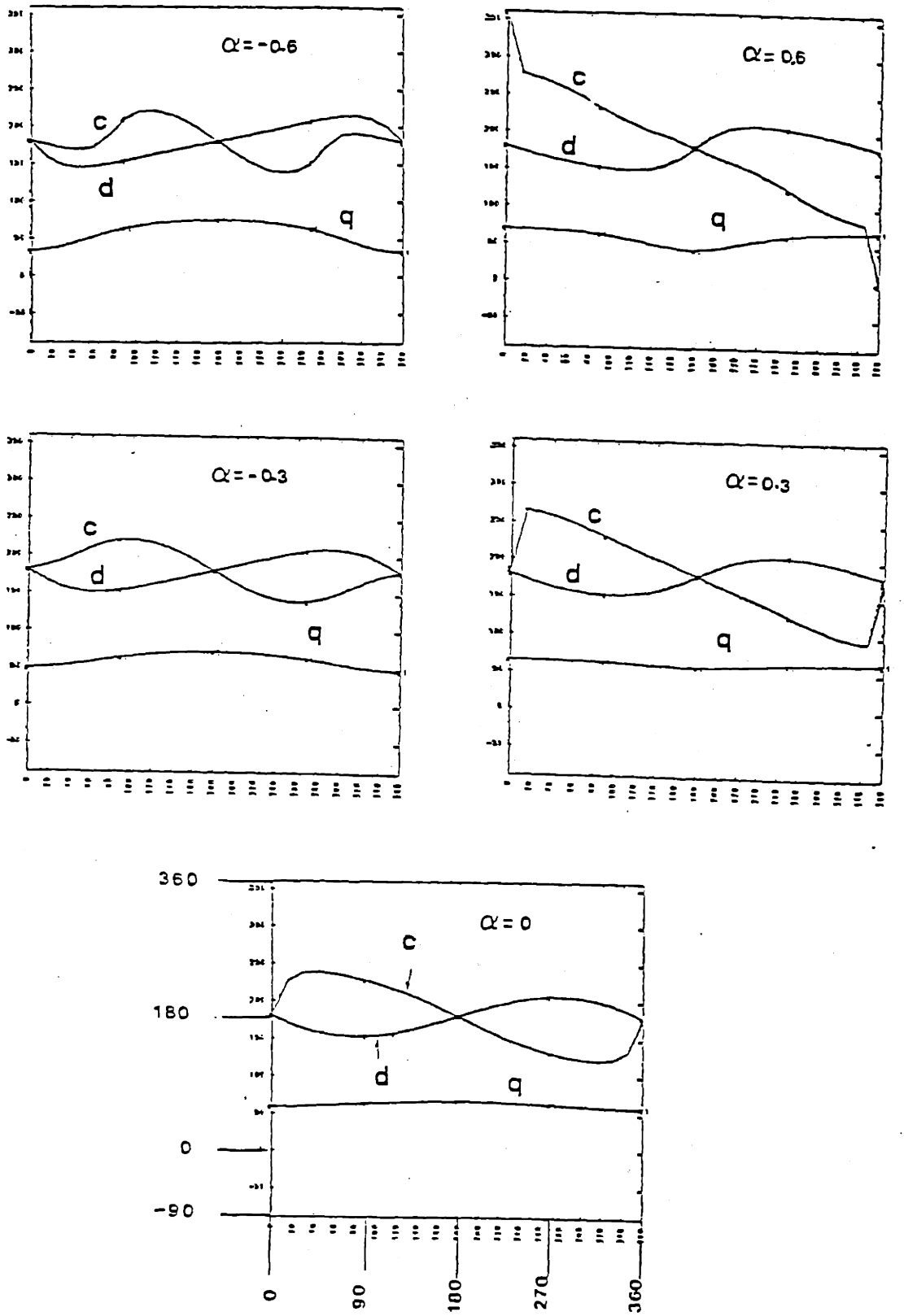

Figure C.8 Variation of the angles q, c and d

angle of the winding law through (see Fig. C.10)

$$\left(\frac{n}{m}\right)^2 = \frac{1 - \frac{r_c}{R_a}}{\frac{r_c}{R_a}}\left[1 + \sum \alpha_\ell\right]^2 \qquad (C.20)$$

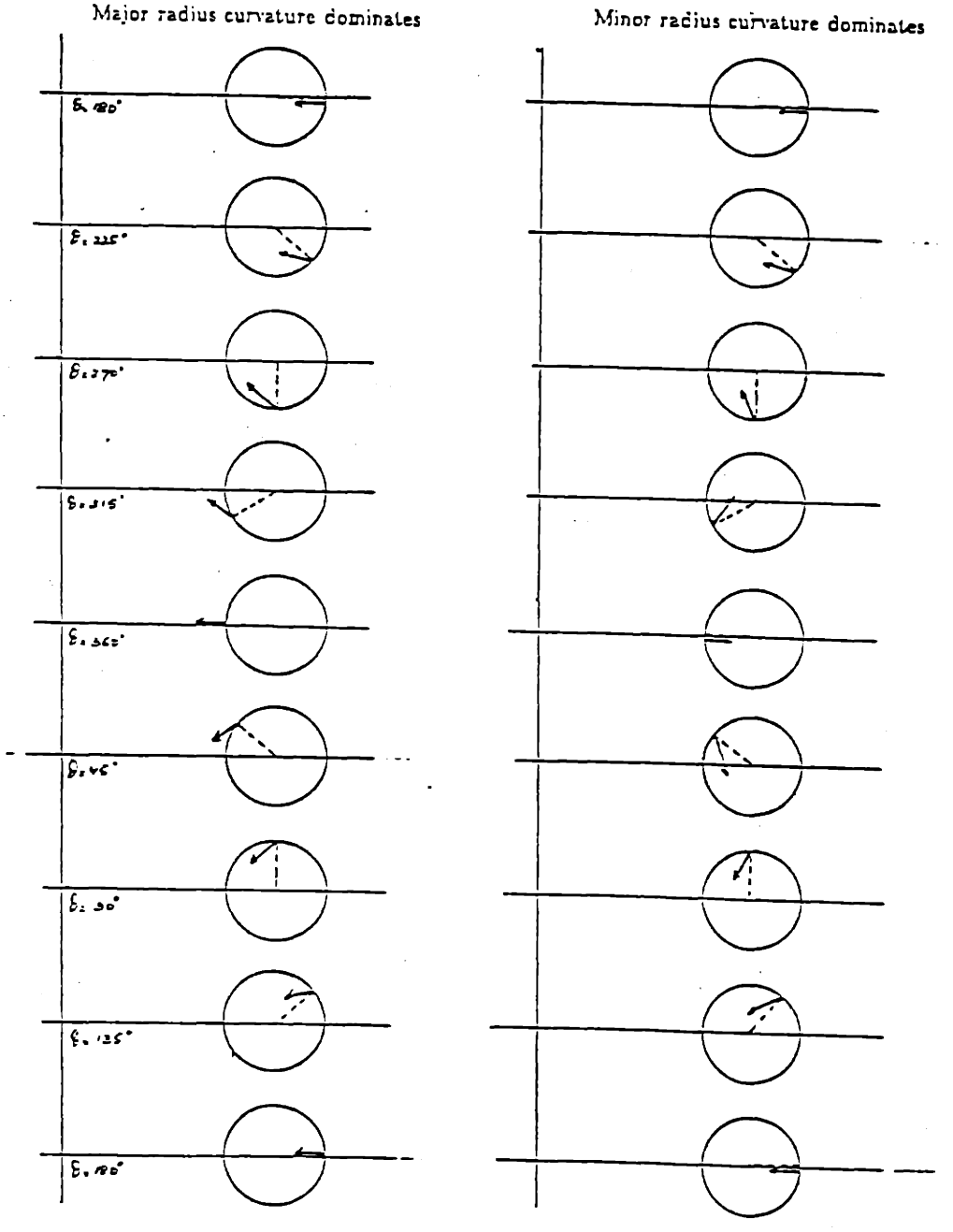

Figure C.9 Difference in the behavior of the normal when minor radius curvature dominates or when major radius dominates

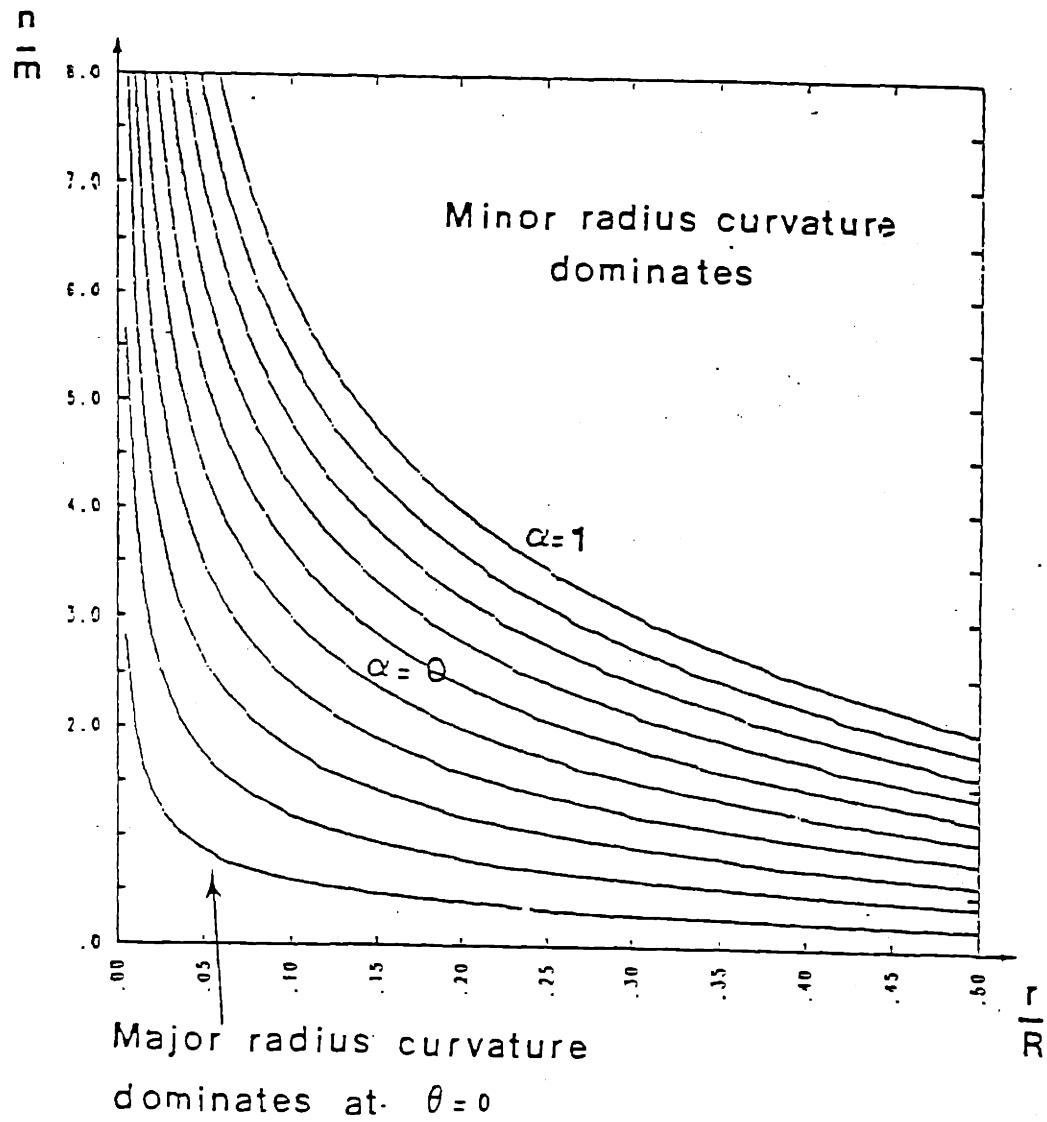

Figure C.10 Regions in parameter space where the major radius curvature dominates

Appendix D. Parametric variation of the geometric properties of the magnetic axis with ring current I_R and vertical field B_v.

In order to be able to extend the numerical work reported in section 4.3.2 and obtain some feeling for the parameter variations it was imperative to understand the behavior. In addition there was a need for some analytical guidelines as well as for the possibility to investigate a broader parameter space without the need to resort to extensive numerical calculations.

The following model provides those analytical guidelines to a first order approximation, explains the major findings of the numerical work, and in a refined version obtains very efficiently the major geometrical parameters associated with the magnetic axis.

Recalling formula (C.9) the angle of the magnetic axis with $\bar{e}_\phi$ is given by

$$\tan p = \frac{\frac{r_c}{R_c}}{\left(1 - \frac{r_c}{R_c}\cos\theta\right)\frac{d\phi}{d\beta}} \qquad (D.1)$$

Now we have that $\tan p$ at $\theta = 0$ and $\theta = \pi$ is also equal to

$$\tan p = \frac{B_\theta}{B_\phi} \qquad (D.2)$$

so that we can write, using $\frac{n}{m}\phi = \theta + \alpha_a \sin\theta$

At $\theta = 0$

$$\left(\frac{B_\theta}{B_\phi}\right)_o = \frac{\frac{n}{m}\frac{r_c}{R_c}}{\left(1 - \frac{r_c}{R_c}\right)(1 + \alpha_a)} \qquad (D.3)$$

At $\theta = \pi$

$$\left(\frac{B_\theta}{B_\phi}\right)_\pi = \frac{\frac{n}{m}\frac{r_a}{R_a}}{\left(1+\frac{r_a}{R_a}\right)(1-\alpha_a)} \tag{D.4}$$

By eliminating α_a, we obtain

$$2 = \frac{n}{m}\frac{r_a}{R_a}\left[\frac{1}{1-\frac{r_a}{R_a}}\left(\frac{B_\phi}{B_\theta}\right)_o + \frac{1}{1+\frac{r_a}{R_a}}\left(\frac{B_\phi}{B_\theta}\right)_\pi\right] \tag{D.5}$$

while α_a can be written as

$$\alpha_a = \frac{1}{2}\frac{n}{m}\frac{r_a}{R_a}\left[\frac{1}{1-\frac{r_a}{R_a}}\left(\frac{B_\phi}{B_\theta}\right)_o - \frac{1}{1+\frac{r_a}{R_a}}\left(\frac{B_\phi}{B_\theta}\right)_\pi\right] \tag{D.6}$$

Equation (D.5) gives a relation between R_a and r_a that has to be fulfilled. Note that the values of $\left(\frac{B_\theta}{B_\phi}\right)_o$ and $\left(\frac{B_\theta}{B_\phi}\right)_\pi$ also depend on the R_a and r_a so that the equation can not be solved exactly in explicit form. However, by making some approximations it is possible. The toroidal field is produced by toroidal coils and the poloidal field is the sum of a component due to the ring current I_R, a component due to the toroidal field coils and the external vertical field B_v. Take B_ϕ to be a constant, and the poloidal field due to the ring to go as $\frac{1}{r}$. Further assume the ratio of the poloidal component ($B_{\theta c}$) at $\theta = 0$ and $\theta = \pi$ due to the toroidal field coils and the ϕ component (B_ϕ) due to the same coils to be a constant. From this we obtain

$$\begin{aligned}
\left(\frac{B_\theta}{B_\phi}\right)_o &= \frac{B_{\theta c} - B_v + \frac{\mu_o I_R}{2\pi r_o}}{B_\phi} \\
\left(\frac{B_\phi}{B_\theta}\right)_o &= B_\phi \frac{2\pi r_o}{\mu_o I_R}\frac{1}{1+\frac{B_{\theta c}-B_v}{\frac{\mu_o I_R}{2\pi r_o}}} \\
&\simeq B_\phi \frac{2\pi r_o}{\mu_o I_R}\left(1 - \frac{B_{\theta c} - B_v}{\frac{\mu_o I_R}{2\pi r_c}}\right)
\end{aligned} \tag{D.7}$$

Similarly

$$\left(\frac{B_\phi}{B_\theta}\right)_\pi = \frac{B_\phi 2\pi r_\pi}{\mu_o I_R}\left(1 - \frac{B_{\theta c} + B_v}{\frac{\mu_o I_R}{2\pi r_\pi}}\right) \tag{D.8}$$

The condition (D.5) can then be written as

$$2 = \frac{\frac{n}{m}\frac{r_a}{R_a}}{1 - \frac{r_a}{R_a}}\left(\frac{B_\phi}{B_\theta}\right)_o + \frac{\frac{n}{m}\frac{r_c}{R_c}}{1 + \frac{r_c}{R_a}}\left(\frac{B_\phi}{B_\theta}\right)_\pi$$

or

$$2 = \frac{n}{m}\frac{r_a}{R_a}\left(\left(\frac{B_\phi}{B_\theta}\right)_o + \left(\frac{B_\phi}{B_\theta}\right)_\pi\right) + \frac{n}{m}\frac{r_a^2}{R_a^2}\left(\left(\frac{B_\phi}{B_\theta}\right)_o - \left(\frac{B_\phi}{B_\theta}\right)_\pi\right) \tag{D.9}$$

Substituting the values for $\left(\frac{B_\phi}{B_\theta}\right)_o$ and $\left(\frac{B_\phi}{B_\theta}\right)_\pi$ and using

$$r = \frac{r_o + r_\pi}{2} \tag{D.10}$$

$$R = R_R + \frac{r_\pi - r_o}{2} \tag{D.11}$$

We obtain

$$\begin{aligned} 2 = {} & \frac{n}{m}\frac{r_a}{R_a}\frac{B_\phi}{\frac{\mu_o I_R}{2\pi}}\left[2r_a - \frac{B_\theta}{\frac{\mu_o I_R}{2\pi}}\left(2r_a^2 + 2(R_a - R_R)^2\right) + \frac{B_v}{\frac{\mu_o I_R}{2\pi}}4r_a(R_a - R_R)\right] \\ & + \frac{n}{m}\frac{r_a^2}{R_a^2}\frac{B_\phi}{\frac{\mu_o I_R}{2\pi}}\left[2(R_R - R_a) + \frac{B_\theta}{\frac{\mu_o I_R}{2\pi}}4r(R_a - R_R) + \frac{B_v}{\frac{\mu_o I_R}{2\pi}}\left(2r_a^2 + 2(R_a - R_R)^2\right)\right] \end{aligned} \tag{D.12}$$

Which is approximately

$$2 = \frac{n}{m}\frac{r_a}{R_a}\frac{B_\phi}{\frac{\mu_o I_R}{2\pi}}\left[2r_a - 2\frac{B_{\theta c} r_a^2}{\frac{\mu_o I_R}{2\pi}}\right]$$

or

$$\frac{m}{n} = \frac{r_a}{R_a}\frac{B_\phi}{\frac{\mu_o I_R}{2\pi r_a}}\left[\frac{1}{1+\frac{B_{\theta c}}{\frac{\mu_o I_R}{2\pi r_a}}}\right] \qquad (D.13)$$

Note that this is similar to

$$q = \frac{r_a}{R_a}\frac{B_\phi}{B_\theta} \qquad (D.14)$$

except that B_θ is now composed of a component due to the current I_R and a component from the toroidal coils. Solving (D.13) for r_a

$$r_a = R_a\sqrt{\frac{\mu_o I_R m}{2\pi R_a B_\phi n} + \left(\frac{m}{n}\frac{1}{2}\frac{B_{\theta c}}{B_\phi}\right)^2} + \frac{m}{n}\frac{1}{2}\frac{B_{\theta c}}{B_\phi} \qquad (D.15)$$

To a first approximation we can take $R_a = R_c$. This gives values for r_a in close agreement with the numerical results and shows it further to be function of the ring current I_R only (not the vertical field coils).

The way we obtain a second condition (in addition to the first (D.5)) is by noting that, quite independent of the winding law, at $\theta_c = \frac{\pi}{2}$ the total vertical field must be zero.

The total vertical field is the vertical field due to the ring, the external vertical field and a component from the toroidal coils.

In Fig. D.1, I show normalized the loci of constant vertical component due to a poloidal ring.

Together with formula (D.15) it can be used to obtain an first approximation of the values of r_a and R_c for a given current and vertical field. In Figures D.2 and D.3 I show how the combination of the two conditions leads to the appropriate values of R_a and r_a.

It can be gathered from those figures why r_a changes very little with the vertical field, and also why R_a varies both with I_R and B_v.

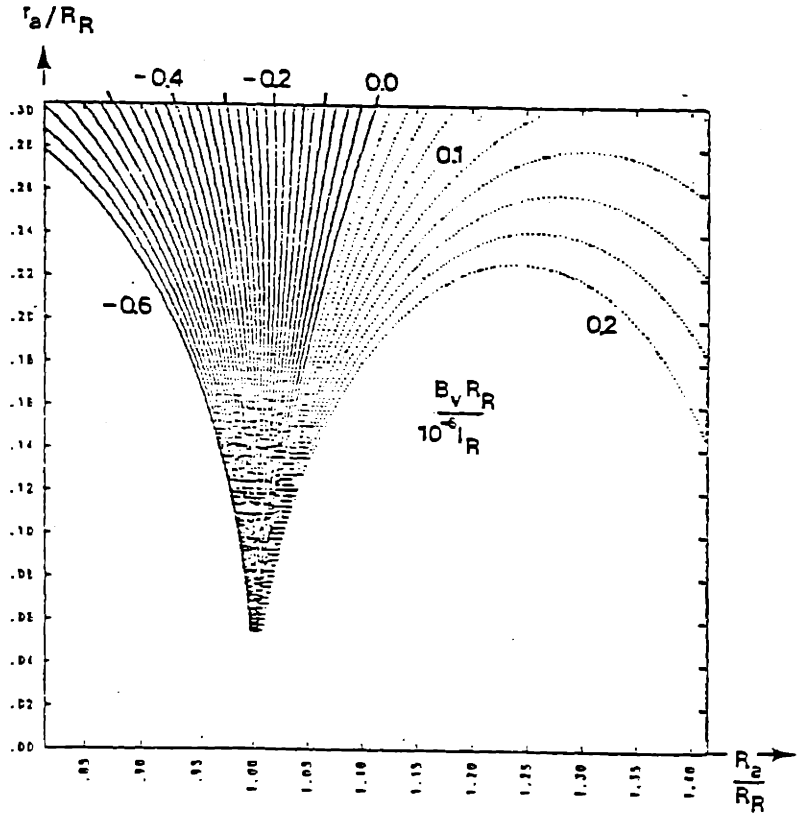

Figure D.1 Loci of constant vertical field component for a ring current, distances have been normalized to the radius of the ring, the magnetic field has been normalized to the product of the ring current and the radius of the ring

---

An interesting analytical result is obtained by noting that for

$$\frac{B_v R_c}{I_R} = -\frac{\mu_o}{2\pi} \qquad (D.16)$$

the locus where the total vertical field is zero is nearly a straight line at $R = R_c$ Thus for this value of the vertical field the major radius of the magnetic axis would be centered on the ring.

A very approximate value for r_c

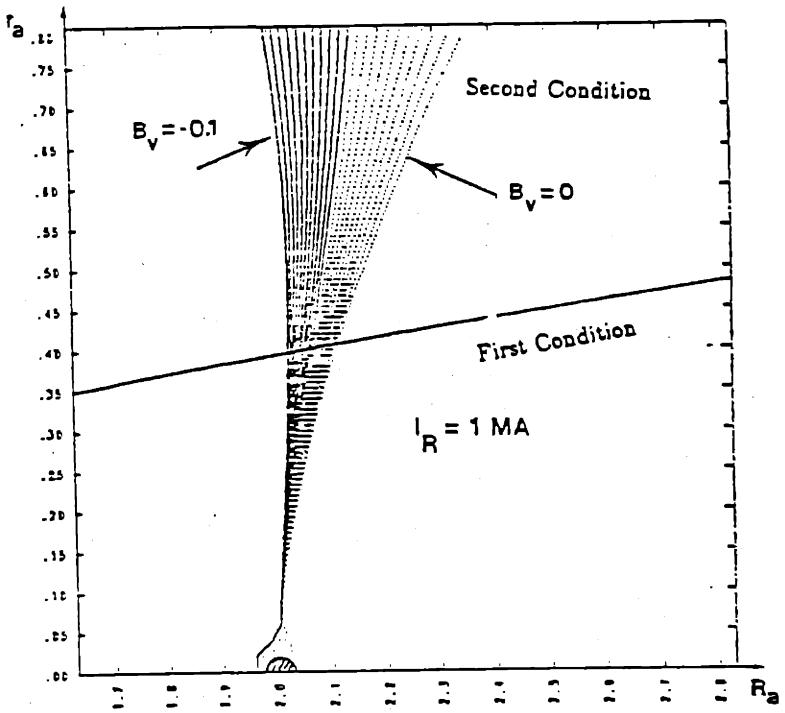

Figure D.2 Combination of first and second condition

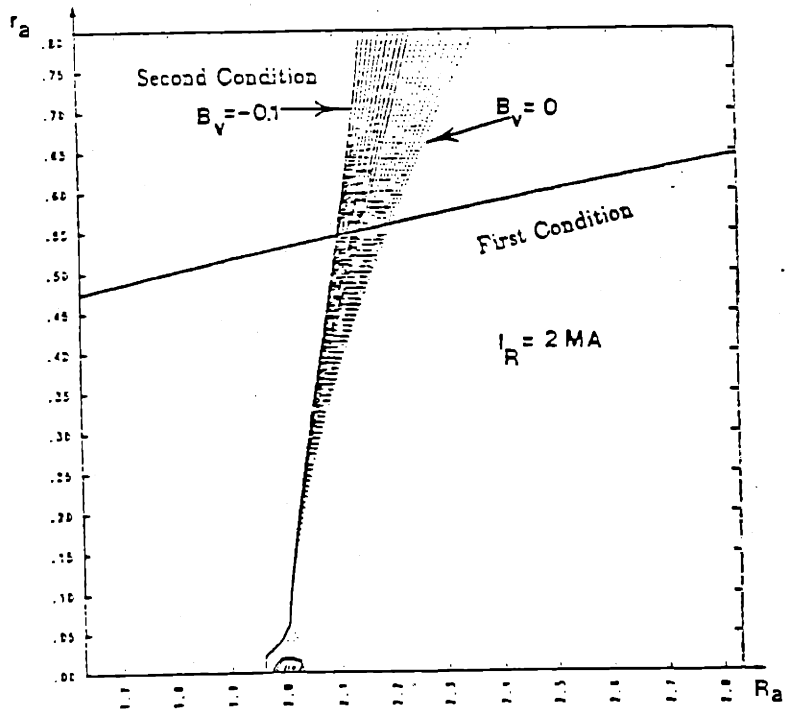

Figure D.3 Combination of first and second condition

$$r_a = \sqrt{\frac{\mu_o I_R R_c}{2\pi B_\phi} \frac{m}{n}} \qquad (D.17)$$

is obtained by simplifying even more (D.15). Thus formulas (D.16) and (D.17) give rule of thumb calculations for I_R and B_v if one wants to achieve a helical solenoid with given r_a and $R_a = R_R$.

While those results are quick and easy it is not completely justified to neglect the contribution to the vertical field at $R = R_a$ due to the toroidal coils if $R_a \neq R_c$ this for the simple reason that although the contribution is small, so is the vertical field and the component due to the poloidal ring.

A computer model was set up, so that in addition to be able to explain the trends I would also get results in better agreement with the numerical results. The methodology is the same as outlined above, but the correct fields rather then the simple approximation are used.

Using the exact fields along the lines $\theta = 0$ and $\theta = \pi$ the combinations of R_a and r_a that fulfill the first condition are sought.

For each combination of R_a and r_a we know the point in space where $\theta = \frac{\pi}{2}$. Taking into account the field of the solenoid we check if the total vertical field is zero. The single combination of R_a and r_a that fulfills both conditions is the value that correspond to the given I_R and B_v.

In fact, to make the program more efficient, we first select the combination of R_a and r_a that fulfills $B_{vtot} = 0$ by neglecting the contribution of the toroidal coils, then, keeping r_a constant R_c is slightly varied, taking into account the contribution of the toroidal coils, to find the new R_c which fulfills $B_{vtot} = 0$

Centering the coils on the magnetic axis increases the space available for the magnetic surfaces.

It is simple to include it in the model. After a first approximate evaluation of r_a and R_a, the angle is changed, r_a is kept constant and R_a is reevaluated including

the fields of the solenoid with the modified modulation angle. By looping on the evaluation of R_a and the angle α_c a convergent solution is very quickly found.

Results for r_a, R_a in the case where $\alpha_c = \alpha_R$ are shown in Fig. D.4 and D.5. The angle α_R appears in Fig. D.6. The model reproduces here too the features noticed in the numerical calculations, namely that as the angle of the solenoid is changed, r_a , R_a and α_c will vary , but α_R will stay very nearly constant.

The rotational transform calculated as an integral of the torsion is shown in Fig. D.7. The modulation angle of the magnetic axis is shown in Fig. D.8 . Comparison of Fig. D.4 to D.7 with Fig. 4.9 to 4.12 shows excellent agreement of our model with the numerical calculations, except for the rotational transform.

There is a slight discrepancy ($< 20\%$) in the calculation of the rotational transform. The reason is the ellipticity of the surfaces, which also contributes to the rotational transform as one can see from formula (4.1) and is not included in the model. An excentricity of 1.5 would give reasonably close agreement between the numerically calculated rotational transform and the one calculated from our model. The value of 1.5 corresponds with the shape of the flux surfaces as obtained by puncture plots.

The basis of our model is the assumption that the magnetic axis can be defined as

$$\begin{aligned} \frac{n}{m}\phi &= \theta_a + \alpha_a \sin\theta_a \\ r &= r_a \\ R &= R_a \end{aligned}$$

or in words that the magnetic axis can be modeled by a single harmonic for the angle with a constant minor and major radius. Based on this assumption we calculate three parameters α_a, r_a, R_a from three datapoints (the field at $\theta = 0$, at $\theta = \pi$ and $\theta = \frac{\pi}{2}$. That this assumption is realistic follows from the close agreement between our results and the numerical results. An additional check was made by applying a fast Fourier transformation to the coordinates of the magnetic axis as obtained from numerical field line following. For a particular case, ($R_R = 2m$, $r_c = 0.4m$, $a_c = 0.4$, $I_R = 800kA$, $B_v = 0.04T$, $n = 3$,

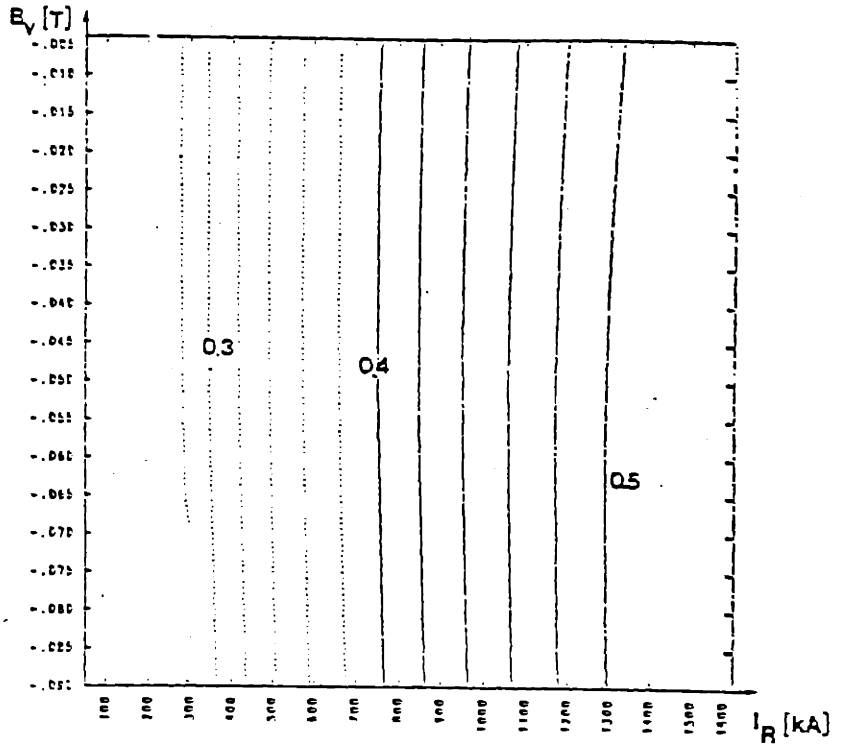

Figure D.4 Variation of r_a as a function of B_v and I_R

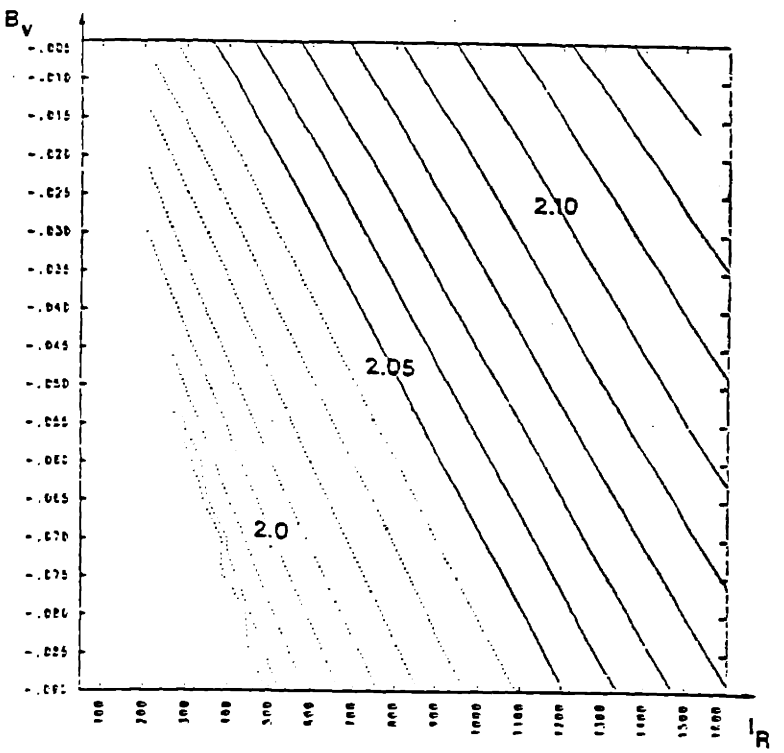

Figure D.5 Variation of R_a as a function of B_v and I_R

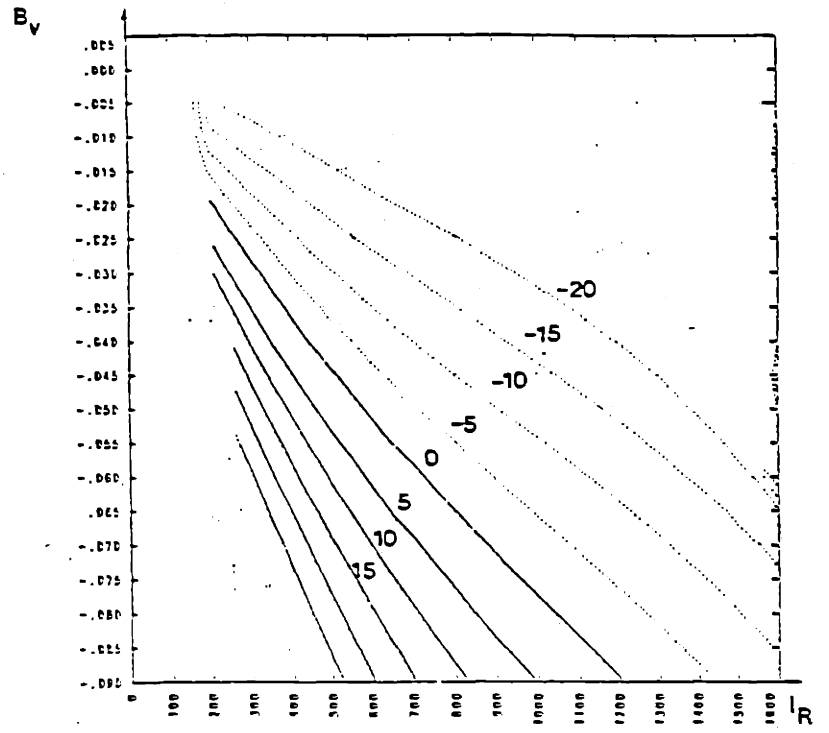

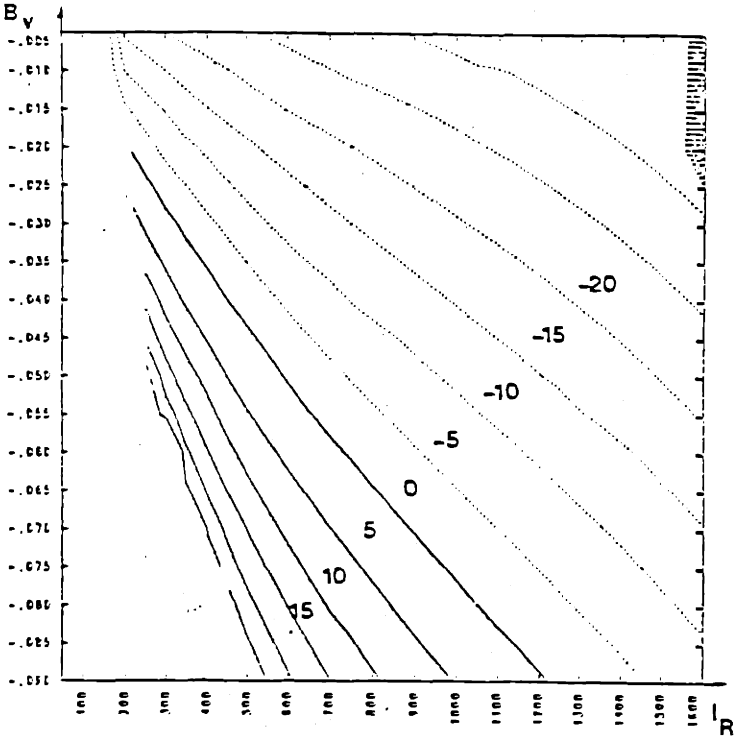

Figure D.6 Value of α_R when $\alpha_c = 0$ and when $\alpha_c = \alpha_R$

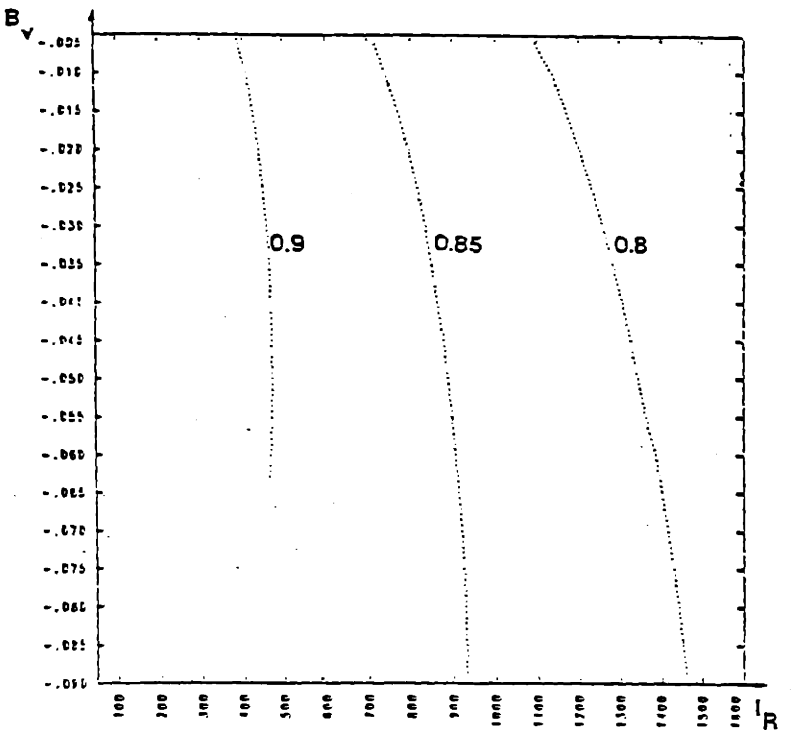

Figure D.7 Rotational transform calculated as an integral of the torsion

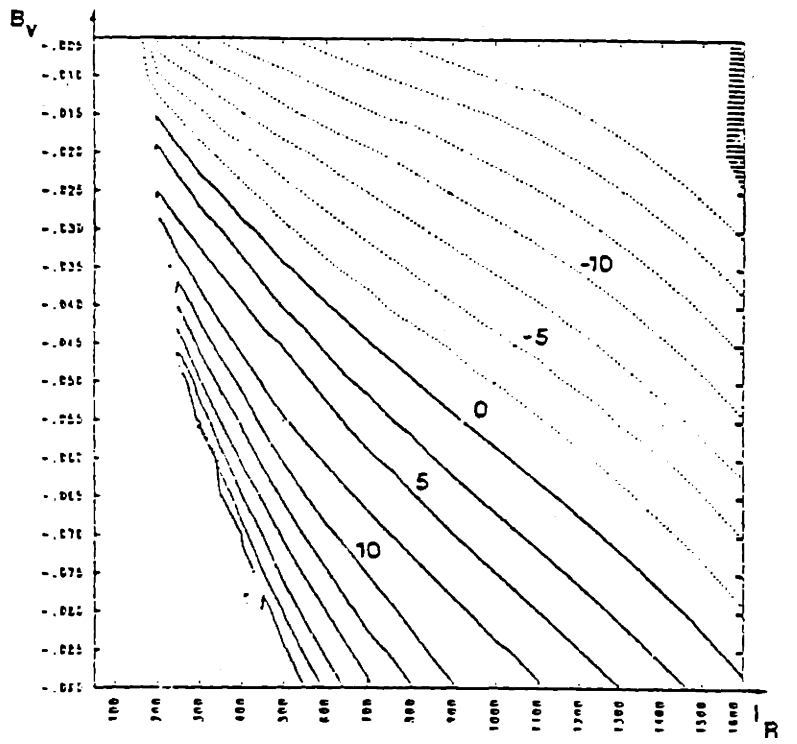

Figure D.8 Modulation angle α_c of the magnetic axis

and 60 coils with $194365 A/coil$) we obtain for the Fourier transform of the coordinates of the helical axis in a cylindrical system (R, 2, ϕ)

$$R = 2.0985 + 0.4031\cos 3\phi - 0.00189\sin 3\phi - 0.03915\cos 6\phi + 0.004667\cos 3\phi$$

$$z = 0.00191\cos 3\phi - 0.4084\sin 3\phi + 0.03982\sin 6\phi - 0.00463\sin 9\phi$$

$$\theta - 3\phi = 0.03\sin 3\phi + 0.00608 sin6\phi - 0.001059\sin 9\phi$$

We see that the amplitude of the harmonics higher than the first ($n = 3$) are an order of magnitude lower than the amplitude of the first harmonic, which justifies our assumption. We have also made a even more direct calculation. For the case $I_R = 900kA$, $B_v = -0.025T$, we first estimated R_a as the average of R at $\theta = 0$ and $\theta = \pi$. Calculating then from the cylindrical coordinates $r_a = \sqrt{z^2 + (R - R_a)^2}$ and performing a fast Fourier transform on r_a, we obtain $r_a = 0.42105 + 0.001969\cos 3\phi$. The harmonic on r_a is less than 0.5%. The underlying basic assumption of our model is thus completely justified.

Let us summarize : this simple model explains the variation of parameters associated with the magnetic axis of a helical axis stellarator. It provides analytical formulas which can be used as first estimates and in a more refined version obtains those parameters accurately and efficiently (a non-vectorized code on the Cray calculates a 32×18 mesh, 32 points for the current and 18 points for the vertical field, with adjustment of the toroidal coil so as to center the coil on the magnetic axis in, about 0.3 min).

Appendix E. Relationship between Ring Radius and Coil Height

This appendix briefly addresses the issue of how to allocate the space $r_c - b_c$ between the height of the coil h_c and the ring radius r_R, taking into account the relationship between the current in the ring (I_R) and in the coil (I_c), the number of coils (N), the displacement ($\frac{r_c}{R}$) and the number of periods (n). In addition the requirements set by non-interference of the coils on the inside have to be met.

Let

$$h_c + r_R = r_c - b_c$$

and

$$R_i + \frac{h_c}{2} = R - r_c - b_c$$

Further we have

$$\frac{2\pi R_i}{N} = w_c$$

$$J_c = \frac{I_c}{w_c h_c}$$

$$J_R = \frac{I_R}{\pi r_R^2}$$

Set the ratio $\frac{I_R}{I_c} = \lambda$, where λ can be calculated from the approximate formulas

$$I_R = \frac{2\pi R B_\phi}{\mu_o} \frac{n}{m} \left(\frac{r_a}{R}\right)^2$$

$$B_\phi 2\pi R \sqrt{1 + \left(\frac{n}{m}\frac{r_c}{R}\right)^2} = \mu_o N I_c$$

Alternatively one could use the actual currents obtained from a computer code that follows field lines and plots magnetic surfaces. We can eliminate from the equations w_c, h_c, r_R, R_i, I_R to obtain

$$\frac{\frac{I_c}{J_c}(\lambda\frac{J_c}{J_R}+N)}{2\pi(R-2r_c)}+\sqrt{\frac{I_c}{J_c}}\sqrt{\frac{\lambda J_c}{\pi J_R}}-(r_c-b_c)\left[\frac{r_c-b_c}{2(R-2r_c)}+1\right]=0$$

This can be solved for I_c

$$\frac{I_c}{(R-2r_c)^2}=J_c\left[\frac{-\sqrt{\frac{\pi\lambda J_c}{J_R}}+\sqrt{\frac{\pi\lambda J_c}{J_R}+\frac{2\pi(r_c-b_c)}{(R-2r_c)}\left[\frac{r_c-b_c}{2(R-2r_c)}+1\right]\left(\frac{\lambda J_c}{J_R}+N\right)}}{\frac{\lambda J_c}{J_R}+N}\right]^2$$

The value of I_c can then be used to obtain

$$r_R=\sqrt{\frac{I_R}{\pi J_R}}=\sqrt{\frac{\lambda J_c}{\pi J_R}}\sqrt{\frac{I_c}{J_c}}$$

and

$$h_c=r_c-b_c-r_R$$

Those last two equations give the values of r_R and h_c that meet the constraints.

Appendix F. Relationship between number of coils, displacement of the coils, bore of the coils and plasma size.

We take here the simple approach that the plasma is centered in the coils. This is justified by the fact that the aspect ratio is larger on the outside, so that not much can be gained, as in a tokamak by pushing the plasma more to a region of lower ripple. The second reason is that, as is discussed elsewhere, the plasma has a tendency to position itself there for choices of ring current and vertical field that give a magnetic well.

Another simplifying assumption used here is the following : surfaces of constant ripple can be obtained by deducting from the radius of the coil a distance proportional to the distance between the coils (Fig. F.1). The proportionality constant depends on the value of the ripple. For $\xi = 3$ the ripple is about 10%, and $\xi = 2$ corresponds to about 2%.

With Δ_{ic} the intercoil distance and Δ_{fc} the distance from the coil we have

$$\xi = \frac{\Delta_{ic}}{\Delta_{fc}}$$

Defining the plasma radius a_p as

$$a_p = b_c - \Delta_{fc}$$

and the ratio η as

$$a_p = \eta b_c$$

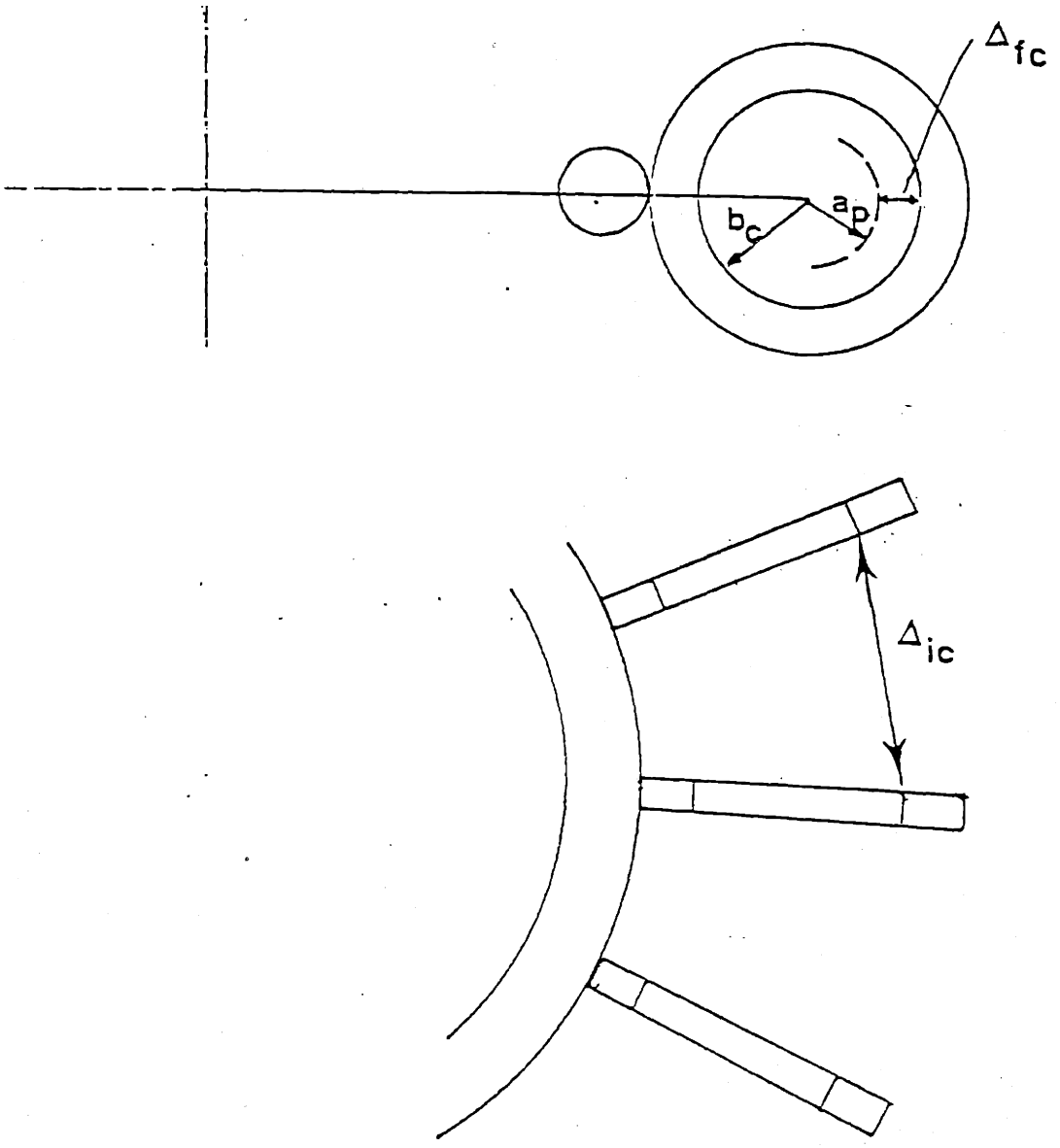

Figure F.1 Geometry

We can write

$$(1-\eta)b_c = \frac{\Delta_{ic}}{\xi}$$

or, using $b_c = \delta r_c$

$$(1-\eta)\delta r_c = \frac{\Delta_{ic}}{\xi} \qquad (F.1)$$

we obtain

$$\xi = \frac{\frac{2\pi}{N}\sqrt{1+2(1+\delta)\frac{r_f}{R}+(1+n^2)(1+\delta^2)(\frac{r_f}{R})^2}}{\frac{r_f}{R}(1-\eta)\delta}$$

By writing this as follows

$$\xi N(1-\eta) = \frac{2\pi\sqrt{1+2(1+\delta)\frac{r_f}{R}+(1+n^2)(1+\delta^2)(\frac{r_f}{R})^2}}{\frac{r_f}{R}\delta}$$

we obtain on the left hand side a dimensionless number Q from which, given ξ, and the fraction η we can calculate the number of coils needed. Or alternatively, for a given ξ, and N we can calculate the value of η.

We have plotted this number in Fig. F.2 to Fig. F.3 under two different formats. Figure F.2 gives for $n = 2$ the value of Q as level lines in a diagram of $\delta = \frac{b_c}{r_c}$ versus $\frac{r_f}{R}$. Figure F.3 shows the value of Q as a function of $\frac{r_f}{R}$ for different values of $\delta = \frac{b_c}{r_c}$ as level lines. Fig. F.4 to F.5 use the same format for the number of periods n equal to 3 and Fig. F.6 to F.7 for $n = 4$.

An example is shown in Figure F.4 Assume that we want $\frac{r_f}{R} = 0.3$ and $\delta = \frac{b_c}{r_c} = 0.5$, we obtain from the figure $Q = 80$. With $Q = \xi N(1-\eta)$ this tells us that if we want $\xi = 2$ (for 2% ripple) and $\eta = \frac{c_p}{b_c} = 0.5$ then N should be equal to 80. The same information can be gathered from Figure F.5. (which can be considered also as showing the number of coils -if we fix $\xi = 2$ and $\eta = 0.5$- as a function of $\frac{r_f}{R}$)

It may seem strange that Q decreases as $\frac{r_f}{R}$ increases, for constant $\delta = \frac{r_f}{R}$. The reason is that as $\frac{r_f}{R}$ increases, the bore of the coil increases. While the absolute distance Δ_{fc} increases as $\frac{r_f}{R}$ increases, because the coils are further apart, this increase is slower than the increase of the bore of the coil. Thus $\frac{c_p}{R}$ increases faster than $\frac{r_f}{R}$ or alternatively, if we keep $\frac{c_p}{r_c} = \eta$ constant, the number of coils can be reduced.

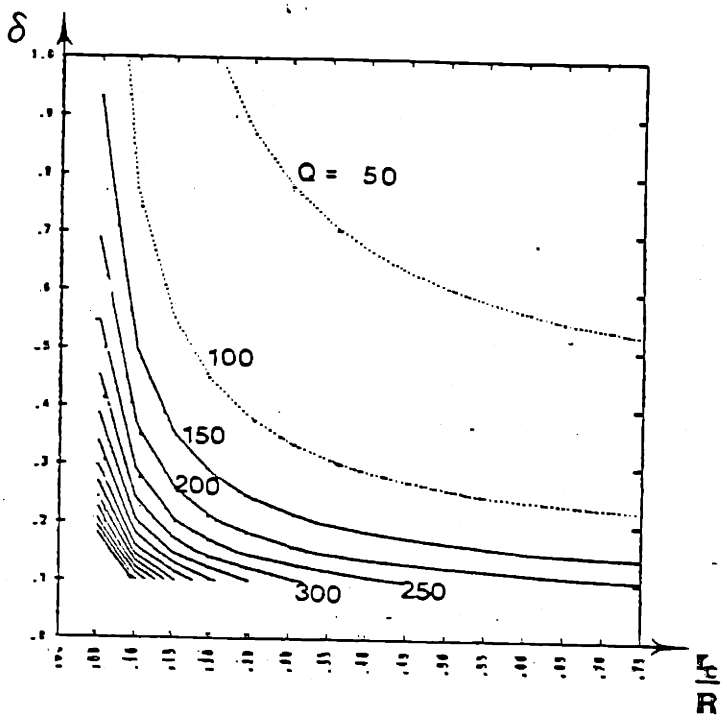

Figure F.2 Value of Q in $\frac{b_c}{r_c}$ versus $\frac{r_c}{R}$ diagram, for $n = 2$

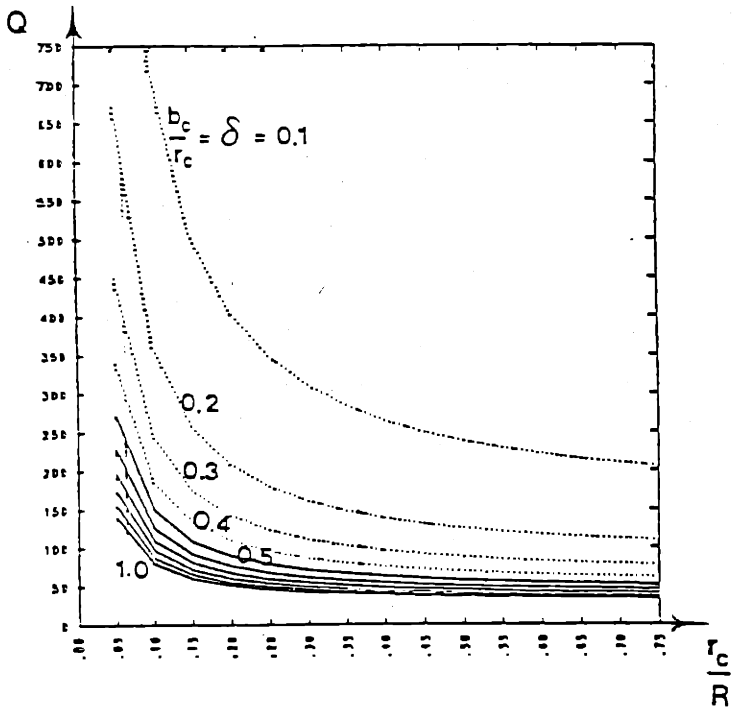

Figure F.3 Value of δ in Q versus $\frac{r_c}{R}$ diagram, for $n = 2$

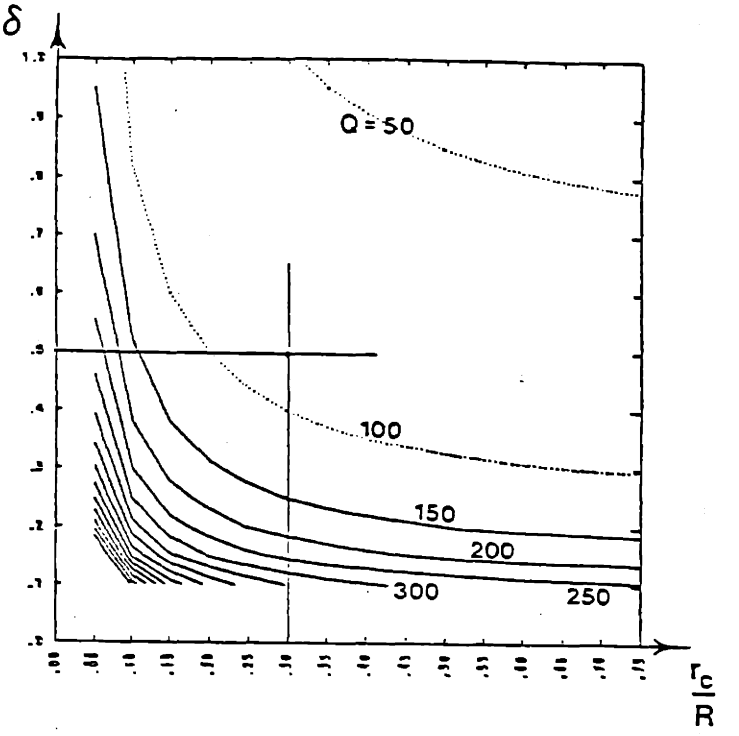

Figure F.4 Value of Q for $n = 3$

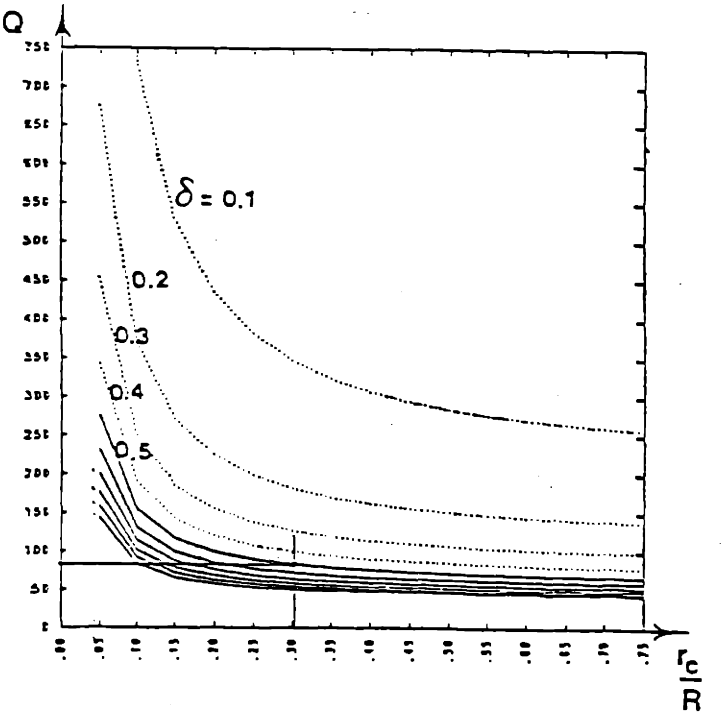

Figure F.5 Value of δ for $n = 3$

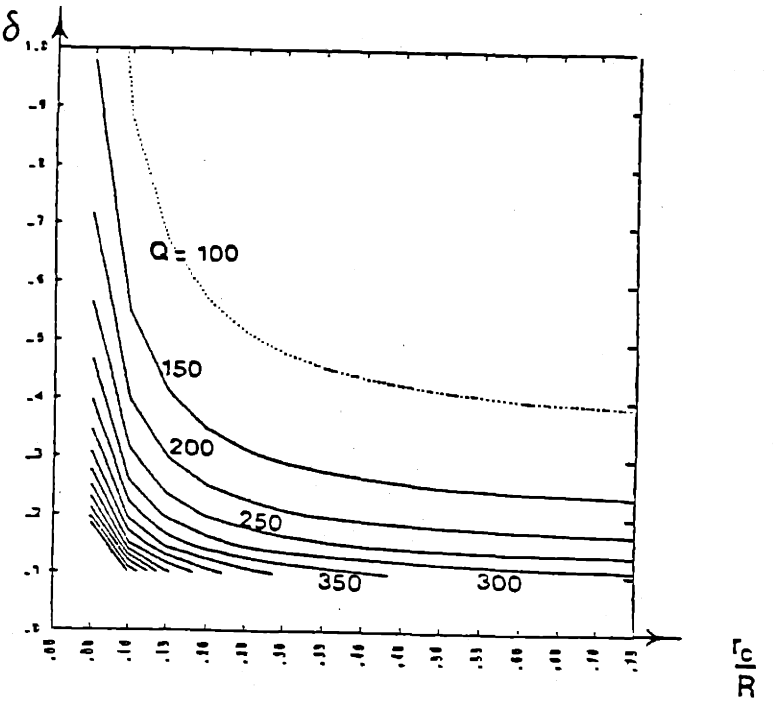

Figure F.6 Value of Q for $n = 4$

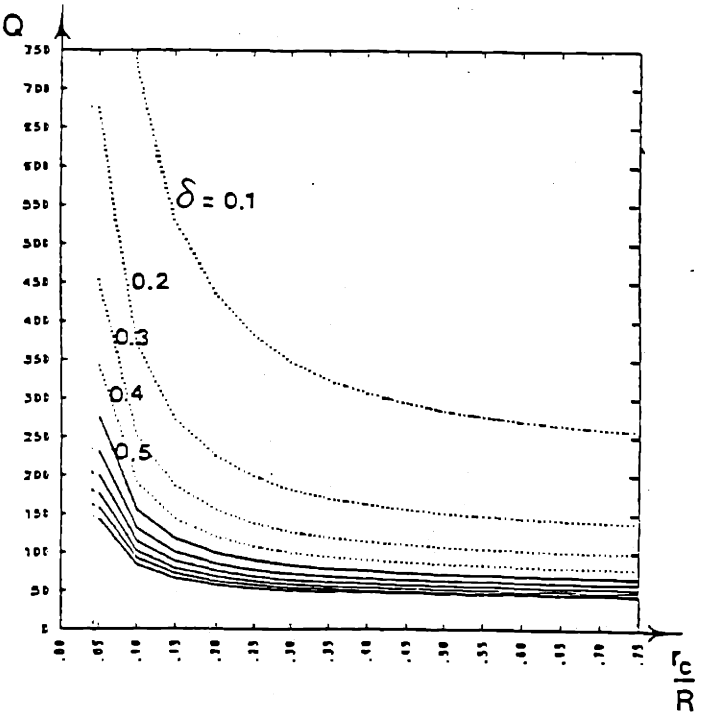

Figure F.7 Value of δ for $n = 4$

Appendix G. Similarity and derivation of the number of independent dimensionless parameters for plasma physics

In this appendix we plan first to show the relationship between both methods discussed in the example in chapter 2, and we will identify in more detail a formalism that can be used with the second method to obtain the number of independent dimensionless parameters. Applying this formalism to the equations governing the plasma physics phenomena rigorously identifies the number of independent dimensionless parameters.

G.1. Relationship between the two models

Define IV_1 to be the number of independent variables according to the first method. The number of basic dimensions is Dim. The first method says that the number of independent dimensionless parameters (IDP_1) is

$$(IDP_1) = IV_1 - Dim$$

The actual number of variables, and the number of basic dimensions depend on the choice of systems of units chosen. It is well known that there is an arbitrariness in the number of fundamental units and in the dimensions of any physical quantity in terms of those units (see for example Jackson [146]). The number of independent dimensionless parameters however, is not affected by this choice. The number of possible transformations, assuming all the independent variables IV_1 can be freely chosen, is then given by the number of dimensions. If some (FX_1) of the independent variables IV_1 however are fixed, or chosen as such (as in our example : taking μ and ρ fixed, thus not changing the fluid),

the number of possible transformations (TR_1) is reduced accordingly. Thus

$$TR_1 = [IV_1 - FX_1] - IDP_1$$

Using the second method we have a set of equations EQ_2. Taking V_2 to be the total number of variables, dependent and independent, assuming at first that all can be changed, we will have a number K_2 of scaling variables. Requesting that the equations are invariable under transformation will yield a number of independent relations (IR_2) from which dimensionless variables can be constructed. The equations can then be written in the dimensionless form, yielding $EQ_{2'}$ relations between the dimensionless parameters (note $EQ_{2'}$ can be different from EQ_2 since homogeneous equations, as $\overline{\nabla} \cdot \overline{v} = 0$ in our example do not give a relation).

The number of independent dimensionless parameters IDP_2 is then equal to

$$IDP_2 = IR_2 - EQ_{2'}$$

Note that taking some variables (FX_2) fixed can be done formally by adding FX_2 equations of the form *Variable* $=$*constant*. This will not change the number of dimensionless parameters since we now have FX_2 more relations for the k's, but also FX_2 more equations

$$\begin{aligned} IDP_2 &= (IR_2 + FX_2) - (EQ_{2'} + FX_2) \\ &= IR_2 - EQ_{2'} \end{aligned}$$

The number of transformations possible is equal to the number of k's (K_2) minus the number of relationships between the k's ($IR_2 + FX_2$). This gives

$$TR_2 = K_2 - (IR_2 + FX_2)$$

showing that the number of possible transformations is indeed affected by fixing FX_2 variables. With

$$IDP_2 = IR_2 - EQ_{2'}$$

we also obtain

$$TR_2 = K_2 - (EQ_{2'} + FX_2) - IDP_2$$

The relationship between the first and the second method follows from the equality of the number of dimensionless parameters and the number of transformations. This yields

$$IV_1 - FX_1 = K_2 - (EQ_{2'} + FX_2)$$

giving us a way to count the number of independent variables for the first method:

$$IV_1 = K_2 - EQ_{2'}.$$

G.2. Formalism for the second method

The formalism, using the second method is simple (the application of it however, may not be). First write down the set of equations governing the phenomena. Count all the variables (K_2). Count the number of *independent* relations (IR_2) for the k's resulting from the requirement that the equations are invariant under transformation. Count the number ($EQ_{2'}$) of equations that would result between dimensionless parameters from the set of equations. The number of independent dimensionless parameters (IDP_2) then is

$$IDP_2 = IR_2 - EQ_{2'}$$

The number of possible transformations (TR_2) is

$$TR_2 = K_2 - IR_2$$

Fixing a number of parameters reduces the number of possible transformations TR_2.

G.3. Application to plasma physics

We can write down the Boltzman equation for the ions and the electrons, and the Maxwell equation, in a simplified, suitable form for our dimensional analysis

(since the geometry has to be to scale, we only use one component for vector quantities). This results in

$$\frac{\partial f_e}{\partial t} + v_e \frac{\partial f_e}{\partial x} + \frac{e_e}{m_e}(E + v_e B)\frac{\partial f_e}{\partial v_e} = \left(\frac{\partial f}{\partial t}\right)_c + h_e \qquad (G.1)$$

$$\frac{\partial f_i}{\partial t} + v_i \frac{\partial f_i}{\partial x} + \frac{e_i}{m_i}(E + v_i B)\frac{\partial f_i}{\partial v_i} = \left(\frac{\partial f}{\partial t}\right)_c + h_i \qquad (G.2)$$

$$\frac{\partial B}{\partial x} = 0 \qquad (G.3)$$

$$\frac{\partial E}{\partial x} = \frac{1}{\epsilon_o}\left(n_e e_e \int f_e dv_e + n_i e_i \int f_i dv_i\right) \qquad (G.4)$$

$$\frac{\partial E}{\partial x} = -\frac{\partial B}{\partial t} \qquad (G.5)$$

$$\frac{\partial B}{\partial x} = \mu_o(n_e e_e \int v_e f_e dv_e + n_i e_i \int v_i f_i dv_i) + \mu_o J + \mu_o \epsilon_o \frac{\partial E}{\partial t} \qquad (G.6)$$

The notation is standard except for h_e and h_i which are to be considered as terms to model additional heating. In (G.6) we have also included a term $\mu_o J$ (for external currents), in order to easily obtain that, if there are currents in the plasma, they must scale the same way as external currents. This is needed because the geometry must not change.

Let us take the electric and magnetic field to be the sum of an imposed (p) and a self-consistent (s) field

$$E = E_p + E_s \qquad (G.7)$$

$$B = B_p + B_s \qquad (G.8)$$

and the particle distribution function to be defined completely by a temperature, and a drift velocity for each species.

$$\frac{f_e}{\left(\frac{m_e}{2\pi k T_e}\right)^{1/2}} = F_e\left(\frac{m_e(v_e - v_{oe})^2}{kT_e}\right) \qquad (G.9)$$

$$\frac{f_i}{\left(\frac{m_i}{2\pi k T_i}\right)^{1/2}} = F_i\left(\frac{m_i(v_i - v_{oi})^2}{kT_i}\right) \qquad (G.10)$$

Taking first the case considered in the body of the text namely, steady state, no motion $v_{oe} = v_{oi} = 0$, and no imposed electrical field $E_p = 0$. The equations reduce to

$$v_e \frac{\partial f_e}{\partial x} + \frac{e_e}{m_e}(E + v_e B)\frac{\partial f_e}{\partial v_e} = \left(\frac{\partial f}{\partial t}\right)_c + h_e$$

$$\frac{f_e}{\frac{m_e}{2\pi k T_e}^{1/2}} = F_e\left(\frac{m_e v_e^2}{k T_e}\right)$$

with a similar set for the ions and

$$\frac{\partial E}{\partial x} = \frac{1}{\epsilon_o}(n_e e_e \int f_e dv_e + n_i e_i \int f_i dv_i)$$

$$\frac{\partial B}{\partial x} = \mu_o J$$

$$E = E_s$$

$$B = B_p + B_s$$

The total number of k's equals 21. The number of *independent* relations between the k's is 17, giving 17 dimensionless parameters. The number of equations between the dimensionless parameters is 8, giving $17 - 8 = 9$ independent dimensionless parameters, one more than in the body of the text, since we have here assumed that we could heat the electrons and ions independently. They are β, ν, N_λ, $\frac{\rho}{\varepsilon}$, $\frac{\epsilon_i}{\epsilon_i}$, $\frac{m_e}{m_i}$, $\frac{n_e}{n_i}$, $\frac{T_e}{T_i}$ and $\frac{h_e}{h_i}$. This set reduces to eight if we only heat electrons *or* ions.

The number of transformations is $21 - 17 = 4$. Assuming only one heating method does not change this number $20 - 16 = 4$. If we want to keep all the eight parameters constant, and since we can not scale the charge of the electron, the mass of the electron, ϵ_o or μ_o, we loose all possibility to make a transformation.

The same number of parameters can be derived using two fluid transport equations (continuity, momentum, and energy for ions and electrons) and Maxwell's equations. Extreme care must be exercised there to count the

independent relationship between the k, since the energy equation is obtained, as the momentum equation, from an integration of the Boltzman equation.

Let us now briefly discuss the case of a tokamak, where we do have a drift velocity v_{oe} of the electron (assume $v_{oi} = 0$) and an imposed electrical field E_p. The equations (G.1) to (G.10) can be rewritten in steady state and yield a total number of 23 k's. The number of independent relations between the k's increases only by 1, while the number of equations does not change. Thus for a tokamak, assuming additional heating of the electrons and ions, the total number of independent dimensionless parameters is 11, one more than the case with $v_{oe} = v_{oi} = E_p = 0$. For this additional independent dimensionless parameter we can take

$$\xi = \frac{v_{oe}}{\sqrt{\frac{kT_e}{me}}}$$

the drift parameter.

References

[1] GIBSON, A., et al. *The Experimental Investigation of Single-Particle Containment in a High-Shear Stellarator* in Plasma Physics and Controlled Nuclear Fusion Research (Proc. 3rd Int. Conf. Novosibirsk 1968) IAEA, Vienna (1969) Vol.1, 465

[2] KOPPENDORFER, W., *The Zephyr Experiment* in Fusion Technology (Proc. 11th Symp. Oxford 1980) published for the Commission of the European Communities by Pergamon Press, Oxford (1980)Vol.1, 77

[3] BUCKINGHAM, E., *On Physically Similar Systems : Illustrations of the Use of Dimensional Equations* Phys. Rev. 4 (1914) 349

[4] BRIDGMAN, P.W., *Dimensional Analysis* Yale University Press, New Haven, 1963

[5] KADOMTSEV, B.B., *Tokamaks and Dimensional Analysis* Fiz. Plasmy 1 (1975) 531 (Sov. Journal of Plasma Physics 1 (1975) 531)

[6] MYNICK, H.E., CHU, T.K., BOOZER, A.H., *An Enhanced-Confinement Class of Stellarators* PPPL-1822

[7] YOSHIKAWA,S., CHRISTOFILOS, N., *Implication of Pseudo-Classical Diffusion for Toroidal Confinement Devices* in Plasma Physics and Controlled Nuclear Fusion Research (Proc. 4th Int. Conf. Madison 1971) IAEA, Vienna (1971) Vol.2, 387

[8] CONNOR, J.W., TAYLOR, J.B., *Scaling Laws for Plasma Confinement* Nucl. Fusion 17 (1977) 1047

[9] CONNOR, J.W., TAYLOR, J.B., *Scaling Laws for Plasma Confinement* European Physical Society Prague (1977) Vol1, 14

[10] CONNOR, J.W., TAYLOR, J.B., *Implications of Theoretical Scaling Laws* Heating in Toroidal Plasmas 1978 (Joint Varenna-Grenoble Int. Symp.) Vol 1, 1 (1978)

[11] ROSE, D.J., CLARK, M.J., *Plasmas and Controlled Fusion* MIT Press Cambridge, 1965

[12] IOFFE, M.S., et al., *Loss of Plasma from a Magnetic-Mirror System II* Sov. Phys. JETP 13 (1961) 27

[13] BARNEY, G.O., SPROTT, J.C., *Double Vortex Flows in Plasmas Axially Traversing Multipole Magnetic Fields* Phys. Fluids 12 (1969) 707

[14] DRAKE, J.R., GREENWOOD, J.R., NAVRATIL, G.A., POST, R.S., *Diffusion Coefficient Scaling in the Wisconsin Levitated Octupole* Phys. Fluids 20 (1977) 148

[15] NAVRATIL, G.A., POST, R.S., BUTCHER-EHRHARDT, A., *Transition from Classical to Vortex Diffusion in the Wisconsin Levitated Octupole* Phys. Fluids 20 (1977) 156

[16] FUJIWARA, M., MIJAMOTO, K., *Viscosity Damping of Convective Coils in J.I.P.P.-Stellarator-Confined Plasmas* Nucl. Fusion 12 (1972) 587

[17] HOFFMAN, D.J., TALMADGE, J.N., SHOHET, J.L., *Plasma Gun Injection in the Proto-Cleo Stellarator* Nucl. Fusion 21 (1981) 1330

[18] OKUDA, H., DAWSON, J.M., *Theory and Numerical Simulation on Plasma Diffusion across a Magnetic Field* Phys. Fluids 16 (1973) 408

[19] HASEGAWA, A., OKUDA, H., WAKATANI, M., *Effect of Finite β on Diffusion Wave Turbulence and Particle Confinement* Phys. Rev. Lett. 44 (1980) 248

[20] AXON, K.B., et al., *Results from the Dite Experiment* in Plasma Physics and Controlled Nuclear Fusion Research (Proc. 9th Int. Conf. Baltimore 1982) IAEA, Vienna (1983)

[21] JOHNSON, D., et al., *Neutral Beam Heating Experiments on PDX* in Plasma Physics and Controlled Nuclear Fusion Research (Proc. 9th Int. Conf. Baltimore 1982) IAEA, Vienna (1983)

[22] MURAKAMI, M., *Beta Scaling Experiments in ISX-B* in Plasma Physics and Controlled Nuclear Fusion Research (Proc. 9th Int. Conf. Baltimore 1982) IAEA, Vienna (1983)

[23] CARRERAS, B.A., ET AL., *MHD Activity and Neutral Beam Driven Transport Effects in ISX-B Tokamak* in Plasma Physics and Controlled Nuclear Fusion Research (Proc. 9th Int. Conf. Baltimore 1982) IAEA, Vienna (1983)

[24] THOMPSON, W., *An Introduction to Plasma Physics* Pergamon Press, New York, Oxford, 1962

[25] JOHNSON, L.C., HINNOV, E., *Ionization, Recombination and Population of Excited Levels in Hydrogen Plasmas* J. Quant. Spectrosc. Radiat. Transfer 13 (1973) 333

[26] GARCIA, J.D., MAEK, J.E., *Energy Levels and Line Tables for One Electron Atomic Spectra* J. Opt. Soc. Am. 55 (1965) 654

[27] GOLDSTON, R.G., *Diagnostic Techniques for Magnetically Confined High Temperature Plasmas II : Magnetic and Electric Measurements, Charge Exchange Diagnostics, Particle Beam Diagnostics and Fusion Products Measurements* PPPL-1924 UC20-f

[28] GORDEEV, Y.S., ZINOVEV, A.N., PETROV, M.P., *Recombination of Hydrogen in a Quasi-Stationary Thermonuclear Plasma* JETP Lett. 25 (1977) 204

[29] FREEMAN, R.J., JONES, E.M., *Analytic Expressions for Selected Cross Sections and Maxwellian Rate Coefficients* Culham Laboratory Report CLM R137 (1974)

[30] REHKER, S., WOBIG, H., *A Kinetic Model for the Neutral Gas between Plasma and Wall* Plasma Physics 15 (1973) 1083

[31] HACKMANN, J., KIM, Y.C., UHLENBUSCH, J., *Numerical Investigation of the Build-up phase of the Neutral Hydrogen layer near the Wall during Transient Gas Feed in Tokamak Discharges* (Proc. 3rd Int. Conf. on Plasma Surface Interaction in Controlled Fusion Devices, Abingdon 1978) J. Nucl. Mat. 76/77 (1978) 346

[32] HACKMANN, J., KIM, Y.C., et al., *Investigation of Neutral Particle Behavior Between Plasma and Wall Interactions* Plasma Phys. 20 (1978) 309

[33] TENDLER, M., CHHABRA, R.S., *Transport of Neutrals in a Multi-component Cool Plasma Mantle* Phys. Fluids 25 (1982) 2101

[34] BURRELL, K.H., *Kinetic Theory of Neutral Hydrogen Atoms in a Bounded Hydrogen Plasma Slab* Phys. Fluids 21 (1978) 2202

[35] PARSONS, C.R., MEDLEY, S.S., *On the Interpretation of Charge-Exchange Ion Temperature Measurements in Tokamaks.*Plasma Physics 16 (1974) 267

[36] HUGILL, J., SHEFFIELD, J., *Empirical Tokamak Scaling* Nucl. Fusion 18 (1978) 15

[37] GOEDHEER, W.J., et al. *Studies of Cold-Plasma/Gas Blankets* in Plasma Physics and Controlled Nuclear Fusion Research (Proc. 8th Int. Conf. Brussels 1980) IAEA, Vienna (1981) Vol.2, 635

[38] GILLIGAN, J.G., et al., *Multigroup Calculations of Low-Energy Neutral Transport in Tokamak Plasmas* Nucl. Fusion 18 (1978) 63

[39] PODESTA, G., ENGELMAN, F., *Cold Neutrals and Charge Exchange in Toroidal Plasmas* Toroidal Plasma Confinement (Proc. 3rd Int. Symp. Garching)

[40] ASDEX UPGRADE DESIGN TEAM AND TOKAMAK THEORY GROUP *Asdex Upgrade : Definition of a Tokamak Experiment with a Reactor*

Compatible Poloidal Divertor IPP 1/197 March 1982 Max Planck Institut fur Plasmaphysik

[41] GAUDREAU, M.P.J., KISLYAKOV, A.I., SOKOLOV, Yu.A., *Investigation of Fast-Atom Fluxes in the High-Density Plasma in Alcator* Nucl. Fusion 18 (1978) 1725

[42] LEHNERT, B., *On the Scaling Laws of Permeable and Impermeable Tokamak Plasmas* Third International Symposium on Toroidal Plasma Confinement Garching 1973

[43] LEHNERT, B., *Gas Blanket Concept* Third International Symposium on Toroidal Plasma Confinement Garching 1973

[44] SCATURRO, L.S., PICKRELL, M.M., *Bolometric Measurements and the Role of Radiation in Alcator Power Balance* Nucl. Fusion 20 (1980) 527

[45] POST, D.E., GRISHAM, L.R., FONCK, R.J., *Several Atomic Physics Issues Connected with the Use of Neutral Beams in Fusion Experiments* PPPL-1962 August 1982

[46] CAROLAN, P.G., PIOTROWICZ, V.A., *The Behavior of Impurities out of Coronal Equilibrium* UKAEA CLM-P 672 June 1982

[47] SUCKEWER, S., HINNOV, E., BITTER, M., HULSE, R., POST, D., *Experimental Evidence of Charge Exchange Recombination of Highly Ionized Iron and Titanium in Princeton Large Torus* PPPL-1636

[48] HOGAN, J.T., *The Effect of Low Energy Electron Capture Collisions* $(H_o + C^{n+})$ *on the Particle and Energy Balance of Tokamak Plasmas* Physics of Electronic and Atomic Collisions 1982 769

[49] HULSE, R.A., POST, D.E., MIKKELSON, D.R., *Charge Exchange as a Recombination Mechanism in High Temperature Plasmas* PPPL-1633 1980

[50] VOLKOV, T.F., IGITKHANOV, J.L. *Kinetics of Neutral Atoms Near the Wall of a Fusion Reactor and Impurity Formation* QC S7273 1977

[51] BROWN, S.C., *Introduction to Electrical Discharges in Gases* Wiley, n.y. 1966

[52] MCDANIEL, E.W., *Collision Phenomena in Ionized Gases* Wiley, New York 1964

[53] BARNETT et al., *Atomic and Molecular Collision Cross Sections of Interest in Controlled Thermonuclear Research* ORNL-3113

[54] MCCRACKEN, G.M., FIELDING, S.J., ERENTS, S.K., POSPIESZCZYK, A., STOTT, P.E., *Recycling Experiments in the Dite Tokamak* Nucl. Fusion 18 (1978) 35

[55] GORBUNOV, E.P., MIRNOV, S.V., PARFENOV, D.S., *Measurements of the Diffusion Lifetime of a Plasma in Tokamak-3 by Neutral Hydrogen Injection Method* Nucl. Fusion 11 (1971) 433

[56] ARTSIMOVICH, L.A., MIRNOV, S.V., STRELKOV, V.S., *Investigation of Ohmic-Heating of the plasma in the Tokamak-3 Toroidal Assembly* Atom. Energy 17 (1964) 170

[57] TAYLOR, R.J., BUNSHAH, R.F., SCHWIRZKE, F., *Impurity Control of Tokamaks with in situ Metal Deposition* (Proc. 4rd Int. Conf. on Plasma Surface Interaction in Controlled Fusion Devices, Garmisch-Partenkirchen 1980) J. Nucl. Mat. 93/94 (1980) 338

[58] EQUIPE TFR *Experiments with a Limiter of Variable Radius in the TFR Tokamak* Nucl. Fusion 18 (1978) 791

[59] FIELDING, S.J., MCCRACKEN G.M., STOTT, P.E., *Recycling in Gettered and Diverted Discharges in DITE Tokamaks* (Proc. 3rd Int. Conf. on Plasma Surface Interaction in Controlled Fusion Devices, Abingdon 1978) J. Nucl. Mat. 76/77 (1978) 273

[60] HOWE, H.C., *Hydrogen Recycle Modeling and Measurements in Tokamaks* (Proc. 4rd Int. Conf. on Plasma Surface Interaction in Controlled Fusion Devices, Garmisch-Partenkirchen 1980) J. Nucl. Mat. 93/94 (1980) 44

[61] CLAUSING, R.E., EMERSON, L.C., HEATHERLY, L., *Studies of Hydrogen Recycle from the Walls in Tokamaks Using a Plasma-Wall*

Interaction Simulator (Proc. 3rd Int. Conf. on Plasma Surface Interaction in Controlled Fusion Devices, Abingdon 1978) J. Nucl. Mat. 76/77 (1978) 267

[62] WILSON, K.L., BASKES, M.I., *Deuterium Trapping in Irradiated 316 Stainless Steel* (Proc. 3rd Int. Conf. on Plasma Surface Interaction in Controlled Fusion Devices, Abingdon 1978) J. Nucl. Mat. 76/77 (1978) 291

[63] BLEWER, R.S., BEHRISCH, R., SCHERZER, B.M.U. SCHULZ, R., *Trapping and Replacement of 1-14 keV Hydrogen and Deuterium in 316 Stainless Steel* (Proc. 3rd Int. Conf. on Plasma Surface Interaction in Controlled Fusion Devices, Abingdon 1978) J. Nucl. Mat. 76/77 (1978) 305

[64] HAYZEN, A.J., OVERSKEI, D.O., MORENO, J., *Probe Measurements of the Boundary Plasma in Alcator C* PFC/JA-81-10

[65] CLAUSING, R.E., EMERSON, L.C., HEATHERLY, L., *Studies of Mechanisms of Hydrogen Recycle Using a Plasma-Wall Interaction Experiment* (Proc. 4rd Int. Conf. on Plasma Surface Interaction in Controlled Fusion Devices, Garmisch-Partenkirchen 1980) J. Nucl. Mat. 93/94 (1980) 542

[66] BRAGANZA, C.M., ERENTS, S.K., HOTSTON E.S., MCCRACKEN, G.M., *Ion-Induced Release of Deuterium Trapped in Stainless Steel* (Proc. 3rd Int. Conf. on Plasma Surface Interaction in Controlled Fusion Devices, Abingdon 1978) J. Nucl. Mat. 76/77 (1978) 298

[67] MARMAR, E.S., OVERSKEI, D., HELAVA, H., et al., *The Effect of Wall Temperature on Light Impurities in Alcator* Nucl. Fusion 19 (1979) 485

[68] LANGLEY, R.A., BLEWER, R.S., ROTH, J., *Behavior of Implanted D and He Pyrolytic Graphite* (Proc. 3rd Int. Conf. on Plasma Surface Interaction in Controlled Fusion Devices, Abingdon 1978) J. Nucl. Mat. 76/77 (1978) 313

[69] HUGHES, M.H., POST, D.E., *A Monte-Carlo Algorithm for Calculating Neutral Gas Transport in Cylindrical Plasmas* J. Comp. Phys. 28 (1978) 43

[70] PFEIFFER, W., WALTZ, R.E., *Empirical Scaling Laws for Energy Confinement in Ohmically-Heated Tokamaks* Nucl. Fusion 19 (1979) 51

[71] ZAMPAGLIONE, V., *On the Transport of Electron Energy in Ohmically-Heated Tokamaks* Frascati 82-20/ March (1982)

[72] GIBSON, A., *Radiation Limits to Tokamak Operation* Nucl. Fusion 16 (1976) 546

[73] MCCRACKEN, G.M., STOTT, P.E., *Plasma Surface Interactions in Tokamaks* Nucl. Fusion 19 (1979) 889

[74] POST, D.E., et al. *Steady State Radiative Cooling Rates for Low-Density, High-Temperature Plasmas* PPPL-1352

[75] MCCRACKEN, G.M., *A Review of the Experimental Evidence for Arcing and Sputtering in Tokamaks* (Proc. 4rd Int. Conf. on Plasma Surface Interaction in Controlled Fusion Devices, Garmisch-Partenkirchen 1980) J. Nucl. Mat. 93/94 (1980) 3

[76] WIECKERT, C., *Plasma Induced Arcs* (Proc. 3rd Int. Conf. on Plasma Surface Interaction in Controlled Fusion Devices, Abingdon 1978) J. Nucl. Mat. 76/77 (1978) 499

[77] BOHDANSKY, J., *Important Sputtering Yield Data for Tokamaks : a Comparison of Measurements and Estimates* (Proc. 4rd Int. Conf. on Plasma Surface Interaction in Controlled Fusion Devices, Garmisch-Partenkirchen 1980) J. Nucl. Mat. 93/94 (1980) 44

[78] BODIN, H.A.B., MCCRACKEN, G.M., in Plasma Physics and Controlled Nuclear Fusion Research (Proc. 5th Int. Conf. Tokyo 1974) IAEA, Vienna (1975) vol 2, 303

[79] MARMAR, E.S., RICE, J.E., TERRY, J.L., *Impurity Injection Experiments on the Alcator Tokamak* PFC Report PFC/JA-82-12

[80] MARMAR, E.S., RICE, J., *Fully-Ionized and Total Silicon Abundances in the Alcator C Tokamak* PFC/JA-82-22

[81] BEHRISCH, R., ROTH, J., BOHDANSKY, J., MARTINELLI, A.P., RUSBULDT, D., HINTZ, E., *Dependence of Light-Ion Sputtering yields of Iron on Ion Fluence and Oxygen Partial Pressure* (Proc. 4rd Int. Conf. on Plasma Surface Interaction in Controlled Fusion Devices, Garmisch-Partenkirchen 1980) J. Nucl. Mat. 93/94 (1980) 645

[82] OREN, L., TAYLOR, R.J., *Trapping and Removal of Oxygen in Tokamaks* Nucl. Fusion 17 (1979) 1143

[83] PENG, Y-K.M., BOROWSKI, S.K., KAMMASH, T., *Microwave Start-up of Tokamak Plasmas Near Electron Cyclotron and Upper Hybrid Resonance* Nucl. Fusion 18 (1978) 1489

[84] DIKY,A.G., KUZNETSOV, Y.K., *Thermal Isolation and Confinement of Plasma in the URAGAN Stellarator* in Plasma Physics and Controlled Nuclear Fusion Research (Proc. 5th Int. Conf. Tokyo 1974) IAEA, Vienna (1975) paper 133-1

[85] TOLOK, V.T., SUPRUNENKO, V.A., *Heating of Plasmas In Stellarators* 3rd Int. Symp. on Toroidal Plasma Conf. Garching 1973

[86] PAVLENKO, V.P., et al. *Diffusion due to Strongly Non-Linear Convective Cells in Plasmas* Nucl. Fusion 21 (1981) 1283

[87] SAITO, H., et al *Experimental and Theoretical Studies on Filling a Stellarator with Laser- Produced Plasma* IEEE PS 9 (1981) 199

[88] MIYAMOTO, K., *Plasma Physics for Nuclear Fusion* MIT Press Cambridge 1980

[89] PIEKAAR, H.W., KLUIVER, H. Phys. Lett. 62A (1977) 413

[90] WOLFE, S.M., et al., *Characteristics of Electron-Cyclotron Resonance Heated Tokamak Power Reactors* PFC Research Report RR-78-3

[91] KREISCHER, K.E., *High Frequency Gyrotron and their Application to Tokamak Plasma Heating* MIT Plasma Fusion Center Research Report RR-81-1

[92] BRAMBILLA, M., *The theory of Lower Hybrid Heating of Tokamak Plasmas* Heating in Toroidal Plasmas 1978

[93] BRAUN, M., EMMOTH, B., WAELBROECK, F., WIENHOLD, P., *Determination of Deuterium Surface Recombination Rates on Stainless Steel* (Proc. 4rd Int. Conf. on Plasma Surface Interaction in Controlled Fusion Devices, Garmisch-Partenkirchen 1980) J. Nucl. Mat. 93/94 (1980) 861

[94] RAEDER, J., et al. *Kontrollierte Kernfusion.* Teuber Stuttgart 1981

[95] PORKOLAB, M., et al., *Observations of Parametric Instabilities in Lower-Hybrid Radio-Frequency Heating of Tokamaks* Phys. Rev. Lett. 38 (1977) 230

[96] MONTGOMERY, D.B., PIERCE, N.T., *The Alcator Liquid Nitrogen Cooled Tokamaks* in Applications of Cryogenic Technology Vol.7 J.R. Missig, R.W. Vance Ed. Scholium Int. Inc. 1978 (Proceedings of Cryo 78, Oak Brook 1978)

[97] BRENTARI, E., SMITH, R.V., *Nucleate and Film Pool Boiling Design Correlations for* O_2, N_2,H_2 *and*He International Advances in Cryogenic Engineering 10 (1964) 327

[98] LITTLETON RESEARCH AND ENGINEERING CORPORATION, *Report to the Francis Bitter National Magnet Laboratory, Massachusetts Institute of Technology* April 1980

[99] MADDOCK, B.J., JAMES, G.B., *Protection and Stabilization of Large Superconducting Coils* Proc. IEE 115 (1968) 545

[100] THOME, R.J., TARRH, J.M. *MHD and Fusion Magnets : Fields and Force Design Concepts* Wiley-Interscience New York 1982

[101] MONTGOMERY, D.B., *Solenoid Magnet Design* Wiley-Interscience New York 1969

[102] WEGGEL, C., HAMBURGER, W., MONTGOMERY, B., PIERCE, N., *The Alcator C Magnetic Coils Systems* in Engineering Problems of Fusion

Research (Proc. 7th Symp. Knoxville 1977) IEEE, New York (1977) Vol.1, 54.

[103] STEKLY, Z.J.J., PUNCHARD, W.F.B., *Effects of Operating Temperature, Heat Load, and Magnetic Field on the Economics of Toroidal Magnet for Fusion Reactors* in Engineering Problems of Fusion Research (Proc. 6th Symp. San Diego 1975) IEEE, New York (1975)

[104] MOON, F.C., *The Virial Theorem and Scaling Laws for Superconducting Magnet Systems*. Topical Report Cornell University May 1981

[105] SCHULTZ, J.H., *Comparison of Magnet Requirements for Fusion and MHD Reactors ; Use of Equivalent Stress to Reach Disturbing Conclusions* MITN-81-005 May 1981

[106] CAIN, W.D., GRAY, W.H., *On Maximum Attainable Magnetic Fields in Toroids and Solenoids Subject to Strain Limitation* in Engineering Problems of Fusion Research (Proc. 8th Symp. San Francisco 1979) IEEE, New York (1979) Vol.1, 94

[107] BONANOS, P., et al., *The Design of the Toroidal and Poloidal Field Coils for TFTR* in Engineering Problems of Fusion Research (Proc. 6th Symp. San Diego 1975) IEEE, New York (1975) 738

[108] HUGUET, M., BOOTH, J.A., POHLCHEN, R., *The Design and Manufacture of the Joint European Torus Toroidal Field Coils* in Engineering Problems of Fusion Research (Proc. 7th Symp. Knoxville 1977) IEEE, New York (1977) 28

[109] KASAI,. M., et al. *The Sensivity Study Code for Tokamak Devices* in Engineering Problems of Fusion Research (Proc. 9th Symp. Chicago 1981) IEEE, New York (1981)

[110] WAGANER, L.M., *Establishment of Design and Performance Requirements Using Cost and System Analysis* in Engineering Problems of Fusion Research (Proc. 7th Symp. Knoxville 1977) IEEE, New York (1977)

[111] SPITZER, L., *The Stellarator Concept* Proceedings of the Second U.N. International Conference on Peaceful Use of Atomic Energy 32 (1958) 181

[112] SHAFRANOV, V.D., *Stellarators* Nucl. Fusion 20 (1980) 1075

[113] MERCIER, C., *Equilibre et Stabilite d'un Systeme Toroidal Magneto-hydrodynamique au Voisinage d'un Axe Magnetique* Nucl. Fusion 4 (1964) 213

[114] ALESKIN, V.F., SEBKO, V.P., *Magnetic Surfaces of a Helical Magnetic Field in the Presence of an Axial Current* Sov. Phys. Tech. Phys 9 (1967) 1189

[115] ALESKIN, V.F., SEBKO, V.P., *Three Turn Helical Magnetic Configuration with Shear and Minimum $\bar{B}$* Nucl. Fusion 8 (1968) 145

[116] GEORGIEVSKIJ, A.V., *Magnetic Systems of the Stellarator Type in the Presence of a Solenoid with a Helical Magnetic Axis* Nucl. Fusion 14 (1974) 87

[117] SOLOVEV, L.S., SHAFRANOV, V.D., *Plasma Confinement in Closed Magnetic System* in Review of Plasma Physics, Ed. M.A. Leontovitch, Consultants Bureau New York, Vol.5

[118] GEORGIEVSKIJ, A.V., et al., *Toroidal Solenoids with a Space Magnetic and a Plane Geometric Axis* Nucl. Fusion 14 (1974) 79

[119] POTOK, R.E., et al., *Physical and Engineering Constraints for Tokamak Reactors and Helical Coils* PFC/RR-82-10 June 1982

[120] POLITZER, P.A., NOTERDAEME, J.-M., *Optimization of the Magnetic Geometry in Helical Axis Stellarators* Bull Am. Phys. Soc. 27 (1982) 1019

[121] KONDOH, Y., NAGAO, S., SUGITA, K., WATANABE, H., *On the Minimization of Displacement of Plasma Column in a Toroidal Magnetic Field with a non-planar Axis* J. Phys. Soc. Jpn 36 (1974) 852

[122] HUGUET, M., REBUT P.H., TOROSSIAN A., *A Large 100 MW Pulsed Magnetic Coil for Fusion Research* in Engineering Problems of Fusion Research (Proc. 4th Symp. ?? 1971) IEEE, New York (1971) 60

[123] KALYUZHNYJ, V.N., NEMOV, V.V., *Plateau and Banana Diffusion Regimes in Traps with a Helical Magnetic Axis* Nucl. Fusion 19 (1979) 1379

[124] BOOZER, A.H., *Transport and Isomorphic Equilibria* PPPL-1804 UC-20G July 22, 1981

[125] BOOZER, A.H., *Transport and Isomorphic Equilibria* Phys Fluids 26 (1983) 496

[126] NEMOV. V.V., *Neoclassical Diffusion in Traps with a Helical Magnetic Axis* Nucl. Fusion 17 1 (1977) 101

[127] KALYUZHNYJ, V.N., KRYUKOV, A.V., NEMOV, V.V., *Neoclassical Diffusion in Helical Solenoids* Nucl. Fusion 18 (1978) 1438

[128] SHAFRANOV, V.D., *Equilibrium of a Plasma Column that does not possess Axial Symmetry II* Nucl. Fusion 4 (1964) 232

[129] BAZHANOVA, A.E., GLAGOLEV, V.M., SHAFRANOV, V.D., *Toroidal Plasma Traps with Three-Dimensional Magnetic Axis* Sov. Phys. Techn. Phys. 11 (1967) 1177

[130] NAGAO. S., SUGITA, K., WATANABE, H., GOTO, Y., KONDOH, Y., *Equilibrium of a High Beta Plasma in a Toroidal Magnetic Field with a Non-Planar Axis* J. Phys. Soc. Jpn 27 (1969) 1082

[131] WATANABE, H., et al., *Equilibrium and Stability of a System with a Non-Planar Magnetic Axis* J. Phys. Soc. Japan 49 (1980) 1542

[132] ZAKHAROV, L.S., SHAFRANOV, V.D. *Equilibrium and MHD Stability of a Plasma in Stellarators with Spatial magnetic Axis* in Plasma Physics and Controlled Nuclear Fusion Research (Proc. 6th Int. Conf. Berchtesgaden 1976) IAEA, Vienna (1977) Vol.2, 155

[133] MOND, M., WEITZNER, H., *Stability of Helically Symmetric Straight Equilibria* Phys. Fluids 25 (1982) 2056

[134] SOLOVEV, L.S., SHAFRANOV, V.D., YURCHENKO, Eh.I., *Plasma Stability in Closed Systems* in Plasma Physics and Controlled Nuclear

Fusion Research (Proc. 3rd Int. Conf. Novosibirsk 1968) IAEA, Vienna (1969) Vol.1, 175

[135] MIKHAILOVSKII, A.B., SHAFRANOV, V.D., *Self-Stabilization of High-Pressure Plasma in Toroidal Traps* Sov. Phys. JETP Vol39, (1974) 88

[136] WAGNER, F., et al., *Variation of the Particle Confinement During Neutral Injection into Asdex Divertor Plasmas* IPP III /78 June 1982, Max Planck Institut Fur Plasma Physik

[137] FILE, J., SHEFFIELD, G.V., *A Large Superconducting Magnet For Fusion Research* Proc. 4th Int. Conf. on Magnet Techn Springfield VA (1972) 240

[138] WEISSENBURGER, D.W., CHRISTENSEN, U.R., BIALEK, J., *The Pure Tension Shape of a Thick Torus* PPPL-1353 Princeton NJ. July 1977 .

[139] MOSES, R.W., YOUNG, W.C., *Analytic Expressions for Magnetic Forces on Sectored Toroidal Coils* in Engineering Problems of Fusion Research (Proc. 6th Symp. San Diego 1975) IEEE, New York (1975)

[140] OJALVO, I.U., *Structural Support Design Method for Minimizing in Plane Toroidal Field Coil System* in Engineering Problems of Fusion Research (Proc. 8th Symp. San Francisco 1979) IEEE, New York (1979)

[141] GRAY, W.H., STODDART, W.C.T., AKIN, J.E., *A Derivation of Bending Free Toroidal Shell Shapes for Tokamak Fusion Reactors* Journ. Appl. Mech. 46 (1979) 1

[142] BOBROV, E.S., SCHULTZ, J.H., *A Model of Toroidal Magnet Systems as Orthotropic Shells of Finite Thickness* in Engineering Problems of Fusion Research (Proc. 9th Symp. Chicago 1981) IEEE, New York (1981) Vol 1, 115

[143] BLUMENAU, L., CITROLO, J., BIALEK, J., *TFTR TF Coil Support Restraint Structure* in Engineering Problems of Fusion Research (Proc. 8th Symp. San Francisco 1979) IEEE, New York (1979)

[144] MONTALVO, E., SANTARIUS, J.F., SIRATOSLAVSKY, I.N., *A Parametric Cost Analysis for Tandem Mirror Reactors Similar to WITAMIR-I* UW FDM-412 March 1981

[145] HETENYI, M., *Beams on Elastic Foundations* Ann Harbor : the University of Michigan Press 1946

[146] JACKSON, J.D., *Classical Electrodynamics* John Wiley and Sons, New York 1975